

Feedback Control of Brownian Motion for Single-Particle Fluorescence Spectroscopy

Thesis by

Andrew J. Berglund

In Partial Fulfillment of the Requirements
for the Degree of
Doctor of Philosophy



California Institute of Technology
Pasadena, CA

2007

(Defended September 27, 2006)

© 2007

Andrew J. Berglund

All Rights Reserved

Acknowledgements

My years in graduate school have been exciting, challenging, and above all, rewarding, and for all of these things I have my advisor to thank. Hideo has always given me the freedom to follow my instincts as a scientist, even from my very first days at Caltech when such trust could not have stemmed from anything more than good-natured optimism. His willingness to treat students as colleagues and not subordinates is a unique and extraordinary trait, and the experience of working with him through the formative years of my career as a scientist and his as an advisor has been incomparable.

My time at Caltech has been influenced almost as much by Hideo's guidance as an advisor as by the outstanding group of students and postdocs he has assembled. We have always had a close-knit group, and every member has brought something unique into the fold. Thank you to Ramon van Handel, Asa Hopkins, Nathan Hodas, Tony Miller, Nicole Czakon, Joe Kerckhoff, and to Luc Bouten, André Conjusteau, Andrew Doherty, J.M. Geremia, Chungsook Lee, Jennifer Sokol, Jon Williams, and Naoki Yamamoto. Much credit should go to Sheri Stoll, our peerless administrator, for keeping the group running seamlessly. Kevin McHale, whose addition to the experiment made an immediate positive impact, has been a top-notch lab partner and friend. Jason McKeever and Chin-Wen "James" Chou, group members in spirit, if not officially, have been great colleagues and great friends. And to the grad students I have worked with since day one: Mike Armen, John Au, Ben Lev, John Stockton, and Tim McGarvey, I can only say that wherever I go, I will be lucky to find just one person as talented, likeable, and, well, "foolish," as you guys.

My scientific perspective has been greatly enhanced by interactions with a number

of excellent researchers outside our group, including Erik Winfree, Niles Pierce, Bernie Yurke, Rob Phillips, Igor Mezic, Atac Imamoglu, Salman Habib, Miles Blencowe, Sean Andersson, Shimon Weiss, Adam Cohen, and W. E. Moerner. And life has been made much more enjoyable by a number of good friends, in particular, Nathan Lundblad and Ian Swanson at Caltech, and Austin Schenk, James May, and Chris Johnson, my best friends and medical cohorts, scattered across the country but never more than a phone call away.

Finally, thank you to my family. Thank you to my sisters, Kay and Liz and to your families; and thank you especially to my parents, John and Mary Kate, who I can say in full literality have loved, supported, and encouraged me for longer than I can remember. And to my wife Kim, my newest family member, thank you for not just putting up with my long hours and frequent distractions, but for marrying me along the way! I could not have asked for a more perfect person with whom to share my work, my thoughts, and my life.

Abstract

The stochastic Brownian motion of individual particles in solution constrains the utility of single-particle fluorescence microscopy both by limiting the dwell time of particles in the observation volume and by convolving their internal degrees of freedom with their random spatial trajectories. This thesis describes the use of active feedback control to eliminate these undesirable effects. We designed and implemented a feedback tracking system capable of locking the position of a fluorescent particle to the optic axis of our microscope, *i.e.*, capable of tracking the two-dimensional, planar Brownian motion of a free particle in solution. A full theoretical description of the experiment is given in the language of linear stochastic control theory. The model describes both the statistics of the tracking system and provides a generalization of the theory of open-loop Fluorescence Correlation Spectroscopy (FCS) that accounts for fluctuations in fluorescence arising from competition between diffusion and damping. We find excellent agreement between theory and experiment. Using fluorescent polymer microspheres as test particles, we find that the observation time for these particles can be increased by 2–3 orders of magnitude over the open-loop scenario. The system achieves nearly optimal performance for moderately fast-moving particles at very low fluorescent count rates, comparable to those of a single fluorescent protein molecule. The system can classify particles in a binary mixture based on a real-time estimate of their diffusion coefficients (differing by a factor of ~ 4), achieving 90% success using fewer than 600 photons detected over 120 ms. Future directions for both the experimental and theoretical techniques are briefly discussed.

Contents

Acknowledgements	iii
Abstract	v
Contents	vii
List of Figures	xi
List of Tables	xv
Preface	xvii
1 Introduction and Motivation	1
1.1 Why collect fluorescence from single molecules?	1
1.2 Fluctuations due to particle diffusion	2
1.3 Fluctuations due to photon counting statistics	6
1.4 Context and relation to other work	10
1.5 Publications from graduate work	13
I Theory	15
2 Feasibility Study: LQG Controller Design	17
2.1 State-space dynamics and position estimation	18
2.2 Optimal LQG control	23
2.3 Performance analysis	27

3	Sensing the Position of a Fluorescent Particle	33
3.1	Rate-modulated Poisson statistics	35
3.2	Power spectrum of a rate-modulated Poisson process	37
3.3	Application to position sensing	41
3.4	Autocorrelation functions: More statistics!	44
4	Tracking Limits: Photon Counting Noise	51
4.1	Static position estimation	52
4.2	Dynamic position estimation	57
4.3	Optimal position estimation	62
4.4	Numerical simulations	63
4.5	Commentary	67
5	Full Linear Theory of Closed-Loop Particle Tracking	71
5.1	Linear control system model	71
5.1.1	Specification of transfer functions	73
5.1.2	State-space realizations and the Fokker-Planck equation	75
5.1.3	Marginally stable systems	78
5.1.4	Statistics of $X(t)$ and $E(t)$ for low-order systems	80
5.2	Closed-loop Fluorescence Correlation Spectroscopy	83
5.2.1	Calculation of the fluorescence autocorrelation function	84
5.2.2	Recovery of open-loop results in the weak-tracking limit	87
5.2.3	Behavior of $g(\tau)$ for $\tau \approx 0$	88
5.2.4	Relation to other literature results	90
II	Experiment	91
6	Experimental Apparatus	93
6.1	Laboratory components	93
6.1.1	Optics	93
6.1.2	Sample volume	98

6.1.3	Electronics	100
6.1.4	Data acquisition and computer software	104
6.2	Calibration and diagnostics	107
6.2.1	Open-loop measurements	107
6.2.2	Measuring the error signal	112
7	Closed-Loop Particle Tracking	115
7.1	Closing the loop	115
7.2	Early experimental success	116
7.2.1	Tracking data	117
7.2.2	Estimation of D	118
7.2.3	Fluorescence fluctuations and Tracking-FCS	121
7.3	Tracking improvement	122
7.4	Comparison with the theory	128
8	Detailed Studies of a Binary Mixture	133
8.1	Raw data	133
8.2	Near-optimal tracking	147
8.3	Classification by diffusion coefficient estimation	150
8.3.1	Statistics of $\hat{D}_{\Delta t}$	151
8.3.2	Hypothesis testing	156
8.3.3	Results	158
8.4	Summary and commentary	160
A	Closed-Loop Correlation Spectroscopy with Internal State Transitions	163
A.1	Review of the scalar case and statement of the general problem	164
A.2	The commuting case $[\mathbb{F}_1, \mathbb{F}_2] = 0$	167
A.3	Adiabatic elimination of fast dynamics	170
A.4	Generalization of van Kampen's method to the noncommuting case	173
	References	179

List of Figures

1.1	Schematic diagram of a free-diffusion SMD apparatus	3
1.2	Single particle Brownian trajectory through a Gaussian laser	4
1.3	Fluorescence intensity fluctuations of a particle in a Gaussian laser	5
1.4	Signal-to-noise ratio SNR of the autocorrelation of a Poisson process given	9
2.1	Bode plot of the transfer function $T(s)$	19
2.2	Schematic diagram of the coordinates used for two-dimensional tracking	22
2.3	Bode diagrams of the transfer function $H_\lambda(s)$	27
2.4	Simulated tracking performance in two dimensions	28
2.5	Radial tracking error e_τ over a range of diffusion coefficients	29
3.1	Example of a rate-modulated Poisson process	34
3.2	Particle tracking coordinates in the reference frame of the laser	42
3.3	Mappings between the (ρ, θ) and (\hat{x}, \hat{y}) planes	43
3.4	$g_{\mathbf{x}}(\tau)$ for a single immobilized particle in a rotating laser	47
4.1	Expectation value of the position estimator $\mathbb{E}[\hat{x}_t]$	55
4.2	Numerical simulation of \hat{x}_t	57
4.3	Mean-square tracking error $\mathbb{E}[e_t^2]$ as a function of bandwidth B	58
4.4	Two-dimensional tracking simulation in the linear regime	64
4.5	Two-dimensional tracking simulation in the nonlinear regime	65
4.6	Numerical simulation showing tracked and untracked regimes	68
4.7	Tracking phase diagram in the D - B plane	69

5.1	Block diagram of the particle tracking control system.	72
6.1	Schematic diagram of the optics for single-particle tracking	94
6.2	Schematic diagram of the sample volume for single-particle tracking . .	99
6.3	Schematic diagram of the electronics for single-particle tracking	101
6.4	Controller transfer function implemented on the digital microcontroller	103
6.5	Open-loop transit of a 60 nm microsphere through the excitation volume	107
6.6	Open-loop transit of a 60 nm microsphere through a rotating excitation laser	108
6.7	Open-loop FCS curve	109
6.8	Open-loop FCS curve with the rotating laser	110
6.9	Measured laser intensity profile for the stationary beam	111
6.10	Measured laser intensity profile for the rotating beam	111
6.11	Measured error signal for closed-loop tracking	112
7.1	Bode plot of the closed-loop transfer function of the tracking system .	116
7.2	Qualitative shape of a closed-loop transfer function	117
7.3	Fluorescence intensity and sample stage position from an early tracking run	118
7.4	Diffusion coefficient estimate for the data in Fig. 7.3	119
7.5	Fluorescence correlation function for the data in Fig. 7.3	121
7.6	Improved tracking trajectory	124
7.7	Running diffusion coefficient estimates for the data shown in Fig. 7.6 .	125
7.8	Diffusion coefficient estimates $\hat{D}_{\Delta t}(X)$ and $\hat{D}_{\Delta t}(X)$ averaged over the 74 trajectories in our data set and plotted as a function of the sample time Δt	126
7.9	Fluorescence autocorrelation function recorded during tracking	127
7.10	Histogram of tracking trajectory lengths	128
7.11	Tracking trajectories of the same particle at different brightness values	129
7.12	Mean-square deviations for the trajectories in Fig. 7.11	130

7.13	Fluorescence autocorrelation functions $g(\tau)$ for the trajectories in Fig. 7.11	131
8.1	Data from a single shot of the binary mixture experiment	134
8.2	Data showing the controller reset procedure at the tracking boundaries.	135
8.3	Histogram of observed diffusion coefficients	137
8.4	Scatter plot of diffusion coefficients along the x and y directions	138
8.5	Comparison of the diffusion coefficient determined from the mean-square deviation and velocity autocorrelation of the sample stage.	139
8.6	Three-dimensional scatter plot of diffusion coefficient, excitation power, and confinement determined from $g(\tau)$	140
8.7	Excitation power versus total tracked time	141
8.8	RMS fluorescence during tracking	142
8.9	Mean-square deviation for one trajectory of each type of particle	143
8.10	Fluorescence autocorrelation functions $g(\tau)$	143
8.11	$g(\tau)$ for one trajectory of each type of particle	144
8.12	Comparison of feedback bandwidth parameters determined from $MSD(\Delta t)$ and $g(\tau)$	145
8.13	Comparison of measurement noise determined from $MSD(\Delta t)$ and $g(\tau)$	146
8.14	Inferred localization L versus D for 62 individual tracking trajectories	148
8.15	Comparison of the localization L determined from $MSD(\Delta t)$, $g(\tau)$, and g_0	149
8.16	Convergence of $\hat{D}_{\Delta t}$ as the number of samples is increased	152
8.17	Typical tracking trajectory showing T , Δt , $\Delta X_{\Delta t}$ and N used for particle classification	153
8.18	Diffusion coefficient estimates $\hat{D}_{\Delta t}$	155
8.19	χ^2 statistics of $\hat{D}_{\Delta t}$	156
8.20	Measured probability of correct classification P_{corr} as the estimation time T and the sample time Δt are varied.	158

8.21	Probability of correct identification as D_{th} and the number of samples N are varied.	159
8.22	Plot of the D - Γ parameter space for values relevant to single-molecule biophysics	161

List of Tables

4.1	Optimum localization error for a particle with diffusion coefficient D	61
5.1	Table of state-space realizations for the first- and second-order tracking model	81
7.1	Table of fit parameters for the mean-square deviation curves of Fig. 7.12 and fluorescence autocorrelation functions of Fig. 7.13.	132
8.1	Table comparing the localization determined from $MSD(\Delta t)$, $g(\tau)$, and g_0 for the 210 nm diameter particles	150
8.2	Table comparing the localization determined from $MSD(\Delta t)$, $g(\tau)$, and g_0 for the 60 nm diameter particles	151

Preface

I arrived at Caltech and joined the Mabuchi Lab on August 1, 2000. At that time, a few experiments were already underway in our corner of the Sloan sub-basement, but the “bio lab” in the back still contained nothing but an optical table populated by a HeNe laser, a single-photon counter and a few scattered optical filters. These were the skeletal beginnings of a single-molecule fluorescence experiment without a full-time experimenter. The nominal goal was to monitor some of Erik Winfree’s programmable DNA reactions. Because I had experience with single-photon counters, I decided this was a tractable opportunity to get involved in a project. My first week or two of experimental work at Caltech culminated in a detection efficiency calibration of two single-photon counting avalanche photodiodes (APDs) and an appreciation for the merits of absorptive versus reflective metallic neutral density filters.

Almost immediately, I launched into a serious experimental effort with crucial early tutelage from Erik Winfree. My goal was to build a confocal fluorescence microscope for collecting fluorescence from individual dye-labeled DNA molecules diffusing freely in buffer solution. On a memorable morning in April 2001, I saw the tell-tale bursts of fluorescence from individual DNA molecules. Fresh from Jeff Kimble’s Quantum Optics class, I thought it only natural that we should confirm that these fluorescence signals arose from individual (singly labeled) DNA molecules by investigating the photon statistics of the emitted fluorescence light: true single-molecule fluorescence should exhibit strong photon antibunching. So I built a Hanbury-Brown Twiss apparatus and succeeded in measuring not only photon autocorrelations but also cross-correlations from FRET-coupled dye pairs on individual DNA molecules. At that time, Andrew Doherty, then a postdoc in the group, sat me down and taught

me how to calculate photon correlation functions using the quantum regression theorem. With this tool, we could compare my measurements to our expectation based on the standard Forster theory of FRET. In addition to the expected photon antibunching, our photon statistics measurements contained interesting dynamical signatures in the nanosecond range (not predicted by a straightforward application of the Forster model) and demonstrated a capability to use FRET in order to monitor dynamics at these fast timescales. We published these results in *Physical Review Letters* in 2002 [1].

Following this experimental success, it was clear that we had a working experiment, but it was not immediately clear how to proceed. While Hideo and I could think of a host of interesting dynamical biomolecular processes to investigate with our new capability, none of these piqued my interest quite strongly enough (or seemed to exploit sufficiently my sensibilities as a quantitatively minded physicist) for me to begin a full experimental push. At this point, I began a period of scientific exploration and rumination. During this time I performed many preliminary measurements and simulations both individually and with other graduate students from other groups, in an effort to carve out a direction for our new experimental capability. It is a testament to Hideo's patience and confidence as an advisor that he allowed me to "shop around" and hone my interests during this period. Ultimately, I think my scientific efforts have been far more successful than they might have otherwise turned out had I not been given this opportunity.

I do not mean to imply that I was inactive during this exploratory period. On the contrary, I studied a range of problems, and many calculations and considerations deriving from this period ultimately resurfaced as useful components of my later work. With John Stockton, I made a foray into atomic physics, building stabilized diode lasers and putting together a magneto-optical trap as part of the (very) early stages of John's cesium experiments. More central to my own work, I investigated a variety of experimental, theoretical, and numerical ideas with varying degrees of success: integration of ultra-small microfluidic plumbing into our apparatus (with Dave Barsic and Axel Scherer); "heralded" single-photon generation from a FRET-coupled dye pair;

sequence-dependent mechanical dynamics in double-stranded DNA (together with Paul Wiggins, Andrew Spakowitz, Zhen-Gang Wang, and Rob Phillips); Bayesian quantum parameter estimation of energy transfer rates in a FRET system; FRET cascades between more than two dye molecules (with Saurabh Vyawahare and Stephen Quake); rapid micromixing designs for controlling chemical reaction kinetics (with Igor Mezic at UCSB); monitoring DNA “walkers” (with Suvir Venkataraman and Niles Pierce).

By the middle of 2003, my theoretical investigations of Bayesian estimation applied to single-molecule spectroscopy finally sparked a focused and very exciting experimental effort. After considering how to extract “all” the information about a dynamical parameter from a measurement record consisting of a stream of photon arrival times, I began to think seriously about how much information about a particle’s *position* can be derived solely from the fluctuations in photon arrival times as the particle explores a spatially varying excitation laser profile. One aspect of this project, estimation of a Brownian particle’s diffusion coefficient, was passed on to Kevin McHale, a graduate student who had recently joined the group. For my part, the idea of tracking a single fluorescent particle using a linear control law and a time-varying excitation laser intensity had crystallized into a full-blown experimental design. I wrote extensive simulations based on a realistic model of the response of our experimental apparatus, in order to investigate the feasibility and limits of a single-molecule tracking apparatus. Kevin and I wrapped up our parallel numerical studies and submitted two papers [2, 3] in two days in December 2003.

I indulged myself in one more diversion, a technical clarification really. In what was originally conceived as a comment or perhaps a letter to the editor and grew into a paper in the Journal of Chemical Physics [4], I pointed out that one should not immediately conclude that a measurement resulting in nonexponential statistics implies heterogeneity in molecular sample, since heterogeneity in the measurement apparatus can just as easily give such results.

That diversion aside, since 2004, I have been singularly focused on closed-loop particle tracking. A brief summary of the field and my own contributions to it are

contained in Sect. 1.4, and of course, a long and detailed description of such matters constitutes the remainder of this thesis.

Chapter 1

Introduction and Motivation

1.1 Why collect fluorescence from single molecules?

Large biological macromolecules, such as proteins and nucleic acids, are complex systems that exhibit stochastic dynamics over a huge range of timescales. Vibrational relaxation occurs in dye molecules as fast as 10^{-12} s; individual chemical subunits rotate and flex at characteristic timescales of 10^{-10} s; fluorescence lifetimes fall typically around 10^{-9} to 10^{-8} s; chemical binding kinetics and conformational transitions may occur over a large range from 10^{-6} s to 10^{-2} s (or more); additional optical processes such as forbidden transitions from singlet to triplet electron angular momentum states and slow phosphorescent emission may occur between 10^{-7} and 10^{-4} s; irreversible photobleaching may occur on similarly broad timescales between 10^{-3} and 10^1 s. Many of these isolated processes also exhibit multiscale power-law statistics, making them difficult to study even with a broadband experiment sensitive to a (relatively) large range of timescales.

In addition to the inherently multiscale nature of biological molecular dynamics, at the single-molecule level most of these dynamics are also *stochastic* and unsynchronized between distinct molecules. As a result, bulk measurements performed on large numbers ($\gtrsim 10^3$) of such molecules are simply not sensitive to the uncorrelated fluctuations of the individual components of the sample. Thus, broadband experiments with few- or single-molecule sensitivity are a necessity for resolving the complex dynamics of such systems.

Fluorescence microscopy shows great promise for satisfying the technical demands of broadband, single-molecule sensitivity. In a generic single-molecule fluorescence experiment, one wishes to measure some property of a molecular system by monitoring its laser-excited fluorescence. For example, if the rate of fluorescence from a biological macromolecule (perhaps a protein or nucleic acid) depends on its conformation through a clever arrangement of dye labels, then an experimenter can monitor the shape of this large biological molecule simply by collecting and recording its fluorescence [5]. Because bright fluorescent molecules exhibit excited-state emission lifetimes as short as one nanosecond, single-molecule fluorescence spectroscopy is, in principle at least, sensitive to these extremely fast timescales.

Even when such sensitivity is achievable, however, the extraction of useful information from inevitable noise processes (both technical and fundamental) can be quite a challenging statistical problem. While it may seem intuitively obvious that performing a measurement on a single particle locked to the experimental apparatus is preferable to a passive approach, the moderate increase in technical requirements for performing this task demands justification. In order to introduce and motivate the bulk of this thesis the next two sections discuss two sources of noise in single-molecule fluorescence experiments, stochastic particle motion and photon counting noise, both of which may be strongly suppressed using the single-particle tracking methods presented in later chapters.

1.2 Fluctuations due to particle diffusion

To begin, we will briefly discuss fluctuations in free-diffusion experiments arising from the Brownian motion of a particle within a tightly focused Gaussian laser. Consideration of these fluctuations leads very naturally to the basic equations of fluorescence correlation spectroscopy (FCS). The original literature references for FCS can be found in Refs. [6–8] and a very nice recent review is given in Ref. [9].

A schematic diagram of a typical free-diffusion single-molecule fluorescence experiment is shown in Fig. 1.1. An excitation laser is tightly focused into a liquid

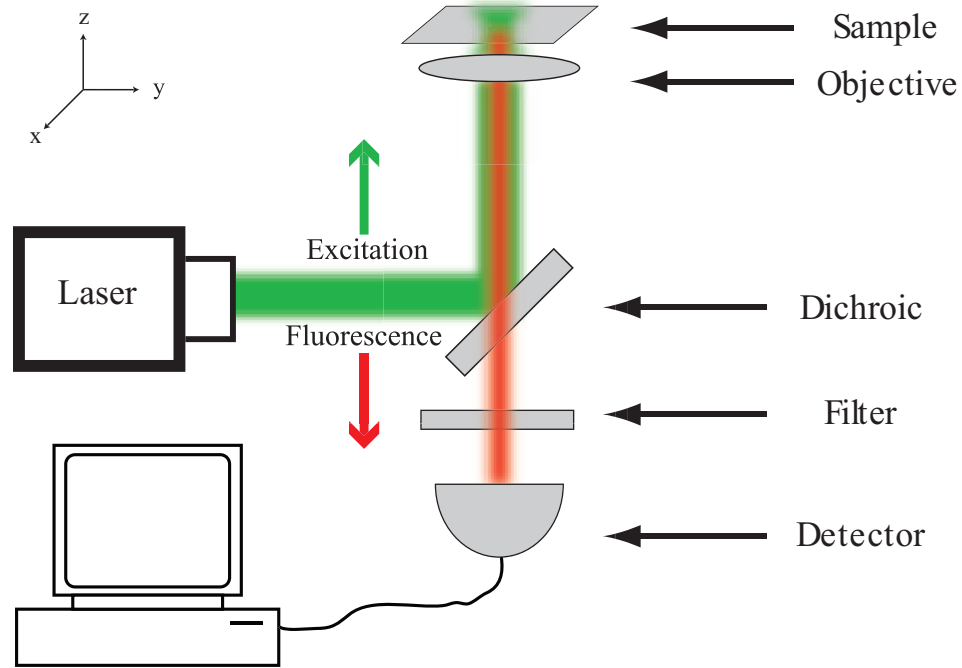


Figure 1.1: Schematic diagram of a typical free-diffusion single-molecule fluorescence detection apparatus.

sample using a high power microscope objective. The liquid sample contains a very low concentration of fluorescent molecules of interest, so that only a small number are present in the laser focus at any time. When a fluorescent molecule is present in the laser focus, it is strongly excited by the focused laser intensity and its (spectrally shifted) fluorescence is collected by the microscope objective, separated from the excitation light by a dichroic filter, further filtered with a bandpass filter, and detected using a single-photon detector or high-sensitivity CCD camera.

Of particular interest here is the Gaussian intensity profile of the excitation laser in the focus of the imaging optics. For most of this thesis, we will be concerned with very thin samples (in the direction of laser propagation) in which the laser intensity varies very little over the depth of the sample. In this *quasi-two-dimensional* geometry, we may neglect the motion of the particle in the (axial) z direction. However, the laser intensity profile $I(x, y)$ varies steeply in the x and y directions with a Gaussian

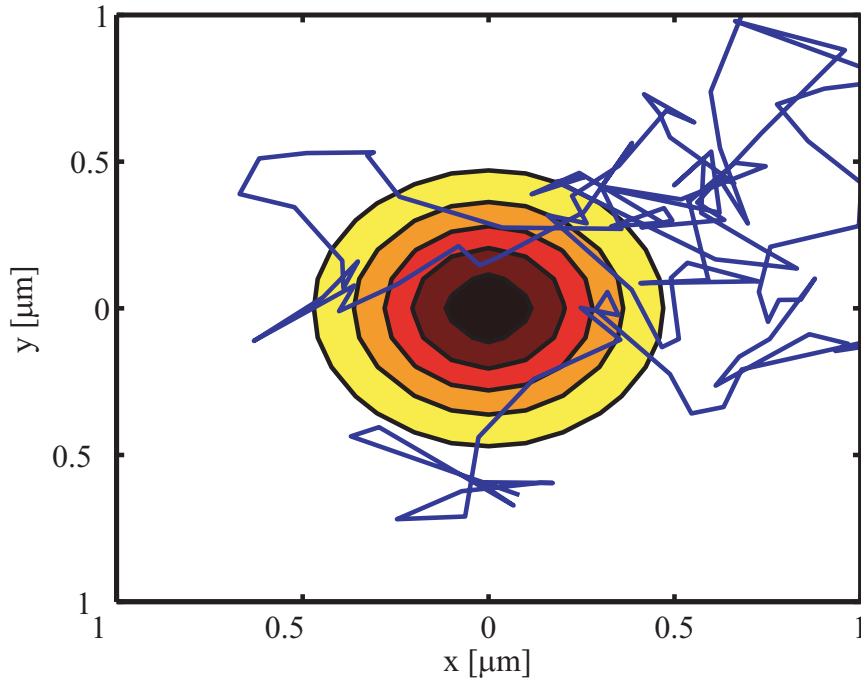


Figure 1.2: Simulated trajectory of a Brownian particle moving through a Gaussian laser with beam waist $w = 0.5 \mu\text{m}$. A contour plot of the laser intensity distribution is superimposed on the trajectory.

profile:

$$I(x, y) \propto \exp \left[-\frac{2}{w^2} (x^2 + y^2) \right], \quad (1.1)$$

where the beam waist w is typically in the range $0.5\text{-}1 \mu\text{m}$.

As long as a fluorescent particle is not excited so strongly that its fluorescence begins to saturate, then the rate of photon detections $\Gamma(t)$ from a particle at (time-dependent) position (X_t, Y_t) will simply be proportional to the laser intensity:

$$\Gamma(t) = \Gamma_0 \exp \left[-\frac{2}{w^2} (X_t^2 + Y_t^2) \right], \quad (1.2)$$

where Γ_0 parameterizes the photon count rate at the peak laser intensity. The actual number of photons collected in any time interval is again a random process, drawn from a Poisson distribution with rate $\Gamma(t)$. The results of a simple simulation of this process are shown in Figs. 1.2-1.3. The main point here is that a particle in a

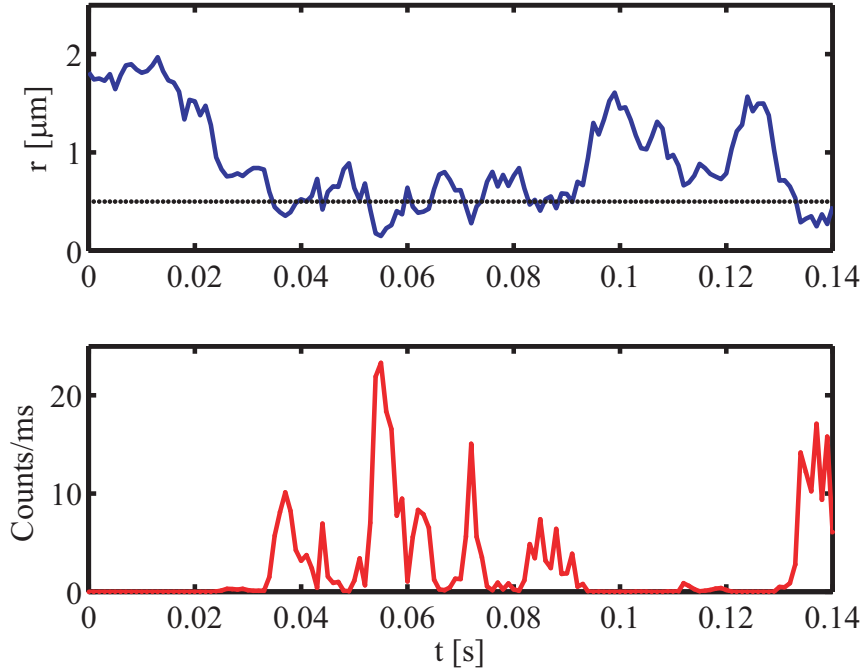


Figure 1.3: Simulated fluorescence intensity fluctuations for the same trajectory displayed in Fig. 1.2. The upper plot shows the radial distance $r = \sqrt{x^2 + y^2}$ of the particle from the laser centroid, and the lower plot shows the fluorescence intensity. The parameters used for the simulation were diffusion coefficient $D = 10 \mu\text{m}^2/\text{s}$, beam waist $w = 0.5 \mu\text{m}$, and peak fluorescence intensity $\Gamma_0 = 28000 \text{ s}^{-1}$. The beam waist w is indicated by the dotted line in the upper plot.

Gaussian laser exhibits strong fluorescence fluctuations as it moves randomly through the spatially-varying excitation intensity.

In an experimental scenario, correlation spectroscopy is a natural method for analyzing fluctuations such as those shown in Fig. 1.3 and we may calculate the expectation value of such a correlation function relatively easily. A comparison between data and theory then gives a simple method for extracting parameters such as the diffusion coefficient D from the data (provided the beam waist w , which sets the length scale of the measurement, is well calibrated). For the case presented here, if we denote the time-dependent fluorescence signal by $f(t)$, then the normalized autocorrelation

function $g(\tau)$ is found to be

$$g(\tau) = \frac{\langle f(t)f(t+\tau) \rangle_t}{\langle f(t) \rangle_t^2} - 1 = \frac{1}{\bar{N}} \left(1 + \frac{\tau}{\tau_D} \right)^{-1}, \quad \tau_D = \frac{w^2}{4D} \quad (1.3)$$

where $\langle \rangle_t$ denotes a time average and \bar{N} parameterizes the average number of particles in the laser focus, *i.e.*, it is the sample concentration in units of the observation volume.

In an open-loop FCS experiment of the type described here, by fitting the observed autocorrelation function to Eq. (1.3) one can extract the *diffusion time* τ_D , and if the beam waist w is known, then the particle's diffusion coefficient D can also be determined. In practice, it is quite difficult to determine D with high accuracy due to the difficulty in determining w and the deviations of real lasers from ideal Gaussian form; neither of these difficulties exist in the closed-loop tracking case, as we will see in later chapters.

The simple form of Eq. (1.3) will be generalized in later chapters to account for the statistics of a *tracked* or *trapped* fluorescent particle. In particular, Ch. 5 contains a detailed discussion of fluorescence correlation functions and methods of calculation. We will see that these fluctuations may be eliminated, or at least strongly suppressed, by tracking a single particle using the methods in this thesis. Tracking a particle by actively locking it to the laser focus decouples the motion of the particle from fluorescence fluctuations, thus simplifying the analysis of both data channels (the particle's position and fluorescence fluctuations).

1.3 Fluctuations due to photon counting statistics

In addition to suppressing fluorescence fluctuations arising from particle diffusion and enabling direct observation of a particle's motion, single-particle tracking methods also extend the length of time that an individual particle can be observed. For example, in an open-loop FCS experiment, the typical transit time for a molecule across the laser focus is measured in milliseconds; on the contrary, we will demonstrate

the capability to track and observe individual fluorescent particles for up to 100 s. Such increased observation times have dramatic consequences for suppressing photon counting noise. In this section, I will give some general arguments about photon counting statistics in order to make this statement concrete.

The measurement record in a fluorescence photon-counting experiment is a list of photon arrival times or a sequence of (integral) photon numbers arriving in time bins of specified length (the latter can always be derived from the former but not *vice versa*). Ignoring non-classical, *i.e.*, quantum mechanical, photon statistics for the moment, we may represent a generic fluorescence photon arrival stream as a Poisson process with a time-dependent *rate* of photon arrivals denoted by $\Gamma(t)$. It is the goal of an experimenter to measure the statistics of this rate $\Gamma(t)$. However, even for the brightest dye molecules, one may typically collect at most a few tens of thousands of photons per second during a single-molecule fluorescence experiment. Statistical fluctuations in the rate of photon arrivals are always of fundamental importance in such experiments, and considerations of photon counting noise set limits on the dynamical timescales that are accessible in any experiment.

Let us quantify these statements. Suppose for simplicity that the rate of photon arrivals in some experiment is constant $\Gamma(t) = \Gamma$ and that data is recorded for a total time T . The dynamics of a fluctuating rate may be assessed by binning the data into N time intervals of length $\Delta t \ll T$ and calculating a correlation function. Let n_k be the number of photons arriving in the k th time interval of length Δt , and let our correlation function, denoted by g_m , be defined as

$$g_m = \sum_{k=1}^{N-m} n_k n_{k+m}. \quad (1.4)$$

For large T , compared to Δt , the total number of time intervals is approximately $N \approx T/\Delta t$, and for small m we may neglect the difference between $N - m$ and N .

Using basic Poisson properties ($\mathbb{E}[\cdot]$ denotes an expectation value)

$$\mathbb{E}[n_k] = \Gamma \Delta t \quad (1.5a)$$

$$\mathbb{E}[n_j n_k] = \begin{cases} (\Gamma \Delta t)^2 & , \quad j \neq k \\ (\Gamma \Delta t)^2 + \Gamma \Delta t & , \quad j = k \end{cases} \quad (1.5b)$$

we find the average value of the correlation function

$$\mathbb{E}[g_m] \approx N \Gamma \Delta t = \Gamma^2 T \Delta t \quad , \quad (m \neq 0), \quad (1.6)$$

while the variance in g_m is found to be

$$\mathbb{E}[g_m^2] - \mathbb{E}[g_m]^2 = \Gamma^2 T \Delta t (1 + 2\Gamma \Delta t) \quad , \quad (m \neq 0). \quad (1.7)$$

The *signal-to-noise* ratio for resolving this correlation function is therefore given by

$$SNR = \frac{\mathbb{E}[g_m]}{\sqrt{\mathbb{E}[g_m^2] - \mathbb{E}[g_m]^2}} = \sqrt{\frac{\Gamma^2 T \Delta t}{1 + 2\Gamma \Delta t}}. \quad (1.8)$$

It is important to note that Eq. (1.8) is only valid for Δt smaller than T , and in fact it is not even sensible to calculate a correlation function with a time resolution Δt larger than the entire measurement interval. Although it is somewhat loose as Δt approaches T , let us take Eq. (1.8) together with the ansatz that $\Delta t < T/2$ is the signal-to-noise ratio for a fluorescence correlation measurement.

SNR is plotted in Fig. 1.4 for $\Gamma = 5000 \text{ s}^{-1}$ (a typical value for a fluorescent protein), as a function of the time resolution Δt for three different values of the observation time T . Note that $T = 0.01 \text{ s}$ is a typical diffusion time for a biological molecule through a diffraction-limited laser focus, while the closed-loop tracking methods described in this thesis are capable of achieving $T = 100 \text{ s}$ or greater.

A few features of SNR given by Eq. (1.8) deserve mention. For small bin times

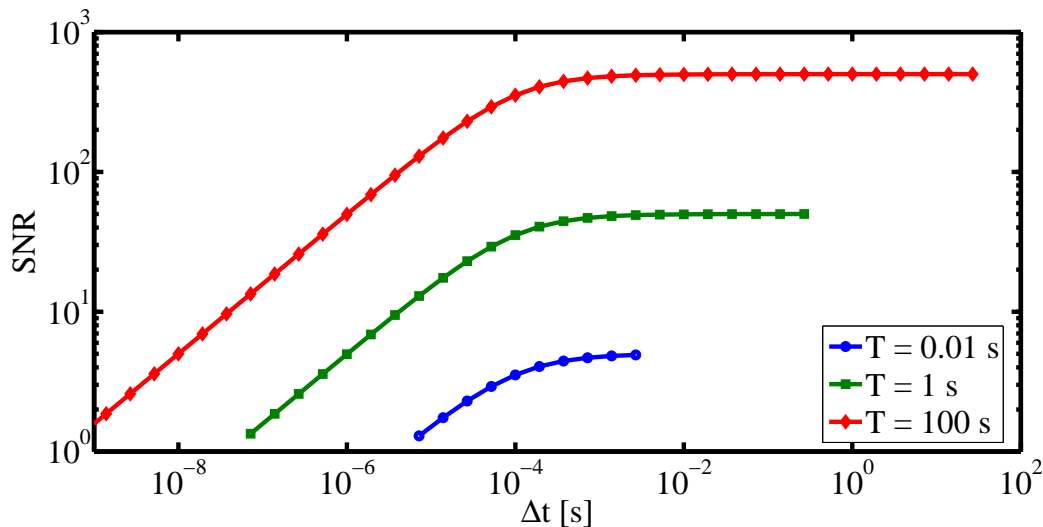


Figure 1.4: Signal-to-noise ratio SNR of the autocorrelation of a Poisson process given by Eq. 1.8. The photon arrival rate was taken to be $\Gamma = 5000 \text{ s}^{-1}$, a modest fluorescence count rate achievable with dye molecules or intrinsically fluorescent proteins.

Δt , the signal-to-noise ratio is approximately given by

$$SNR \approx \Gamma \sqrt{T \Delta t} \quad , \quad \Gamma \Delta t \ll 1. \quad (1.9)$$

At fixed count rate Γ , this expression depends only on the product $T \Delta t$ so that a decrease in the timescale Δt requires a proportional increase in T to maintain the same signal-to-noise ratio; conversely, an order of magnitude improvement in observation time leads directly to an order of magnitude improvement in time resolution (at short timescales). On the contrary, for long bin times, the signal-to-noise ratio is given by

$$SNR \approx \sqrt{\frac{\Gamma T}{2}} \quad , \quad \Gamma \Delta t \gg 1, \quad (1.10)$$

independent of Δt . As mentioned above, the largest measurable timescale Δt is proportional to T (we took $\Delta t < T/2$ above), so that again an increase in observation time T leads to a proportional increase in accessible time intervals Δt (now at long timescales). These improvements in the observation time of a single particle drasti-

cally improve the experimentally resolvable dynamic regime, both at small and large timescales Δt . For the 4 orders of magnitude improvement in T shown in Fig. 1.4, we gain 8 orders of magnitude in experimentally accessible dynamical regimes (4 orders of magnitude towards each of the large and small Δt sides). It is precisely this massive improvement in dynamical resolution that motivates the development of single-particle tracking methods. These methods may one day provide paradigm-shifting alterations in the accessible dynamic regimes of single-molecule fluorescence experiments.

1.4 Context and relation to other work

From the arguments in Sects. 1.2 and 1.3, we see that locking a fluorescent particle to the focus of a fluorescence microscope enables a number of new experimental advantages. First, the particle’s stochastic motion becomes decoupled from its fluorescence fluctuations, and second, increased observation times provide significantly enhanced signal-to-noise ratios over a broad range of timescales. These are the primary motivations for developing the experimental and theoretical techniques presented in this thesis. Of course, we are not the only people working in this new field, and the work of a few other groups deserves mention here. Some of these provided motivation for the present work, while others represent concurrent research that complements the results described here.

An early and seminal application of feedback control applied to biological physics came 35 years ago with Howard Berg’s apparatus for holding a swimming bacterium in the focus of an optical microscope using a six-channel photodetector and a homemade electromechanical actuator [10]. His paper is enjoyable to read, and the dramatic achievements of his feedback controller are evident: “The scene through the [microscope’s] binocular is extraordinary” he writes. Without explicitly referencing them, Berg describes about many of the control-theoretic considerations considered in this thesis: control loop design, feedback bandwidth, signal-to-noise ratio, oscillation, and instability. In an amusing final comment, he even laments the difficulty of storing

and processing the copious amounts of data that can be generated in a locked experimental apparatus. Though data storage technology has changed substantially since 1971, this problem has no doubt cropped up for anyone who has closed a feedback loop and fully automated an experiment.

More recently, in 1997, Ha *et al.* built a computer-controlled apparatus for locating and locking onto the position of an individual dye-labeled DNA molecule bound to a glass cover slip [11]. Their method involved a rather complicated search-and-optimization algorithm used to locate and lock immobilized particles with typical rise-times of 200 ms, corresponding to a feedback bandwidth of approximately $1/2\pi \times (200 \text{ ms})^{-1} = 0.8 \text{ Hz}$ at fluorescent count rates of a few tens of kHz.

In 2000, Enderlein published a single-molecule (two-dimensional) tracking proposal in which he introduced the use of a spatially modulated excitation intensity to encode a particle's position in a high frequency component of the fluorescence signal [12]. He proposed to rotate the excitation laser (with Gaussian beam waist w) in a circular pattern at a radius r and intuited that good performance could be achieved for $r/w = 0.6$. (In Chapter 4, I will show that optimal localization is in fact achieved for $r/w = 1/\sqrt{2} \approx 0.7$.) Furthermore, he used Monte Carlo simulations to investigate particle escape probabilities. In another 2000 paper, Enderlein used his simulations to explore the fluorescence fluctuations arising during such a tracking experiment [13]. To my knowledge, that paper is the only work other than my own to discuss closed-loop fluorescence correlation spectroscopy. The analytical results presented in Chapter 5 thoroughly characterize these statistics and constitute an important part of this thesis. In a subsequent theoretical study, Andersson [14] studied the use of nonlinear signal processing and control for three-dimensional fluorescent particle tracking. In 2002, Decca *et al.*, demonstrated a technique for localizing test objects driven with computer control by rotating a near-field scanning probe [15].

Significantly, in a series of papers beginning in October 2003, the group of E. Gratton developed a version of Enderlein's proposal, modified for both two- and three-dimensional geometry [16–19]. They demonstrated the ability to track bright, slowly moving objects with high spatial accuracy and performed biological measurements of

chromatin dynamics in a cellular environment using these techniques. Another recent contribution to the field has come from H. Yang’s group, in which near-infrared scattering from metallic particles was used to track their three-dimensional motion [20] while fluorescence in the visible range was recorded. They do not use any modulation techniques, but rather derive their position sensitivity using quadrant avalanche photodiodes and DC signal levels. Furthermore, they have derived and simulated change-point detection algorithms for searching a tracking trajectory and identifying changes in the diffusion coefficient [21].

Finally, the Anti-Brownian Electrophoretic “ABEL” trap developed by Adam Cohen and W. E. Moerner deserves mention as a creative and important component of today’s literature in the field of single-particle closed-loop control [22–24]. They detect the position of a fluorescent object using either CCD cameras or spatial modulation techniques and trap the object using voltage-actuated fluidic forces.

My own contributions to this field began in December 2003 when (unaware of the concurrent work in Gratton’s group) Hideo and I submitted our paper “Feedback controller design for tracking a single fluorescent molecule” to Applied Physics B, in many ways as a follow-up to Enderlein’s 2000 paper in the same journal. In that work, presented in Ch. 2, we considered a realistic plant transfer function as a component of the particle tracking apparatus. We designed an optimal control law using LQG methods, and performed extensive numerical simulations based on this control law. The simulations showed that such methods were more than sufficient for tracking relatively dim and fast moving particles.

Since then, my work has been focused on the tracking problem with experimental success first announced in an Optics Express paper published in 2005 [25]. That paper contains the skeletal beginnings of the theory of closed-loop particle tracking and correlation spectroscopy presented in full detail in Ch. 5. From there, I developed a simple framework for calculating noise figures based on photon counting noise and derived the representation of a tracked particle by Ornstein-Uhlenbeck diffusion statistics using a Kalman filter, which was published in Applied Physics B in 2006 [26]. These results also lay to rest the notion that complex signal processing (for

example, dedicated fast Fourier transform hardware or nonlinear computation) is required for extracting the frequency components of a rate-modulated stream of photon pulses. In 2005, Kevin McHale began working full time on the experiment. Together, we made marked improvements in signal processing and overall experimental stability culminating in June 2006 when much of the data presented chapters 7 and 8 was collected, and submitted as Refs. [27, 28].

It is now an exciting time to work in this new field of closed-loop particle control. Only a few groups have yet contributed to this budding field, and the landscape is ripe for rapid technological and concomitant scientific progress. In this light, it is of primary importance to develop a consistent theoretical framework and vocabulary for discussing these new techniques. When fluorescence correlation spectroscopy (FCS) was introduced by Magde, Elson, and Webb in 1972 [6–9], their elegant statistical description of the technique was just as important as the experimental methods. In fact, it is my belief that their tidy theoretical framework and the resulting simplicity of experimental interpretation has led to the explosion of applications of FCS over the intervening decades. Although the new techniques of particle trapping and tracking are *feedback control* problems, very little of the substantial theoretical apparatus of control theory has been applied in this field. In fact, many of the papers mentioned above do not even use the word “feedback” in reference to their experimental technique. I consider the establishment of a control-theoretic language for closed-loop particle tracking and the demonstration of its quantitative predictive power to be my ongoing contribution to this field.

1.5 Publications from graduate work

The following is a list of publications based at least in part on my work as a graduate student in the Mabuchi lab [1–4, 25–29]. Those denoted by (*) are primary topics of this thesis. Available preprints and reprints can be found online at <http://minty.caltech.edu/papers>.

1. Andrew J. Berglund, Andrew C. Doherty, and Hideo Mabuchi, “Photon statis-

- tics and dynamics of Fluorescence Resonance Energy Transfer,” *Phys. Rev. Lett.* **89**, 068101 (2002).
2. *Andrew J. Berglund and Hideo Mabuchi, “Feedback controller design for tracking a single fluorescent molecule,” *Appl. Phys. B* **78**, 653-659 (2004).
 3. Kevin McHale, Andrew J. Berglund, and Hideo Mabuchi, “Bayesian estimation for species identification in single-molecule spectroscopy,” *Biophys. J.* **86**, 3409-3422 (2004).
 4. Andrew J. Berglund, “Nonexponential statistics of fluorescence photobleaching,” *J. Chem. Phys.* **121**, 2899-2903 (2004).
 5. *Andrew J. Berglund and Hideo Mabuchi, “Tracking-FCS: Fluorescence correlation spectroscopy of individual particles,” *Opt. Express* **13**, 8069-8082 (2005).
 6. *Andrew J. Berglund and Hideo Mabuchi, “Performance bounds on single-particle tracking by fluorescence modulation,” *Appl. Phys. B* **83**, 127-133 (2006).
 7. Kevin McHale, Andrew J. Berglund, and Hideo Mabuchi, “Near-optimal dilute concentration estimation via single-molecule spectroscopy,” *in preparation*, (2006).
 8. *Andrew J. Berglund, Kevin McHale, and Hideo Mabuchi, “Feedback localization of freely diffusing fluorescent particles near the optical shot-noise limit,” to appear in *Opt. Lett.* (2006).
 9. *Andrew J. Berglund, Kevin McHale, and Hideo Mabuchi, “Fast classification of freely diffusing fluorescent nanoparticles,” *in preparation* (2006).

Part I

Theory

Chapter 2

Feasibility Study: LQG Controller Design

In this chapter, we present a numerical feasibility study, in which a full simulation of the proposed tracking experiment with a realistic (finite bandwidth, inertial) actuator is presented. This study, performed in 2003 and published in 2004 [2], contains few analytical results, and historically served essentially to convince us that our intuition about tracking a particle was correct, *i.e.*, that the experiment “should work.” This chapter is taken with only minor modification from Ref. [2].¹

We consider tracking a single particle as a feedback controller design problem. We propose a realistic design for tracking the motion of a particle diffusing in two dimensions with a confocal microscope and analyze its performance by numerical simulation. To estimate the position of a particle which is assumed to be near the laser centroid, the beam is rotated in a circle and a pair of integral transforms of the fluorescence intensity over the rotation period provide estimates of the particle’s coordinates perpendicular to the axis of rotation. The position estimate is then fed back to a piezoelectric translation stage with a frequency-dependent gain and phase. We utilize techniques from optimal control theory, which naturally incorporate realistic limitations such as the response bandwidth of the translation stage and fluorescence signal-to-noise ratios. Our design goal is a controller that can track the two-dimensional position of a particle with a diffusion coefficient $D = 10 \mu\text{m}^2/\text{s}$ (a

¹*N.B.* The definition of diffusion coefficient D used in Ref. [2] does not conform to the literature convention: it should be replaced everywhere with $2D$. That correction has been made here.

typical value for a protein in a bilipid membrane) using a commercially available translation stage. We will show however, that the controller exceeds this criterion by at least an order of magnitude even for limited motion in a third direction. Furthermore, the values of D which can be tracked are limited by the response bandwidth of the xy translation stage, so that a faster stage immediately results in faster tracking.

In Sect. 2.1 the state-space formulation of the particle-plus-translation stage system is introduced and a procedure for estimating the two-dimensional position of a fluorescent particle is described. In Sect. 2.2 we treat the system as a target-tracking problem and present the design of a feedback controller using techniques of optimal control theory. In Sect. 2.3, we perform numerical simulations of the system over a wide range of experimental parameters. We indicate the apparent robustness of this protocol for tracking fast particles with large diffusion coefficients and present surprising results concerning the ability to track in three dimensions under rather general conditions.

2.1 State-space dynamics and position estimation

The standard form for a linear, stochastic dynamical system in state-space is

$$d\mathbf{x} = \mathbf{A}\mathbf{x}dt + \mathbf{B}\mathbf{u}dt + d\mathbf{w}_1 \quad (2.1a)$$

$$\mathbf{v}dt = \mathbf{C}\mathbf{x}dt + d\mathbf{w}_2 \quad (2.1b)$$

where the system state is $\mathbf{x}(t)$, the control input is $\mathbf{u}(t)$ and the measurement is $\mathbf{v}(t)$ [30]. Stochastic noise is introduced by the white-noise increments $d\mathbf{w}_1$ and $d\mathbf{w}_2$. In this section we formulate the dynamics of particle tracking in one dimension in the form of Eqs. (2.1a-2.1b) when the particle's position can be directly measured. A feedback controller then involves the combination of a two-dimensional, fluorescence-based position *estimator* (to replace the unattainable direct measurement) with optimal feedback strategies based on two copies of the tracking dynamics developed in this section.

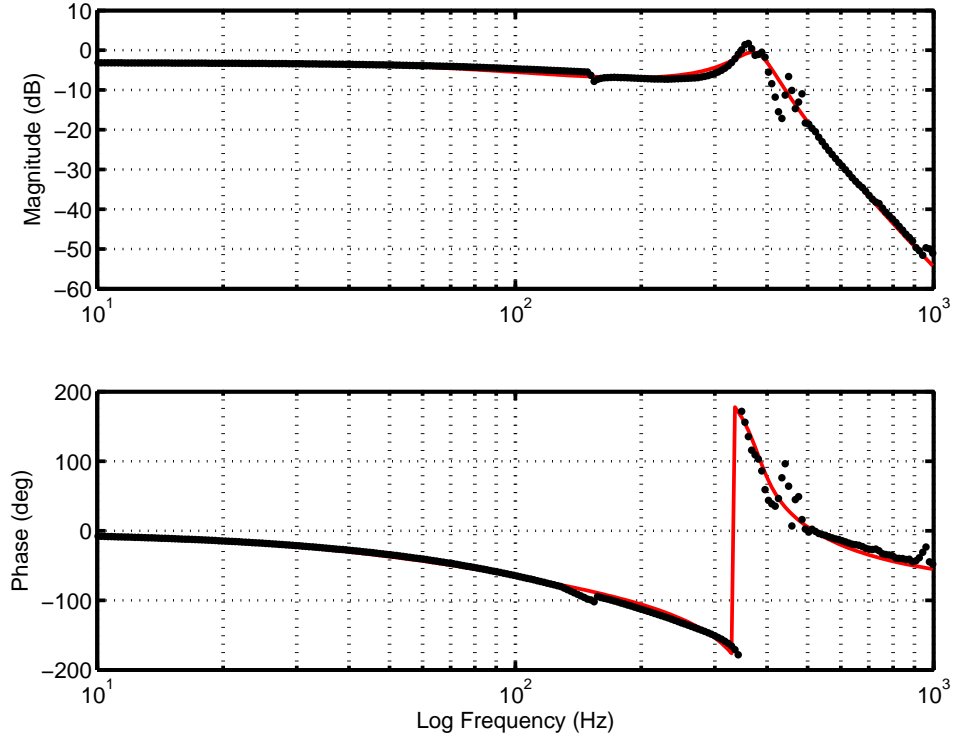


Figure 2.1: Bode plot of the transfer function $T(s)$ from the voltage input of our translation stage to a capacitive position-sensor output. Dots indicate the measured response and the solid line is a fit with $m = 0$ and $n = 5$. In the lower plot, the phase response wraps around at $\pm 180^\circ$.

First we consider one-dimensional Brownian motion of a fluorescent particle. The coordinates that specify the system state are the particle's position $x_P(t)$ within the sample and the displacement of the sample stage $x_S(t)$. The particle's position $x_P(t)$ is driven by Brownian motion through the stochastic differential equation

$$dx_P(t) = \sqrt{2D}dW_x(t) \quad (2.2)$$

where D is the particle's diffusion coefficient and $dW_x(t)$ is an infinitesimal Wiener increment with mean 0 and variance dt [31]. The voltage input $u_x(t)$ to an electro-mechanical actuator such as a piezoelectric device drives the stage coordinate $x_S(t)$. Since any realistic mechanical actuator will suffer from inertial effects and finite-bandwidth response, the full system state must also include higher-order time derivatives of $x_S(t)$. The linear response of $x_S(t)$ to an input $u_x(t)$ is characterized by the

transfer function $T(s)$ which relates the Laplace transforms $X_S(s)$ and $U_x(s)$. (We will use capital letters to denote the Laplace transform of a function. The complex argument s of the Laplace transform should not be confused with the subscript index S , indicating the translation stage coordinates.) For most well-behaved systems, we may write the transfer function $T(s)$ as

$$X_S(s) = T(s)U_x(s) = \frac{p_0 + p_1s + \cdots + p_ms^m}{q_0 + q_1s + \cdots + q_{n-1}s^{n-1} + s^n}U_x(s). \quad (2.3)$$

The coefficients p_j and q_j in Eq. (2.3) can be determined by fitting the measured swept-sine response of the system to an n th order transfer function. We assume $n \geq m \geq 1$ so the system is *proper* and non-trivial. Furthermore, we require that the polynomial in the numerator of Eq. (2.3) has no roots in the right half of the complex s -plane so that the controller is internally stable. In our experiments, we use a commercially available piezoelectric translation stage (see Sect. 6.1) whose frequency response is shown in Fig. 2.1 along with a fit to the data. We find a serviceable fit with $m = 0$ and $n = 5$. If we desire a closer representation of the response around the resonance at 360 Hz we may always use higher-order fits, so long as they represent proper, stable systems as defined above. For all of the remaining calculations, we will use this fit as our plant transfer function $T(s)$.

The inverse Laplace transform of Eq. (2.3) represents an ordinary differential equation relating $x_S(t)$ to $u_x(t)$. Taking the control input $\mathbf{u}(t)$ to be the highest relevant time derivative of the input voltage $u_x(t)$

$$\mathbf{u}(t) = \frac{d^m}{dt^m}u_x(t) \quad (2.4)$$

and including $x_P(t)$, $x_S(t)$ and its first $n - 1$ derivatives, and $u_x(t)$ and its first $m - 1$ derivatives in the state vector $\mathbf{x}(t)$, we may immediately write the matrices \mathbf{A} and \mathbf{B} representing the deterministic dynamics in Eq. (2.1a). The stochastic increment $d\mathbf{w}_1$ drives $x_P(t)$ according to Eq. (2.2) Finally, we consider a noisy (but direct) position

measurement

$$\mathbf{v}(t)dt = v_x(t)dt = [x_P(t) - x_S(t)]dt + \sigma_v dW_v(t) \quad (2.5)$$

which defines \mathbf{C} and $d\mathbf{w}_2$. Finally we let

$$\Sigma_j dt = \mathbb{E}[d\mathbf{w}_j d\mathbf{w}_j^T] \quad (2.6)$$

be covariance matrices for $j = 1, 2$, where E denotes the expectation value over noise realizations, and T represents the matrix transpose. The state-space dynamical system of Eqs. (2.1a-2.1b) is now fully specified by the diffusion coefficient D , measurement noise σ_v , and the coefficients p_j and q_j .

Some general features of the dynamical system are immediately apparent from the preceding specification. Along the diagonal, \mathbf{A} will naturally partition into blocks of size 1×1 , $n \times n$, and $m \times m$ corresponding to the dynamics of $x_P(t)$, $x_S(t)$, and $u_x(t)$ respectively. The coefficients p_j fill an off-diagonal block corresponding to the coupling between $x_S(t)$ and $u_x(t)$, while $x_P(t)$ is not coupled to the other coordinates. As formulated here, this system is not *minimal* since it contains the uncontrollable state $x_P(t)$. However, we consider the benefit of using an explicit representation of all coordinates to outweigh the technical advantages of a minimal formulation. In the special case $m = 0$ we simply set $\mathbf{u}(t) = u_x(t)$ and omit the dimensions of the other matrices corresponding to the $m \times m$ block in \mathbf{A} .

For the remainder of this section, we will describe a procedure for approximating the measurement $\mathbf{v}(t)$ of Eq. (2.5) for each of two spatial dimensions. The coordinate system is shown in Fig. 2.2. The particle's coordinates are $(x_P(t), y_P(t))$ and the sample stage coordinates are $(x_S(t), y_S(t))$, where all coordinates are defined relative to the origin O , which is fixed in the laboratory frame. We consider a Gaussian laser beam with beam waist w focused into the plane of Fig. 2.2 and rotating around an axis normal to the plane and passing through $(x_S(t), y_S(t))$. The laser rotates with a radius r at angular frequency $\omega_0 = 2\pi/T$. We envision an experimental setup in which the laser is made to rotate using acousto-optic modulators (AOMs), so that rotation frequencies in the 10 – 50 kHz range are easily obtainable. Defining Γ_B as

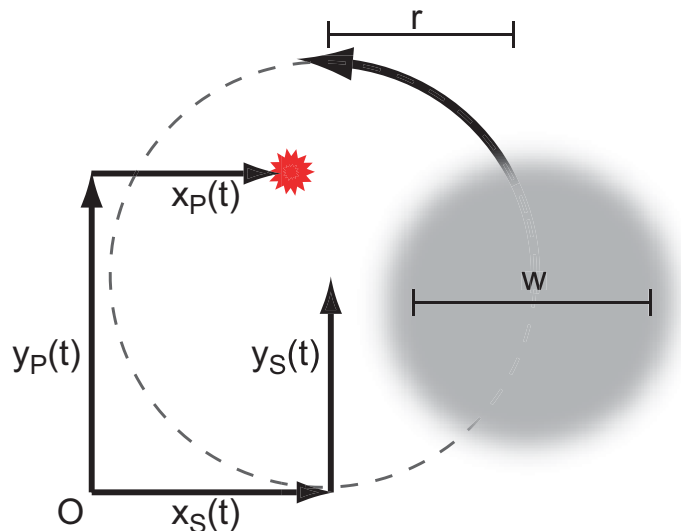


Figure 2.2: Schematic diagram of the coordinates used in the two-dimensional tracking model of Sect. 2.2. All coordinates are referenced to a fixed origin O in the lab frame.

the rate of background photon detections and Γ_0 as the rate of fluorescence photon detections from a particle at the maximum laser intensity, the time-dependent photon detection rate is given by $\Gamma(t)$:

$$\begin{aligned} \Gamma(t) = & \Gamma_0 \exp \left[-\frac{2}{w^2} (x_P(t) - x_S(t) - r \cos(\omega_0 t))^2 \right] \\ & \times \exp \left[-\frac{2}{w^2} (y_P(t) - y_S(t) - r \sin(\omega_0 t))^2 \right] + \Gamma_B. \end{aligned} \quad (2.7)$$

The actual number of detected photons in any time interval is a Poisson process with instantaneous rate given by $\Gamma(t)$.

To find a position estimator, we assume that the particle is close to the laser's axis of rotation and that the rotation period T is fast compared to the motion of both the particle and the stage. Under these assumptions, we may treat the particle's coordinates as fixed, and expand Eq. (2.7) to find a linearized count rate $\tilde{\Gamma}(t)$:

$$\tilde{\Gamma}(t) = \tilde{\Gamma}_0 + \Gamma_B + \frac{4\tilde{\Gamma}_0}{w^2} (x_P - x_S) r \cos(\omega_0 t) + \frac{4\tilde{\Gamma}_0}{w^2} (y_P - y_S) r \sin(\omega_0 t). \quad (2.8)$$

From Eq. (2.8) we see that within the previous assumptions, good estimates \hat{x}_P and \hat{y}_P of x_P and y_P are given by

$$v_x(t) \equiv \hat{x}_P(t) - x_S(t) = \frac{w^2 \int_0^T \Gamma(t) \cos(\omega_0 t) dt}{2r \int_0^T \Gamma(t) dt} \quad (2.9a)$$

$$v_y(t) \equiv \hat{y}_P(t) - y_S(t) = \frac{w^2 \int_0^T \Gamma(t) \sin(\omega_0 t) dt}{2r \int_0^T \Gamma(t) dt}. \quad (2.9b)$$

Eqs. (2.9a-2.9b) define the position estimator, which consists only of normalized cosine and sine transforms of the measured signal over the rotation period T . These transforms could be implemented digitally and phase locked with the same signal that drives the laser rotation, or analog integrations could be performed continuously with a reset signal phase locked to the laser drive frequency. In either case, the algorithm gives an estimate $v_x(t)$ of $x_P(t) - x_S(t)$ which corresponds to the measurement term $\mathbf{v}(t)$ in the dynamics of Sect. 2.1.

2.2 Optimal LQG control

In this section, we will apply some standard results from optimal control theory to estimating the system state $\mathbf{x}(t)$ and feeding back to the control inputs. Again, we will start in one dimension since, aside from the position estimation of Eqs. (2.9a-2.9b), the x and y dynamics are uncoupled. Furthermore, we will make all of our arguments in continuous time, relying on the assumption that the period T of the integral transforms in Eqs. (2.9a-2.9b) is small compared to the diffusion timescale. All of the following arguments can be formulated in discrete time, but the notation is simpler in continuous time, and we will see in Sect. 2.3 that the resulting controller performance justifies this assumption for $1/T \approx 10$ kHz.

We begin with a filter for estimating the full system state $\mathbf{x}(t)$ conditioned on the measurement result $\mathbf{v}(t)$. For the one-dimensional case here, $\mathbf{v}(t) = v_x(t)$ is a scalar. However, we retain the vector notation to emphasize the generality of the controller design. We do not know the initial state of the system, but we assume that it is

distributed according to a Gaussian distribution with mean \mathbf{m}_0 and covariance Σ_0 . The final form of the controller is largely independent of these initial distributions, so the choice of \mathbf{m}_0 and Σ_0 is not critical. Since both the system and the measurement are driven by Gaussian white noise, the optimal probabilistic description of the system state $\mathbf{x}(t)$ remains Gaussian at all times. The equations of motion of the mean $\mathbf{m}(t)$ and covariance $\Sigma(t)$ of the system state conditioned on the measurement record $\mathbf{v}(t)$ up to time t , can be derived from probabilistic arguments and the result is a Kalman filter [32, 30]. We simply state these results here:

$$\frac{d}{dt}\mathbf{m}(t) = \mathbf{A}\mathbf{m}(t) + \mathbf{B}\mathbf{u}(t) + \mathbf{K}_o(t) [\mathbf{v}(t) - \mathbf{C}\mathbf{m}(t)]. \quad (2.10)$$

The observer gain matrix \mathbf{K}_o depends on $\Sigma(t)$

$$\mathbf{K}_o(t) = \Sigma(t)\mathbf{C}^T\Sigma_2^{-1} \quad (2.11)$$

which propagates according to a non-linear matrix Riccati equation

$$\frac{d}{dt}\Sigma(t) = \Sigma_1 + \mathbf{A}\Sigma(t) + \Sigma(t)\mathbf{A}^T - \Sigma(t)\mathbf{C}^T\Sigma_2^{-1}\mathbf{C}\Sigma(t). \quad (2.12)$$

Note that the Riccati equation for the covariance matrix $\Sigma(t)$ is deterministic. Since we are interested in a time-independent form of the estimator, we may numerically propagate Eq. (2.12) with initial condition $\Sigma(0) = \Sigma_0$ to find its steady state solution, or equivalently we can set the left-hand side to 0 and solve the remaining algebraic equation numerically (or analytically if possible). Plugging the steady state solution of Eq. (2.12) into Eq. (2.11) we find the time-independent observer gain matrix \mathbf{K}_o .

Having defined an optimal estimate of the system state $\mathbf{x}(t)$ conditioned on the measurements $\mathbf{v}(t)$, we now turn to the problem of designing a feedback control signal $\mathbf{u}(t)$ for stabilizing the system state. To this end, we define a ‘‘performance criterion’’ $h(t)$ which quantifies both the degree to which the system state is stabilized and also any cost of applying the control signal $\mathbf{u}(t)$. In our system, we wish to minimize the squared tracking error $(x_P(t) - x_S(t))^2$ while acknowledging that the control signal is

a real voltage, limited to finite gain at a finite bandwidth. We therefore penalize the first time-derivative of the input voltage so that the cost function acknowledges the bandwidth limitations of a realistic controller. With this in mind, we define matrices \mathbf{P} and \mathbf{Q} so that a cost function is given by

$$\begin{aligned} h(t) &= \mathbf{x}(t)^T \mathbf{P} \mathbf{x}(t) + \mathbf{u}(t)^T \mathbf{Q} \mathbf{u}(t) \\ &= [x_P(t) - x_S(t)]^2 + \lambda \left(\frac{d}{dt} u_x(t) \right)^2 \end{aligned} \quad (2.13)$$

where λ is a cost parameter characterizing the bandwidth limitations. The desired *optimal* controller is one that minimizes the time integral of $h(t)$. Note that if $m = 0$, as is the case for the fit function $T(s)$ of Fig. 2.1, we must augment the system up to $m = 1$ so that the control input is $\frac{d}{dt} u_x(t)$ and $u_x(t)$ is included in \mathbf{x} , with $p_1 = 0$. We are still guaranteed a proper system because of the non-triviality condition $n \geq 1$.

We have now defined a Linear system with a Quadratic performance criterion and Gaussian noise, an LQG system in the language of optimal control theory [30]. In such systems, the time-integral of $h(t)$ is minimized by applying the feedback signal

$$\mathbf{u}(t) = -\mathbf{K}_c \mathbf{m}(t) \quad (2.14)$$

where the controller gain matrix

$$\mathbf{K}_c = \mathbf{Q}^{-1} \mathbf{B}^T \mathbf{V} \quad (2.15)$$

is again given by the steady-state solution \mathbf{V} to a matrix Riccati equation

$$\frac{d}{d\tau} \mathbf{V}(\tau) = \mathbf{P} + \mathbf{A}^T \mathbf{V}(\tau) + \mathbf{V}(\tau) \mathbf{A} - \mathbf{V}(\tau) \mathbf{B} \mathbf{Q}^{-1} \mathbf{B}^T \mathbf{V}(\tau) \quad (2.16)$$

with initial condition $\mathbf{V}(0) = 0$. We use τ and not t as the time argument in Eq. (2.16) since in an application where we use time varying control [*i.e.* we do not take the steady state solutions of Eqs. (2.12) and (2.16)], Eq. (2.16) propagates \mathbf{V} backwards in time with τ representing the time-to-go in the control problem. In the time-

independent case, this distinction is irrelevant. Since our system contains an uncontrollable state, one component of \mathbf{V} diverges as $\tau \rightarrow \infty$ in Eq. (2.16). However, this component does not enter into the controller gain \mathbf{K}_c .

Finally, by inserting the Laplace transform of Eq. (2.14) into the Laplace transform of Eq. (2.10), and rearranging terms we find the overall controller transfer function relating the control signal $\mathbf{U}(s)$ to the measurement $\mathbf{V}(s)$:

$$\begin{aligned}\mathbf{U}(s) &= -\mathbf{G}_\lambda(s)\mathbf{V}(s) \\ \mathbf{G}_\lambda(s) &= \mathbf{K}_c(s\mathbf{I} - \mathbf{A} + \mathbf{K}_o\mathbf{C} + \mathbf{B}\mathbf{K}_c)^{-1}\mathbf{K}_o.\end{aligned}\tag{2.17}$$

Note that in the one-dimensional tracking case, $\mathbf{G}_\lambda(s) = G_\lambda(s)$ is a single-input-single-output controller with input v_x and output $\frac{d^m}{dt^m}u_x$. We may immediately write the desired controller transfer function $H_\lambda(s)$ from $v_x(s)$ to $u_x(s)$:

$$H_\lambda(s) = s^{-m}G_\lambda(s).\tag{2.18}$$

For tracking in two dimensions, we simply use a second copy of the controller $H_\lambda(s)$ to drive u_y using the measurement v_y .

In Fig. 2.3, $H_\lambda(s)$ is plotted for various values of the cost parameter λ . If we have a controller with large gain at arbitrarily high frequencies, we suspect the optimal controller transfer function is $H(s) = \Omega[sT(s)]^{-1}$ so that the overall open-loop transfer function $H(s)T(s) = \Omega s^{-1}$ looks like an integrator which exhibits ideal stability and sensitivity, closing the servo at angular frequency Ω . In Fig. 2.3, we see that $H_\lambda(s)$ given by the LQG optimization of Eq. (2.18) better approximates $H(s)$ as λ is decreased. For any realistic controller, however, $H_\lambda(s)$ is the optimal approximation to $H(s)$ in the sense of minimizing the cost function. To find a control algorithm for an experimental system, we simply decrease λ until the controller can no longer implement the transfer function $H_\lambda(s)$, for example due to bandwidth limitations, finite voltage slew-rates or output saturation. The final choice of λ is therefore a compromise between steady-state tracking error and the level of aggression a con-

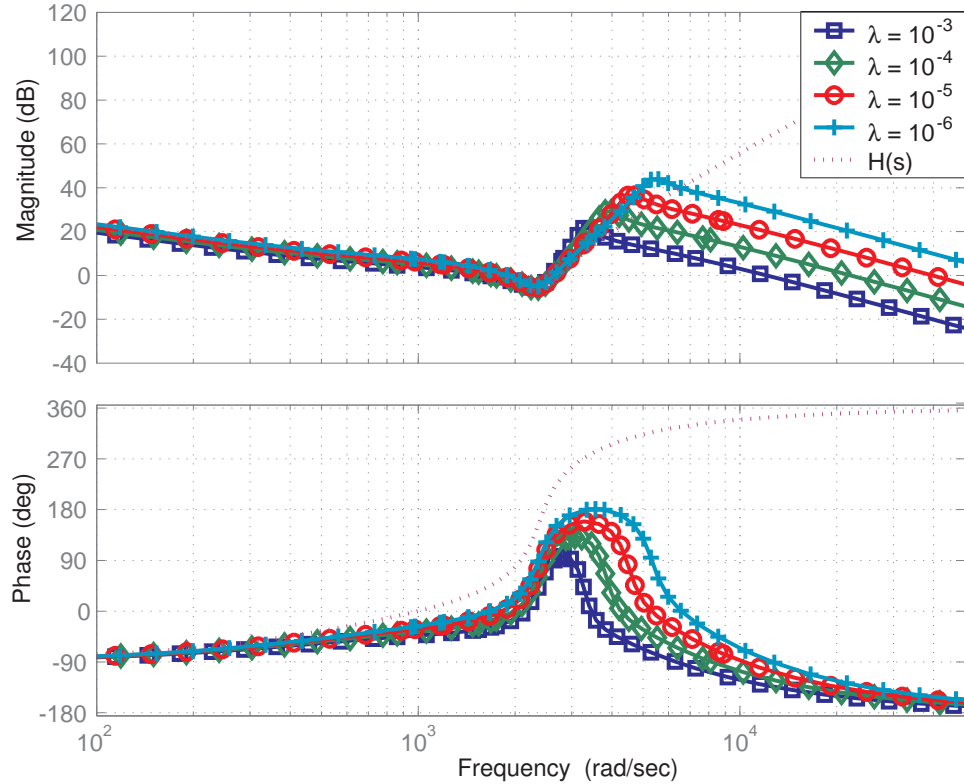


Figure 2.3: Bode diagrams of the transfer function $H_\lambda(s)$ of Eq. (2.18) for various values of the cost parameter λ . As λ decreases, $H_\lambda(s)$ more closely approximates the ideal transfer function $H(s)$ (dotted line), with $\Omega \approx 10^3$ rad/ms.

troller will tolerate. Finally, we note that in this case an important result of the LQG optimization procedure is the tailored phase response near the servo closing point, which minimizes ringing and overshoot in the system's closed-loop step response.

2.3 Performance analysis

To evaluate the performance of the controller design of Sect. 2.2, we numerically integrate the continuous-time system of equations (2.1a-2.1b) for each of two dimensions. Using a fluorescence model based on the rate $\Gamma(t)$ we update the position estimator of Eqs. (2.9a-2.9b) with period T . Finally, we feedback to the control inputs $u_x(t)$ and $u_y(t)$ using the Kalman filter equations (2.10) and the optimal control law given

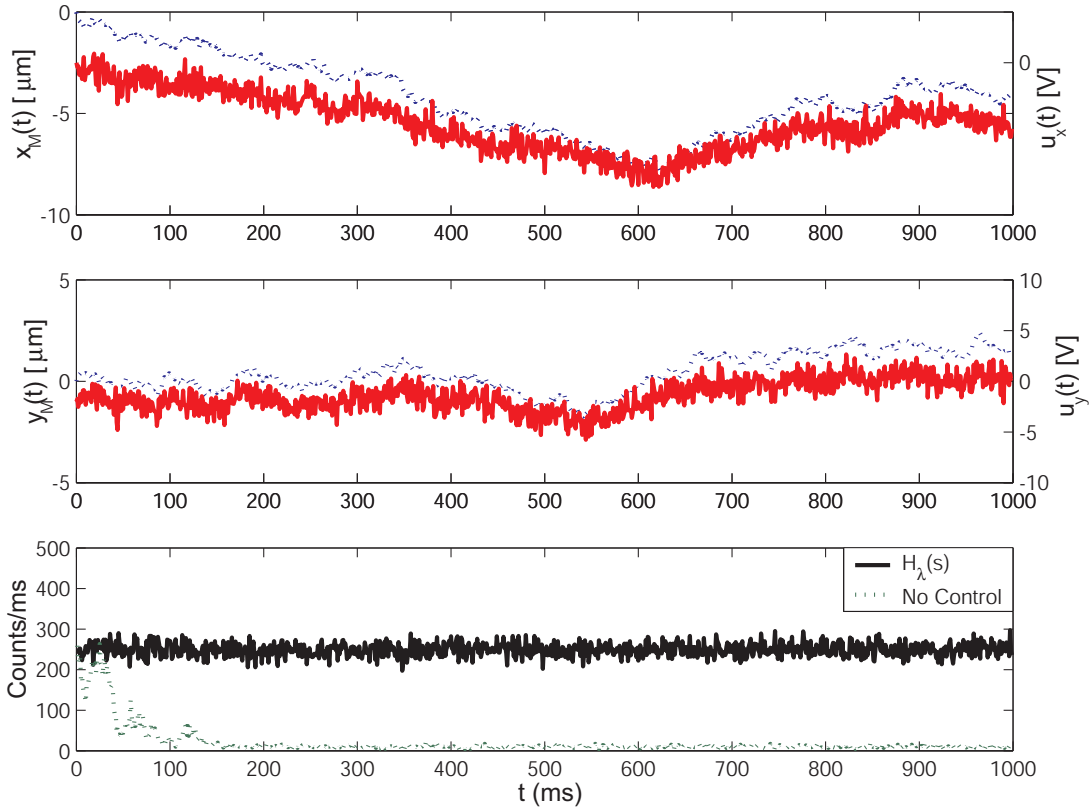


Figure 2.4: Simulated tracking performance in two dimensions for a particle with diffusion coefficient $D = 5 \mu\text{m}^2/\text{s}$ and $\lambda = 10^{-4}$. The top [middle] plot shows the particle's coordinate $x_P(t)$ [$y_P(t)$] as a dotted line relative to the left-hand axis and the control voltage $u_x(t)$ [$u_y(t)$] as a solid line relative to the right-hand axis. The lower plot shows the fluorescence count rate both with (solid line) and without (dotted line) tracking.

by Eq. (2.14). The following parameters are typical of our simulations: $w = 1 \mu\text{m}$, $\omega_0 = 2\pi \times (10 \text{ kHz})$, $\Gamma_0 = 500 \text{ ms}^{-1}$, $\Gamma_B = 10 \text{ ms}^{-1}$, $\sigma_v = \beta\Gamma_B/\Gamma_0$, $\beta \approx 1$, $\lambda = 10^{-4}$, and following Enderlein we choose $r = 0.6w$ [12]. We emphasize that although the controller design is based on Gaussian noise approximations, the simulations always use full Poisson statistics. The integration timestep is $\Delta t = 10^{-5} \text{ s}$, and we integrate the equations of motion using a semi-implicit Euler scheme with implicitness parameter $\alpha = 0.5$ [33].

An example of the controller's performance is shown in Fig. 2.4 for $D = 5 \mu\text{m}^2/\text{s}$.

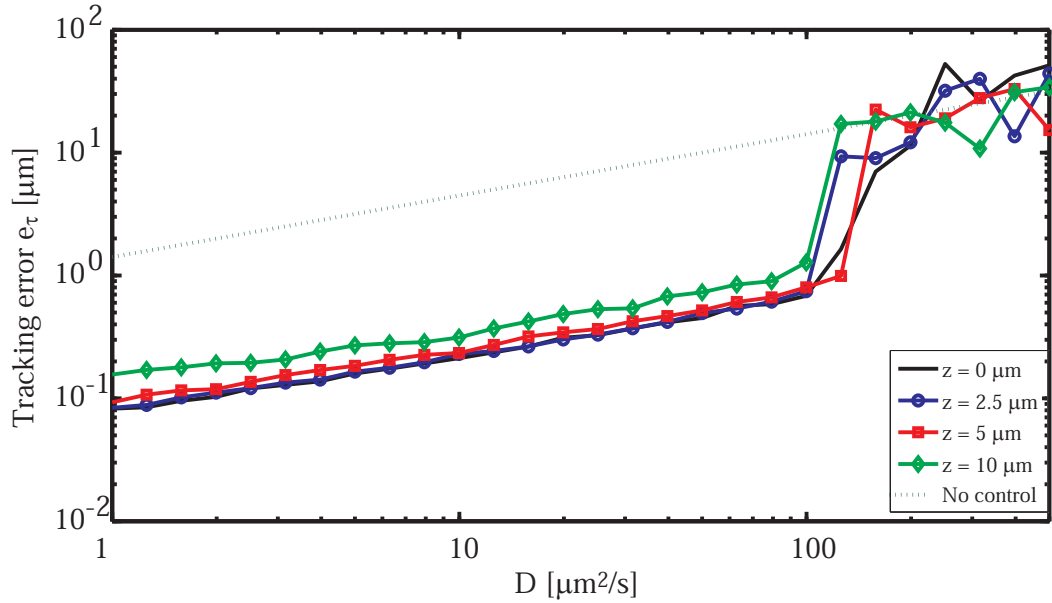


Figure 2.5: Log-log plot showing the radial tracking error e_τ over a range of diffusion coefficients and for particles confined to a plane at an axial distance z from the laser focus. Points which lie a statistically significant distance below the dashed line represent regimes in which the controller stabilizes the particle motion.

It is clear that the controller tracks the particle's position quite well, with fluorescence fluctuations essentially limited to Poisson statistics. We quantify the performance of a trajectory over a time τ by the average RMS tracking error

$$e_\tau = \frac{1}{\tau} \int_0^\tau [(x_P(t) - x_S(t))^2 + (y_P(t) - y_S(t))^2]^{\frac{1}{2}} dt. \quad (2.19)$$

For the trajectory shown in Fig. 2.4, $e_\tau = 0.15 \mu\text{m}$, substantially less than the beam waist w . In fact, the controller exhibits excellent tracking performance with $e_\tau \lesssim 0.6 \mu\text{m}$ for diffusion coefficients up to $50 \mu\text{m}^2/\text{s}$.

Finally, we suspect that the controller will track the radial (xy) motion of particles diffusing in three dimensions but confined along the z -axis, for example in the case of particles diffusing between microscope cover slides separated by only a few microns. For a particle outside of the plane of the laser focus, $z = 0$, the controller works in the same way but with z -dependent values of the beam waist w , and the fluorescence

intensity Γ_0 . However, even for incorrect values of these parameters, the position estimation of Eqs. (2.9a-2.9b) contains information about the *direction* of a particle's motion, while underestimating its displacement. This underestimation is equivalent to a time-dependent gain variation in the controller $H_\lambda(s)$. The negative feedback structure of the controller may provide some robustness, however, and the controller is still able to track confined three-dimensional motion, albeit with reduced performance and at a reduced fluorescence intensity.

In Fig. 2.5 we plot e_τ for trajectories of length $\tau = 1$ s as D is varied over a large range of values and for particles confined to a plane at a distance z from the plane of the laser focus. The solid curve with $z = 0$ represents tracking performance for two-dimensional motion while the dashed line represents the untracked case $e_\tau = \sqrt{2D\tau}$. The curves at non-zero z represent the worst-case tracking of a particle confined to depths between 0 and z . In other simulations, we have seen that the tracking error is less than those displayed in Fig. 2.5 when the particle is allowed to move in z instead of being confined to a plane at the maximum depth. All of the curves show the general feature that the controller stabilizes the tracking error for diffusion coefficients less than $D \approx 100 \mu\text{m}^2/\text{s}$ while above this value, the tracking error follows the uncontrolled, free-particle diffusion statistics $e_\tau = \sqrt{2D\tau}$. This value of D represents a fast-moving particle which can escape the rotating laser focus faster than the response bandwidth of the control system. We estimate this to be $D \approx \pi r^2 \nu_c$ where $\nu_c \approx 200$ Hz is the closing frequency (i.e., unity-gain point) of the open-loop control system $T(s)H_\lambda(s)$. We see that while the magnitude of the tracking error depends on the diffusion coefficient and the depth z , the ability to stabilize the particle motion depends mainly on the controller bandwidth and the ‘‘capture area’’ πr^2 but is only weakly dependent on z . (All of our simulations have used the value $r = 0.6w$ with $w = 1\mu\text{m}$. For a fixed closing bandwidth ν_c , however, we expect the controller to track diffusion coefficients which scale as $r^2 \sim w^2$ so that faster particles can be tracked by simply increasing the focused beam waist w .)

Based on these results, we make the encouraging and perhaps surprising, observation that the controller can stabilize the radial motion of a moderately fast-moving

particle loosely confined to a depth as large as $z = 10\mu\text{m}$. In this chapter, we did not attempt a quantitative analysis of the robustness of the controller to gain variation arising from motion in the uncontrolled z direction. However, well-developed analytical techniques exist for quantifying system stability and controller performance in the face of unknown and uncontrolled dynamical plant variation [34, 35], and future refinements of the controller design presented here could rely on this type of robustness analysis by including a gain variation (position underestimation) with power spectrum determined by the particle's diffusion statistics.

Chapter 3

Sensing the Position of a Fluorescent Particle

Having established the feasibility of closed-loop particle tracking using the realistic numerical simulations in Ch. 2, we now turn to a more focused investigation of the problem of detecting a particle’s position using fluorescence modulation and photon counting. That is, we ask “Why does it work?” The answer, as we shall see, involves a lot of statistics.

In Ch. 2, we used Eqs. (2.9a-2.9b) to show that the cosine and sine components of the photon counting *rate* $\Gamma(t)$ (at the laser rotation frequency ω_0) are proportional to the particle’s x and y positions, respectively. However, in a real experiment, we do not measure $\Gamma(t)$; rather, as shown in Fig. 3.1, we measure a realization of a Poisson process with that rate. For low fluorescent count rates, it is not immediately obvious how the frequency components of the rate appear in the frequency components of the signal itself. To illustrate the problem considered in this section, Fig. 3.1 shows a time-dependent rate $\Gamma(t)$ with a strong oscillation at unit frequency together with a single realization of this process that might be measured in the laboratory.

In our experiment, we rotate the laser at $\omega_0 = 2\pi \times 8$ kHz, while our average photon arrival rate is sometimes as low as 5000 s^{-1} . In that case, *we collect less than one photon per rotation period*. Furthermore, the electronic signal from our single-photon counters has a full analog bandwidth of about 500 MHz (the photon counting pulses have a sub-nanosecond rise time and 25 ns duration), which we demodulate at 8 kHz

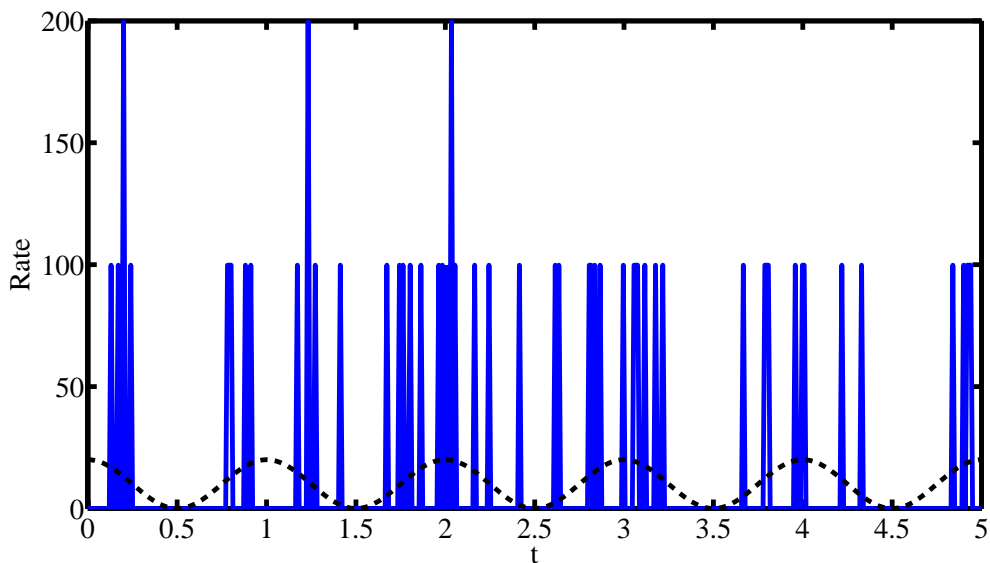


Figure 3.1: Typical realization of a rate-modulated Poisson process. The dashed line is the rate, and the blue “spikes” are a realization of the Poisson process, the signal that can be measured in an experiment. In this section, we ask how the frequency content of the *rate* is encoded in a realization of the process.

using a lock-in amplifier. In practice, the question of whether we lose signal-to-noise during this process arises quite often. Therefore, in this section, we will derive the mean and variance of the frequency components of a rate-modulated Poisson process in terms of the frequency content of the rate itself. We will see here that, under a few very reasonable conditions, there is *no penalty* for this type of signal processing (of course, technical problems such as noise floors may creep into the problem, but these need to be analyzed separately in each case). This is a nice result because it shows that no fancy signal processing is necessary for extracting frequency components from a rate-modulated process; lock-in measurement is quite sufficient.

Primary references for most of the statistical calculations, here and elsewhere in the thesis, are Refs. [36, 31]. There is also a nice summary of properties of Poisson processes at Z. Nenandic’s web site: robotics.caltech.edu/~zoran/Research/poisson.html.

3.1 Rate-modulated Poisson statistics

Consider a scenario in which an incident photon generates a response function $f_0(t)$ with time-dependent probability $\Gamma(t)$. In an experiment, $f_0(t)$ is an electronic pulse that signals a single photon detection event and $\Gamma(t)$ is the time-dependent (modulated) fluorescence photon counting rate. We may then write $f(t)$, the resulting stochastic signal, as

$$f(t) = (f_0 * T)(t) = \int_{-\infty}^{\infty} dt' f_0(t-t')T(t') \quad (3.1)$$

where $*$ denotes a convolution integral, and the photon detection times t_k are recorded in the stochastic variable $T(t)$

$$T(t) = \sum_k \delta(t - t_k) \quad (3.2)$$

whose statistics are determined by $\Gamma(t)$. The next few paragraphs are devoted to a demonstration of the following results, which will resurface many times:

$$\mathbb{E}[T(t)] = \Gamma(t) \quad (3.3a)$$

$$\mathbb{E}[T(t')T(t'')] = \Gamma(t')\Gamma(t'') + \Gamma(t')\delta(t' - t''). \quad (3.3b)$$

$\mathbb{E}[\cdot]$ denotes an expectation value over realization of a process (to be distinguished from $\langle \cdot \rangle$, which we will use to denote a time average in later sections).

We will assume that $\Gamma(t) = 0$ for all t outside some bounds $|t| > t_{max}$, *i.e.*, that the signal turns on and off at finite times, so that we need not worry about convergence of integrals later. Consider the process

$$N_t = \max_{t_k \leq t} k. \quad (3.4)$$

where N_t is the (stochastic) number of photon arrivals up to time t . It follows imme-

diately that

$$\begin{aligned} T(t) &= \frac{d}{dt}N_t \\ N_t &= \int_{-\infty}^t T(t')dt'. \end{aligned} \quad (3.5)$$

We have introduced the linear change of variables from $T(t)$ to N_t since the probability distribution over N_t takes on the usual Poisson form. A standard calculation [31] shows that the probability that N_t takes on the (integer) value n is:

$$P(N_t = n) = \frac{e^{-\lambda_t} \lambda_t^n}{n!} \quad (3.6)$$

where

$$\lambda_t = \mathbb{E}[N_t] = \int_{-\infty}^t \Gamma(t')dt'. \quad (3.7)$$

That is, N_t is just a time-dependent Poisson process with mean value λ_t .

Now that we know the distribution of N_t , we may calculate the moments of $T(t)$.

First,

$$\mathbb{E}[T(t)] = \mathbb{E}\left[\frac{\partial}{\partial t}N_t\right] = \frac{\partial}{\partial t}\mathbb{E}[N_t] = \frac{\partial}{\partial t}\lambda_t = \Gamma(t), \quad (3.8)$$

which already gives the desired result for Eq. (3.3a). We need to do a little more work to show Eq. (3.3b). We have

$$\begin{aligned} \mathbb{E}[T(s)T(t)] &= \mathbb{E}\left[\frac{\partial N_s}{\partial s} \frac{\partial N_t}{\partial t}\right] \\ &= \frac{\partial}{\partial s} \frac{\partial}{\partial t} \mathbb{E}[N_s N_t]. \end{aligned} \quad (3.9)$$

Using standard properties of Poisson processes, we have for $s \leq t$

$$\begin{aligned} \mathbb{E}[N_s N_t] &= \mathbb{E}[N_s(N_t - N_s + N_s)] \\ &= \mathbb{E}[N_s(N_t - N_s)] + \mathbb{E}[N_s^2] \\ &= \lambda_s(\lambda_t - \lambda_s) + (\lambda_s^2 + \lambda_s) \\ &= \lambda_t \lambda_s + \lambda_s, \end{aligned} \quad (3.10)$$

where we have used the fact that N_t and $N_t - N_s$ are uncorrelated for $s \leq t$. In general, we find

$$\mathbb{E}[N_s N_t] = \lambda_s \lambda_t + \lambda_{\min\{s,t\}}. \quad (3.11)$$

Taking the partial derivative with respect to t , we find

$$\begin{aligned} \frac{\partial}{\partial t} \mathbb{E}[N_s N_t] &= \lambda_s \Gamma(t) \quad , \quad s \leq t \\ &= \lambda_s \Gamma(t) + \Gamma(t) \quad , \quad s > t \end{aligned} \quad (3.12)$$

or

$$\frac{\partial}{\partial t} \mathbb{E}[N_s N_t] = \Gamma(t) \lambda_s + \Gamma(t) \Theta(s - t) \quad (3.13)$$

where Θ is the Heaviside step function. Now taking the partial with respect to s , we have the desired result for Eq. (3.3b)

$$\mathbb{E}[T(s)T(t)] = \frac{\partial}{\partial s} \frac{\partial}{\partial t} \mathbb{E}[N_s N_t] = \Gamma(s)\Gamma(t) + \Gamma(t)\delta(s - t). \quad (3.14)$$

3.2 Power spectrum of a rate-modulated Poisson process

We may now address the primary question, what is the frequency content of the signal $f(t)$ defined in Eq. (3.1) and how does it depend on the frequency content of the rate $\Gamma(t)$? In other words, how does a wiggle in the excitation laser's position show up in the photon counting signal at our detectors?

The complex frequency spectrum of $f(t)$ is given by

$$\begin{aligned} F(\omega) &= \int_{-\infty}^{\infty} e^{-i\omega t} f(t) dt \\ &= \int_{-\infty}^{\infty} e^{-i\omega t} (f_0 * T)(t) dt \\ &= F_0(\omega) \int_{-\infty}^{\infty} e^{-i\omega t} T(t) dt \end{aligned} \quad (3.15)$$

where $F_0(\omega)$ is the Fourier transform of the pulse function $f_0(t)$. Because $T(t)$ is stochastic, so is the power spectrum $F(\omega)$. Let us calculate some moments of $F(\omega)$. By the linearity of the Fourier transform,

$$\begin{aligned}\mathbb{E}[F(\omega)] &= F_0(\omega) \int_{-\infty}^{\infty} e^{-i\omega t} \mathbb{E}[T(t)] dt \\ &= F_0(\omega) \int_{-\infty}^{\infty} e^{-i\omega t} \Gamma(t) dt.\end{aligned}\tag{3.16}$$

Defining

$$\Upsilon(\omega) = \int_{-\infty}^{\infty} e^{-i\omega t} \Gamma(t) dt\tag{3.17}$$

to be the frequency spectrum of the rate $\Gamma(t)$, we have

$$\mathbb{E}[F(\omega)] = F_0(\omega)\Upsilon(\omega).\tag{3.18}$$

It is clear that the frequency content of the modulation $\Gamma(t)$ is contained in the overall signal, but the amplitude at any frequency is suppressed or enhanced by the frequency content of the pulse shape $F_0(\omega)$. In a real experimental scenario we are more interested in averages over the real and imaginary parts of $F(\omega)$ since these correspond to the cosine and sine transforms in Eq. (2.9a-2.9b).

$$\mathbb{E}\{\text{Re}[F(\omega)]\} = \text{Re}\{\mathbb{E}[F(\omega)]\} = \text{Re}[F_0(\omega)\Upsilon(\omega)]\tag{3.19}$$

and similarly for the imaginary part. Note however that a similar relation does *not* hold for the magnitude:

$$\mathbb{E}[|F(\omega)|] \neq |\mathbb{E}[F(\omega)]|.\tag{3.20}$$

We may also ask about the fluctuations in the stochastic frequency spectrum $F(\omega)$.

The absolute-square is the easiest to calculate, so we'll start with that. We have

$$\begin{aligned}
\mathbb{E} [|F(\omega)|^2] &= \mathbb{E} \left[\left| \int_{-\infty}^{\infty} e^{-i\omega t} (f_0 * T)(t) dt \right|^2 \right] \\
&= |F_0(\omega)|^2 \iint_{-\infty}^{\infty} dt' dt'' e^{-i\omega t'} e^{i\omega t''} \mathbb{E} [T(t')T(t'')] \\
&= |F_0(\omega)|^2 \int dt' \int dt'' e^{-i\omega t'} e^{i\omega t''} [\Gamma(t')\Gamma(t'') + \Gamma(t')\delta(t' - t'')] \\
&= |F_0(\omega)|^2 [|\Upsilon(\omega)|^2 + \Upsilon(0)]. \tag{3.21}
\end{aligned}$$

Next we will calculate the variance in the real part of $F(\omega)$, using the fact the $f(t)$ is real to write $F(-\omega) = F^*(\omega)$. We have

$$\begin{aligned}
\mathbb{E} \{ \text{Re} [F(\omega)]^2 \} &= \mathbb{E} \left\{ \left[\frac{F(\omega) + F^*(\omega)}{2} \right]^2 \right\} \\
&= \frac{1}{4} \{ F_0(\omega)^2 [\Upsilon(\omega)^2 + \Upsilon(2\omega)] \\
&\quad + F_0^*(\omega)^2 [\Upsilon^*(\omega)^2 + \Upsilon^*(2\omega)] \\
&\quad + 2 |F_0(\omega)|^2 [|\Upsilon(\omega)|^2 + \Upsilon(0)] \}. \tag{3.22}
\end{aligned}$$

The variance in the real part of $F(\omega)$ is then seen to be

$$\Sigma_R^2(\omega) = \mathbb{E} \{ \text{Re} [F(\omega)]^2 \} - \mathbb{E} \{ \text{Re} [F(\omega)] \}^2 \tag{3.23}$$

$$= \frac{1}{4} [F_0(\omega)^2 \Upsilon(2\omega) + F_0^*(\omega)^2 \Upsilon^*(2\omega) + 2 |F_0(\omega)|^2 \Upsilon(0)]. \tag{3.24}$$

A similar calculation shows that

$$\begin{aligned}
\mathbb{E} \{ \text{Im} [F(\omega)]^2 \} &= \mathbb{E} \left\{ \left[\frac{F(\omega) - F^*(\omega)}{2i} \right]^2 \right\} \\
&= -\frac{1}{4} \{ F_0(\omega)^2 [\Upsilon(\omega)^2 + \Upsilon(2\omega)] \\
&\quad + F_0^*(\omega)^2 [\Upsilon^*(\omega)^2 + \Upsilon^*(2\omega)] \\
&\quad - 2 |F_0(\omega)|^2 [|\Upsilon(\omega)|^2 + \Upsilon(0)] \}. \tag{3.25}
\end{aligned}$$

And the variance in the imaginary part of $F(\omega)$ is given by

$$\Sigma_I^2(\omega) = -\frac{1}{4} [F_0(\omega)^2 \Upsilon(2\omega) + F_0^*(\omega)^2 \Upsilon^*(2\omega) - 2 |F_0(\omega)|^2 \Upsilon(0)]. \quad (3.26)$$

Note that Eqs. (3.22) and (3.25) exhibit the general property that

$$\mathbb{E} \{ \text{Re} [F(\omega)]^2 \} + \mathbb{E} \{ \text{Im} [F(\omega)]^2 \} = \mathbb{E} [|F(\omega)|^2]. \quad (3.27)$$

Denoting the signal-to-noise ratio in the real and imaginary parts by $(\text{S/N})_R$ and $(\text{S/N})_I$ respectively, we have

$$(\text{S/N})_R = \frac{\mathbb{E} \{ \text{Re} [F(\omega)] \}}{\sqrt{\Sigma_R^2(\omega)}} = \sqrt{\frac{|F_0(\omega)|^2 |\Upsilon(\omega)|^2 + \text{Re} [F_0(\omega)^2 \Upsilon(\omega)^2]}{|F_0(\omega)|^2 \Upsilon(0) + \text{Re} [F_0(\omega)^2 \Upsilon(2\omega)]}} \quad (3.28a)$$

$$(\text{S/N})_I = \frac{\mathbb{E} \{ \text{Im} [F(\omega)] \}}{\sqrt{\Sigma_I^2(\omega)}} = \sqrt{\frac{|F_0(\omega)|^2 |\Upsilon(\omega)|^2 - \text{Re} [F_0(\omega)^2 \Upsilon(\omega)^2]}{|F_0(\omega)|^2 \Upsilon(0) - \text{Re} [F_0(\omega)^2 \Upsilon(2\omega)]}}. \quad (3.28b)$$

These are the desired results, showing the signal-to-noise ratio when the cosine and sine (real and imaginary) quadratures of a rate-modulated Poisson process are detected using a lock-in method. Now let us consider detection at a specific modulation frequency ω_0 . We assume that our experiment is well-designed, so that $\Upsilon(2\omega_0) \ll \Upsilon(\omega_0)$, *i.e.*, the frequency content of the modulated rate $\Gamma(t)$ is sharply peaked at ω_0 with a negligible component at the first harmonic frequency $2\omega_0$. Then we may neglect the second term in both denominators and, denoting the phases of $F_0(\omega_0)$ and $\Upsilon(\omega_0)$ by ϕ_{F_0} and ϕ_Υ respectively, Eqs. (3.28a-3.28b) become much simpler:

$$(\text{S/N})_R \approx \frac{|\Upsilon(\omega_0) \cos(\phi_\Upsilon + \phi_{F_0})|}{\sqrt{\Upsilon(0)/2}} \quad (3.29a)$$

$$(\text{S/N})_I \approx \frac{|\Upsilon(\omega_0) \sin(\phi_\Upsilon + \phi_{F_0})|}{\sqrt{\Upsilon(0)/2}}. \quad (3.29b)$$

Aside from the phase factor ϕ_{F_0} , which may be eliminated by a suitable choice of the time origin or equivalently the detection phase, *the frequency content of the pulse*

$f_0(t)$ does not contribute to the signal-to-noise ratio. Note that

$$\Upsilon(0) = \int_{-\infty}^{\infty} \Gamma(t) dt \quad (3.30)$$

is the average number N of photons collected during the measurement. Not surprisingly, Eqs. (3.29a-3.29b) characteristically scale as $1/\sqrt{N}$.

3.3 Application to position sensing

Now that we have established in detail how to calculate the signal-to-noise ratio for a rate-modulated Poisson process, let us return to more specific considerations of closed-loop particle tracking. In particular, consider a particle that is immobilized in the xy plane. In the laboratory, such an immobilized particle is a useful diagnostic for signal levels, lock-in phases, and tracking error signal quality. In this section, we will examine some of the shapes that appear when we rotate an excitation laser, focus it onto an immobilized sample, then plot the two quadrature outputs of a lock-in measurement on an oscilloscope.

Before going any further, we can get all of the necessary calculations out of the way in one line. Let p and q be real numbers and let m be an integer. Then consulting Gradshteyn and Ryzhik [37] formula 3.919, we find

$$\frac{1}{2\pi} \int_0^{2\pi} \exp(p \cos \theta + q \sin \theta + im\theta) d\theta = \exp[im \arg(p + iq)] I_m \left(\sqrt{p^2 + q^2} \right) \quad (3.31)$$

where I_m is the modified Bessel function of order m and $\arg(z)$ is the argument (phase angle) of the complex number z . Essentially every integral that we will require for the rest of this chapter (and most other chapters too) comes down to Eq. (3.31) with a suitable choice of p , q , and m .

Now consider the usual Gaussian laser with beam waist w rotating at a radius r at angular frequency ω_0 . We will now move into the reference frame of the laser centroid

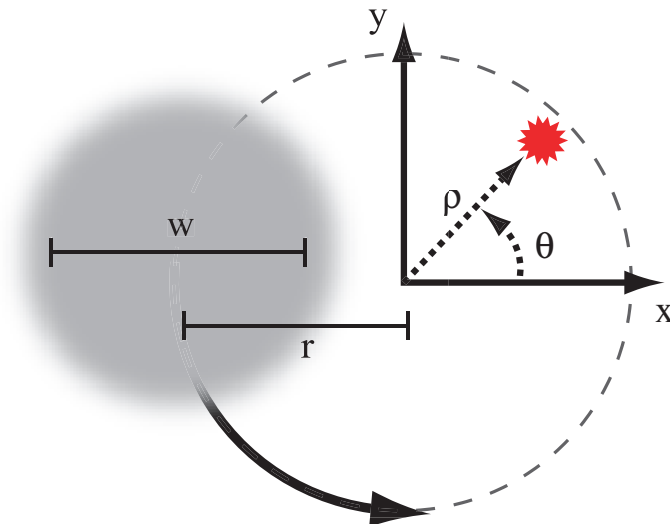


Figure 3.2: Schematic diagram of the coordinates used for the tracking model, in the reference frame of the laser centroid.

and drop the subscript M on the particle's coordinates as shown in Fig. 3.2. In a fixed plane z perpendicular to the axis of rotation, the fluorescence photon arrival rate from a particle at position $\mathbf{x} = (\rho, \theta)$, given in polar coordinates, is

$$\begin{aligned} \Gamma_{\mathbf{x}}(t) &= \Gamma_0 \exp \left\{ -\frac{2}{w^2} [(\rho \cos \theta - r \cos \omega_0 t)^2 + (\rho \sin \theta - r \sin \omega_0 t)^2] \right\} \\ &= \Gamma_0 \exp \left[-\frac{2}{w^2} (r^2 + \rho^2) \right] \exp \left[\frac{4r\rho}{w^2} \cos(\theta - \omega_0 t) \right]. \end{aligned} \quad (3.32)$$

The corresponding frequency spectrum will be denoted by $\Upsilon_{\mathbf{x}}(\omega)$ and defined as in Eq. (3.16).

Now consider making a lock-in detection of the fluorescence signal at the lock-in frequency ω_0 . We will denote the expectation values of the cosine and sine quadrature outputs of this lock-in measurement by $\hat{x}(\rho, \theta)$ and $\hat{y}(\rho, \theta)$, which are special cases of the frequency spectra defined in Sect. 3.2:

$$\hat{x}(\rho, \theta) = \mathbb{E} \{ \text{Re} [\Upsilon_{\mathbf{x}}(\omega_0)] \} = \int_0^{2\pi/\omega_0} \Gamma_{\mathbf{x}}(t) \cos(\omega_0 t) dt \quad (3.33)$$

$$\hat{y}(\rho, \theta) = \mathbb{E} \{ \text{Im} [\Upsilon_{\mathbf{x}}(\omega_0)] \} = \int_0^{2\pi/\omega_0} \Gamma_{\mathbf{x}}(t) \sin(\omega_0 t) dt. \quad (3.34)$$

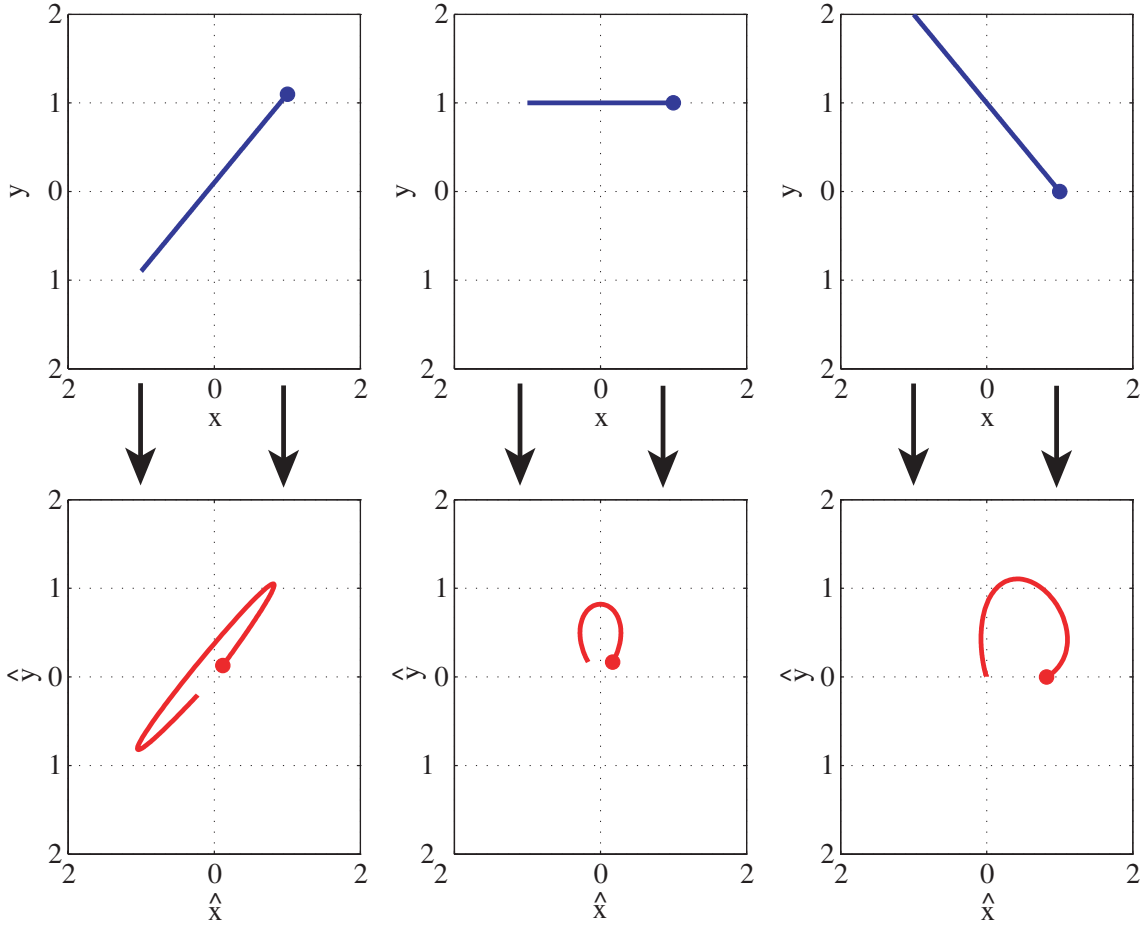


Figure 3.3: Three examples of the mapping defined by equations (3.35) and (3.36). The upper plots show various lines in the $(x, y) \leftrightarrow (\rho, \theta)$ plane, while the lower plots show the resulting curves $(\hat{x}(\rho, \theta), \hat{y}(\rho, \theta))$ in the (\hat{x}, \hat{y}) plane. These lower curves are the result of a lock-in position estimation measurement for a molecule moving along the upper lines, when the resulting quadrature amplitudes are plotted against each other. The parameters used were $\Gamma_0 = \omega_0$, $r = 0.5$ and $w = 1$.

Of course, we chose the symbols \hat{x} and \hat{y} , because these provide our *estimate* of the x and y position of the particle. With some trigonometric identities and formula (3.31), we find \hat{x} and \hat{y} explicitly:

$$\hat{x}(\rho, \theta) = 2\pi \frac{\Gamma_0}{\omega_0} \exp\left[-\frac{2}{w^2}(\rho^2 + r^2)\right] I_1\left[\frac{4r\rho}{w^2}\right] \cos \theta \quad (3.35)$$

$$\hat{y}(\rho, \theta) = 2\pi \frac{\Gamma_0}{\omega_0} \exp\left[-\frac{2}{w^2}(\rho^2 + r^2)\right] I_1\left[\frac{4r\rho}{w^2}\right] \sin \theta. \quad (3.36)$$

This pair of transformations maps lines in the (ρ, θ) plane to curves in the (\hat{x}, \hat{y})

plane, with the interesting property that the angular coordinate θ is unchanged. We may therefore think of it as the radial mapping

$$h(\rho) = 2\pi \frac{\Gamma_0}{\omega_0} \exp \left[-\frac{2}{w^2} (\rho^2 + r^2) \right] I_1 \left[\frac{4r\rho}{w^2} \right] \quad (3.37)$$

such that $(\rho, \theta) \mapsto (h(\rho), \theta)$. In the limit $\rho/w \ll 1$, with $r \sim w$, we have

$$h(\rho) \approx 4\pi \frac{r\rho}{w^2} \exp \left[-2\frac{r^2}{w^2} \right]. \quad (3.38)$$

The above fact, that $h(\rho) \propto \rho$ for small ρ , gives the utility of lock-in position estimation in a closed-loop feedback tracking algorithm. In Fig. 3.3, we show some lines in the $(x, y) \leftrightarrow (\rho, \theta)$ plane and the resulting curves in the (\hat{x}, \hat{y}) plane. In the laboratory, if we translate an immobilized particle along the paths shown at the top of Fig. 3.3, the resulting lock-in quadrature outputs plotted in xy mode on an oscilloscope will resemble the curves shown at the bottom.

3.4 Autocorrelation functions: More statistics!

In addition to plotting lock-in quadrature outputs, it is often useful in the laboratory to calculate autocorrelation functions of the fluorescence intensity recorded when an immobilized sample is illuminated with the rotating laser. In this section, we will calculate various of these autocorrelation functions for the case that one, two, or a random distribution of many particles are distributed on the surface. These calculations are a little tedious, but I think it is useful to record them here for exactly that reason.

We will use the same notation as Sects. 3.1-3.2, where $f(t)$ is a rate-modulated Poisson process with rate $\Gamma_{\mathbf{x}}(t)$ defined by Eq. (3.32). The autocorrelation function of $f(t)$ is defined to be

$$C(\tau) = \int_{-\infty}^{\infty} dt f(t) f(t + \tau). \quad (3.39)$$

As before, we assume that the signal $f(t)$ turns on and off at finite times, so that the

integral from $t = -\infty$ to $t = \infty$ represents only a finite time average. In fact, the signals we work with will have periodic expectation values, so we will only need to calculate time integrals over a single period in those cases.

Since $C(\tau)$ is stochastic, we will want to know its expectation value, and for this it is convenient to rewrite it using the Wiener-Khinchin theorem [38, 36]

$$C(\tau) = \frac{1}{2\pi} \int_{-\infty}^{\infty} e^{i\omega\tau} |F(\omega)|^2 d\omega. \quad (3.40)$$

The expectation value of $C(\tau)$ is now easily calculated with Eq. (3.21)

$$\begin{aligned} \mathbb{E}[C(\tau)] &= \frac{1}{2\pi} \int_{-\infty}^{\infty} e^{i\omega\tau} \mathbb{E}[|F(\omega)|^2] d\omega \\ &= \frac{1}{2\pi} \int_{-\infty}^{\infty} e^{i\omega\tau} |F_0(\omega)|^2 [|\Upsilon_{\mathbf{x}}(\omega)|^2 + \Upsilon_{\mathbf{x}}(0)] d\omega. \end{aligned} \quad (3.41)$$

Finally, let us make the simplifying assumption that the pulse shape $f_0(t)$ is very sharply peaked so that its spectrum $F_0(\omega)$ is very broad and can be considered constant, $\sim F_0$, over the range where $\Upsilon_{\mathbf{x}}(\omega)$ is peaked. Then we can move $F_0(\omega) \approx F_0$ outside of the integral and use the inverse of the Wiener-Khinchin theorem to find

$$\mathbb{E}[C(\tau)] \approx F_0^2 \langle \Gamma_{\mathbf{x}}(t)\Gamma_{\mathbf{x}}(t+\tau) \rangle_t + \Upsilon_{\mathbf{x}}(0) \langle f_0(t)f_0(t+\tau) \rangle_t. \quad (3.42)$$

The angle brackets $\langle \rangle_t$ represent a time average over t . The second term is just the autocorrelation function of the pulse $f_0(t)$, so aside from prefactors, all of the interesting dynamical signatures occur in the term

$$G_{\mathbf{x}}(\tau) = \langle \Gamma_{\mathbf{x}}(t)\Gamma_{\mathbf{x}}(t+\tau) \rangle_t = \langle \Gamma_{\mathbf{x}}(t-\tau/2)\Gamma_{\mathbf{x}}(t+\tau/2) \rangle_t \quad (3.43)$$

where we have simply symmetrized the time argument in the second term. We will also compute normalized fluorescence autocorrelation functions defined as

$$g_{\mathbf{x}}(\tau) = \frac{\langle \Gamma_{\mathbf{x}}(t-\tau/2)\Gamma_{\mathbf{x}}(t+\tau/2) \rangle_t}{\langle \Gamma_{\mathbf{x}}(t) \rangle_t^2} - 1. \quad (3.44)$$

Now let us calculate these autocorrelation functions for a few different cases.

Autocorrelation for a single particle. First, consider a single fluorescent particle immobilized to a two-dimensional surface at position $\mathbf{x} = (\rho, \theta)$ in a rotating Gaussian laser. For this case, again with the aid of Eq. (3.31), we find

$$\begin{aligned} G_{\mathbf{x}}(\tau) &= \langle \Gamma_{\mathbf{x}}(t - \tau/2) \Gamma_{\mathbf{x}}(t + \tau/2) \rangle_t \\ &= \frac{\omega_0}{2\pi} \int_0^{2\pi/\omega_0} \Gamma_{\mathbf{x}}(t - \tau/2) \Gamma_{\mathbf{x}}(t + \tau/2) dt \\ &= \Gamma_0^2 \exp \left[-\frac{4}{w^2} (r^2 + \rho^2) \right] I_0 \left[\frac{8r\rho}{w^2} \cos(\omega_0\tau/2) \right] \end{aligned} \quad (3.45)$$

where the time average was computed simply as the average over a single period of the rotation. The normalized autocorrelation $g_{\mathbf{x}}(\tau)$ for a single molecule in a rotating laser field is therefore given by

$$g_{\mathbf{x}}(\tau) = \frac{1}{I_0 (4r\rho/w^2)^2} I_0 \left[\frac{8r\rho}{w^2} \cos(\omega_0\tau/2) \right] - 1. \quad (3.46)$$

Average autocorrelation for a single particle. We may also compute the *average* correlation function $\bar{G}(\tau)$, averaged over uniformly distributed positions \mathbf{x} :

$$\begin{aligned} \bar{G}(\tau) &= 2\pi \int_0^\infty G_{\mathbf{x}}(\tau) \rho d\rho \\ &= \frac{\Gamma_0^2 w^2 \pi}{4} \exp \left\{ -\frac{4r^2}{w^2} \left[1 - \cos^2 \left(\frac{\omega_0\tau}{2} \right) \right] \right\}. \end{aligned} \quad (3.47)$$

Cross-correlation for a pair of particles. Letting $\mathbf{x}_j = (\rho_j, \theta_j)$ be the position of particle j , we define the cross-correlation between fluorescence from particles j and k as follows:

$$\begin{aligned} G_{\mathbf{x}_j, \mathbf{x}_k}(\tau) &\equiv \langle \Gamma(\rho_j, \theta_j, t - \tau/2) \Gamma(\rho_k, \theta_k, t + \tau/2) \rangle_t \\ &= \xi \frac{\omega_0}{2\pi} \int_0^{2\pi/\omega_0} \exp [p \cos(\omega_0 t) + q \sin(\omega_0 t)] dt \end{aligned} \quad (3.48)$$

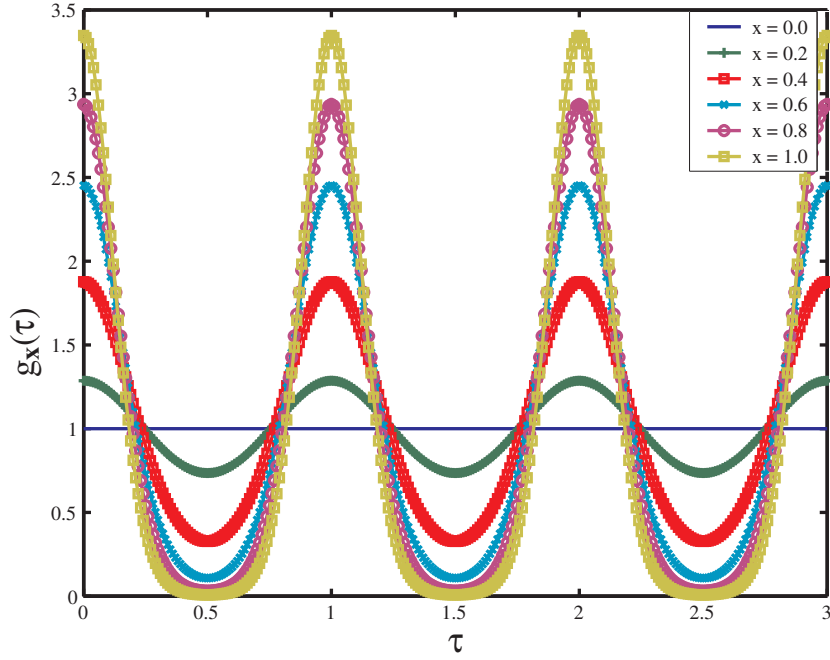


Figure 3.4: $g_{\mathbf{x}}(\tau)$ as given by Eq. (3.46), for various values of the parameter $x = r\rho/w^2$.

where

$$\xi = \Gamma_0^2 \exp \left[-\frac{2}{w^2} (\rho_j^2 + \rho_k^2 + 2r^2) \right] \quad (3.49a)$$

$$p = \frac{4r}{w^2} \left[\rho_j \cos \left(\theta_j + \frac{\omega_0 \tau}{2} \right) + \rho_k \cos \left(\theta_k - \frac{\omega_0 \tau}{2} \right) \right] \quad (3.49b)$$

$$q = \frac{4r}{w^2} \left[\rho_j \sin \left(\theta_j + \frac{\omega_0 \tau}{2} \right) + \rho_k \sin \left(\theta_k - \frac{\omega_0 \tau}{2} \right) \right]. \quad (3.49c)$$

Using Eq. (3.31), we have

$$G_{\mathbf{x}_j, \mathbf{x}_k}(\tau) = \Gamma_0^2 \exp \left[-\frac{2}{w^2} (\rho_j^2 + \rho_k^2 + 2r^2) \right] I_0 \left[\frac{4r}{w^2} \sqrt{\rho_j^2 + \rho_k^2 + 2\rho_j \rho_k \cos(\theta_j - \theta_k + \omega_0 \tau)} \right]. \quad (3.50)$$

Note that, unlike the autocorrelation $G_{\mathbf{x}}(\tau) = G_{\mathbf{x}, \mathbf{x}}(\tau)$, $G_{\mathbf{x}_j, \mathbf{x}_k}(\tau)$ is not restricted to be symmetric around $\tau = 0$, nor is it necessarily a maximum at $\tau = 0$.

Because the laser rotates at a fixed radius r , the cross-correlation $G_{\mathbf{x}_j, \mathbf{x}_k}(\tau)$ is sensitive only to the angular separation between the particles. To see this, we can integrate $G_{\mathbf{x}_j, \mathbf{x}_k}(\tau)$ over the angular variables θ_j, θ_k to find

$$\begin{aligned} & \int_0^{2\pi} \frac{d\theta_j}{2\pi} \int_0^{2\pi} \frac{d\theta_k}{2\pi} G_{\mathbf{x}_j, \mathbf{x}_k}(\tau) \\ &= \Gamma_0^2 \exp\left[-\frac{2}{w^2}(\rho_j^2 + r^2)\right] I_0\left(\frac{4r\rho_j}{w^2}\right) \exp\left[-\frac{2}{w^2}(\rho_k^2 + r^2)\right] I_0\left(\frac{4r\rho_k}{w^2}\right) \\ &= \langle \Gamma_{\mathbf{x}_j}(t) \rangle_t \langle \Gamma_{\mathbf{x}_k}(t) \rangle_t. \end{aligned} \quad (3.51)$$

In the last line, we see explicitly that there is no radial contribution to the two-particle cross-correlation. By the way, the following integral was useful for getting to Eq. (3.51):

$$\frac{1}{2\pi} \int_0^{2\pi} I_0\left(\sqrt{\alpha^2 + \beta^2 + 2\alpha\beta \cos \theta}\right) d\theta = I_0(\alpha)I_0(\beta). \quad (3.52)$$

Autocorrelation for a distribution of particles. Finally, let us construct the full two-time fluorescence correlation function from a surface immobilized *distribution* of particles characterized by the set of coordinates $\mathcal{R} = \{\mathbf{x}_j\}$. The total intensity is given by

$$\Gamma_{\mathcal{R}}(t) = \sum_{\mathbf{x}_j \in \mathcal{R}} \Gamma_{\mathbf{x}}(t) \quad (3.53)$$

and the two-time fluorescence correlation function is given by

$$\begin{aligned} G_{\mathcal{R}}(\tau) &= \langle \Gamma_{\mathcal{R}}(t - \tau/2) \Gamma_{\mathcal{R}}(t + \tau/2) \rangle_t \\ &= \sum_{j, k \neq j} G_{\mathbf{x}_j, \mathbf{x}_k}(\tau) + \sum_j G_{\mathbf{x}_j}(\tau). \end{aligned} \quad (3.54)$$

Eq. (3.54) is the exact two-time fluorescence correlation function measured from a fixed arrangement of particles at positions specified by \mathcal{R} . We may now average over arrangements \mathcal{R} to find the result of a trajectory-averaged experimental run. Let $c(\mathbf{x})$ be the probability density for a particle to be at position \mathbf{x} and let $c(\mathbf{x}_1, \mathbf{x}_2)$ be

the joint probability to find a pair of particles at positions \mathbf{x}_1 and \mathbf{x}_2 . Then we have

$$G_c(\tau) = \iint d\mathbf{x}_1 d\mathbf{x}_2 G_{\mathbf{x}_1, \mathbf{x}_2}(\tau) c(\mathbf{x}_1, \mathbf{x}_2) + \int d\mathbf{x} G_{\mathbf{x}}(\tau) c(\mathbf{x}). \quad (3.55)$$

Eq. (3.55) together with Eqs. (3.45) and (3.50) reproduces all of the preceding correlation functions in appropriate limits. The case with the most experimental relevance is a uniform surface distribution with $c(\mathbf{x}) = c_0$ and $c(\mathbf{x}_1, \mathbf{x}_2) = c_0^2$. In this case, the two-time fluorescence correlation function averaged over individual trials can be written very simply in terms of previously calculated quantities.

$$\begin{aligned} G_{c_0}(\tau) &= c_0^2 \iint d\mathbf{x}_1 d\mathbf{x}_2 G_{\mathbf{x}_1, \mathbf{x}_2}(\tau) + c_0 \int d\mathbf{x} G_{\mathbf{x}}(\tau) \\ &= \left(\frac{\pi \Gamma_0 w^2 c_0}{2} \right)^2 + c_0 \bar{G}(\tau) \\ &= \left(\frac{\pi \Gamma_0 w^2 c_0}{2} \right)^2 \left\{ 1 + \frac{1}{\pi w^2 c_0} \exp \left[-\frac{4r^2}{w^2} (1 - \cos^2(\omega_0 \tau / 2)) \right] \right\}. \end{aligned} \quad (3.56)$$

Eq. (3.56) depends only on the peak photon count rate Γ_0 , the rotation frequency ω_0 , the dimensionless parameter r/w , which characterizes the beam geometry, and $w^2 c_0$, which characterizes the surface density and controls the measured feature contrast.

Chapter 4

Tracking Limits: Photon Counting Noise

In Ch. 3, we considered in detail the statistics of position sensing based on fluorescence modulation for *static* particles. In this chapter, we move to the *dynamic* regime by allowing the particle to move by Brownian motion during the position sensing process. In particular, we ask, “How well can we track a Brownian particle using fluorescence modulation?” We will now bring notions from control theory into our analysis, drawing strongly on the Kalman filter [30]. The fundamental limit on the localization will depend on the number of photons collected during the characteristic particle tracking time, *i.e.*, the feedback bandwidth. Everything in this chapter is theoretical, but in Ch. 8, we will show how close we come in practice to the fundamental limits derived here. This chapter is taken with minor modification from Ref. [26].

Because of the Poisson statistics of fluorescence detection, the experimental signal in our tracking experiment is fundamentally noisy. As a result, any estimate of the particle’s position based on this signal also inherits this noise. For a static particle, this uncorrelated noise can be removed by sufficient temporal averaging (both for imaging and non-imaging techniques), a fact exploited by Yildiz *et al.* to achieve nanometer fluorescent particle localization [39]. However, if a particle moves during the measurement, either stochastically or in an unknown deterministic way, the fluorescence noise results in a fundamental limit on the accuracy with which its position can be determined. Roughly speaking, a fast particle cannot be localized as accu-

rately as a slow particle. In tracking applications, if a particle cannot be sufficiently localized within the characteristic tracking timescale, then it cannot be tracked at all. In this chapter, we consider these fundamental constraints, and we place upper limits on the performance of particle tracking by fluorescence modulation in the presence of photon counting noise. We do not consider the finite bandwidth response of a realistic actuator; here, we only consider tracking performance limits based on photon counting statistics. In Sect. 4.1, we derive a simple expression for the noise spectral density in a fluorescence modulation measurement using the statistics developed in Ch. 3. In Sect. 4.2, we consider the statistical task of estimating a *moving* particle's position by filtering a noisy measurement. In Sect. 4.4, we present the results of numerical simulations of the tracking process, including in the nonlinear regime where some of our approximations break down, and give a qualitative method for determining the parameter regimes in which a particle can be tracked.

4.1 Static position estimation

In this section, we are concerned with estimating the position of a *static* particle using fluorescence modulation and demodulation techniques. We will derive results for our own quasi-two-dimensional tracking geometry, but the arguments generalize in a straightforward way to different experimental geometries. The definitions and notation are similar to preceding chapters, but not identical so we will reintroduce everything briefly here. We still consider a particle's two-dimensional position in the $xy \leftrightarrow \rho\theta$ plane as shown in Fig. 3.2. The *rate* of fluorescence from a particle at position $\mathbf{x} = (x, y) \leftrightarrow (\rho, \theta)$ is given by

$$\Gamma_{\mathbf{x}}(t) = \Gamma_0 \exp \left\{ -2 \left[\frac{\rho^2}{w^2} + \frac{r^2}{w^2} - 2 \frac{r\rho}{w^2} \cos(\theta - \omega_0 t) \right] \right\} \quad (4.1)$$

where Γ_0 is the peak fluorescence rate, w is the beam waist, r is the radius of rotation of the beam, and ω_0 is the angular rotation frequency.

As discussed previously, the measured fluorescence signal is a stochastic train of

voltage pulses from the output of a single-photon counter, with the arrival times of the pulses governed by the rate $\Gamma_{\mathbf{x}}(t)$. Letting $V(t)$ denote the shape of the electronic pulses, the full stochastic fluorescence signal $s(t)$ is given by a convolution integral

$$s(t) = (T * V)(t) \equiv \int_{-\infty}^{\infty} V(t-t')T(t')dt' \quad (4.2)$$

where $T(t)$ is defined as in Eq. (3.2).

In order to estimate the particle's position \mathbf{x} , we must extract the component of $s(t)$ [actually the component of $\Gamma_{\mathbf{x}}(t)$] at the laser rotation frequency ω_0 , a statistical task we have already discussed in detail in Ch. 3. We assume that ω_0 is much faster than the timescale of the particle's motion, so that over a single rotation period the particle can be considered to be stationary. Furthermore, we assume that the voltage pulses are very narrow (in time) compared to all other frequencies of interest, so that we may write $V(t) \approx V_0\delta(t)$ or equivalently $s(t) \approx V_0T(t)$.¹ We define the “instantaneous” component of $s(t)$ at angular frequency ω to be

$$\begin{aligned} \tilde{s}_t(\omega) &= \int_t^{t+2\pi/\omega_0} e^{-i\omega t} s(t) dt \\ &\approx V_0 \int_t^{t+2\pi/\omega_0} e^{-i\omega t} T(t) dt \equiv V_0 \tilde{T}_t(\omega) \end{aligned} \quad (4.3)$$

where $\tilde{T}_t(\omega)$ is the finite-windowed Fourier transform of $T(t)$, over one rotation period $2\pi/\omega_0$ beginning at time t . The real and imaginary parts of $\tilde{s}_t(\omega)$, or at least a bandwidth-limited filtration of these components, can be measured using phase-sensitive lock-in detection. These measurements probe a time-dependent, stochastic frequency spectrum $\tilde{s}_t(\omega)$. The expectation value of the component of $s(t)$ at $n\omega_0$, where n is a positive integer, is given by [*cf.* Eqs. (3.3a)-(3.3b) and (3.31)]:

$$\mathbb{E}[\tilde{s}_t(n\omega_0)] = V_0 \mathbb{E}[\tilde{T}_t(n\omega_0)] = V_0 h_n(\rho) e^{in\theta} \quad (4.4)$$

¹For our experiments, we use avalanche photodiodes with a pulse width of approximately 25 ns, while the rotation period is 125 μ s, so this approximation is quite valid.

with

$$h_n(\rho) = 2\pi \frac{\Gamma_0}{\omega_0} \exp \left[-\frac{2}{w^2} (r^2 + \rho^2) \right] I_n \left(\frac{4r\rho}{w^2} \right). \quad (4.5)$$

I_n is the n th-order modified Bessel function. For $\rho/w \ll 1$ and $\rho r/w^2 \ll 1$ (we will further assume that $r \sim w$), we may write

$$h_n(\rho) \approx \frac{2\pi}{n!} \left(\frac{\Gamma_0}{\omega_0} \right) \left(\frac{2\rho r}{w^2} \right)^n \exp \left[-2\frac{r^2}{w^2} \right] + O \left(\frac{\rho}{w} \right)^{n+1}. \quad (4.6)$$

For $n = 1$, Eq. (4.6) for $h_1(\rho)$ shows that the component of $s(t)$ at frequency ω_0 is, on average, *linear* in the radial coordinate ρ near the origin. Information about the angular coordinate θ is contained in the complex exponential phase, whose real and imaginary parts are accessible by lock-in detection. Near the origin, the real part of $\tilde{s}_t(\omega_0)$ is linear in the particle's x coordinate and the imaginary part is linear in the y component (on average). This linear dependence of the mean values of $\tilde{s}_t(\omega_0)$ near the origin provides the error signal for lock-in detection. Furthermore, the time-averaged fluorescence intensity is given by the $n = 0$ component, $\tilde{s}_t(0)$ while the variance will be shown to depend on the $n = 2$ component.

We may now construct an explicit estimator of the (stationary) particle's x position based on the measured frequency component $\tilde{s}_t(\omega_0)$. An analogous argument will hold for the y component. Note that measurement noise results in a time-dependent position estimate even for a stationary particle, so we must continue to use the subscript t . Let us define a reciprocal distance k_x by

$$k_x = 4\pi \left(\frac{\Gamma_0}{\omega_0} \right) \left(\frac{r}{w^2} \right) \exp \left[-2\frac{r^2}{w^2} \right] \quad (4.7)$$

and a stochastic, time-dependent estimate \hat{x}_t of the particle's position x by

$$\hat{x}_t = \frac{2\pi B}{V_0 k_x \omega_0} \text{Re} \int_t^{t+1/B} e^{-i\omega_0 t} s(t) dt. \quad (4.8)$$

In Eq. (4.8), B is the filter bandwidth, which is assumed to be much larger than the rotation frequency $\omega_0/2\pi$; with this separation of timescales, we may make the

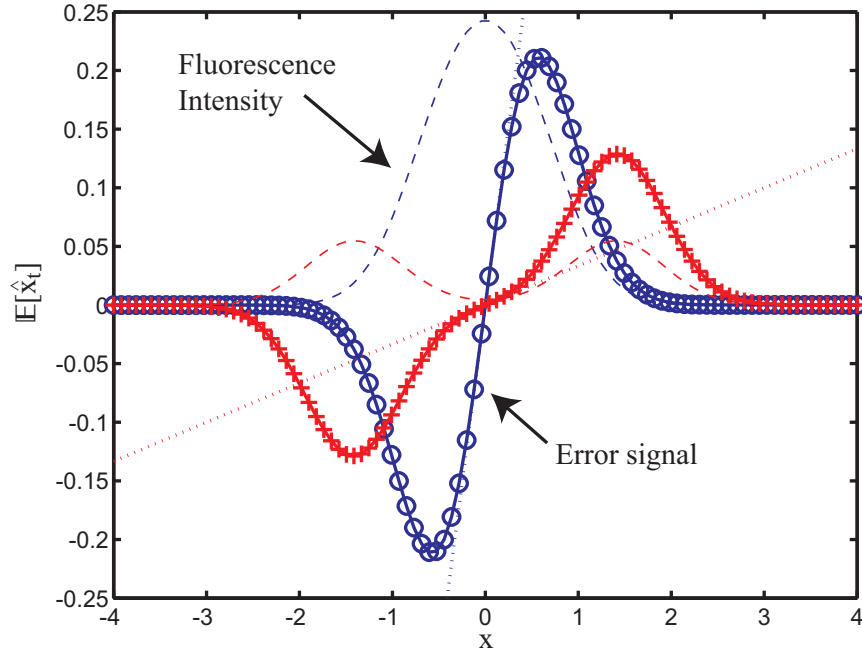


Figure 4.1: Expectation value $\mathbb{E}[\hat{x}_t]$ of the estimator \hat{x}_t (arbitrary units) for $r/w = 0.5$ (blue \circ) and $r/w = 1.5$ (red $+$). The dotted lines are the linear approximation of Eq. (4.6), while the dashed lines show the time-average laser intensity in arbitrary units.

approximation $\omega_0/2\pi B \approx N$ where N is a (large) integer. \hat{x}_t has the desired property that

$$\mathbb{E}[\hat{x}_t] = \frac{2w}{r^2} \exp\left[-\frac{2\rho^2}{w^2}\right] I_1\left(\frac{4r\rho}{w^2}\right) \approx \rho \cos\theta. \quad (4.9)$$

The approximation is valid near the origin, which is why it is useful as an error signal for locking the particle's position to the origin using feedback control. The expectation value of the estimator $\mathbb{E}[\hat{x}_t]$ is shown in Fig. 4.1 for two values of the offset parameter r/w .

We can now derive the primary result of this section. We may find the estimator variance, or squared tracking error, \hat{x}_t by plugging in to the preceding formulas to find

$$\mathbb{E}[(x - \hat{x}_t)^2] = \frac{1}{2Nk_x^2} [h_0(\rho) + h_2(\rho) \cos\theta] \approx \frac{h_0(\rho)}{2Nk_x^2} \quad (4.10)$$

where the approximation is valid in the linear regime near the origin. The rightmost expression in Eq. (4.10) does not depend on ρ , since $h_0(\rho)$ also does not, so plugging

back in for N and $h_0(\rho)$, we find

$$\mathbb{E} [(x - \hat{x}_t)^2] = \left[w\psi\left(\frac{r}{w}\right) \sqrt{\frac{B}{\Gamma_0}} \right]^2, \quad \psi(x) = \frac{1}{\sqrt{8}} \frac{e^{-x^2}}{x} \quad (4.11)$$

where ψ is a dimensionless function characterizing the beam geometry. The standard deviation in the tracking error scales as \sqrt{B} , a characteristic feature of shot noise processes. The measurement noise density n_m arising from photon counting statistics is given by

$$n_m = \frac{\sqrt{\mathbb{E} [(x - \hat{x}_t)^2]}}{\sqrt{B}} = \psi\left(\frac{r}{w}\right) \frac{w}{\sqrt{\Gamma_0}} \quad (4.12)$$

which has dimensions of (for example) $\mu\text{m}/\sqrt{\text{Hz}}$. This noise spectral density is valid for feedback bandwidths B that are large compared to the rotation frequency ω_0 . However, note that ω_0 appears nowhere within the expression for n_m so that we are free to make ω_0 arbitrarily large with no effect on the noise figure. Also, note that a similar noise figure will apply to noise in the measurement of each Cartesian component of the particle's position (for the case described here, the noise figures for x and y detection are identical).

The specific form of $\psi(x)$ was derived for our particular experimental geometry. For this case, $\psi(r/w)$ achieves its minimum value at $r/w = 1/\sqrt{2}$ where $\psi(1/\sqrt{2}) = \psi_{opt} \approx 0.82$. Recall that the expression for the noise density is only valid in the linear regime $\rho/w \ll 1$ together with the additional assumption that $r \sim w$, but ψ_{opt} is accessible well within this regime.

If we add a finite background count rate Γ_b to $\Gamma_{\mathbf{x}}(t)$ and carry out the same analysis, we find a measurement noise density $n_m \rightarrow \sqrt{n_m^2 + n_b^2}$ where the background contribution to the measurement noise density is

$$n_b = \psi\left(\frac{\sqrt{2}r}{w}\right) w \sqrt{\frac{2\Gamma_b}{\Gamma_0^2}}. \quad (4.13)$$

Finally, note that the results derived here require only the *linear* relationship between the frequency components of $s(t)$ and the particle's position near the origin, which is

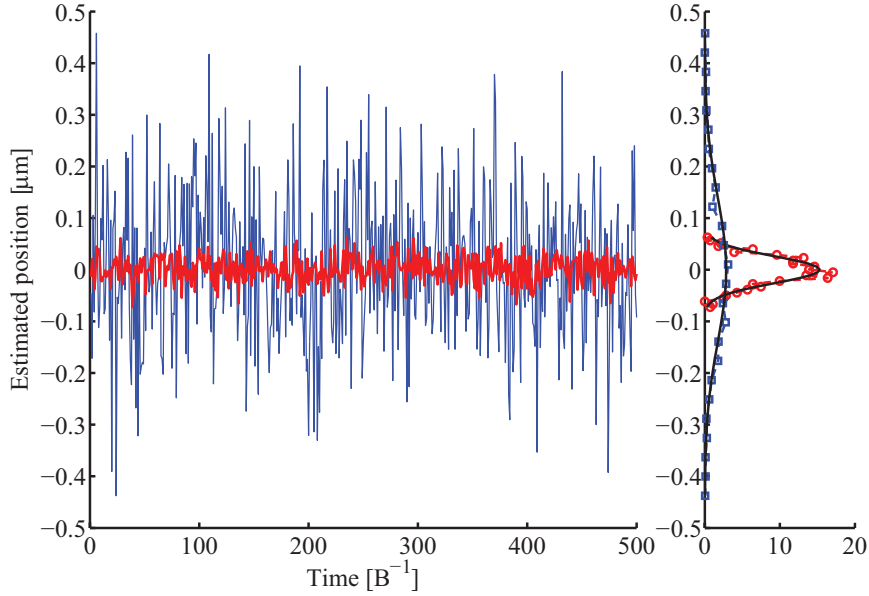


Figure 4.2: (Left) Numerical simulation of the estimate \hat{x}_t of a particle's position based on fluorescence demodulation. The particle was fixed at the coordinate origin. The red, more localized results are for $r/w = 1/\sqrt{2}$, $w = 1 \mu\text{m}$, $\Gamma_0 = 10^5 \text{ s}^{-1}$, and $\Gamma_B = 0$. The blue, wider distribution was computed with $r/w = 1.4$, $\Gamma_0 = 10^5 \text{ s}^{-1}$, $\Gamma_B = 10^4 \text{ s}^{-1}$. For both curves, the laser rotation period was $\omega_0 = 2\pi \times 8 \text{ kHz}$ and the bandwidth was $B = 100 \text{ Hz}$. (Right) Simulated distributions together with those predicted by $n_m\sqrt{B}$ as calculated in the text.

an essential ingredient for linearizing and locking a nonlinear system using feedback control. For a different experimental geometry, or tracking in higher dimensions, these methods can be applied in exactly the same way to derive the measurement noise spectral density n_m for each Cartesian coordinate. A simulation of the position estimator \hat{x}_t applied to a stationary particle at the coordinate origin is shown in Fig. 4.2.

4.2 Dynamic position estimation

In Sect. 4.1, we derived a noise spectral density n_m by considering the effect of photon counting statistics on fluorescence demodulation measurements. This noise density determines the standard deviation in estimating a *static* particle's position in a time $1/B$ to be $n_m\sqrt{B}$: a static particle can be localized arbitrarily well by averaging

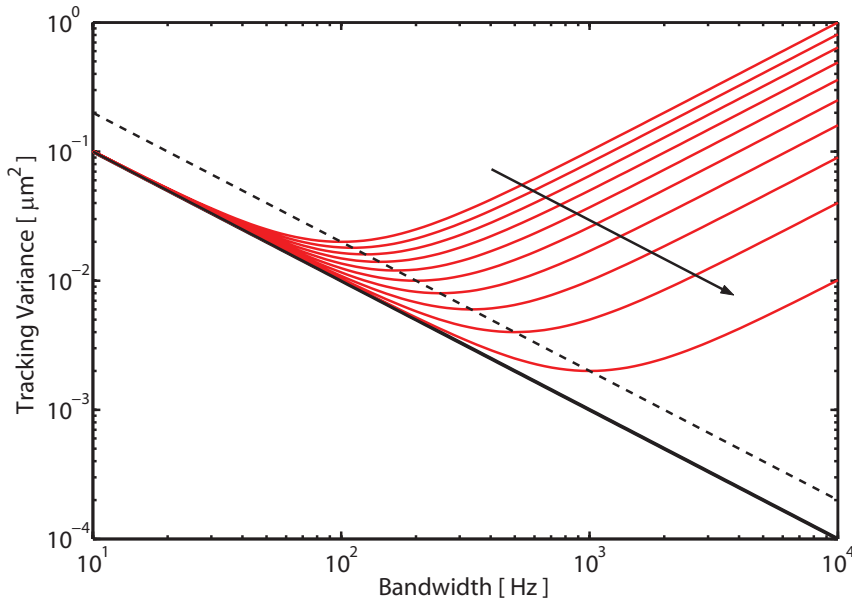


Figure 4.3: Mean-square tracking error $\mathbb{E}[e_t^2]$ as a function of bandwidth B as predicted by Eq. (4.16) for $D = 1 \mu\text{m}^2/\text{s}$ and the noise spectral density ranging from $n_m = 10^{-2}$ to $n_m = 10^{-3} \mu\text{m}/\sqrt{\text{Hz}}$. The solid arrow indicates the direction of decreasing n_m . The solid black line is the zero-noise limit where the tracking error is D/B and the dashed line is the locus of minima in the tracking error given by Eqs. (4.18a-4.18b).

the measurement for a sufficiently long time. In this section, we will take the noise spectral density n_m as given and consider *dynamic* position estimation of a diffusing particle. For this case, there exists an optimal bandwidth and a finite lower bound on the noise in the particle's estimated position. In the first part of this section, we will calculate the localization noise for a first-order low-pass filtration of a diffusing particle's position plus measurement noise. We will find the optimal bandwidth and minimum localization noise for this case. We will discuss particle position *estimation* and particle tracking *control* interchangeably, since we are interested here in fundamental tracking limits where we assume that the tracking control apparatus can respond instantaneously to the optimal estimate.² Therefore, optimal estimation results are equivalent to optimal control results for this idealized case.

²This is not an unattainable experimental scenario if a particle is tracked, for example, by translating an excitation laser using acousto-optic modulators whose response bandwidth may exceed the particle's motional timescale by several orders of magnitude.

Consider the time-dependent position X_t of a particle diffusing in one dimension with diffusion coefficient D . If we measure this particle's position with noise n_m , then form our estimate \hat{X}_t of the particle's position by filtering the result at a bandwidth B , we find the following coupled stochastic differential equations for X_t and \hat{X}_t

$$d \begin{pmatrix} X_t \\ \hat{X}_t \end{pmatrix} = \begin{pmatrix} 0 & 0 \\ -B & B \end{pmatrix} \begin{pmatrix} X_t \\ \hat{X}_t \end{pmatrix} dt + \begin{pmatrix} \sqrt{2D} & 0 \\ 0 & n_m B \end{pmatrix} \begin{pmatrix} dW_1 \\ dW_2 \end{pmatrix} \quad (4.14)$$

where dW_1 and dW_2 are independent stochastic Wiener increments [31] driving the particle's diffusion and the measurement noise, respectively. Eq. (4.14) represents a two-dimensional Ornstein-Uhlenbeck process where the components have an obvious interpretation in terms of the particle's position and the estimated position. Since the Ornstein-Uhlenbeck process is Gaussian, the particle's position will remain Gaussian distributed so long as its initial position is either deterministic or Gaussian distributed as well. We may collapse Eq. (4.14) to a single equation for the measurement error $e_t = X_t - \hat{X}_t$:

$$de_t = -Be_t dt + \sqrt{2\bar{D}} dW \quad , \quad \bar{D} = D + \frac{n_m^2 B^2}{2}, \quad (4.15)$$

which is a simple one-dimensional Ornstein-Uhlenbeck process with effective diffusion coefficient \bar{D} . Eq. (4.15) suggests that a particle tracked at bandwidth B looks (statistically) like a freely diffusing particle tracked with no measurement noise, but with an effectively larger diffusion coefficient \bar{D} given by the sum of D and the contribution from measurement noise $n_m^2 B^2/2$.

We are interested in steady-state tracking, not transient behavior during the locking process, so we will use steady-state solutions. For long times compared to the feedback timescale $1/B$, we find $\mathbb{E}[e_t] = 0$ and

$$\mathbb{E}[e_t^2] = \frac{\bar{D}}{B} = \frac{D}{B} + \frac{n_m^2 B}{2}. \quad (4.16)$$

The steady-state time-correlation function is

$$G(\tau) = \lim_{t \rightarrow \infty} \mathbb{E}[e_{t+\tau} e_t] = \frac{\bar{D}}{B} \exp(-B\tau) \quad (4.17)$$

which may prove to be useful result for performing fluorescence correlation spectroscopy (FCS) while tracking a single particle [25]. Eq. (4.16) gives an asymptotic limit for particle localization with a simple first-order filtration of the demodulated fluorescence signal. The optimal bandwidth and estimator variance are given by

$$B_{opt} = \sqrt{2D}/n_m \quad (4.18a)$$

$$\mathbb{E}[e_t^2]_{opt} = \sqrt{2D}n_m. \quad (4.18b)$$

In Sect. 4.3, the same optimal bandwidth and localization are found by applying a Kalman filter to the system consisting of the particle's position X_t and a noisy measurement of that position. Since the Kalman filter is optimal in the mean-square sense, that analysis shows that the simple first-order filtration at bandwidth B is in fact the *optimal control law* when the experimental response time is not a limiting factor.

Now suppose we wish to track a particle's position and we require a squared tracking error (in the x direction) less than some value σ_x^2 . The maximum diffusion coefficient D_{max} for which a particle can be tracked within this tracking error constraint can be found by setting Eq. (4.18b) equal to σ_x^2 and using the full expression for the measurement noise n_m including a finite background:

$$D_{max} = \left(\frac{\Gamma_0 \sigma_x^4}{2w^2} \right) \left[\psi \left(\frac{r}{w} \right)^2 + 2 \frac{\Gamma_b}{\Gamma_0} \psi \left(\frac{\sqrt{2}r}{w} \right)^2 \right]^{-1}. \quad (4.19)$$

Eq. (4.19) is an explicit expression for the largest diffusion coefficient D_{max} that can be tracked (in one dimension only) by fluorescence modulation; solving for σ_x , we find an expression for the smallest position variance that can be achieved when tracking a given diffusion coefficient. Note that at fixed r/w , D_{max} strictly decreases with

D	$\sigma(d=2)$	$\sigma(d=3)$
0.001	14	18
0.01	26	31
0.1	45	55
1.0	81	99
10.0	143	175
100.0	255	310

Table 4.1: Table showing the best possible standard deviation σ [nm] in localizing a particle with diffusion coefficient D [$\mu\text{m}^2/\text{s}$] ranging over relevant values for single-molecule spectroscopy in $d = 2$ or 3 dimensions. The remaining parameters were fixed at $w = 0.5\mu\text{m}$, $r = w/\sqrt{2}$, $\Gamma_0 = 50$ kHz, $\Gamma_b = 10$ kHz.

increasing beam waist w ; however, at fixed fractional localization σ_x/w , D_{max} strictly increases with w .

Now consider tracking isotropic diffusion in 3 dimensions. This may be achieved by rotating the excitation laser in the xy plane and periodically modulating the focal depth in the z direction at a sufficiently different frequency that the three components may be demodulated separately (see for example [16, 18]). Let the measurement noise in the estimate of the x position be n_x and similarly for y and z . The total tracking error is given by the quadrature sum of the error in each dimension. Therefore, for three-dimensional localization such that the variance in distance from the origin is less than $\sigma^2 = \sigma_x^2 + \sigma_y^2 + \sigma_z^2$, the largest “trackable” diffusion coefficient is

$$D_{max} = \frac{\sigma^4}{2(n_x + n_y + n_z)^2}. \quad (4.20)$$

If the noise densities are equal in all directions, $n_x = n_y = n_z = n_m$ and we desire a variance in the distance to the origin less than σ^2 , then in d dimensions, we have the general result

$$D_{max} = \frac{\sigma^4}{2d^2n_m^2} \iff \sigma_{min} = (2Dd^2n_m^2)^{1/4}. \quad (4.21)$$

A few values of the optimum localization $\sigma = \sigma_{min}$ as a function of D are given in Table 4.1 for typical experimental parameters. The σ^4 scaling is quite steep, so that a moderate increase in the acceptable variance leads to a much larger “trackable” diffusion coefficient; conversely, a moderate decrease in the acceptable variance strongly

reduces the trackable diffusion coefficient.

Throughout this section, we have assumed that a particle is tracked near the coordinate origin, so that linear approximations to $\mathbb{E}[\hat{x}]$ and $\sigma_{\hat{x}}^2$ are accurate. However, before the final approximation, Eq. (4.10) is the exact variance for the linear estimator. We see that any deviations from the linear regime result in an estimator bias ($\mathbb{E}[\hat{x}] \neq x$) and increased estimator noise (since $h_2(\rho)$ is strictly positive away from the origin). Therefore, it is reasonable to assume that any tracking controller based on the linear position estimator \hat{x} will only perform worse than our linear approximation results when non-linear correction terms are included in the noise density and estimator error. On the other hand, we cannot rule out the possibility that a more sophisticated, non-linear signal processing scheme may be capable of exploiting the structure of $h_n(\rho)$ in order to improve the tracking capability based on fluorescence modulation.

4.3 Optimal position estimation

In this Section, we return to Eqs. (4.18a-4.18b), and show that these are optimal results that can be found from a simple application of the Kalman filter [30]. Consider the one-dimensional position X_t of a Brownian particle with diffusion coefficient D at time t , and consider an *unfiltered* measurement of this position, denoted by ξ_t , subject to a measurement noise density n_m . These quantities constitute a simple pair of coupled stochastic differential equations

$$dX_t = \sqrt{2D}dW_1 \quad (4.22a)$$

$$\xi_t dt = X_t dt + n_m dW_2 \quad (4.22b)$$

where dW_1 and dW_2 are uncorrelated Wiener increments, as in Eq. (4.14). In the main text, we dealt only with the *filtered* estimate of the particle's position given by \hat{X}_t . In the notation of this section, the unfiltered measurement ξ_t is proportional to the finite-windowed Fourier transform $\tilde{s}_t(\omega_0)$ of Sect. 4.1.

Assuming the initial position of the particle is known, or is Gaussian distributed,

we may apply a Kalman filter to the system in Eqs. (4.22a-4.22b) to find the filtration of ξ_t , denoted by \hat{X}_t , that minimizes the mean-square error $e_t = \mathbb{E}[(\hat{X}_t - X_t)^2]$. The result of the Kalman filtration gives the following update rule for the estimate \hat{X}_t :

$$d\hat{X}_t = \frac{\sqrt{2D}}{n_m} (\hat{X}_t - \xi_t) dt. \quad (4.23)$$

Eliminating $\xi_t dt$ in Eqs. (4.22a)-(4.23) results in the coupled system of Eq. (4.14) provided we make the identification $B = \sqrt{2D}/n_m$. Thus the optimal filtration of the position measurement ξ_t is in fact a first-order filtration with the filter bandwidth given by B_{opt} of Eq. (4.18a). The Kalman filter also describes the deterministic evolution of the estimator variance $\mathbb{E}[(\hat{X}_t - X_t)^2]$ via an associated Riccati equation. Denoting this variance by Σ_t , the Riccati equation is

$$\frac{d\Sigma_t}{dt} = 2D - \frac{\Sigma_t^2}{n_m^2} \quad (4.24)$$

whose solution is

$$\Sigma_t = \sqrt{2D}n_m \tanh \left[\frac{\sqrt{2D}}{n_m}(t + t_0) \right] \quad (4.25)$$

where t_0 parametrizes the initial uncertainty in the particle's position. In the long-time limit, the stationary solution of Eq. (4.24) is easily seen to reproduce Eq. (4.18b).

4.4 Numerical simulations

In the preceding sections, we developed a model for particle-tracking experiments in the presence of measurement noise arising from photon counting statistics. In our model, we linearized the demodulated fluorescence signal around the coordinate origin. This approximation is valid in the *linear tracking* regime in which the error in tracking a particle is well described by the model of Sects. 4.1 and 4.2. In this regime, the Ornstein-Uhlenbeck model of the tracking error is sufficient for describing the position of the particle, including the correlation statistics given by Eq. (4.17)

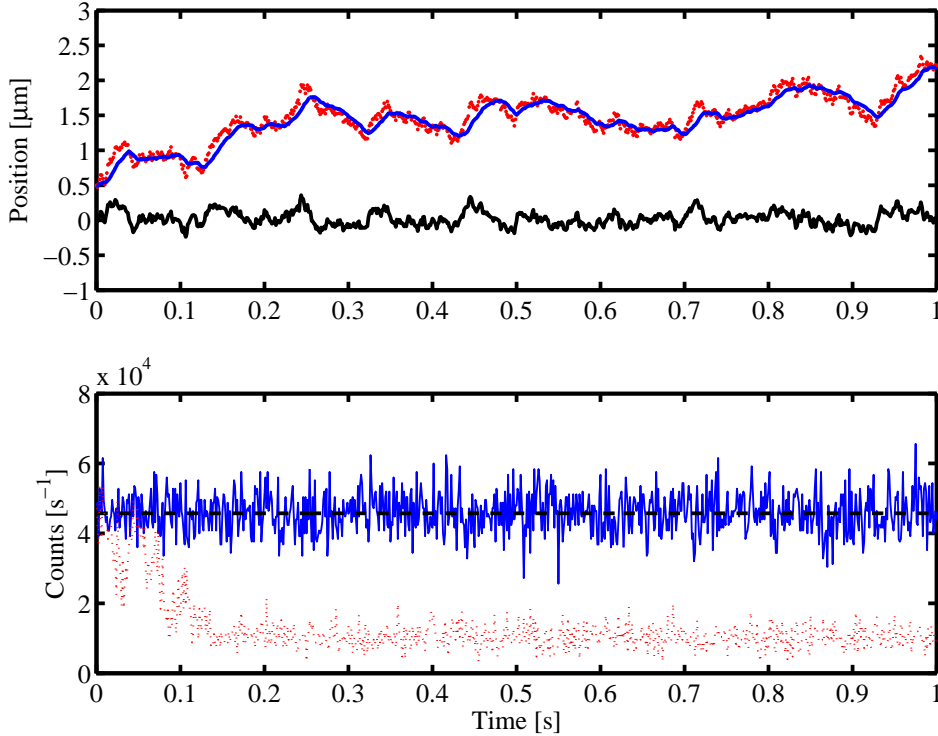


Figure 4.4: Two-dimensional tracking simulation in the linear regime. The position estimator \hat{X}_t and a particle with diffusion coefficient $D = 1\mu\text{m}^2/\text{s}$ were started at the origin at time $t = 0$. The remaining parameters were $w = 532\text{ nm}$, $r = w/\sqrt{2}$, $\omega_0 = 2\pi \times 8000\text{ Hz}$, $B = 100\text{ Hz}$, $\Gamma_0 = 10^5\text{ Hz}$, and $\Gamma_b = 10^4\text{ Hz}$. The upper plot shows the x position of the particle X_t (red \cdot) and position estimator \hat{X}_t (blue $-$), with the same offset added to each curve for clarity. Also shown is the tracking error e_t (black $-$). The lower plot shows the fluorescence count rate for this trajectory both with (blue $-$) and without (red $\cdot\cdot\cdot$) tracking control. The dashed curve is the expected fluorescence rate based on the linearized model, which is in good agreement with the full simulation.

which will be useful for performing Fluorescence Correlation Spectroscopy (FCS) [25]. In a true experiment (with a Gaussian excitation laser), when the feedback bandwidth is either too low or too high, it may be impossible to localize a particle well enough to contain it within the linear regime. In some cases, it may not even be possible to contain the particle within the excitation laser focus so that it cannot be tracked at all; this is the *untracked* regime. Finally, there is an intermediate *nonlinear tracking* regime, in which a particle may be at least partially tracked, but it cannot be localized tightly enough to warrant the linearized model of the position estimator and tracking statistics. While the linear tracking and the untracked regimes may be

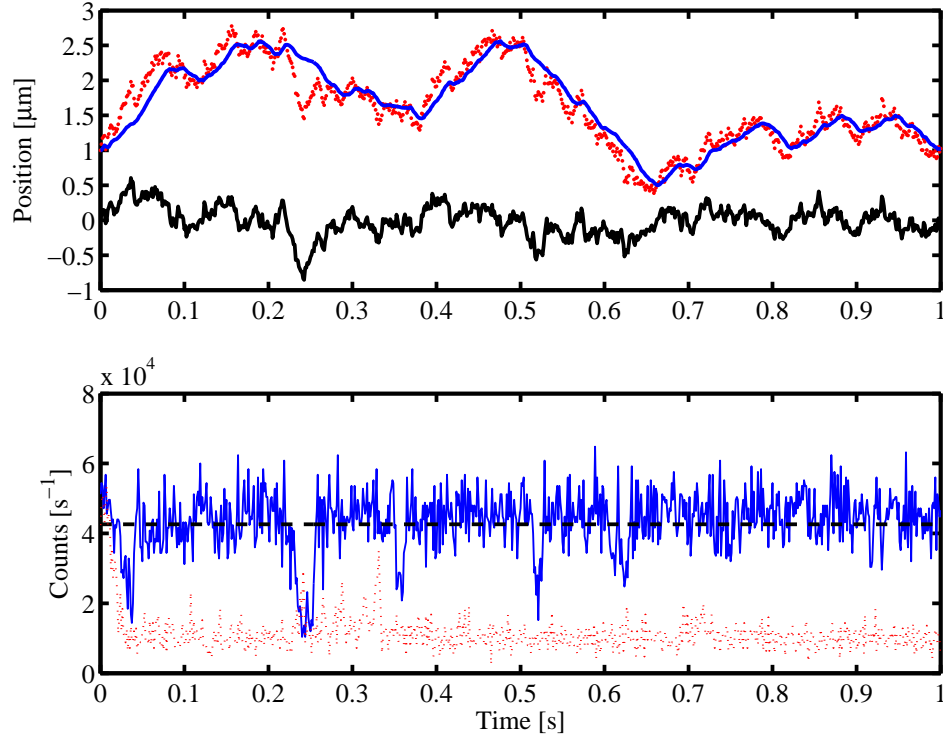


Figure 4.5: Two-dimensional tracking simulation in the nonlinear regime. The simulation parameters are the same as in Fig. 4.4, except that the particle's diffusion coefficient was increased to $D = 2.5\mu\text{m}^2/\text{s}$. In the nonlinear regime, the particle explores much more of the laser intensity, resulting in greater fluctuations of the tracking error e_t and the fluorescence intensity. The particle nearly escapes the Gaussian laser but is recaptured a number of times during the simulation period.

treated exactly, using Ornstein-Uhlenbeck or free diffusion statistics respectively, the nonlinear tracking regime is difficult to treat analytically. In this section, we present the results of numerical simulations across all of these regimes, both to illustrate the previously described statistics and to develop intuition about the intermediate nonlinear tracking regime.

The results of typical two-dimensional simulations are shown in Figs. 4.4 and 4.5. The simulations explicitly treat all aspects of the tracking process including particle diffusion, Poisson fluorescence statistics in a rotating Gaussian laser, lock-in detection at the rotation frequency, and translation of the laser centroid according to a bandwidth-limited filtration of the position estimate \hat{X}_t . Fig. 4.4 is an example of linear tracking, while Fig. 4.5 shows nonlinear tracking. See the figure captions for

details of the simulation parameters. Qualitatively, we expect that the transition between the linear tracked regime and the untracked regime (passing through the nonlinear regime) occurs when the tracking error in the linear model reaches some threshold fraction of the beam waist w . Near this point in the parameter space, a tracked (or partially tracked) particle may escape from the tracking laser and become untracked. Without calculating any details of escape probabilities, which would require a full nonlinear model of the tracking process, we can construct a qualitative picture of the transition between the linear and untracked regimes (treating the nonlinear tracking regime as a fuzzy boundary between the two). In Fig. 4.6 we explore the transition between the untracked and tracked regimes as a function of the feedback bandwidth B , with all other parameters held constant.

The simulation results displayed in Fig. 4.6 show that our qualitative picture of the transition between the linear and untracked regimes (detailed in the figure caption) agrees well with the actual behavior of the system. In this qualitative picture, the system exhibits threshold behavior, jumping discontinuously from the linear tracked regime to the untracked, free diffusion regime at points in parameter space where the squared tracking error calculated in the linear model exceeds some critical value, which we took to be $0.1w^2$. Using this rule, we may fix the experimental geometry and fluorescence parameters and construct a phase diagram in the space of the particle's diffusion coefficient D and the feedback bandwidth B indicating the boundaries between tracked and untracked regions. For tracking in d dimensions, we simply add the tracking errors from each Cartesian direction in quadrature. A tracking phase diagram constructed in this way is shown in Fig. 4.7.

With this qualitative model, based on the exact statistics of the linear and untracked regimes and verified by numerical simulation in the nonlinear regime, we have succeeded in partitioning the experimental parameter space into “trackable” and “untrackable” regions.

4.5 Commentary

In Sect. 4.1, we derived the noise spectral density n_m arising from photon counting statistics in a fluorescence modulation particle-tracking scheme. We also showed the generic σ^4/n_m^2 dependence of the maximum trackable diffusion coefficient in a particle tracking experiment subject to measurement noise, and combined these result to find explicit upper bounds on tracking performance for our own, and similar, experiments in Sect. 4.2. The steep scaling of D_{max} with σ suggests that particle tracking by fluorescence modulation is useful for localizing a particle to a moderate fraction of the beam waist; however, it is very difficult to obtain high resolution position information for particle tracking in the presence of measurement noise. Our calculations were performed for the case of two-dimensional tracking in a rotating Gaussian laser field; however, we attempted to partition the details of the experimental geometry into the function $\psi(x)$, while the remaining arguments are generically applicable to any linear position measurement of a diffusing particle subjected to measurement noise. Finally, in Sect. 4.4, we combined the analytical results of Sects. 4.1 and 4.2 with numerical simulations in the intermediate nonlinear tracking regime in order to verify a simple, qualitative procedure for determining the regions of parameters space in which a particle can be successfully tracked.

For future particle tracking experiments, it will be crucial to understand the limits of particle tracking and particle localization by noisy fluorescence measurements. Although we have concentrated on the case of fluorescence modulation, any particle localization scheme based on fluorescence detection will be subject to some degree of measurement noise arising from the fundamental stochastic nature of photon counting statistics. While the precise form of the noise will depend on all aspects of the experimental geometry and signal processing, most of the analysis in this chapter will be applicable to these other cases.

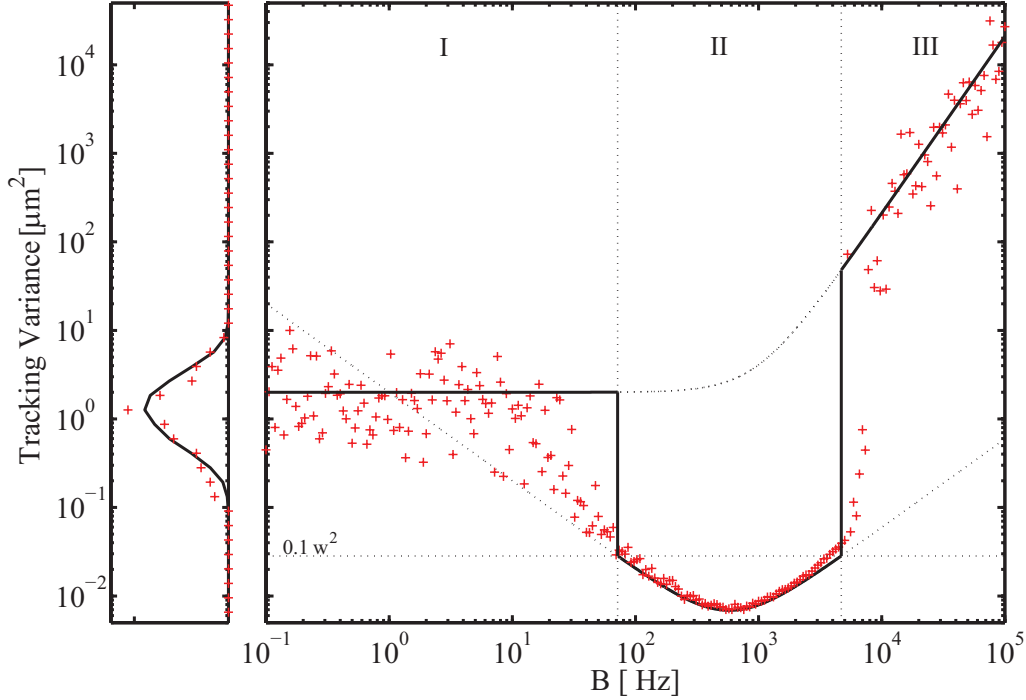


Figure 4.6: Two-dimensional ($d = 2$) Monte Carlo simulation results showing the mean (time-averaged) value of the squared tracking error $\mathbb{E}[e_t^2]$ over a $T = 1s$ simulation. Regions I and III are untracked while Region II is the linear tracked regime. The solid black line is a qualitative guide constructed as follows: In regions I and III, the solid black curve follows the free diffusion result $\mathbb{E}[e_t^2] = d(D + n_B^2 B^2/2)T$ expected for free particle diffusion and estimator position driven by background fluorescence, while in region II the solid black line jumps to the expected value of the tracking error for the linear regime where the mean tracking error is $d\bar{D}/B$ independent of T . The jump point was conservatively chosen to be the bandwidth where the linear tracking error reaches $0.1w^2$; beyond this threshold value the simulations show that particles are at least partially tracked in the nonlinear regime, especially on the smaller B side. The expected distribution of free diffusion tracking errors (in the limit $B \ll \sqrt{D}/n_B$) is plotted at left, together with a histogram of the simulated values with $B < 30$ Hz, showing that the points at the low bandwidth end follow free diffusion statistics. In addition to reducing the average tracking error, linear tracking drastically reduces the variance in the tracking error. The remaining simulation parameters were $w = 532$ nm, $r = w/\sqrt{2}$, $\omega_0 = 2\pi \times 10^5$ Hz, $D = 1\mu\text{m}^2/\text{s}$, $\Gamma_0 = 5 \times 10^4$ Hz, and $\Gamma_0 = 10^4$ Hz.

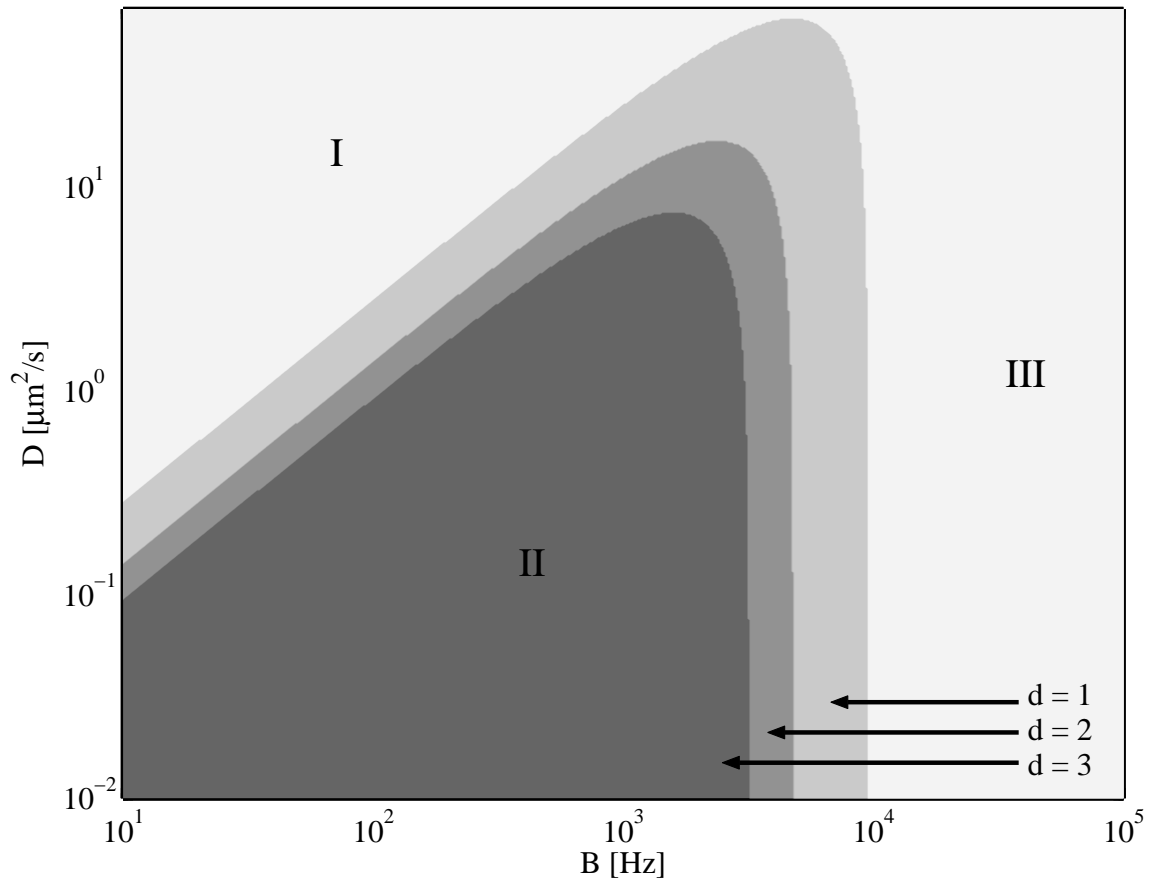


Figure 4.7: d -Dimensional tracking phase diagram in the parameter space of diffusion coefficient D versus feedback bandwidth B , with all other parameters fixed. Regions I and III represent untracked phases where the feedback bandwidth is too slow and too fast, respectively. Region II is the linear tracking region. The nonlinear tracking region lies outside region II, extending into the untracked region. The simulations in Fig. 4.6 lie on a horizontal slice along the $D = 1\mu\text{m}^2/\text{s}$ line of this phase diagram, with $d = 2$. All other parameters are the same as in Fig. 4.6.

Chapter 5

Full Linear Theory of Closed-Loop Particle Tracking

In this chapter, we will unify our preceding results from Chs. 2-4 by constructing a control theoretic model of the particle tracking system that includes arbitrary order feedback control and sensor noise. We will show that such a model can be used to calculate all of the relevant statistical quantities in the experiment. Furthermore, our knowledge of the statistics of the tracked particle's motion relative to the laser allows us to calculate *fluorescence correlation functions* to find a generalization of FCS to the closed-loop regime.

A good reference for control theory, including good sections on linear stochastic control and Kalman filtering, is Ref. [30]. Good references for solving linear Fokker-Planck equations are Refs. [36, 31, 40].

5.1 Linear control system model

We take as our model the linear feedback network shown in Fig. 5.1, where the tracking controller is represented by the (Laplace space) transfer function $C(s)$ and the piezoelectric stage, the “plant,” is represented by $P(s)$. We will consider the control system in one dimension only, since the Cartesian coordinates of a Brownian particle are statistically independent. The particle is driven by Brownian motion,

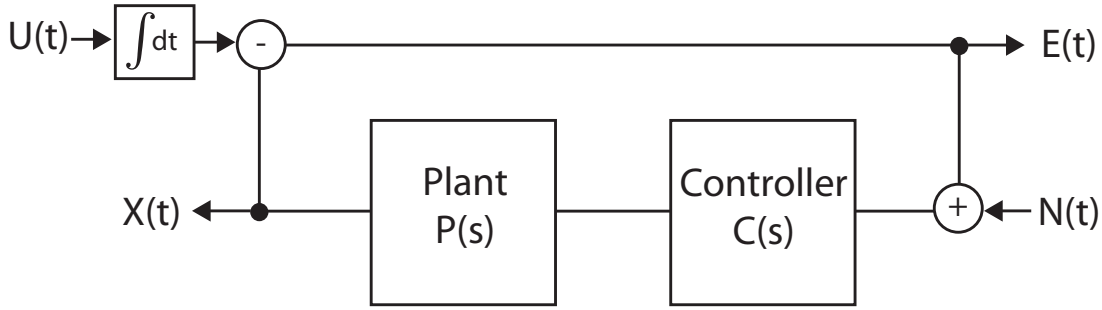


Figure 5.1: Block diagram of the particle tracking control system.

and we represent its “velocity” by

$$U(t) = \sqrt{2D} \frac{dW_p(t)}{dt} \quad (5.1)$$

where D is the diffusion coefficient and $dW_p(t)$ is a stochastic Wiener increment [31, 36]. The time-integral of $U(t)$ is the position of the particle, $X_p(t)$, at time t :

$$X_p(t) = \int_0^t U(t') dt' = \sqrt{2D} \int_0^t \frac{dW_p(t')}{dt'} dt' = \sqrt{2D} \int_0^t dW_p(t'). \quad (5.2)$$

The position of the sample stage is denoted by $X(t)$, and the error signal

$$E(t) = X(t) - X_p(t) \quad (5.3)$$

is the difference between the stage position $X(t)$ and the particle’s position. Finally, Gaussian white noise

$$N(t) = n \frac{dW_n(t)}{dt} \quad (5.4)$$

with a noise density n is added to the error signal; $W_n(t)$ is another Wiener process statistically independent of $W_p(t)$.

As discussed extensively in virtually every textbook treatment of stochastic processes, the Wiener process $W_p(t)$ is continuous but nowhere differentiable. You may therefore worry about our “velocity” $U(t)$, which strictly speaking is undefined. However, this term will always drive a *linear* differential equation, where it serves as conve-

nient shorthand notation for a more carefully written stochastic differential equation (SDE), for example

$$dU(t) = \sqrt{2D}dW_p(t). \quad (5.5)$$

So long as our equations are linear, we are fine [31]. We will also never need to differentiate between Ito and Stratonovich type SDEs for the same reason.

Our discussions in Chs. 3 and 4 connect to the treatment here through the error signal $E(t)$ and the measurement noise density n . The error signal, *i.e.*, the deviation of the particle from the laser centroid (the sample stage position and the laser centroid are one and the same) is given by the position estimator of Eq. (4.8) while the noise floor due to photon counting statistics is given by Eq. (4.12). Once we have found the measurement noise density n using the statistical treatments from earlier chapters, we can plug it into the model presented here and promptly forget all about Gaussian beams and photon statistics, that is, until we get around to calculating fluorescence correlation functions.

5.1.1 Specification of transfer functions

The two output functions $X(t)$, the sample stage position, and $E(t)$, the deviation of the particle from the laser centroid, play integral roles in analyzing a tracking experiment. In particular, during tracking, we cannot access the particle's position $X_p(t)$ directly; rather, we measure the sample stage position $X(t)$, which tracks $X_p(t)$ but is not identically equal to it, of course. Similarly, we cannot directly access the tracking error $E(t)$. but we can measure the particle's *fluorescence*, which is a time-dependent Poisson process driven by $E(t)$. Therefore, we are particularly interested in the statistics of these two signals. In this section, we will show how to calculate the autocorrelation function of the two processes $X(t)$ and $E(t)$ for a generic stable control system of arbitrary order, and we will explicitly record the results for a first- and second-order system. We will see later, that the second-order treatment turns out to be sufficient for our experimental apparatus.

Let us begin by writing the entire system in Laplace space, where $\tilde{\sim}$ represents the

Laplace transform:

$$\begin{pmatrix} \tilde{X}(s) \\ \tilde{E}(s) \end{pmatrix} = \begin{pmatrix} T_{XU}(s) & T_{XN}(s) \\ T_{EU}(s) & T_{EN}(s) \end{pmatrix} \begin{pmatrix} \tilde{U}(s) \\ \tilde{N}(s) \end{pmatrix}. \quad (5.6)$$

Denoting the loop transfer function by $L(s) = C(s)P(s)$, the four transfer functions in Eq. (5.6) are given by inspection of Fig. 5.1

$$T_{XU}(s) = \frac{L(s)}{s[1 + L(s)]} \quad (5.7a)$$

$$T_{XN}(s) = \frac{L(s)}{1 + L(s)} \quad (5.7b)$$

$$T_{EU}(s) = \frac{1}{s[1 + L(s)]} \quad (5.7c)$$

$$T_{EN}(s) = \frac{L(s)}{1 + L(s)}. \quad (5.7d)$$

Before going further, we will get some terminology straight. A (closed-loop) transfer function $T(s)$ is strictly proper if it is the ratio of two polynomials in s with the order of the denominator greater than the order of the numerator. For a strictly proper transfer function, we will say that its order is the order of its denominator polynomial. $T(s)$ is *stable* if all of its poles, *i.e.*, the zeros of its denominator polynomial, lie in the left half of the complex s -plane. The astute reader will note that $T_{EU}(s)$ and $T_{XU}(s)$ as defined in Eq. (5.6) have a pole at the origin $s = 0$, and it is at least possible (if this pole is not canceled by a zero) that these are unstable. However, a pole at the origin represents a particularly innocuous form of instability, *marginal stability*, and we will see how to deal with it later (the transfer function representing the *derivative* of this process is stable).

Because our system is linear, the output is given by the sum of the output due to each of the inputs, so we may write

$$\tilde{X}(s) = \tilde{X}_U(s) + \tilde{X}_N(s) = T_{XU}(s)\tilde{U}(s) + T_{XN}(s)\tilde{N}(s) \quad (5.8)$$

$$\tilde{E}(s) = \tilde{E}_U(s) + \tilde{E}_N(s) = T_{EU}(s)\tilde{U}(s) + T_{EN}(s)\tilde{N}(s). \quad (5.9)$$

We may now calculate the statistics for each of the four quantities $\tilde{X}_U(s)$, $\tilde{X}_N(s)$, $\tilde{E}_U(s)$, and $\tilde{E}_N(s)$ separately and sum them to find the total output.

5.1.2 State-space realizations and the Fokker-Planck equation

Let us now take a step back to calculate the statistics of a generic, stable linear system (with some suggestive notation of course). Consider the closed-loop transfer function $T(s)$ driven by a stochastic input $U(t)$ with output $X(t)$. It is a straightforward task to convert this system back into the time domain by finding a *state-space realization*, consisting of three matrices \mathbf{A} , \mathbf{B} , \mathbf{C} , satisfying¹

$$T(s) = \mathbf{C} (s\mathbf{I} - \mathbf{A})^{-1} \mathbf{B}. \quad (5.10)$$

If $T_{XN}(s)$ is of order m , then \mathbf{A} , \mathbf{B} , and \mathbf{C} have sizes $m \times m$, $m \times 1$ and $1 \times m$ respectively. The specification of these matrices is not unique, but as long as they satisfy Eq. (5.10), they represent a valid realization. Letting $\boldsymbol{\xi}$ be an m -component internal state vector, the system's dynamics can now be written in the form

$$d\boldsymbol{\xi}(t) = \mathbf{A}\boldsymbol{\xi}(t)dt + \mathbf{B}U(t)dt \quad (5.11)$$

$$X(t) = \mathbf{C}\boldsymbol{\xi}(t). \quad (5.12)$$

Finally, consider a stochastic input $U(t)dt = dW(t)$. The equation of motion for $\boldsymbol{\xi}(t)$ then becomes the multivariate Ornstein-Uhlenbeck process

$$d\boldsymbol{\xi}(t) = \mathbf{A}\boldsymbol{\xi}(t)dt + \mathbf{B}dW(t). \quad (5.13)$$

$\boldsymbol{\xi}$ is a vector-valued random process, whose statistics are given by a linear Fokker-

¹Actually, a general state-space realization includes a fourth matrix \mathbf{D} representing the direct feedthrough of input signal to output signal. For our systems, which will be strictly proper, we will always find $\mathbf{D} = 0$.

Planck equation

$$\frac{\partial}{\partial t} p(\boldsymbol{\xi}, t) = \sum_{jk} A_{jk} \frac{\partial}{\partial \xi_j} \xi_k p(\boldsymbol{\xi}, t) + \frac{1}{2} \sum_{jk} [\mathbf{B}\mathbf{B}^T]_{jk} \frac{\partial^2}{\partial \xi_j \partial \xi_k} p(\boldsymbol{\xi}, t) \quad (5.14)$$

where ξ_k is the k th component of $\boldsymbol{\xi}$ and A_{jk} is the jk element of \mathbf{A} .

It will be convenient to write probability distributions in terms of their characteristic functions. The stationary solution to Eq. (5.14) is

$$p(\boldsymbol{\xi}_0) = \int \frac{d^{(n)}\mathbf{k}}{(2\pi)^n} \exp \left[-i\mathbf{k}^T \boldsymbol{\xi}_0 - \frac{1}{2} \mathbf{k}^T \boldsymbol{\Sigma}_\infty \mathbf{k} \right] \quad (5.15)$$

and the full solution for a δ -function initial condition $p(\boldsymbol{\xi}, 0) = \delta^{(m)}(\boldsymbol{\xi} - \boldsymbol{\xi}_0)$ is given by

$$p(\boldsymbol{\xi}, t | \boldsymbol{\xi}_0, 0) = \int \frac{d^{(n)}\mathbf{k}}{(2\pi)^n} \exp \left[-i\mathbf{k}^T (\boldsymbol{\xi} - e^{\mathbf{A}t} \boldsymbol{\xi}_0) - \frac{1}{2} \mathbf{k}^T \boldsymbol{\Sigma}(t) \mathbf{k} \right]. \quad (5.16)$$

Eq. (5.16) is a Gaussian distribution with mean and covariance

$$\mathbb{E}[\boldsymbol{\xi}] = e^{\mathbf{A}t} \boldsymbol{\xi}_0 \quad (5.17)$$

$$\mathbb{E}[\boldsymbol{\xi} \boldsymbol{\xi}^T] = \boldsymbol{\Sigma}(t) \quad (5.18)$$

satisfying

$$\frac{d}{dt} \boldsymbol{\Sigma}(t) = \mathbf{A} \boldsymbol{\Sigma}(t) + \boldsymbol{\Sigma}(t) \mathbf{A}^T + \mathbf{B}\mathbf{B}^T, \quad \boldsymbol{\Sigma}(0) = 0. \quad (5.19)$$

The solution to Eq. (5.19) is given by

$$\boldsymbol{\Sigma}(t) = \int_0^t e^{\mathbf{A}(t-t')} \mathbf{B}\mathbf{B}^T e^{\mathbf{A}^T(t-t')} dt' \quad (5.20)$$

$$= \boldsymbol{\Sigma}_\infty - e^{\mathbf{A}t} \boldsymbol{\Sigma}_\infty e^{\mathbf{A}^T t}, \quad (\mathbf{A} < 0). \quad (5.21)$$

The integral solution Eq. (5.20) holds for all \mathbf{A} even when $\boldsymbol{\Sigma}(t)$ becomes unbounded, for example in the simple uncontrolled Brownian motion case where $\mathbf{B} = \sqrt{2D}$ and $\mathbf{A} = 0$ we find $\boldsymbol{\Sigma}(t) = 2Dt$. For a stable system in which the eigenvalues of \mathbf{A} all have negative real part (corresponding to left-half plane poles of $T(s)$), a stationary

solution Σ_∞ exists, defined by the Lyapunov equation

$$\mathbf{A}\Sigma_\infty + \Sigma_\infty\mathbf{A}^\top + \mathbf{B}\mathbf{B}^\top = 0. \quad (5.22)$$

The two-time probability distribution for the state vector $\boldsymbol{\xi}(t)$ is easily found with Eqs. (5.15), (5.16) and (5.21) and a little manipulation. Denoting the joint probability that $\boldsymbol{\xi}(t + \tau) = \boldsymbol{\xi}_2$ and $\boldsymbol{\xi}(t) = \boldsymbol{\xi}_1$ by $p_\tau(\boldsymbol{\xi}_2, \boldsymbol{\xi}_1)$, we find

$$p_\tau(\boldsymbol{\xi}_2, \boldsymbol{\xi}_1) = \int \frac{d^{(2n)}\mathbf{k}}{(2\pi)^{2n}} \exp \left[-i\mathbf{k}^\top \begin{pmatrix} \boldsymbol{\xi}_1 \\ \boldsymbol{\xi}_2 \end{pmatrix} - \frac{1}{2}\mathbf{k}^\top \begin{pmatrix} \Sigma_\infty & e^{\mathbf{A}|\tau|\Sigma_\infty} \\ e^{\mathbf{A}|\tau|\Sigma_\infty} & \Sigma_\infty \end{pmatrix} \mathbf{k} \right]. \quad (5.23)$$

We can now marginalize Eq. (5.23) to find the joint probability distribution of $X(t+\tau)$ and $X(t)$:

$$p_\tau(X_2, X_1) = \int \frac{d^2\mathbf{k}}{(2\pi)^2} \exp \left[-i\mathbf{k}^\top \begin{pmatrix} X_1 \\ X_2 \end{pmatrix} - \frac{1}{2}\mathbf{k}^\top \begin{pmatrix} \mathbf{C}\Sigma_\infty\mathbf{C}^\top & \mathbf{C}e^{\mathbf{A}|\tau|\Sigma_\infty}\mathbf{C}^\top \\ \mathbf{C}e^{\mathbf{A}|\tau|\Sigma_\infty}\mathbf{C}^\top & \mathbf{C}\Sigma_\infty\mathbf{C}^\top \end{pmatrix} \mathbf{k} \right]. \quad (5.24)$$

And we're done! The first- and second-order statistics of the Gaussian process $X(t)$ can be read off of the mean and covariance of Eq. (5.24). It will be useful to record a few other statistics, too. Let

$$\Delta X_{\Delta t}(t) = X(t + \Delta t) - X(t), \quad (5.25)$$

which arises when we sample data at interval Δt . The autocorrelation of this function is useful in practice and can be derived from the same relations. Summarizing results,

we have

$$\mathbb{E}[X(t)] = 0 \quad (5.26a)$$

$$\mathbb{E}[X(t)^2] = \mathbf{C}\boldsymbol{\Sigma}_\infty\mathbf{C}^T \quad (5.26b)$$

$$\mathbb{E}[X(t+\tau)X(t)] = \mathbf{C}e^{\mathbf{A}|\tau|}\boldsymbol{\Sigma}_\infty\mathbf{C}^T \quad (5.26c)$$

$$\mathbb{E}\{[X(t+\tau) - X(t)]^2\} = 2\mathbf{C}(\mathbf{I} - e^{\mathbf{A}\tau})\boldsymbol{\Sigma}_\infty\mathbf{C}^T \quad (5.26d)$$

$$\mathbb{E}[\Delta X_{\Delta t}(t+\tau)\Delta X_{\Delta t}(t)] = \mathbf{C}[2e^{\mathbf{A}\tau} - e^{\mathbf{A}(\tau-\Delta t)} - e^{\mathbf{A}(\tau+\Delta t)}]\boldsymbol{\Sigma}_\infty\mathbf{C}^T \quad (5.26e)$$

$$\approx -\Delta t^2\mathbf{C}\mathbf{A}^2e^{\mathbf{A}\tau}\boldsymbol{\Sigma}_\infty\mathbf{C}^T \quad (\Delta t \text{ small}). \quad (5.26f)$$

For any strictly proper, stable transfer function $T(s)$ driven by a stochastic input signal of the form $dU(t) = \alpha dW(t)$, Eqs. (5.26) give the statistics of the resulting output signal in terms of the state-space realization of $T(s)$ and the solution of the Lyapunov equation (5.22). For low-order systems, we may calculate these quantities explicitly (see the first- and second-order examples below). However, much of the analysis here is easily implemented numerically even for quite complicated systems. In MATLAB, for example, the function `tf2ss.m` finds a state-space realization of a given transfer function and returns it in canonical form. Also, the function `lyap.m` solves a Lyapunov equation to find $\boldsymbol{\Sigma}_\infty$. With these tools, we may investigate quite complicated systems, including (for example) plant resonances and time delays using Padé approximants (`pade.m` in MATLAB). In a real implementation, you will also find it necessary to use the function `pzcancel.m` in order to cancel pole-zero pairs in $T(s)$ before finding a state-space realization.

5.1.3 Marginally stable systems

We mentioned a few times in Sects. 5.1.1 and 5.1.2 that some of our systems are only *marginally stable* because they have a pole at the origin $s = 0$, or equivalently zero is an eigenvalue of the system matrix \mathbf{A} . We could rewrite these systems as

$$\tilde{X}(s) = \frac{1}{s}\bar{T}(s)U(s) \quad (5.27)$$

where $\bar{T}(s) = sT(s)$ is the closed-loop transfer function of a *stable* system. In this case, we can simply consider the time derivative

$$\dot{X}(t) = \frac{d}{dt}X(t) \leftrightarrow \dot{\tilde{X}}(s) = s\tilde{X}(s). \quad (5.28)$$

This new system has stable dynamics represented by

$$\dot{\tilde{X}}(s) = s\tilde{X}(s) = \bar{T}(s)\tilde{U}(s) \quad (5.29)$$

and we can solve for the statistics of $\dot{X}(t)$ as before.

Assuming we have solved for the statistics of $\dot{X}(t)$ in terms of a state-space realization $\mathbf{A}, \mathbf{B}, \mathbf{C}$ and Σ_∞ of $\bar{T}(s)$ and $U(s)$, the statistics of $X(t)$ can be found by integration:

$$X(t) = \int_0^t \dot{X}(t') dt'. \quad (5.30)$$

We quickly see that

$$\mathbb{E}[X(t)] = 0. \quad (5.31)$$

For the two-time correlations, we need to do some work. For $\tau \geq 0$, we have

$$\begin{aligned} \mathbb{E}[X(t)X(t+\tau)] &= \mathbb{E}\left[\int_0^t dt' \int_0^{t+\tau} dt'' \dot{X}(t')\dot{X}(t'')\right] \\ &= \int_0^t dt' \int_0^{t+\tau} dt'' \mathbb{E}[\dot{X}(t')\dot{X}(t'')] \\ &= \mathbf{C} \left[\int_0^t dt' \int_0^{t+\tau} dt'' e^{\mathbf{A}|t'-t''|} \right] \Sigma_\infty \mathbf{C}^T. \end{aligned} \quad (5.32)$$

Performing the last integral, and summarizing the results (for $\tau \geq 0$), we find

$$\mathbb{E}[X(t)] = 0 \quad (5.33a)$$

$$\mathbb{E}[X(t)^2] = 2\mathbf{C}\mathbf{A}^{-2} (e^{\mathbf{A}t} - \mathbf{A}t - \mathbf{I}) \boldsymbol{\Sigma}_\infty \mathbf{C}^T \quad (5.33b)$$

$$\mathbb{E}[X(t)X(t+\tau)] = \mathbf{C}\mathbf{A}^{-2} (e^{\mathbf{A}(t+\tau)} + e^{\mathbf{A}t} - e^{\mathbf{A}\tau} - 2\mathbf{A}t - \mathbf{I}) \boldsymbol{\Sigma}_\infty \mathbf{C}^T \quad (5.33c)$$

$$\mathbb{E}\{[X(t+\tau) - X(t)]^2\} = 2\mathbf{C}\mathbf{A}^{-2} [e^{\mathbf{A}\tau} - \mathbf{A}\tau - \mathbf{I}] \boldsymbol{\Sigma}_\infty \mathbf{C}^T \quad (5.33d)$$

$$\mathbb{E}[\Delta X_{\Delta t}(t+\tau)\Delta X_{\Delta t}(t)] = \mathbf{C}\mathbf{A}^{-2} [2e^{\mathbf{A}\tau} - e^{\mathbf{A}(\tau-\Delta t)} - e^{\mathbf{A}(\tau+\Delta t)}] \boldsymbol{\Sigma}_\infty \mathbf{C}^T \quad (5.33e)$$

$$\approx \Delta t^2 \mathbf{C}e^{\mathbf{A}\tau} \boldsymbol{\Sigma}_\infty \mathbf{C}^T \quad (\Delta t \text{ small}). \quad (5.33f)$$

5.1.4 Statistics of $\mathbf{X}(t)$ and $\mathbf{E}(t)$ for low-order systems

Having finished all the necessary calculations, we can now record some results for two low-order systems. In particular, consider the sample stage position $X(t)$ and tracking error $E(t)$ driven by the particle's motion $U(t)$ and measurement noise $N(t)$ as described in Sect. 5.1. We consider two systems, specified by the transfer functions $C(s)$ and $P(s)$:

$$C(s) = \frac{\gamma_c}{s}, \quad P(s) = 1 \quad (5.34)$$

$$C(s) = \frac{\gamma_c}{s}, \quad P(s) = \frac{\gamma_p}{s + \gamma_p}. \quad (5.35)$$

In both cases, we consider an integral control law $C(s)$ with response frequency γ_c . However, in the first case given by Eq. (5.34), the plant has a flat transfer function that can be driven arbitrarily hard with no amplitude or phase rolloff. This first-order system corresponds to the ideal tracking case, in which the bandwidth is just set by the level of aggression of our controller γ_c . The second case given by Eq. (5.35) has the same control law, but the plant transfer function is now a low-pass filter, exhibiting both amplitude and phase rolloff at frequencies above $\gamma_p/2\pi$.

State space realizations of the various transfer functions in Eq. (5.6) are given in Table 5.1 for both the first- and second-order models of $C(s)$ and $P(s)$. Using these

	$C(s) = \frac{\gamma_c}{s}$ $P(s) = 1$	$C(s) = \frac{\gamma_c}{s}$ $P(s) = \frac{\gamma_p}{\gamma_p + s}$
$T_{EU}(s)$	$\mathbf{A} = -\gamma_c$ $\mathbf{B} = \sqrt{2D}$ $\mathbf{C} = 1$ $\Sigma_\infty = \frac{D}{\gamma_c}$	$\mathbf{A} = \begin{pmatrix} -\gamma_p & -\gamma_p \\ \gamma_c & 0 \end{pmatrix}$ $\mathbf{B} = \begin{pmatrix} \sqrt{2D} \\ 0 \end{pmatrix}$ $\mathbf{C} = \begin{pmatrix} 1 & \frac{\gamma_p}{\gamma_c} \end{pmatrix}$ $\Sigma_\infty = \begin{pmatrix} \frac{D}{\gamma_p} & 0 \\ 0 & \frac{D\gamma_c}{\gamma_p^2} \end{pmatrix}$
$T_{EN}(s)$	$\mathbf{A} = -\gamma_c$ $\mathbf{B} = n$ $\mathbf{C} = \gamma_c$ $\Sigma_\infty = \frac{n^2}{2\gamma_c}$	$\mathbf{A} = \begin{pmatrix} -\gamma_p & -\gamma_p \\ \gamma_c & 0 \end{pmatrix}$ $\mathbf{B} = \begin{pmatrix} n \\ 0 \end{pmatrix}$ $\mathbf{C} = \begin{pmatrix} 0 & \gamma_p \end{pmatrix}$ $\Sigma_\infty = \begin{pmatrix} \frac{n^2}{2\gamma_p} & 0 \\ 0 & \frac{n^2\gamma_c}{2\gamma_p^2} \end{pmatrix}$
$T_{XN}(s)$	$\mathbf{A} = -\gamma_c$ $\mathbf{B} = n$ $\mathbf{C} = \gamma_c$ $\Sigma_\infty = \frac{n^2}{2\gamma_c}$	$\mathbf{A} = \begin{pmatrix} -\gamma_p & -\gamma_p \\ \gamma_c & 0 \end{pmatrix}$ $\mathbf{B} = \begin{pmatrix} n \\ 0 \end{pmatrix}$ $\mathbf{C} = \begin{pmatrix} 0 & \gamma_p \end{pmatrix}$ $\Sigma_\infty = \begin{pmatrix} \frac{n^2}{2\gamma_p} & 0 \\ 0 & \frac{n^2\gamma_c}{2\gamma_p^2} \end{pmatrix}$
$sT_{XU}(s)$	$\mathbf{A} = -\gamma_c$ $\mathbf{B} = \sqrt{2D}$ $\mathbf{C} = \gamma_c$ $\Sigma_\infty = \frac{D}{\gamma_c}$	$\mathbf{A} = \begin{pmatrix} -\gamma_p & -\gamma_p \\ \gamma_c & 0 \end{pmatrix}$ $\mathbf{B} = \begin{pmatrix} \sqrt{2D} \\ 0 \end{pmatrix}$ $\mathbf{C} = \begin{pmatrix} 0 & \gamma_p \end{pmatrix}$ $\Sigma_\infty = \begin{pmatrix} \frac{D}{\gamma_p} & 0 \\ 0 & \frac{D\gamma_c}{\gamma_p^2} \end{pmatrix}$

Table 5.1: Table of state-space realization for the first- and second-order tracking model described in the text. These matrices together with Eq. (5.26) for the first three rows and Eq. (5.33) for the final row give a prescription for calculating second-order statistics in both models.

realizations and Eqs. (5.26) and (5.33), we can explicitly calculate expectation values.

First-order statistics of $\mathbf{E}(t)$. Consider the tracking error $E(t) = E_U(t) + E_N(t)$ for the first-order system. For $E_U(t)$, we find $\mathbf{A} = -\gamma_c$, $\mathbf{C} = 1$, and $\mathbf{\Sigma}_\infty = D/\gamma_c$ so that, for example,

$$\mathbb{E} [E_U(t)^2] = \mathbf{C}\mathbf{\Sigma}_\infty\mathbf{C}^T = \frac{D}{\gamma_c} \quad (5.36)$$

$$\mathbb{E} [E_U(t)E_U(t + \tau)] = \mathbf{C}e^{\mathbf{A}\tau}\mathbf{\Sigma}_\infty\mathbf{C}^T = \frac{D}{\gamma_c}e^{-\gamma_c\tau}. \quad (5.37)$$

We can make similar manipulations for the other signals as well.

$E_U(t)$ and $E_N(t)$ are uncorrelated, because they are driven by uncorrelated processes, so the statistics of the full error signal are just given by summing the means and variances calculated separately:

$$\mathbb{E} [E(t)^2] = \mathbb{E} [E_U(t)^2] + \mathbb{E} [E_N(t)^2] = \frac{\bar{D}}{\gamma_c} \quad (5.38)$$

$$\mathbb{E} [E(t)E(t + \tau)] = \mathbb{E} [E_U(t)E_U(t + \tau)] + \mathbb{E} [E_N(t)E_N(t + \tau)] = \frac{\bar{D}}{\gamma_c}e^{-\gamma_c\tau} \quad (5.39)$$

with

$$\bar{D} = D + \frac{n^2\gamma_c^2}{2}. \quad (5.40)$$

These are exactly the results we found in Ch. 4 in Eqs. (4.16) and (4.17).

Second-order statistics of $\mathbf{E}(t)$. For a richer example, we can calculate statistics of $E_U(t)$ for the second order system to find

$$\mathbb{E} [E_U(t)^2] = D \left(\frac{1}{\gamma_c} + \frac{1}{\gamma_p} \right) \quad (5.41)$$

$$\begin{aligned} \mathbb{E} [E_U(t)E_U(t + \tau)] = \\ D e^{-\gamma_p\tau/2} \left[\left(\frac{1}{\gamma_c} + \frac{1}{\gamma_p} \right) \cosh \left(\frac{\lambda\tau}{2} \right) + \frac{\gamma_p}{\lambda} \left(\frac{1}{\gamma_c} - \frac{1}{\gamma_p} \right) \sinh \left(\frac{\lambda\tau}{2} \right) \right] \end{aligned} \quad (5.42)$$

where $\lambda = \sqrt{\gamma_p^2 - 4\gamma_p\gamma_c}$. Similarly, we find

$$\mathbb{E} [E_N(t)^2] = \frac{\gamma_c n^2}{2} \quad (5.43)$$

$$\mathbb{E} [E_N(t)E_N(t + \tau)] = \frac{n^2\gamma_c}{2} e^{-\gamma_p\tau/2} \left[\cosh\left(\frac{\lambda\tau}{2}\right) + \frac{\gamma_p}{\lambda} \sinh\left(\frac{\lambda\tau}{2}\right) \right] \quad (5.44)$$

The autocorrelation function exhibits damped oscillatory behavior for $\gamma_c > \gamma_p/4$, however it remains stable for all $\gamma_p, \gamma_c > 0$. The first-order tracking results are reproduced in the limit $\gamma_p \rightarrow \infty$, that is, in the limit that the plant rolloff becomes much larger than the controller bandwidth. This second-order-plus-noise model will be used to analyze our experiment in Chs. 7 and 8.

5.2 Closed-loop Fluorescence Correlation Spectroscopy

In Sect. 5.1, we found a prescription for calculating the statistics of the position of the sample stage $X(t)$ and tracking error $E(t)$. The former signal can be measured directly during a tracking experiment. The latter, cannot be measured directly, but it can be sensed through the statistics of the fluorescence photon count rate. To see this, consider a particle at position $X_p(t)$ when the sample stage is at position $X(t)$. Since the Gaussian excitation laser is centered at the sample stage position, the rate of photon arrivals from the particle is given by (for the one-dimensional case)

$$\Gamma(t) = \Gamma_0 \exp \left\{ -\frac{2}{w^2} [X_p(t) - X(t)]^2 \right\} = \Gamma_0 \exp \left[-\frac{2}{w^2} E(t)^2 \right]. \quad (5.45)$$

Just as in the open-loop case, where fluorescence fluctuations arise from the particle's motion, the fluorescence autocorrelation function measured in *closed loop* gives access to the statistics of $E(t)$. In this section, we will calculate fluorescence autocorrelation functions for a tracked particle, where the fluctuations arise from competition between diffusion and feedback-assisted damping. This is a generalization of the open-loop case, and we will show that it includes those results in the appropriate (weak feedback)

limit. We will only calculate the expectation value of the correlation functions (which are stochastic of course). The standard deviations could in principle be calculated in exactly the same way as the expectation values, but with more integrals, because we know the full Gaussian distribution of the relevant statistical quantities. As an example, see [41] for calculations of the noise in open-loop correlation spectroscopy.

5.2.1 Calculation of the fluorescence autocorrelation function

Tracking in one dimension We will begin in one dimension as usual. In our tracking apparatus, the laser moves in a deterministic (circular) fashion around the centroid $X(t)$. If we denote the time-dependent offset of the laser from $X(t)$ by $x_L(t)$, and let

$$\Phi(x) = \Gamma_0 \exp\left(-\frac{2}{w^2}x^2\right) = \int \frac{dk}{2\pi} e^{-ikx} \tilde{\Phi}(k) \quad (5.46)$$

where

$$\tilde{\Phi}(k) = \Gamma_0 \left(\sqrt{\frac{\pi w^2}{2}}\right) \exp\left[-\frac{w^2 k^2}{8}\right]. \quad (5.47)$$

The expression as a Fourier transform will be useful below. We can now write the average fluorescence signal as

$$\Gamma(t) = \Phi[E(t) - x_L(t)] \quad (5.48)$$

and find the two-time fluorescence correlation function (in the average sense discussed in 3.4):

$$G(t; \tau) = \mathbb{E}[\Gamma(t)\Gamma(t + \tau)] = \mathbb{E}\{\Phi[E(t) - x_L(t)]\Phi[E(t + \tau) - x_L(t + \tau)]\}. \quad (5.49)$$

Note that $\Gamma(t)$, the rate of the stochastic photon detection process as discussed in Ch. 3, is itself stochastic here.

Let us make a shorthand vector notation, suppressing the time dependence of the

error signal and the spatial path of the excitation laser,

$$\mathbf{E} = \mathbf{E}(t; \tau) = \begin{pmatrix} E(t) \\ E(t + \tau) \end{pmatrix}, \quad \mathbf{x}_L = \mathbf{x}_L(t; \tau) = \begin{pmatrix} x_L(t) \\ x_L(t + \tau) \end{pmatrix}. \quad (5.50)$$

\mathbf{E} is stochastic, with a Gaussian probability distribution characterized by its mean and covariance

$$\mathbb{E}[\mathbf{E}] = 0 \quad (5.51)$$

$$\mathbb{E}[\mathbf{E}\mathbf{E}^T] = \boldsymbol{\sigma}_\tau = \begin{pmatrix} \sigma_0^2 & \sigma_\tau^2 \\ \sigma_\tau^2 & \sigma_0^2 \end{pmatrix} \quad (5.52)$$

where the elements of $\boldsymbol{\sigma}_\tau$ were calculated in Sect. 5.1

$$\sigma_0^2 = \mathbf{C}\boldsymbol{\Sigma}_\infty\mathbf{C}^T, \quad \sigma_\tau^2 = \mathbf{C}e^{\mathbf{A}\tau}\boldsymbol{\Sigma}_\infty\mathbf{C}^T. \quad (5.53)$$

By using Fourier transforms judiciously, we can calculate $G(t; \tau)$ quite efficiently:

$$\begin{aligned} G(t; \tau) &= \iint dE_1 dE_2 p(\mathbf{E}) \Phi[E_1 - x_L(t)] \Phi[E_2 - x_L(t + \tau)] \\ &= \iint d^2\mathbf{E} p(\mathbf{E}) \iint \frac{d^2\mathbf{k}}{(2\pi)^2} e^{-i\mathbf{k}^T(\mathbf{E} - \mathbf{x}_L)} \tilde{\Phi}(k_1) \tilde{\Phi}(k_2) \\ &= \left(\frac{\pi w^2 \Gamma_0^2}{2} \right) \iint \frac{d^2\mathbf{k}}{(2\pi)^2} \exp \left[i\mathbf{k}^T \mathbf{x}_L - \frac{1}{2} \mathbf{k}^T \left(\boldsymbol{\sigma}_\tau + \frac{w^2}{4} \mathbf{I} \right) \mathbf{k} \right]. \end{aligned} \quad (5.54)$$

Letting

$$\mathbf{M}_\tau = \boldsymbol{\sigma}_\tau + \frac{w^2}{4} \mathbf{I} = \begin{pmatrix} \sigma_0^2 + \frac{w^2}{4} & \sigma_\tau^2 \\ \sigma_\tau^2 & \sigma_0^2 + \frac{w^2}{4} \end{pmatrix}, \quad (5.55)$$

we find the simple result

$$G(t; \tau) = \left(\frac{\Gamma_0^2 w^2}{4 \sqrt{\det \mathbf{M}_\tau}} \right) \exp \left(-\frac{1}{2} \mathbf{x}_L^T \mathbf{M}_\tau^{-1} \mathbf{x}_L \right) \quad (5.56a)$$

$$= \left(\frac{\Gamma_0^2 w^2}{4 \sqrt{\bar{\sigma}_0^4 - \sigma_\tau^4}} \right) \exp \left\{ -\frac{1}{2} \frac{\bar{\sigma}_0^2 [x_L(t)^2 + x_L(t + \tau)]^2 - 2\sigma_\tau^2 x_L(t) x_L(t + \tau)}{\bar{\sigma}_0^4 - \sigma_\tau^4} \right\} \quad (5.56b)$$

where

$$\bar{\sigma}_0^2 = \sigma_0^2 + \frac{w^2}{4}. \quad (5.57)$$

The normalized form in matrix notation is given by

$$\begin{aligned} g(\tau) &= \frac{\mathbb{E}[\Gamma(t)\Gamma(t+\tau)]}{\mathbb{E}[\Gamma(t)]^2} - 1 \\ &= \frac{\bar{\sigma}_0^2}{\sqrt{\det \mathbf{M}_\tau}} \exp \left[-\frac{1}{2} \left(\mathbf{x}_L^T \mathbf{M}_\tau^{-1} \mathbf{x}_L - \frac{1}{\bar{\sigma}_0^2} \mathbf{x}_L^T \mathbf{x}_L \right) \right] - 1 \end{aligned} \quad (5.58)$$

Tracking in higher dimensions. Eqs. (5.56) and (5.58) represent the fluorescence autocorrelation function for a particle tracked by an arbitrary linear feedback law, represented through the covariances σ_0^2 and σ_τ^2 of Eq. (5.53). The laser may also move along any time-dependent path described by \mathbf{x}_L as long as the lock point of the tracking control moves with it. For tracked diffusion in more dimensions, even with asymmetric tracking and Gaussian beam profiles, the fluorescence autocorrelation functions are just products of terms of the form of Eq. (5.56),

$$G(t; \tau) = \Gamma_0^2 \left(\frac{G_x(t; \tau)}{\Gamma_0^2} \right) \left(\frac{G_y(t; \tau)}{\Gamma_0^2} \right) \left(\frac{G_z(t; \tau)}{\Gamma_0^2} \right) \quad (5.59a)$$

$$g(\tau) = [g_x(\tau) - 1][g_y(\tau) - 1][g_z(\tau) - 1] + 1. \quad (5.59b)$$

Two-dimensional tracking in a rotating laser. For the experimentally relevant case of isotropic diffusion and tracking in a rotating laser, we take

$$x_L(t) = r \cos \omega_0 t \quad (5.60)$$

$$y_L(t) = r \sin \omega_0 t \quad (5.61)$$

to find

$$G(t; \tau) = \left(\frac{\Gamma_0^2 w^2}{4 \sqrt{\det \mathbf{M}_\tau}} \right)^2 \exp \left[-\frac{1}{2} \left(\mathbf{x}_L^T \mathbf{M}_\tau^{-1} \mathbf{x}_L + \mathbf{y}_L^T \mathbf{M}_\tau^{-1} \mathbf{y}_L \right) \right] \quad (5.62)$$

$$= \left(\frac{\Gamma_0^2 w^2}{4 \sqrt{\bar{\sigma}_0^4 - \sigma_\tau^4}} \right)^2 \exp \left[-r^2 \left(\frac{\bar{\sigma}_0^2 - \sigma_\tau^2 \cos \omega_0 \tau}{\bar{\sigma}_0^4 - \sigma_\tau^4} \right) \right] \quad (5.63)$$

which we can normalize to give

$$g(\tau) = \frac{\bar{\sigma}_0^4}{\bar{\sigma}_0^4 - \sigma_\tau^4} \exp \left[-r^2 \left(\frac{\bar{\sigma}_0^2 - \sigma_\tau^2 \cos \omega_0 \tau}{\bar{\sigma}_0^4 - \sigma_\tau^4} \right) + \frac{r^2}{\bar{\sigma}_0^2} \right] - 1. \quad (5.64)$$

Finally, the deterministic oscillatory factor $\cos \omega_0 \tau$ is often distracting in the measured value of $g(\tau)$, but we can suppress it by averaging the correlation function over rotation periods. Denoting this averaged correlation function by $\bar{g}(\tau)$, we have

$$\bar{g}(\tau) = \frac{\omega_0}{2\pi} \int_{\tau}^{\tau+2\pi/\omega_0} g(\tau) d\tau = \frac{\bar{\sigma}_0^4}{\bar{\sigma}_0^4 - \sigma_\tau^4} \exp \left[-r^2 \left(\frac{\bar{\sigma}_0^2}{\bar{\sigma}_0^4 - \sigma_\tau^4} - \frac{1}{\bar{\sigma}_0^2} \right) \right] I_0 \left[\frac{r^2 \sigma_\tau^2}{\bar{\sigma}_0^4 - \sigma_\tau^4} \right]. \quad (5.65)$$

5.2.2 Recovery of open-loop results in the weak-tracking limit

In order to recover the standard results for open-loop FCS, we want to find the limit of $G(t; \tau)$ when the tracking is very weak. This limit is a bit tricky, however, because it involves taking the matrix limit $\mathbf{A} \rightarrow 0$ while also letting the particle's standard deviation $\sigma_0^2 \rightarrow \infty$. That is, the tracking becomes infinitely weak, so the particle's confinement becomes infinitely large. If we just blindly try to take this limit, we can easily get nonsensical results in which the unnormalized correlation functions goes to 0 and the normalized version diverges, as the mean and variance of the fluorescence signal both go to zero at different rates.

We will not worry about prefactors here; these are discussed in the next section. In order to take the open loop limit, we have to let \mathbf{A} go to zero and σ_0^2 go to infinity such that their product remains fixed. To accomplish this, note that for very small

\mathbf{A} , we have

$$\begin{aligned}
\sigma_\tau^2 &= \mathbf{C} e^{\mathbf{A}\tau} \boldsymbol{\Sigma}_\infty \mathbf{C}^\mathbf{T} \\
&\approx \mathbf{C} (\mathbf{I} + \mathbf{A}\tau) \boldsymbol{\Sigma}_\infty \mathbf{C}^\mathbf{T} \\
&= \sigma_0^2 + \tau \mathbf{C} \mathbf{A} \boldsymbol{\Sigma}_\infty \mathbf{C}^\mathbf{T} \\
&= \sigma_0^2 + \frac{\tau}{2} \mathbf{C} (\mathbf{A} \boldsymbol{\Sigma}_\infty + \boldsymbol{\Sigma}_\infty \mathbf{A}^\mathbf{T}) \mathbf{C}^\mathbf{T} \\
&= \sigma_0^2 - \frac{\tau}{2} \mathbf{C} \mathbf{B} \mathbf{B}^\mathbf{T} \mathbf{C}^\mathbf{T} \tag{5.66}
\end{aligned}$$

$$= \sigma_0^2 - D\tau \tag{5.67}$$

where in the last line we used the fact that $\mathbf{C} \mathbf{B} = \sqrt{2D}$ for E_U and $\mathbf{C} \mathbf{B} = 0$ for E_N , as seen in Table (see Table 5.1). Actually, the result is always valid for $\mathbf{A} = 0$, as can be seen directly from the system in Eq. (5.11).

Now let's fix the prefactor of $G(t; \tau)$, use Eq. (5.67), and take the large σ_0^2 limit:

$$\begin{aligned}
\frac{G(t; \tau)}{\left(\frac{\Gamma_0^2 w^2}{4\sqrt{\det \mathbf{M}_0}}\right)} &= \sqrt{\frac{\det \mathbf{M}_0}{\det \mathbf{M}_\tau}} \exp\left(-\frac{1}{2} \mathbf{x}_L^\mathbf{T} \mathbf{M}_\tau^{-1} \mathbf{x}_L\right) \\
&\approx \frac{\bar{\sigma}_0^4 - \sigma_0^4}{\bar{\sigma}_0^4 - (\sigma_0^2 - D\tau)^2} \exp\left[-\frac{1}{2} \mathbf{x}_L^\mathbf{T} \begin{pmatrix} \bar{\sigma}_0^2 & \sigma_0^2 - D\tau \\ \sigma_0^2 - D\tau & \bar{\sigma}_0^2 \end{pmatrix}^{-1} \mathbf{x}_L\right] \\
&\rightarrow \frac{1}{\sqrt{1 + \tau/\tau_D}} \exp\left[-\frac{|x_L(t) - x_L(t + \tau)|^2}{w^2 (1 + \tau/\tau_D)}\right], \tag{5.68}
\end{aligned}$$

with

$$\tau_D = \frac{w^2}{4D}. \tag{5.69}$$

Apart from the usual prefactor, Eq. (5.68) is the usual open-loop FCS result for one-dimensional motion in a time-dependent laser intensity [9].

5.2.3 Behavior of $g(\tau)$ for $\tau \approx 0$

In a traditional (open-loop) FCS measurement, the value of the correlation function $g(\tau)$ at $\tau = 0$ is a measure of the fraction of the beam which is filled with particles, or

equivalently, it is a measure of the overlap between the beam profile and the distribution of particles in the sample. That is, it is a measure of the sample concentration. In that situation, a lower concentration leads to greater fluctuations, relative to the mean intensity. In the usual notation, the one-dimensional fluorescence correlation function takes the form

$$g(\tau) = \frac{1}{\bar{N}\sqrt{1 + \tau/\tau_D}} \implies g(0) = \frac{1}{\bar{N}}, \quad (5.70)$$

where \bar{N} is the average number of particles in the laser focus.

In closed-loop tracking, the value of $g(\tau)$ near $\tau = 0$ is also a measure of the overlap of the trapped particle's position distribution with the beam profile. However, in closed-loop tracking, there is only one particle in the laser focus at any time, and the concentration becomes difficult to define. Furthermore, as the tracking becomes better, the fluctuations decrease and $g(\tau)$ tends to 0. However, for the two-dimensional rotating laser case in our experiment, the value of the correlation function near $\tau = 0$ still gives a measure of the particle's confinement, *i.e.*, the steady-state tracking error (variance) σ_0^2 .

To see this, first consider the simple case in which a particle is tracked but the laser does not move, $r = 0$. From Eq. (5.64), we may define $g_0 = g(\tau = 0)$ to find

$$\frac{\sigma_0^2}{w^2} = \frac{1}{4} \left(g_0 + \sqrt{g_0(1 + g_0)} \right). \quad (5.71)$$

Now let us consider the slightly more complicated case of $r \neq 0$. We suppose that the laser rotation frequency ω_0 is much larger than any diffusion or control timescale (*i.e.* $\omega_0/2\pi$ is much larger than the largest eigenvalue of \mathbf{A}). We may then assume that at $\tau = \pi/\omega_0$ (*i.e.*, at the first minimum of $\cos \omega_0\tau$) we have $\sigma_{\tau=\pi/\omega_0}^2 \approx \sigma_0^2$. Now define two quantities g_0^\pm by

$$g_0^+ = g(\tau = 0) \quad (5.72)$$

$$g_0^- = g(\tau = \pi/\omega_0) \quad (5.73)$$

and let

$$\xi = \log \left(\frac{1 + g^+}{1 + g^-} \right). \quad (5.74)$$

Using the preceding approximation for $\sigma_{\tau=\pi/\omega_0}^2$, we have

$$\frac{\sigma_0^2}{w^2} = \frac{\xi}{8 \left[4 \left(\frac{r}{w} \right)^2 - \xi \right]}. \quad (5.75)$$

5.2.4 Relation to other literature results

Our analytical results are a generalization of the theory of open-loop correlation spectroscopy, and a number of models from the spectroscopy literature are contained in the general form of Eqs. (5.56), (5.58), and (5.59). For \mathbf{x}_L constant and $\mathbf{A} \rightarrow 0$, Eq. (5.59) reproduces the standard FCS result as shown above. For $\mathbf{A} \rightarrow 0$ and \mathbf{x}_L describing a two-dimensional circular orbit with the radius of rotation r much larger than the beam waist w , Eq. (5.59) reproduces the “fluorescence particle counting” results of [42]. Under the same conditions on \mathbf{x}_L and \mathbf{A} , but with an arbitrary radius of rotation, we find the recent results of [43] for the temporal autocorrelation in a laser scanning configuration.

Finally, Enderlein has studied a closely related model, with \mathbf{x}_L tracing a circular orbit for use in tracking control [13]. In that work, Monte Carlo simulation results including simple kinetic state transitions in the particle are presented and particle escape probabilities are investigated as well. In contrast to the other models just mentioned, an analytical version of this model requires $\mathbf{A} \neq 0$, with the diffusive component of this model solved in this chapter. However, the inclusion of kinetic state transitions in the closed-loop FCS model is much more difficult in the general case than for open-loop FCS. Some results can be derived in certain limits and these are discussed in Appendix A. Analytical calculation of escape statistics requires a truly *nonlinear* model beyond the scope of this thesis.

Part II

Experiment

Chapter 6

Experimental Apparatus

In this chapter, we finally move from the theory developed in Chs. 2-5 to its application in an experiment. We will begin with a detailed discussion of the experimental apparatus, followed by a tour of experimental measurements and results.

6.1 Laboratory components

Three diagrams of the experimental apparatus are shown in Figs. 6.1, 6.2, and 6.3. They emphasize the optics, sample volume, and electronics respectively, and we will discuss these in that order.

6.1.1 Optics

The optics for single-particle tracking are shown in Fig. 6.1. The beam path essentially follows that of a home-built epifluorescence microscope in which the excitation laser is focused into the sample using a high-power microscope objective; fluorescence is collected by the same objective but spectrally separated and imaged onto the detection optics.

Laser We use a diode-pumped solid-state laser (Melles-Griot) rated for 5 mW output power at 532 nm. In practice we get about 8-10 mW total power. Our demands for pointing, intensity and polarization stability are not too stringent, and this laser has performed reliably.

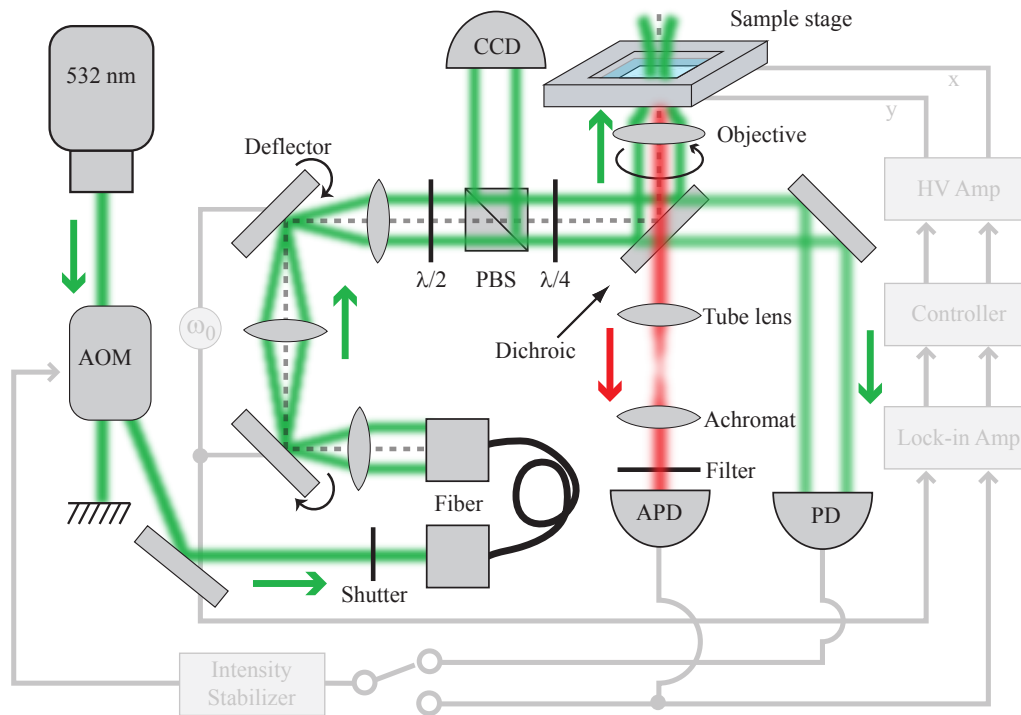


Figure 6.1: Schematic diagram of the optics for single-particle tracking.

Acousto-optic modulator The main excitation beam is taken from the first-order diffracted beam out of an Acousto-Optic Modulator (AOM) driven at 40 MHz. We can electronically control the total excitation laser power by varying the radio frequency (rf) power to the AOM using a voltage-controlled attenuator (VCA). This is a critical component of two intensity servos described below.

We can also use the AOM as a beam shutter by electronically switching rf power onto and off of the AOM. This is a good technique for fast shuttering, but we have found in practice that temperature drifts in the AOM strongly degrade performance if it is used for slow switching, at timescales of seconds. Because a few watts of rf power are incident on the AOM crystal, its temperature equilibrates above room temperature while it is diffracting. This means that when the rf power is initially switched onto the AOM, as its temperature equilibrates over many seconds or minutes, the diffraction efficiency drifts resulting in output power drift. We overcome this problem by using a mechanical shutter for slow control, and the AOM for fast shuttering and power

modulation.

Mechanical shutter We use a clever mechanical shutter, brought from Germany to the Mabuchi lab by Benjamin Lev. We use a small audio speaker, a tweeter, and attach a flag onto its solenoid by cutting out the speaker fabric and gluing a stopper into the speaker. Then by driving positive or negative current around the solenoid, we pull the flag down or push the flag up into the laser. We have not optimized our shutter, but it can easily block or unblock the laser in a few (1-10) ms, with excellent extinction due to the mechanical beam blockage.

Optical fiber After the AOM and mechanical shutter, we run the beam through a single-mode optical fiber (Thorlabs) both to achieve a nice Gaussian TEM₀₀ beam profile and to decouple the alignment of the AOM from the later optics. The fiber introduces very large (and slow) drifts in output intensity and polarization, which we think are caused by small pointing drifts at the fiber input. These drifts may arise from air currents in the room, temperature drifts affecting the AOM, or just general pointing instability in the laser itself. Because these are quite large amplitude, we use an intensity servo (discussed below) to lock either the laser intensity itself or to lock the fluorescence photon count rate during particle tracking. Because of the polarization noise, one must take care to sense the correct polarization for the intensity servo, because locking one of the polarization's intensities increases noise in the other.

Beam deflection For particle tracking, we require a circularly rotating beam, which we create using two resonant beam deflectors (Electro-Optic Parts Corporation, EOPC) driven at 8 kHz. The deflectors are just small mirrors mounted on torsion pendulums and driven sinusoidally (electromagnetically) with a phase difference of 90° provided by a phase-locked driver. In retrospect, 8 kHz was not a great choice for the rotation frequency because it is at the upper end of the audible frequency spectrum, so the experiment makes a somewhat excruciating high-pitched whine while operating. I would strongly suggest either acousto-optic modulation (with no moving

parts to radiate acoustically) or modulation at a frequency that is safely outside of your audible range.

It was convenient to mount these deflectors so that they both deflect in the horizontal direction, but of course for circular rotation of the beam, we need to convert one horizontal deflection into a vertical deflection. To accomplish this, we used a four-mirror arrangement that imparts a geometric phase and can in principle rotate the beam shape (including polarization) by any angle. I thought this was a pretty clever design, and it turns out it has been discussed in the literature in Refs. [44, 45]. It is quite a useful device though, so I suggest checking those references out.

Lenses should be arranged in such a way that they match the divergence angle of the beam deflection pattern with the divergence of the beam waist. Actually, by slightly misaligning the beam waist divergence and the angular deflection, we can achieve the desired situation in which the beam is focused to its minimum waist but still rotates in a circular pattern at the focal plane of the microscope inside the sample.

Filter optics Following the beam deflectors, the rotating beam is sent through a standard half-waveplate, polarizing beamsplitter, quarter waveplate ($\lambda/2$ -PBS- $\lambda/4$) anti-retroreflection combination. This serves the dual purpose of circularly polarizing the excitation beam and separating the retroreflected light from the sample for imaging onto a CCD camera (discussed below). Since we focus light to a very sharp focus, it is good to use circularly polarized excitation light so that interference effects at glass interfaces cannot (by symmetry) result in any radially asymmetric intensity profiles. During tracking, we are sensitive to radial asymmetries in the excitation intensity, which turn up as offsets on the lock-in quadrature outputs, and these may arise when focusing linearly polarized light through an interface at high numerical aperture (N.A.) [46–49].

Dichroic filter 532 nm excitation light is reflected off of a 550 nm cutoff dichroic long-wave pass beamsplitter. We have used a few different brands of optical filter

here and ultimately found superior performance with Chroma filters in virtually every situation. In practice, because 532 nm is very close to the 550 nm cutoff wavelength, a significant fraction of laser light is transmitted through the filter. We take advantage of this imperfection, and focus this light onto a photodiode (PD) as a laser intensity monitor.

Microscope objective We have used two infinity-corrected microscope objectives in different situations: a Zeiss 100x/N.A. 1.4 plan-apochromat oil immersion objective and a Zeiss 63x/N.A. 1.2 c-apochromat water immersion objective. The former objective was used for our earliest tracking results [25]. It has the advantage of very tight beam focusing and is much lighter than the water immersion objective, but as an oil immersion objective, it introduces substantial beam aberrations when focused more than a few microns into an aqueous sample. The water immersion objective provides slightly less tight focusing but much cleaner beam shapes and higher quality tracking error signals. This objective was used for the studies of Refs. [27, 28].

CCD Camera We use an off-the-shelf CCD camera to image the retroreflected 532 nm laser intensity, which is separated from the incident light by the $\lambda/2$ -PBS- $\lambda/4$ unit. The incident and retroreflected beams interfere and give far-field diffraction patterns at the CCD camera that are sensitive to the z position of the glass cover slides that hold the sample at sub-wavelength distance scales [50]. These diffraction patterns give a very useful visual queue to aid in focusing the apparatus.

Fluorescence collection Fluorescence is collected by the microscope objective and transmitted through the dichroic filter. A Zeiss tube lens ($f = +160$ mm) then refocuses the light. The microscope can be operated confocally by placing a pinhole, typically 100 μm in diameter, at the tube lens focus. Fluorescence light is then recollected by an achromatic doublet lens, and finally refocused by a second achromat onto the single-photon counters (only one of these doublets is shown in Fig. 6.1).

Single-photon counters Fluorescence light is detected by a single-photon counting avalanche photodiode operated in Geiger mode (Perkin-Elmer SPCM-14-AQR). Each incident photon generates a 25 ns TTL pulse that is electronically split into four signal paths at a digital fanout. The photon count rate is recorded at a computer, sent to the lock-in amplifier for the tracking servo, low-pass filtered and displayed on an oscilloscope for real-time monitoring, and finally the photon count rate can be used as an error signal for feedback to the AOM controlling the intensity of the excitation laser (see below). The computer and oscilloscope signal paths are not shown in Figs. 6.1 and 6.3.

6.1.2 Sample volume

A schematic diagram of the sample volume for single-particle tracking experiments is shown in Fig. 6.2.

Sample preparation For tracking, our samples are aqueous solutions of fluorescent particles between glass microscope cover slides. We typically put between 1 and 10 μL of liquid between glass microscope cover slips (22 \times 40 mm, nominal thickness of 160 μm). The solution typically fills or almost fills the space between the slides, resulting in a liquid layer around 1-2 μm deep. The sample depth can be determined by using a confocal pinhole to limit detection efficiency in the z direction and subsequently scanning a sample with high fluorophore concentration through the focus.

Our particles are fluorescently embedded polystyrene microspheres from Bangs Laboratories. We use the dyes “Envy Green” and “Suncoast Yellow” and have beads at diameters of 60 nm and 210 nm. Adding about 0.1% Tween-20 to deionized water helps reduce aggregation in the beads. On the other hand, adding salt to the aqueous solution strongly enhances aggregation and surface adhesion. Bangs Laboratories has a very helpful website, <http://www.bangslabs.com> and a useful tech note about aggregation in particular at <http://www.bangslabs.com/technotes/202.pdf>.

Also, preparation of the slides strongly affects adhesion of microspheres. We have found that slides soaked for 30-60 min in 1M KOH are sufficiently clean that

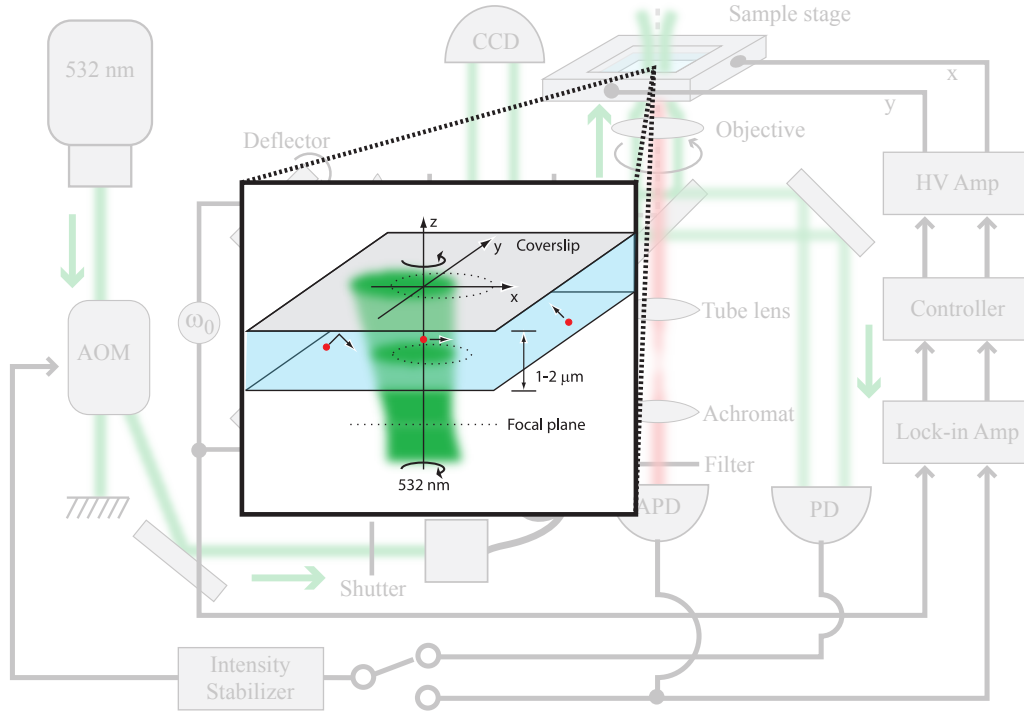


Figure 6.2: Schematic diagram of the sample volume for single-particle tracking. Fluorescent particles in aqueous solution diffuse freely in the xy plane, but are confined by glass coverslips in the z direction. A tracked particle diffuses freely (in the axially confined geometry) in the reference frame of the bulk fluid while the feedback control translates the entire sample volume in order to hold the particle on the laser axis defined by $x = y = 0$. Because the sense of the laser rotation, and therefore the sign of the feedback controller, reverses upon crossing the focal plane of the microscope optics, the sample mount is adjusted in the z direction so that the focal plane lies just outside of the sample volume.

liquids spread nicely and adhesion is low. When we clean slides with more aggressive procedures, the rate of surface adhesion actually increases.

The diffusion coefficient of a sphere of diameter d in a solution of viscosity η is given by the Stokes-Einstein relation [51]

$$D = \frac{k_B T}{3\pi\eta d} \quad (6.1)$$

where k_B is Boltzmann's constant and T is the temperature. For water, $\eta \approx 10^{-3}$ Pa·s, so we find $D = 2.1 \mu\text{m}^2/\text{s}$ is the predicted value for the 210 nm diameter beads

and $D = 7.2 \mu\text{m}^2/\text{s}$ is the predicted value for the 60 nm beads. In some of our very thin samples, we find reduced diffusion coefficients, which probably arise due to particle reflections at the sample boundaries [52] and hydrodynamic “wall-drag” effects [53, 54].

Piezo-electric stages Samples are mounted on a two-dimensional $100 \times 100 \mu\text{m}$ piezoelectric translation stage from Polytec, PI. The stage is driven by a high-voltage amplifier module, from the same manufacturer, that also contains high-resolution capacitive position sensors so that we can accurately monitor the x and y position of the sample stage during tracking.

Sample mount The sample mount has evolved through many stages since our early DNA experiments. The final incarnation was machined by Kevin McHale to mate with the piezoelectric translation stage, and gave us easy, repeatable sample switching capability. A key feature of this sample mount is its relative flatness, since earlier sample mounts suffered from some degree of tilt that altered the relative separation between the sample layer and the microscope objective as the sample translated in x and y . To give an idea of the tolerance required, we routinely translate the sample stage over its entire range of $100 \mu\text{m}$, and a change in z of $1 \mu\text{m}$ over this range can drastically alter the tracking parameters. Thus the stage must be level to better than 1 part in 100. This coupling between x , y , and z positions gave us some trouble until Kevin’s newly machined stage eliminated most of the tilt.

6.1.3 Electronics

The electronics for single-particle tracking consist primarily of servos for stabilizing the laser intensity, signal-processing electronics, tracking controllers, and high-voltage amplifiers for driving piezoelectric stage positioners. These are described below, and some of them are displayed in Fig. 6.3.

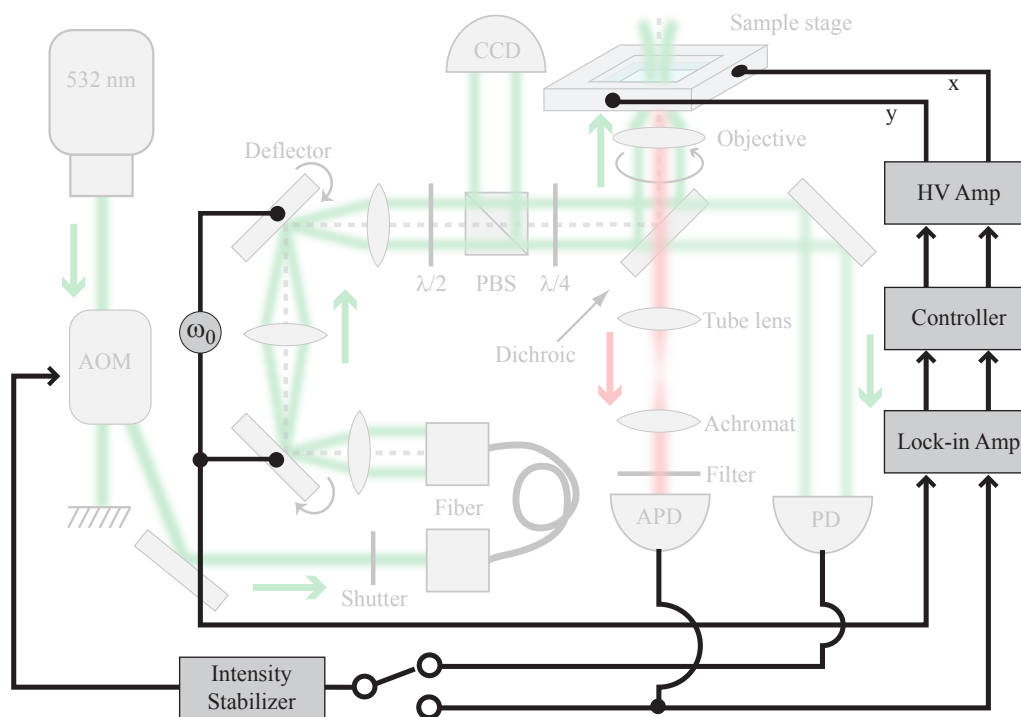


Figure 6.3: Schematic diagram of the electronics for single-particle tracking.

Laser intensity servo Because of intensity and polarization drift in the optical fiber output, we need active servo control of the laser intensity at the sample. We do this in two ways, depending on experimental requirements. In the usual “noise-eater” configuration, we use the laser intensity monitor signal from the photodiode (PD) to electronically lock the intensity by feeding back to a VCA in order to adjust the rf power to the AOM (Fig. 6.3). However, in some of our experiments, we track particles with drastically different brightness. In these cases, we can switch the intensity servo monitor signal so that it locks the *photon count rate*. In practice, this means that when a bright particle enters the focus, the laser intensity is automatically reduced to maintain a constant fluorescence intensity.

Because the VCA operates exponentially, *i.e.*, by providing a certain number of dB attenuation per volt, the gain of our intensity servo depends on its set point. If the lock point is in a very steep region of the attenuation curve, then small changes in intensity give a large amplitude feedback response, and similarly at shallow points of

the attenuation curve the servo is comparatively slow. We can therefore use neutral density filters to adjust the laser power at its source, so that at a given lock point, the intensity servo sits at different points of the attenuation curve and exhibits different gain and bandwidth. This is a convenient way to adjust the bandwidth of our intensity servos, which becomes a critical parameter for the fluorescence intensity lock. Although the VCA is quite fast, and we do not worry about driving it into instability, we have to keep the servo bandwidth low for locking the photon count rate or else we will feed photon counting shot noise into the system.

Lock-in amplifier We use a dual-phase digital lock-in amplifier (Stanford Research Systems, SRS850). The photon counter output is buffered by a digital fanout circuit and then fed directly onto the voltage sensing input of the lock-in. The reference is taken from the beam deflector drive signal. We typically use gain settings in the range 28–54 dB, filter time constants of 300 μ s to 1 ms, and rolloff rates of 12 or 18 dB/oct.

Tracking controllers For tracking, we initially used a programable digital microcontroller (Analog Devices, ADuC7024). Analog Devices supplied us with a test board and software (Keil μ Vision) that allowed us to program the microcontroller in C and download instructions onto the chip via USB interface. I wrote MATLAB software to convert arbitrary transfer functions into discrete time filters and load the coefficients onto the board. An example of one of the LQG control laws of Ch. 2 implemented using the microcontroller is shown in Fig. 6.4. It successfully implemented “arbitrary” transfer functions in this way, but with disappointingly low bandwidth and noise due to sampling and timing errors. Once loaded with even a second-order filter, the effective bandwidth of the microcontroller was barely 1 kHz. For higher-order filters, timing errors (missed samples and updates) accumulate and bandwidth continues to fall. Our original hope had been to implement the LQG filters designed in Ch. 2, but these were simply too high order to implement at sufficient bandwidth.

For our first successful tracking experiments [25], we used a proportional-integral

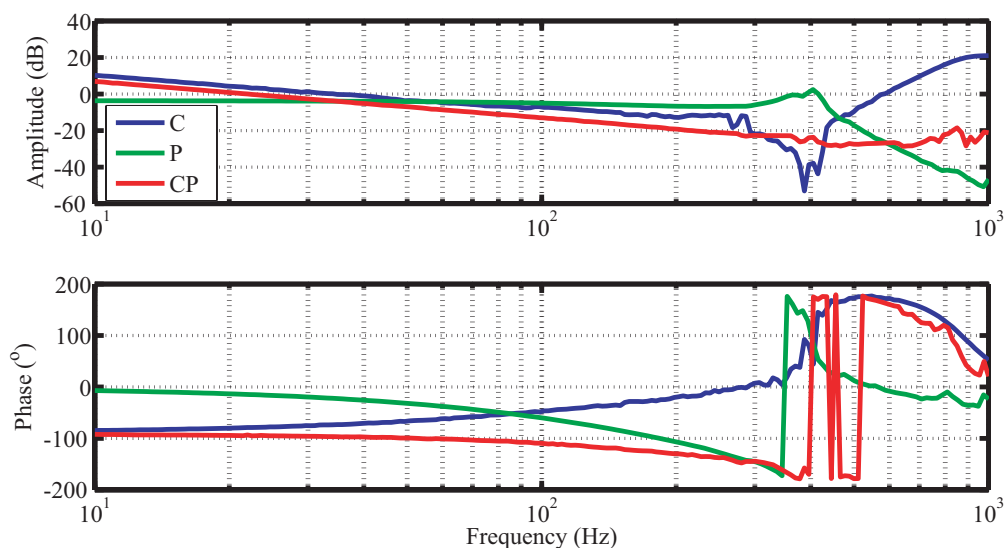


Figure 6.4: Measured Bode plots of the response of our piezoelectric stage (P , green), a controller transfer function implemented on the microcontroller (C , blue), and the resulting open-loop transfer function CP (red). The microcontroller implemented one of the LQG control laws derived in Ch. 2 and does successfully cancel the piezo resonance near 400 Hz. Noise near the phase wrap point causes the jagged lines in CP . The transfer function displayed here is the *average* response, but timing errors in the microcontroller (which are magnified when the control law is implemented along two axes on the same chip) introduced too much noise for these control laws to be usable in the experiment.

(PI) control law implemented on this controller. For later experiments, however, we switched to analog integral controllers, using the microcontroller only to sense the position of the piezo stage and activate a recentering procedure when the stage reaches a boundary. In practice, the analog controllers have been quieter and easier to work with and have resulted in excellent tracking performance [27, 28]. On the other hand, with simple integral controllers, we cannot drive our piezo stage faster than about 40-60 Hz because of uncompensated phase accumulation.

High voltage amplifiers We use off-the-shelf high-voltage (HV) amplifiers supplied by Polytec, PI with their piezo stage. These amplifiers perform adequately, but they are slow (typically rolling off in the 100-300 Hz range). In addition, Polytec, PI provides highly accurate capacitive position sensors through the same amplifier

module, but these too have slow rolloffs at the same bandwidths. So although the amplifiers are nicely packaged and integrated, the experiment could benefit from an upgrade to faster electronics. However, all of the experimental results reported here used these amplifiers. On another note, on three separate occasions, we bought Polytec piezo stages with unstable position servo loops. (even unloaded and right out of the box). In all these cases, we simply locked these using Polytec's position sensors and HV amps and a home-built controller circuit.

Dynamic signal analyzer We measure transfer functions using the swept sine response function of an SR785 dynamic signal analyzer (Stanford Research Systems). This instrument can measure response curves all the way down to DC.

6.1.4 Data acquisition and computer software

Time-interval analyzer We use the GT653 time-interval analyzer (TIA) from Guide Technologies installed on the PCI slot of a Micron PC to record fluorescence photon arrival times. This board has high time resolution (0.5 ns) and is capable of recording $>10^6$ photon arrival times in a single shot before filling the onboard memory. Kevin McHale has also written software to read samples continuously from the board, so that as long as the read rate to the computer is faster than the photon arrival rate the sample memory is limited by the computer hard drive. These boards are nice and easy to program, but they suffer from the major drawback that they have only two channels and synchronization between separate boards does not work (although software calls and documentation for this function exist). This is not an issue for the experimental results presented here, but our experiment is actually capable of recording data on two TIA boards and four photon counters simultaneously, but these still cannot be synchronized in the data acquisition despite repeated inquiries with technical support.

National Instruments DAQ card In addition to the TIAs for recording photon arrivals, we use a National Instruments data acquisition card (NI-DAQ), the PCI-

MIO-16E-4, installed on a Dell PC. This card provides analog and digital inputs and outputs as well as timing capability so it really is a workhorse of the experiment. All of the software to drive it was written in C (we do not use LabView). In a typical experimental run, the x and y position of the piezoelectric stage and the monitor photodiode signal are all digitized and recorded with the NI-DAQ card. Furthermore, beam shutters (both through the AOM and mechanical shutter) and APD gates are computer-controlled using the digital outputs from the same card and (when not tracking) the x and y position of the piezoelectric stage can be set using the analog outputs from the NI-DAQ card.

Interfacing the computers The TIAs and NI-DAQ cards are on separate computers to alleviate the large computational, memory, and scheduling demands of running these cards simultaneously on a single computer. Furthermore, the broad functionality of the NI-DAQ card, and my own creative C coding, has led to some extremely violent system crashes, and it seemed wise to physically isolate the delicate and expensive TIA cards from the specter of physical memory dumps and paging file errors. In a typical experiment, we wish to make software alternating software calls at different cards, for example:

1. Step sample stage (NI-DAQ analog output).
2. Ungate APD (NI-DAQ digital output).
3. Begin photon counting (TIA).
4. Unblock laser (NI-DAQ digital output).
5. Begin record laser intensity (NI-DAQ analog input).
6. Wait for memory to fill (TIA).
7. Gate APD (NI-DAQ digital output).
8. Block laser (NI-DAQ digital output).

In order to make these types of software calls, I defined a master (Micron) and a slave (Dell) computer and used Windows sockets to pass messages such as those above back and forth between the separate computers, via ethernet. With these socket protocols, and MATLAB wrappers for all the C executables, we can execute sequence such as the one shown above entirely in a MATLAB script on the master computer. This has turned out to be extremely useful in practice. A great socket programming guide is online: <http://beej.us/guide/bgnet/>.

Correlation software A note about calculating correlation functions is warranted here. Because our TIAs record individual photon arrival times, we have the capability to measure FCS curves $g(\tau)$ over many orders of magnitude in τ by post-analyzing the data. However, calculation of $g(\tau)$ using standard methods based on the Wiener-Khinchin theorem and the fast-Fourier transform (FFT), for example `xcorr.m` in MATLAB, has two primary drawbacks. First, statistical bias at large lag times (compared to the length of the entire data sequence) arises from the redundant weighting of noise. This problem is easily circumvented using a symmetric normalization:

$$g(\tau) = \frac{\frac{1}{T-\tau} \int_0^{T-\tau} \delta I(t) \delta I(t + \tau) dt}{\left(\frac{1}{T-\tau} \int_0^{T-\tau} I(t) dt \right) \left(\frac{1}{T-\tau} \int_{\tau}^T I(t) dt \right)}. \quad (6.2)$$

The second more troublesome issue is that the correlation function found using an FFT must be calculated over *linearly* spaced time intervals τ , giving a potentially huge autocorrelation vector. For example, if we use a time bin $\Delta\tau = 0.1 \mu\text{s}$ and calculate the correlation function out to 1 s, the resulting vector contains 10^7 data points. Well-known methods such as the “multiple-tau” algorithm get around this problem by calculating correlation functions at logarithmically spaced time intervals [55]. However, these algorithms still do not satisfy all of our demands, because they *average* the correlation function over logarithmically increasing intervals. For a periodic signal (such as the one obtained with our rotating laser), we may wish to see the fast periodic structure at large time scales. A nice solution to these problems comes from an algorithm described in Ref. [56], which allows us to calculate correlation

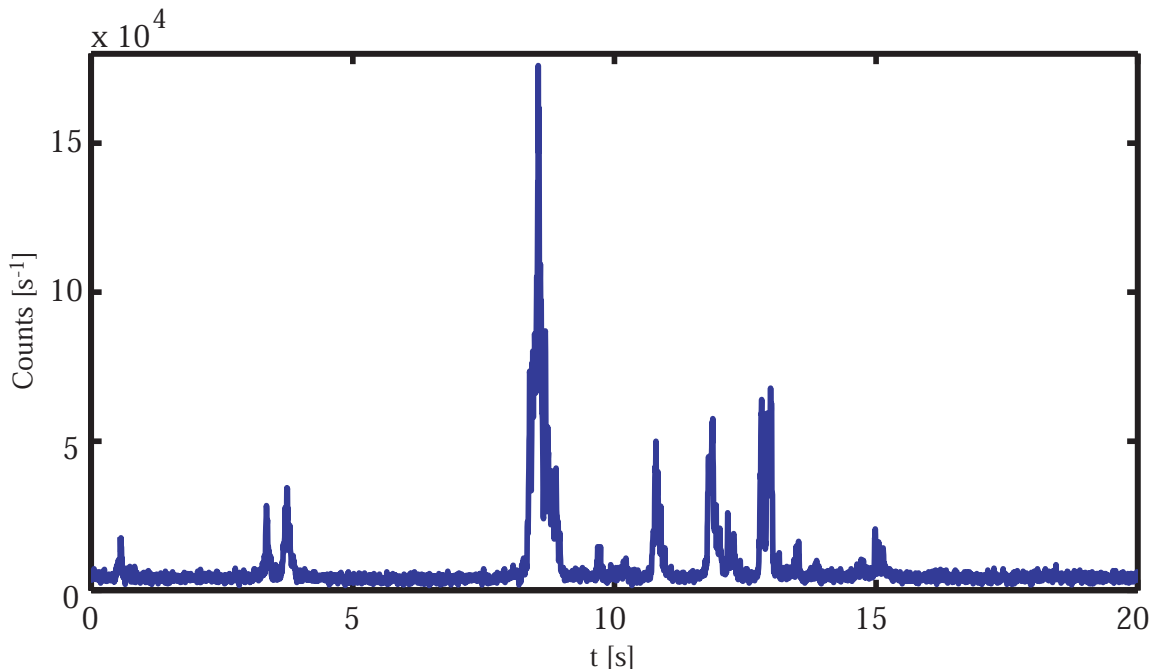


Figure 6.5: Typical open-loop transit of a 60 nm microsphere through the excitation volume. The excitation laser was not rotating for this measurement.

functions at arbitrary time lags and over arbitrary bin sizes directly from photon arrival time data. Using this algorithm, we can easily form a correlation function on, say, 1000 time intervals of size $\Delta\tau = 0.1 \mu\text{s}$ evenly distributed between $\tau = 0.1 \mu\text{s}$ and $\tau = 1 \text{ s}$. We coded a version of this algorithm in C and compiled it into a MATLAB `.m` executable using MEX methods.

6.2 Calibration and diagnostics

In this section, some typical experimental measurements are discussed and examples are given. These include diagnostic and calibration measurements, as well as interesting observations about the behavior of the tracking system.

6.2.1 Open-loop measurements

For a typical open-loop measurement, we load the sample with $2 \mu\text{L}$ of 60 nm “Envy green”-labeled microspheres between glass coverslips, as described above. As these

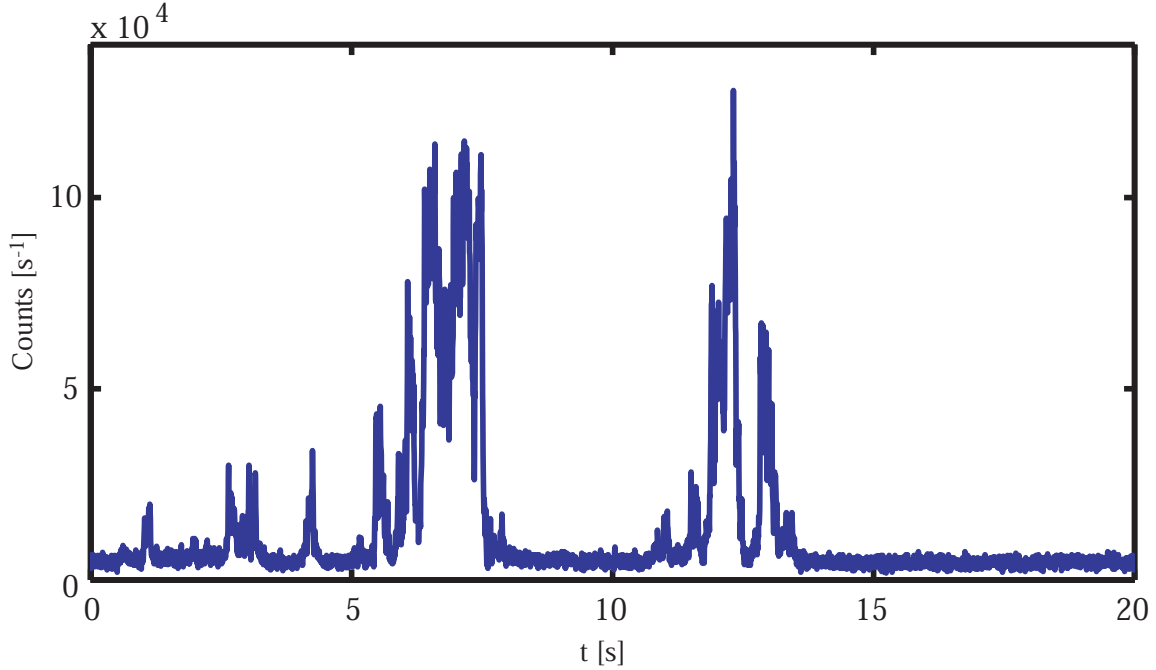


Figure 6.6: Typical open-loop transit of a 60 nm microsphere through the excitation volume with the excitation laser rotating at 8 kHz.

particles diffuse into and out of the laser focus, we collect typical fluorescence transits of the type shown in Fig. 6.5. For that measurement, the excitation beam was static (*i.e.*, not rotating, as in the tracking configuration). A second measurement on the same sample recorded with the rotating excitation laser is shown in Fig. 6.6

To make a quantitative comparison between transits recorded with and without the beam rotation, we performed fluorescence correlation spectroscopy (FCS) on each of these samples. The fluorescence correlation function $g(\tau)$ was calculated as described in Sect. 6.1.4. For a two-dimensional sample, denote by $g_0(\tau)$ the predicted correlation function for particles with diffusion coefficient D diffusing in a Gaussian laser with beam waist w :

$$g_0(\tau) = \frac{1}{N} \left(1 + \frac{\tau}{\tau_D} \right)^{-1}, \quad \tau_D = \frac{w^2}{4D}. \quad (6.3)$$

If we then rotate the excitation laser at frequency ω_0 along a circle of radius r about

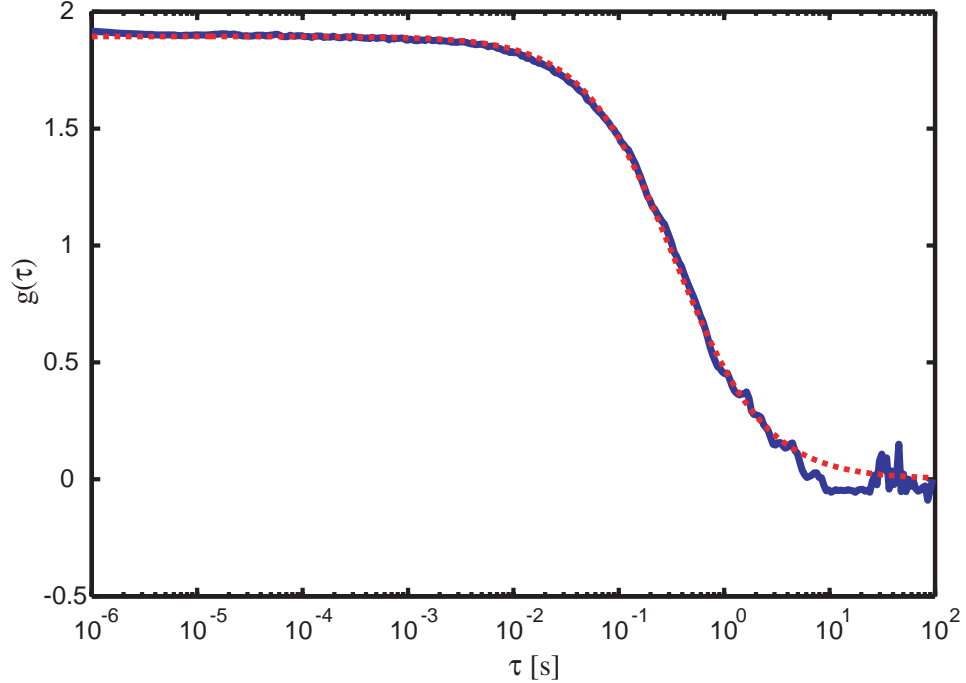


Figure 6.7: Open-loop FCS curve (solid blue line) together with a fit to $g_0(\tau)$ defined by Eq. (6.3) (dashed red line). The fit parameters were $\bar{N} = 0.53$ and $\tau_D = 0.335s$.

its axis of propagation, the correlation function becomes

$$g_r(\tau) = g_0(\tau) \exp \left[-2 \frac{r^2}{w^2} \left(\frac{1 - \cos \omega_0 \tau}{1 + \tau/\tau_D} \right) \right]. \quad (6.4)$$

These are standard calculations that can be derived from the expressions in Sect. 5.2.2.

The correlation functions in Figs. 6.7-6.8 were calculated from photon arrival-time data, and from curve fitting we find a diffusion time $\tau_D = 0.33 - 0.34s$. In order to convert these diffusion time estimates into diffusion coefficients, we require the beam waist w . Later, when we track these particles, we will be able to measure the diffusion coefficient directly from their translational motion. However, we performed a calibration that is typical of open-loop methods: we found a bead adhered to the glass coverslip surface and raster scanned it in order to map the beam profile. The resulting profiles are shown in Fig. 6.9 for both the stationary laser and for the rotating laser.

A Gaussian fit to the beam profile data reveals a slightly asymmetric beam profile

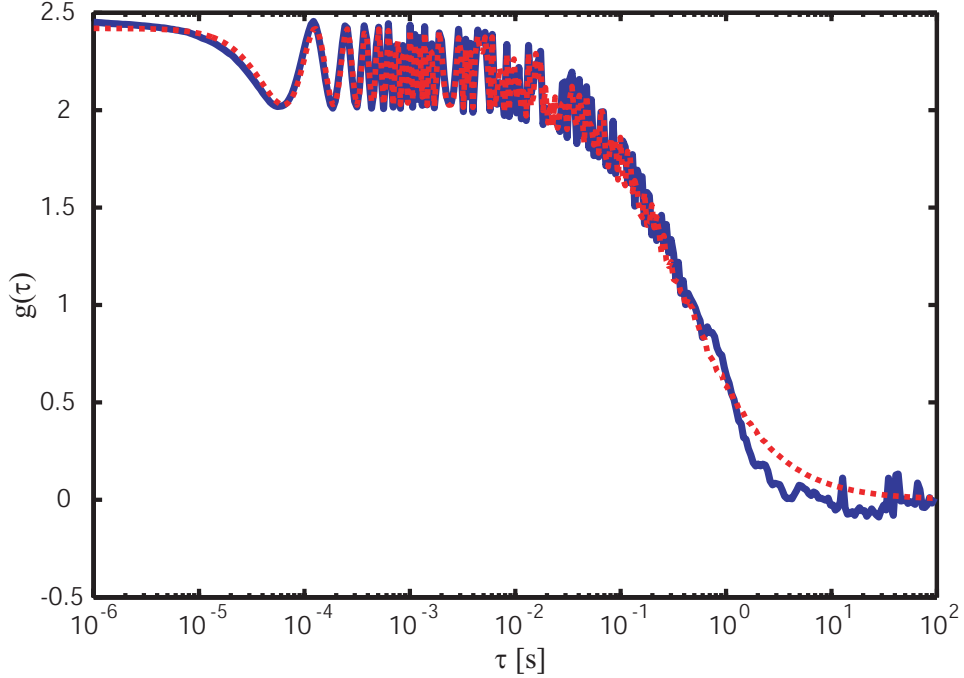


Figure 6.8: Open-loop FCS curve (solid blue line) with the laser rotating, together with a fit to Eq. 6.4 (dashed red line). The fit parameters were $\bar{N} = 0.41$, $\tau_D = 0.330s$, $r/w = 0.21$.

with waist $w_x = 3.2\mu\text{m}$ in the x direction and $w_y = 2.9\mu\text{m}$ in the y direction. Curve fitting of the autocorrelation function in Fig. 6.7 did not detect any asymmetry. [The theoretical form of $g(\tau)$ for the asymmetric case is easily found from Eq. (5.59).] The fit also reveals that our laser has fatter tails than a Gaussian. Such deviations from a Gaussian profile can have a profound effect on particle transport properties inferred from open-loop FCS, and it becomes a major advantage of closed-loop methods that we can completely suppress such complications. Incidentally, a fit to a scan of the same stuck bead, but with the rotating laser, gives a rotation radius of $r = 1.0\mu\text{m}$ or $r/w = 0.33$. Note that in later tracking results from Chs. 7 and 8, we will use a smaller beam with $w = 1.0\mu\text{m}$ and $r = 0.6\mu\text{m}$.

Taking the mean of w_x and w_y to find $w = 3.05\mu\text{m}$, we estimate a diffusion coefficient $D = 6.9\mu\text{m}^2/\text{s}$ for these particles. This is in good agreement with the Stokes-Einstein value, but note that a $\pm 5\%$ variation in the beam waist leads to a diffusion coefficient ranging between 6.2 and $7.5\mu\text{m}^2/\text{s}$, a 21% variation. This

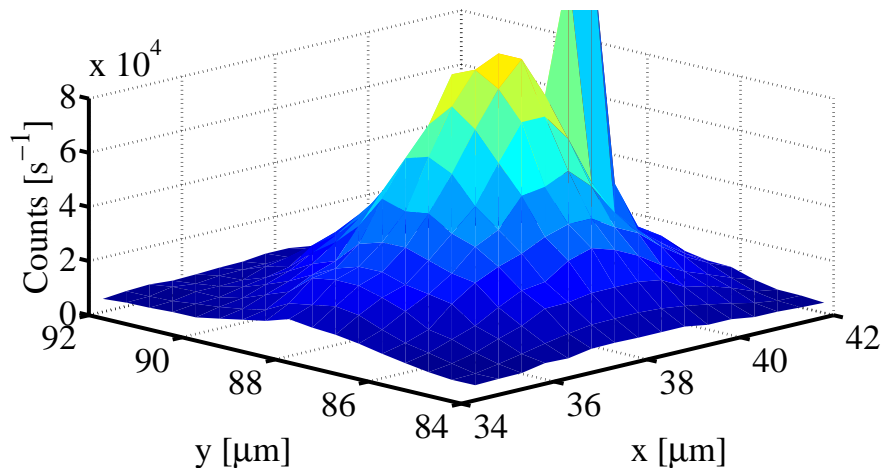


Figure 6.9: Measured Gaussian laser intensity profile. The sample stage was raster scanned across a single immobilized 60 nm diameter bead while the fluorescence intensity was recorded. A fit to this data reveals a slightly asymmetric profile with best-fit Gaussian beam waists of $w_x = 3.2\mu\text{m}$ in the x direction and $w_y = 2.9\mu\text{m}$ in the y direction. The laser has fatter tails than a true Gaussian distribution. The spike in fluorescence near $(x, y) = (41, 88)\mu\text{m}$ appeared when a freely diffusing particle passed through the sample (this data point was omitted in the curve fitting procedure).

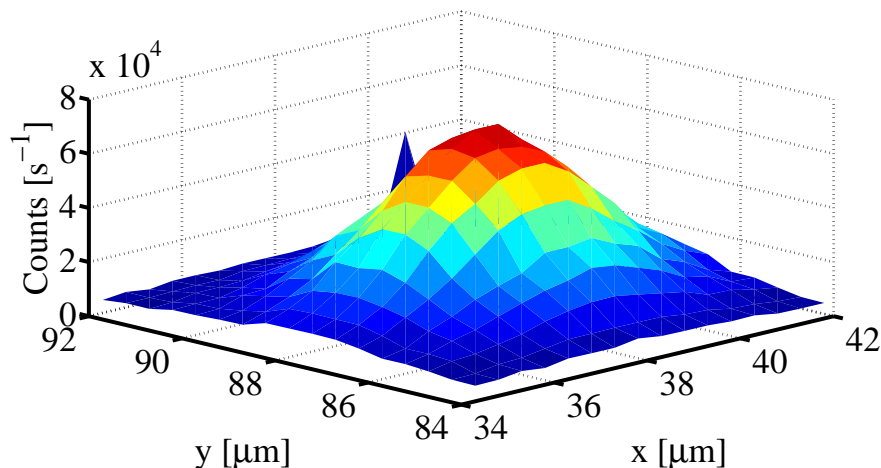


Figure 6.10: Example of the laser intensity profile for the rotating beam, measured in the same way and on the same particle as the data in Fig. 6.9. Using w measured for the stationary beam, we find a rotation radius $r = 1.05\mu\text{m}$ giving a beam shape parameter $r/w = 0.33$. Note that the time average of a rotating beam will not assume a “crater” shape on the rotation axis until $r/w \gtrsim 0.6$.

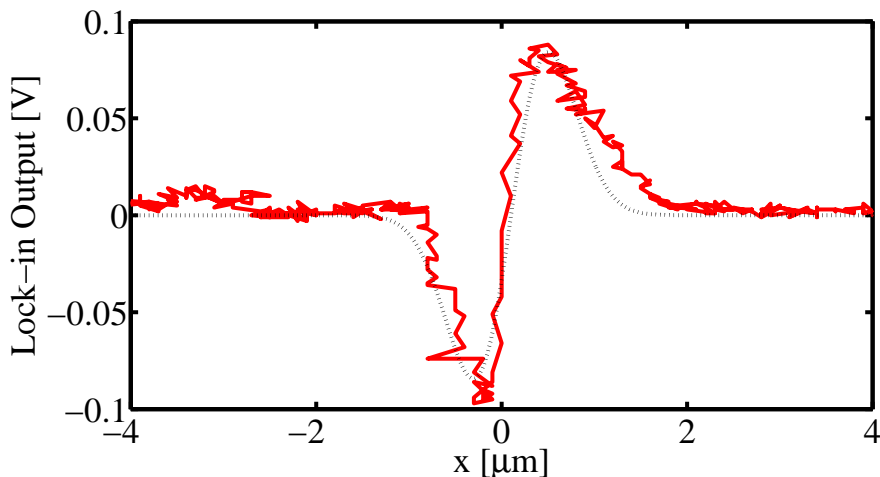


Figure 6.11: Measured error signal for closed-loop tracking. The measurement was made by scanning the piezo stage past a bead that had stuck to the surface either by electrostatic adhesion or pinning between the coverslips. The dotted line is a fit to Eq. (3.35) with $x = \rho \cos \theta$.

step dependence of the diffusion coefficient estimate (an intrinsic property of the particle in its environment) on the beam shape (an experimental artifact) is a major disadvantage of FCS. Again, our closed-loop control techniques allow much more accurate measurements of the diffusion coefficient with very little dependence on beam shape parameters. Furthermore, the parameters measured here are averaged over an ensemble of transits from many different particles, whereas the values we will measure during closed-loop tracking result from truly single-particle interrogations.

6.2.2 Measuring the error signal

For very thin liquid samples, our microspheres occasionally become immobilized on the glass coverslip surfaces by electrostatic adhesion or by pinning between the cover slides as the liquid evaporates from the slide. For long tracking runs (>1 hour), such degradation eventually compromises the sample. However, an immobilized fluorescent particle is a very useful diagnostic tool, and we can study our error signal with it. An example of such a measurement is shown in Fig. 6.11, in which the piezo stage was scanned in the x direction over an immobilized bead and the cosine quadrature of the lock-in output was recorded. The plot does not give all the information about

the scan, because the scanning time is not displayed. However, this error signal was recorded with only a few ms spent over the high-intensity region of the laser, *i.e.*, the linear region of the error signal.

Plotting both the x and y error signals (the cosine and sine quadratures of the lock-in output) against each other on an oscilloscope leads to plots like those shown in Fig. 3.3. Two important features of the error signal can be observed and adjusted using an immobilized bead: the *sign* of the error signal and its symmetry with respect to positive and negative deviations. For a one-dimensional servo, you can usually get away with an inverter switch for finding the correct sign of the control law from the two possibilities. For our two-dimensional tracking problem, there are four possible combinations of signs for the x and y error signals, and a systematic method for finding signs is a little more important than in the one-dimensional case. Second, the symmetry of the error signal can be degraded especially by imperfections in the photon counting collection optics. The APD active area is only $170\ \mu\text{m}$, and imperfect focusing of fluorescent light onto the detector leads to asymmetric error signals and impaired tracking capability. We use achromatic doublet lenses in the fluorescence beam path for good, wide spectrum focusing. While maximizing the observed fluorescent intensity from a bright sample can be a useful alignment method, symmetrization of the error signal turns out to be more directly helpful.

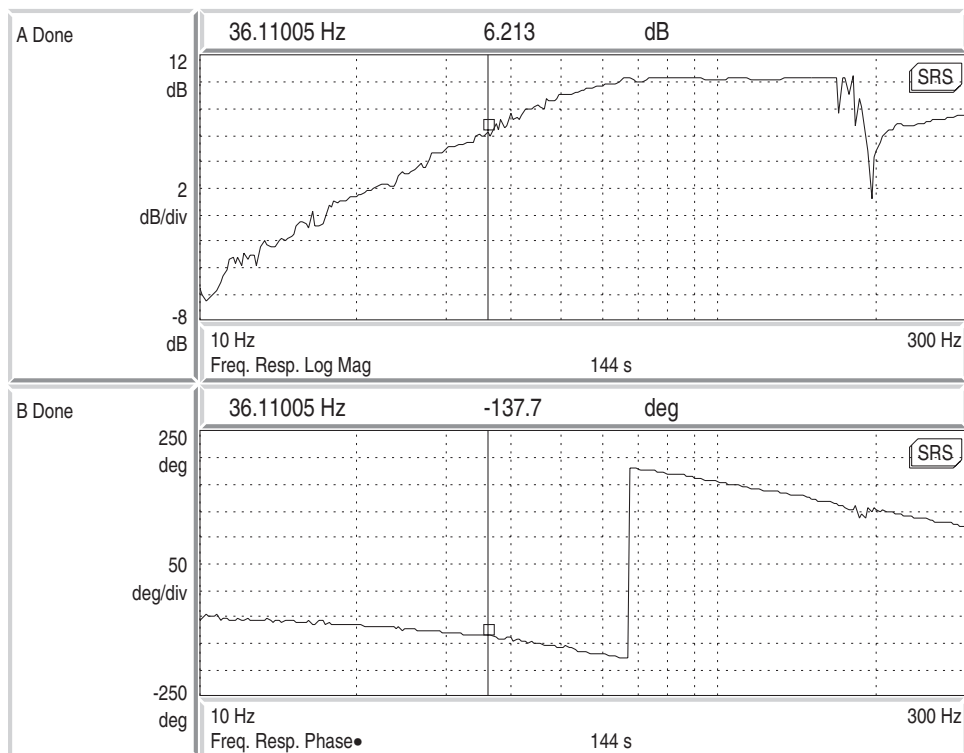
Chapter 7

Closed-Loop Particle Tracking

In this chapter, we finally achieve full closed-loop fluorescent particle tracking. First, we present lock results for an immobilized bead, then take a “historical” perspective, discussing some of our early tracking successes and moving on to more recent and much improved tracking data.

7.1 Closing the loop

Using the same type of immobilized bead discussed in Ch. 6, we can finally attempt to lock a particle’s position by feeding the measured position error signal back to the piezoelectric sample stage. Once the error signals are symmetrized and scaled to have the correct signs and magnitudes, we can use analog integrators or digital microcontrollers to lock an immobilized bead to the optic axis of the microscope. In this configuration, we can measure the transfer function response of the tracking system by adding a sinusoidal driving signal onto the error signal and letting the feedback network compensate for the disturbance by maintaining the locked particle’s position. The transfer function from this added signal to the piezo stage position is $T_{EX} = 1/(1+CP)$ using the controller and plant notation from chapter 5. An example of such a swept sign response is shown in Fig. 7.1 and the expected qualitative shape of such a transfer function is shown in Fig. 7.2. The strong suppression of the disturbance at low frequencies is an unambiguous indication of a locked particle.



6/09/06 17:26:57

Figure 7.1: Bode plot of the measured transfer function of the closed-loop tracking system locked to an immobilized fluorescent microsphere. A swept sine was added to the error signal and the dynamic response of the sample stage was measured. At low frequencies, the disturbance is strongly attenuated. Nonlinear behavior (arising from the Gaussian, not parabolic, shape of the laser profile) sets in near 200 Hz.

7.2 Early experimental success

The data presented in this section was recorded in March 2005 and published in Ref. [25]. For these measurements, we used 1-2 μL 0.1 nM concentration fluorescent microspheres (60 nm diameter). The excitation laser power was $\sim 1\text{--}10\mu\text{W}$ for exciting the fluorescently labeled beads, giving overall photon count rates of $\sim 10^5/\text{s}$, comparable to the count rates of bright individual dye molecules excited by a correspondingly higher laser power.

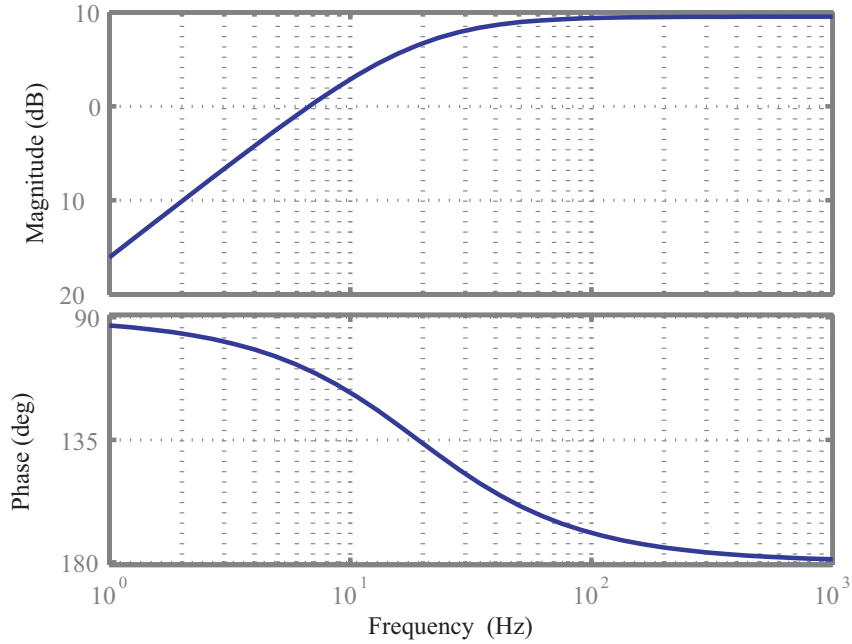


Figure 7.2: Bode plot of a closed loop transfer function $T_{XE} = 1/(1 + CP)$ when CP is a simple integrator. Note the qualitative similarity between the low-frequency behavior of this transfer function and the measured one in Fig. 7.1 both in magnitude and phase.

7.2.1 Tracking data

A successful tracking trajectory is shown in Fig. 7.3. From the data in the figure, we see that the tracking controller maintains a relatively constant fluorescence intensity for about 2.5 s, while the stage position moves well over $10 \mu\text{m}$ along both the x and y axes. The residual fluctuations arise from the feedback control bandwidth, as discussed theoretically in Ch. 5, but also from the uncontrolled motion of the particle in the axial (z) direction. As a comparison, note that the only other closed-loop tracking results in the literature at the time of these measurements were those presented in Ref. [16]. In that study, 500 nm diameter beads in an agarose gel were tracked in three dimensions with impressively high spatial accuracy but at very slow timescales relative to our work. The particle trajectory shown in that study remained within a cube $3 \mu\text{m}$ on a side for 100 s, whereas our data shows a single particle tracked at one point across $\sim 5 \mu\text{m}$ in about less 0.5 s, two to three orders of

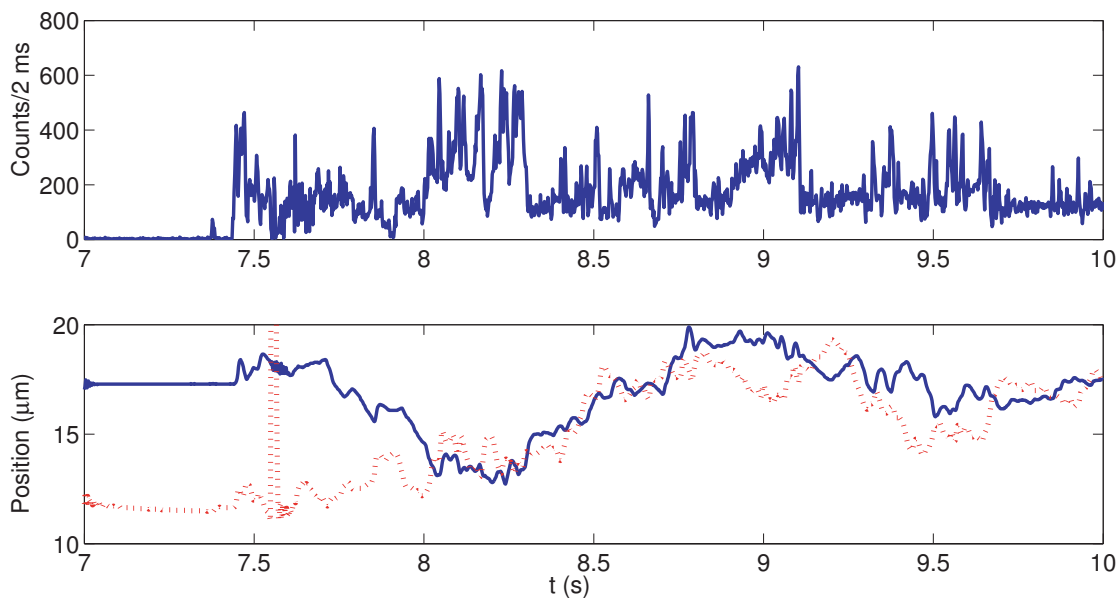


Figure 7.3: Tracking data from one of our earliest successful runs. The upper plot shows fluorescence data, and the lower plot shows the x (solid) and y (dotted) positions of the sample stage during the fluorescence trace. Just before 7.5 s, a particle diffused into the capture region and the controller responded by moving the sample stage to track this particle. The irregular motion of the sample stage at 7.6 s resulted from an (expected) arithmetic overflow in the microcontroller. The residual fluorescence fluctuations during tracking arise from the competition between diffusion and feedback control and also from the uncontrolled motion of the particle in the z direction.

magnitude faster than previously demonstrated.

7.2.2 Estimation of D

As a first interesting measurement based on our data, we can estimate the isotropic diffusion coefficient D for this microsphere from the position of the sample stage during tracking. While the particle is (approximately) locked on the laser axis by the feedback controller, the xy position of the sample stage provides a bandwidth-limited filtration of the particle's position. Let the change in a particle's x position during a time interval Δt be given by $\Delta X_{\Delta t}$, and similarly for y . Then we may construct a simple estimator \hat{D} for a particle's diffusion coefficient D based on the *mean-square-deviation* $MSD(\Delta t)$ of the sample stage trajectory. As usual, let $X(t)$ and $Y(t)$ be

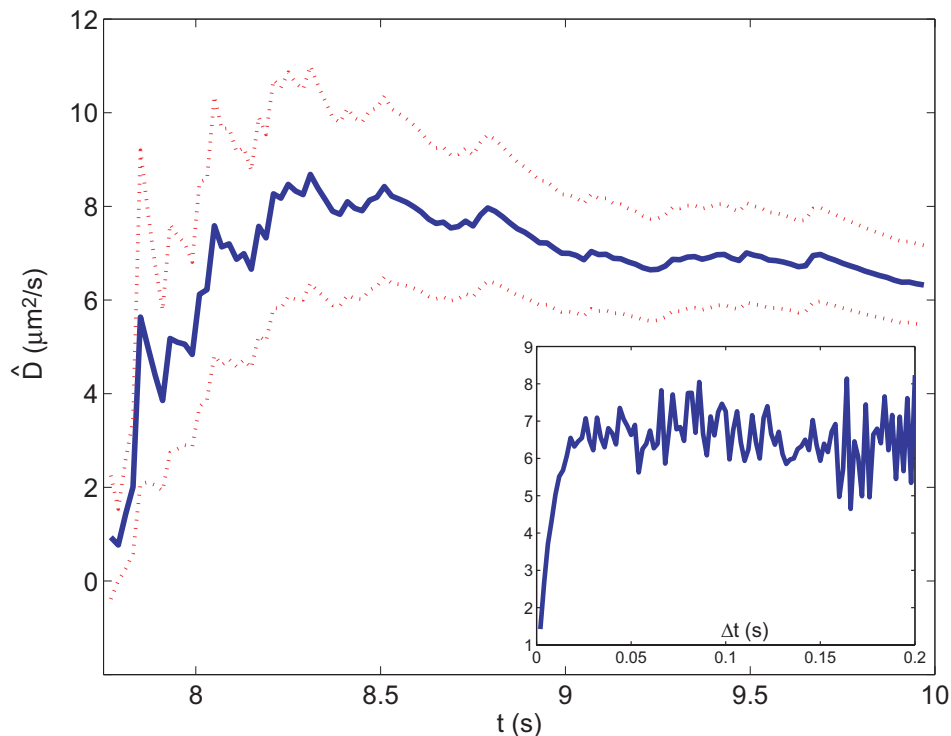


Figure 7.4: Time-converging estimate of the diffusion coefficient D for the microsphere tracking data in Fig. 7.3 with bin time $\Delta t = 20$ ms. The dotted lines are 1σ error estimates calculated for the estimator \hat{D} , assuming underlying Brownian statistics. Inset: Final estimate of D as a function of bin time Δt . For bin times larger than ~ 10 ms, the estimates are roughly constant with mean value $D = 6.2 \mu\text{m}^2/\text{s}$.

the sample stage coordinates during tracking, and let $\Delta X_{\Delta t}(t) = X(t + \Delta t) - X(t)$. Then $MSD(\Delta t)$ and $\hat{D}_{\Delta t}$ are defined by

$$MSD(\Delta t) = \frac{1}{2} \{ \hat{\sigma}_{\Delta t}^2(X) + \hat{\sigma}_{\Delta t}^2(Y) \} \quad (7.1)$$

$$\hat{D}_{\Delta t} = \frac{MSD(\Delta t)}{4\Delta t} \quad (7.2)$$

where $\hat{\sigma}_{\Delta t}^2(X)$ denotes the variance of $\Delta X_{\Delta t}$ over the sample trajectory (we will be very precise about the calculation of this variance in Sect. 8.3). The result of this estimate, formed as an accumulating average over the trajectory shown in Fig. 7.3 is shown in Fig. 7.4. The estimate of D converges to a value $6.2 \mu\text{m}^2/\text{s}$, close to the value $7.2 \mu\text{m}^2/\text{s}$ predicted by the Stokes-Einstein relation for 60 nm diameter beads in water at room temperature. It is possible that surface adhesion slightly reduced the

effective diffusion coefficient. We do not suspect induced optical dipole forces to give any significant trapping effect, since only a moderate trapping effect was observed for 1 mW of near-IR laser power on microspheres with 276 nm diameter in [18], whereas we use smaller microspheres and only 1-10 μW of 532 nm light. A detailed analysis of optical trapping effects in FCS experiments can be found in [57].

We can also vary Δt , which should not change $\hat{D}_{\Delta t}$ for pure Brownian motion. However, when Δt is smaller than the inverse closing bandwidth of the controller, then the sample stage will exhibit reduced variations on this timescale, and we will tend to underestimate the resulting diffusion coefficient with Eq. (7.2). It is easy to see this by considering an extreme case: imagine binning the particle's position over extremely small intervals, much smaller than the response time of our piezoelectric sample stage (say, 1 μs). Then in each time interval Δt , the sample stage cannot track the diffusing particle (although the particle does not move far enough to escape the tracking controller) and only follows an "average" trajectory. The sample stage will move a distance proportional to Δt (*i.e.*, at a fixed velocity along the averaged particle trajectory) for these very small bin times, while the particle itself moves a distance proportional to $\sqrt{\Delta t}$ (the characteristic property of Brownian motion). For small enough Δt , then, the estimator given by Eq. (7.2) will dramatically underestimate the particle's diffusion coefficient (by a factor proportional to $\sqrt{\Delta t}$). As Δt becomes much larger than the inverse closing bandwidth, however, the sample stage can move sufficiently fast to track the detailed motion of the particle within a single bin interval. In this case, we expect a good statistical estimate of D from Eq. (7.2), but with a concomitant increase in the estimator variance due to the smaller number of bin intervals per fixed-length trajectory. Estimates constructed in this way are shown in Fig. 7.4, along with error bars calculated for the estimator Eq. (7.2) assuming underlying Brownian motion statistics (see Ch. 8 and Ref. [58] for details about statistical estimation and error estimates). Of course, a quantitative version of these arguments involves calculation of the statistics of the mean-square deviation in the sample stage position; we already found this result in Ch. 5.

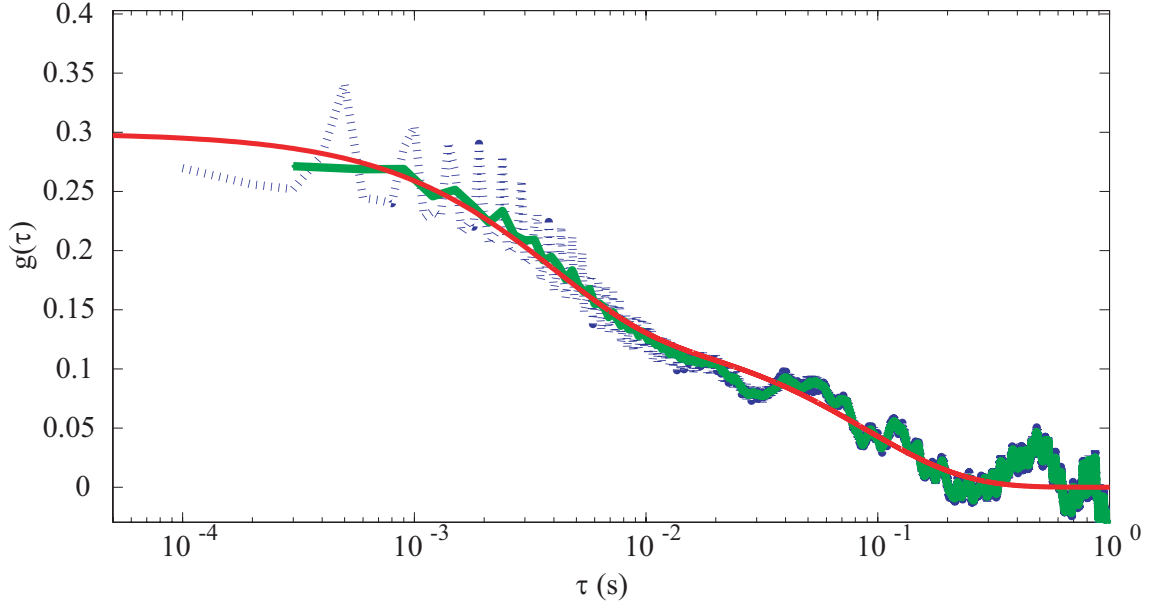


Figure 7.5: Fluorescence correlation functions recorded during the tracking period in Fig. 7.3, normalized to the mean fluorescence. The noisy curves were measured from the tracking data in Fig. 7.3, averaged over coarse-grained time bins of 100 (dotted) and 200 (solid) μs . At higher time resolution, the oscillations due to the deterministic laser rotation make it difficult to resolve the overall shapes of the autocorrelation curve. The smooth solid curve is a fit to the model described in the text. The fit parameters are $\gamma_{xy} = 134 \text{ Hz}$, $D = (6.2 \text{ s}^{-1})w_{xy}^2$, $r = 1.4w_{xy}$, $\gamma_z = 11.3 \text{ Hz}$, $w_z = 4.5 \mu\text{m}$, and $z_0 = 2.8w_{xy}$. γ_{xy} is the damping rate due to the tracking control. All fit parameters are scaled by the true beam waist w_{xy} , which is approximately $1 \mu\text{m}$. For this value or w_{xy} , the diffusion coefficient D determined by the statistical estimate from Fig. 7.4 and the value resulting from these fits are identical.

7.2.3 Fluorescence fluctuations and Tracking-FCS

For this first set of data, we also calculated the fluorescence autocorrelation function $g(\tau)$. The fluctuations captured in these correlation functions arise from the competition between free diffusion and tracking, as discussed in Ch. 5, but they also arise in this data set from the uncontrolled axial (z) motion of the particle.

A key difference between these early measurements and more recent (better) results was the placement of a confocal pinhole. We used a $100 \mu\text{m}$ pinhole in the conjugate image plane at the focus of the tube lens (see Fig. 6.1). This pinhole gave good rejection of out-of-focus light, especially excitation light scattered from the glass coverslip surfaces. However, the spatial discrimination introduced along the axial z

direction by the confocal pinhole leads to strong variation in the fluorescence intensity as a particle “bounces” back and forth between the glass surfaces. This axial discrimination led to enhanced fluorescence fluctuations, beyond those described by the Ornstein-Uhlenbeck statistics of Ch. 5.

To give at least a qualitative model of this axial fluctuation, we may assume the glass surfaces to be reflecting boundaries for the relevant case of low surface adhesion. Green’s functions for free particle motion and corresponding fluorescence autocorrelation functions have been calculated as an infinite series for a Gaussian beam focused *symmetrically* between two reflecting planes [7]; the resulting series have been approximated efficiently in [52], but I am unaware of an extension of these results to reflecting planes in an *asymmetric* configuration. Instead of tackling this difficult analytical problem, we instead approximate the reflecting boundaries in a way that naturally fits the formalism developed here: we introduce a third Ornstein-Uhlenbeck particle trap in the z dimension with corresponding damping rate γ_z and let the beam profile in the z direction be characterized by an offset z_0 and waist w_z . This trap is *not* due to the closed-loop particle tracking; it is nothing more than a tractable approximation for a particle between two reflecting planes that are placed asymmetrically about the laser focus. The measured fluorescence correlation function and the calculated model, with a symmetric beam Gaussian beam profile and first-order damping at rate γ_{xy} along the x and y directions plus another first-order damping rate γ_z along the axial direction, is shown in Fig. 7.5. The fit to this model contains a lot of parameters, so it should be taken mostly as a forward correspondence between reasonable parameters and the measured fluctuations, rather than as a method for *determining* those parameters. In later, cleaner results we will see that the fits can give truly quantitative results.

7.3 Tracking improvement

Following the first set of tracking results described in the previous section, a handful of major experimental improvements were initiated. First, we removed the confocal

pinhole and eliminated virtually all axial (z) discrimination arising from the detection optics. The detrimental effects of the confocal pinhole turned out to outweigh the benefit of reduced background signal at our very low laser powers. This resulted in a scenario much closer to the desired quasi-two-dimensional tracking scenario, and served the dual purpose of reducing the axial-motion-induced fluctuations in fluorescence during tracking and, more importantly, improving the tracking efficiency by suppressing any dependence of the error signal on z . Second, we replaced the digital microcontroller used for the first tracking results with analog integrators and adjusted the gain between lock-in amp and controller circuits to maximize our signal-to-noise ratio. The microcontroller was reassigned to the task of detecting when the piezoelectric sample stage reached the edge of its travel region and subsequently triggering an integrator reset procedure to recenter the apparatus, discarding any currently tracked particle in the process. As an added technical benefit, the analog integrators and their bipolar 15 V output swing, in contrast to the microcontroller's unipolar 2.5 V range, allowed us to track all the way to the limits of the piezoelectric stage travel without additional, noise-inducing post-amplification.

These improvements led to tracking runs of the type shown in Fig 7.6. This run was taken with a sample prepared essentially identically to the one used for the early experiments. In Fig. 7.6, we monitor a 60 nm bead as it traverses $\sim 50 \mu\text{m}$ over 65 s, and fluorescence fluctuations are quite small relative to the earlier measurements. Note that there was no servo controlling fluorescence fluctuations in this data (as will be the case later), and the quieter nature of the fluorescence intensity is a direct consequence of the tight tracking lock. The lack of a fluorescence servo is obvious from the photobleaching decay of the fluorescence observed during the tracking period. Although the beads are very bright and contain many dye molecules, after we have collected tens of millions of photons in closed loop we still see some photodamage.

This data was taken in early 2006, and we recorded 74 trajectories of this type, ranging in duration from a few seconds up to a maximum of 100 s, in the same data set. As usual, during a tracking trajectory, we record time-sequences of positions $X = X(t)$ and $Y = Y(t)$ of the sample stage during tracking. The estimate $\hat{D}_{\Delta t}$

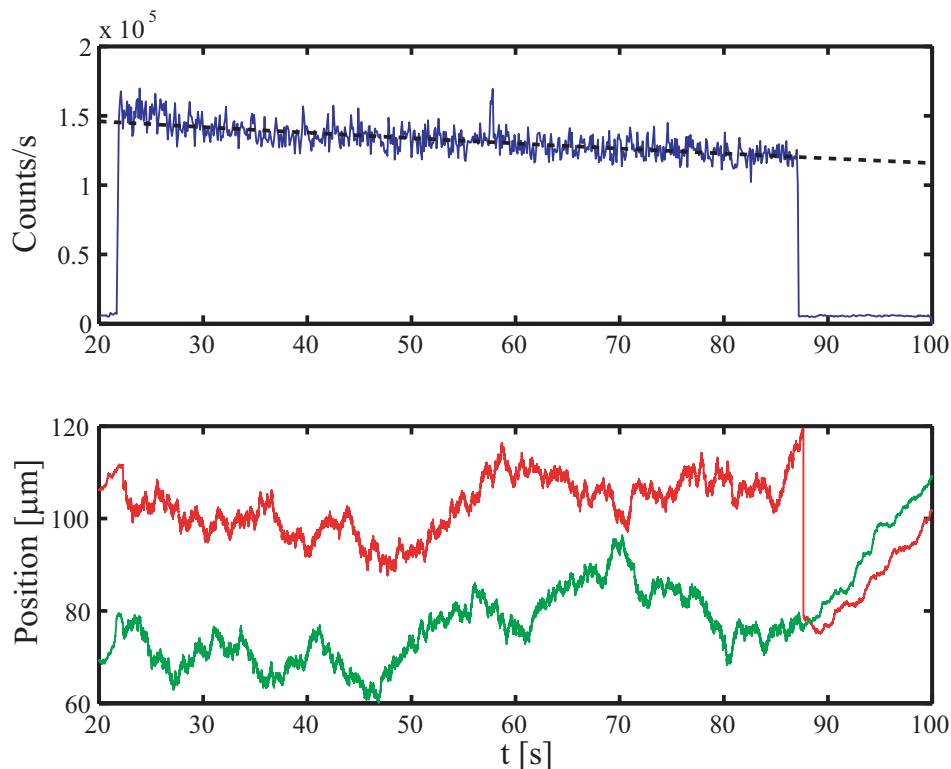


Figure 7.6: Typical tracking trajectory data. The upper plot shows the fluorescence count rate in 10 ms time bins; the lower plot shows the x and y positions of the sample stage during the trajectory. The particle is lost when the sample stage reaches the end of its travel range. Note the 15% decay in fluorescence of the particle due to photobleaching over the ~ 65 s trajectory. The dotted line shows an exponential fit to the decay curve.

from the data in Fig. 7.6 with $\Delta t = 0.4$ s is shown in Fig. 7.7, as a running estimate over the trajectory length. The error bars are at the 2σ level. With our large data set, we can also look at statistics of the tracking events as an ensemble. For each of the 74 two-dimensional trajectories in our data set, we may estimate the diffusion coefficients $\hat{D}_{\Delta t}(X)$ and $\hat{D}_{\Delta t}(Y)$ along separate Cartesian directions and over a range of sample times Δt . The (unweighted) average of the diffusion coefficient estimates formed in this way are displayed in Figure 7.8 as Δt is varied between 0.002 and 2 s. At small time intervals, the $\hat{D}_{\Delta t}$ contains contributions from the particle's diffusion as well as the feedback dynamics of the tracking apparatus. At longer times, the variance is dominated by the particle's motion and depends only on the particle's diffusion coefficient.

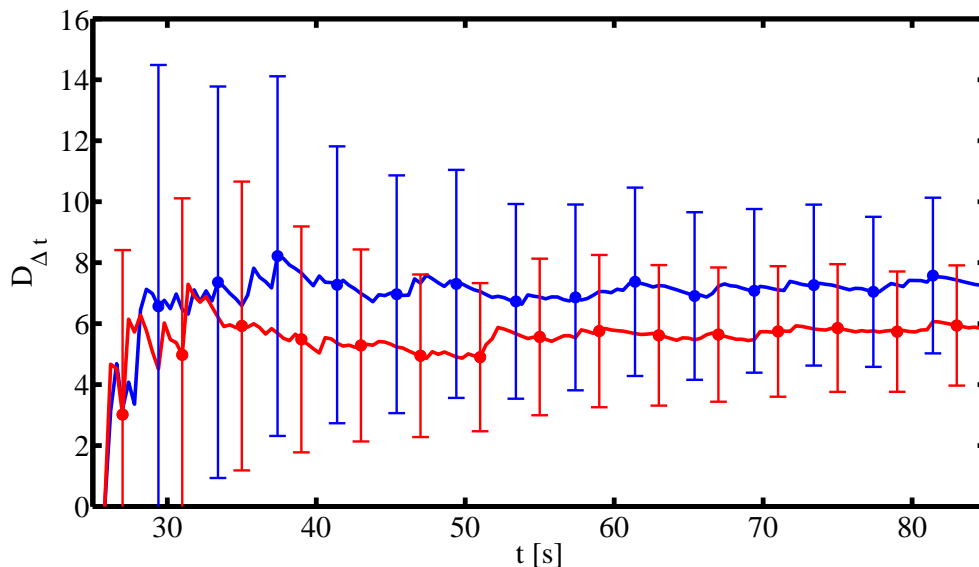


Figure 7.7: Running diffusion coefficient estimates $\hat{D}_{\Delta t}(X)$ and $\hat{D}_{\Delta t}(Y)$ from the data shown in Fig. 7.6, for $\Delta t = 0.4$ s. The error bars are at the 2σ level, assuming underlying Brownian motion statistics.

Correlation functions with exponential fluorescence decay The appearance of exponential photobleaching decay in our fluorescence signals gives a contribution to the fluorescence correlation function that can be easily accounted for. Suppose that a fluctuating signal $I_0(t)$ is also subject to exponential decay so that we may write the total signal $I(t) = e^{-\gamma_d t} I_0(t)$. We can calculate the autocorrelation function of $I(t)$ assuming that the decay timescale γ_d is much longer than the other timescales in the signal $I_0(t)$. Let T be the total measurement time. Plugging in to Eq. 6.2, we easily find

$$g(\tau) = \left[\frac{\gamma(T - \tau)}{2} \right] \coth \left[\frac{\gamma(T - \tau)}{2} \right] [g_0(\tau) - 1] + 1 \quad (7.3)$$

where \coth is the hyperbolic cotangent function and $g_0(\tau)$ is the fluorescence autocorrelation function in the absence of photobleaching fluorescence decay, *i.e.*, the autocorrelation of $I_0(t)$.

Distribution of exit times from a square region One interesting statistical effect arising in the analysis of extremely long tracking runs should at least be mentioned here. At extremely long bin times (and with enough data), we expect $\hat{D}_{\Delta t}$ to

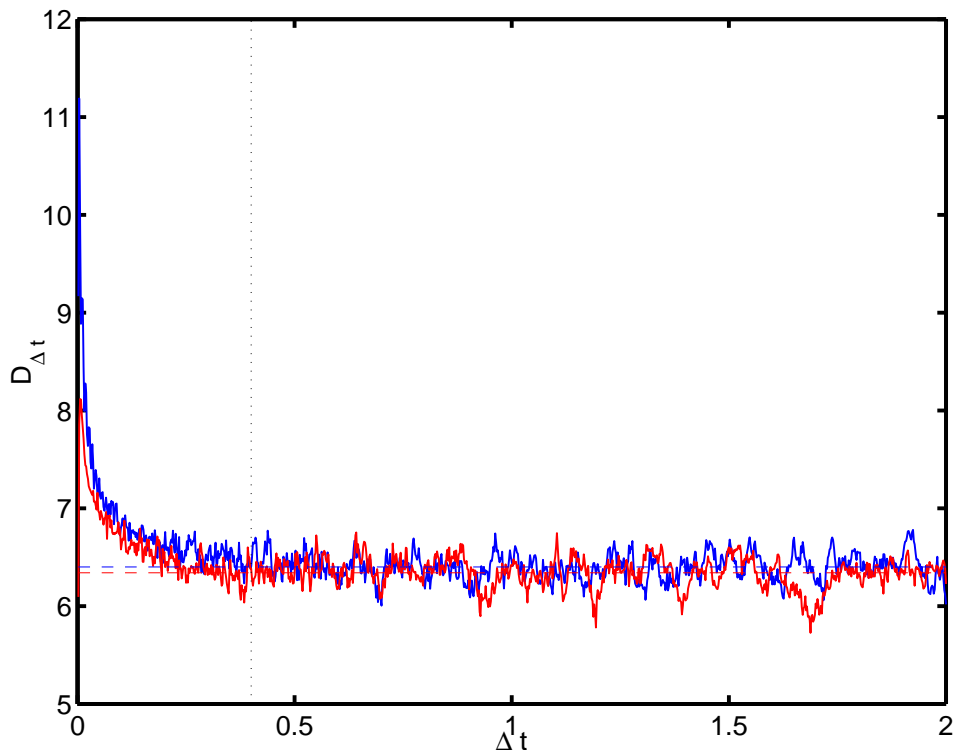


Figure 7.8: Diffusion coefficient estimates $\hat{D}_{\Delta t}(X)$ and $\hat{D}_{\Delta t}(X)$ averaged over the 74 trajectories in our data set and plotted as a function of the sample time Δt .

decrease with Δt because we post-select trajectories which remain within the travel range of our tracking apparatus, approximately $L = 100\mu m$ in each direction. In other words, at extremely long bin times, only trajectories that remained within the trackable region for an anomalously long time contain enough data to form an estimate $\hat{D}_{\Delta t}$. We will not attempt a systematic analysis of this effect, but note that its contribution is expected to arise for trajectories whose length approaches the length-scale $T_{\mathbf{L}} = L^2/\pi^2 D \approx 156$ s.

To see where $T_{\mathbf{L}}$ arises, we should derive the exit-time distribution for a particle in a square region of width L . To do this, we calculate the solution to the free-diffusion Fokker-Planck equation with absorbing boundary conditions, so that the integrated probability over this region is equal to the probability that a particle has not exited the region [36, 31]. It is easy to see that, for a particle restricted to the region $\mathbf{L} = [0, L] \times [0, L]$, with absorbing boundary conditions at the edges of the square, the

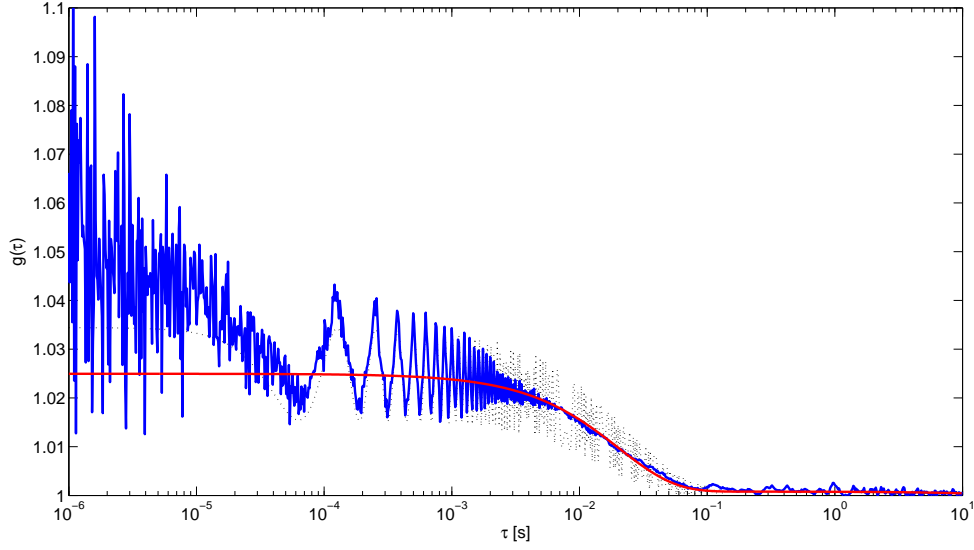


Figure 7.9: Fluorescence autocorrelation function recorded during a 40 s interval. Curve fits to the full [Eq. (5.64)] and averaged [Eq. (5.65)] are shown as dotted and solid lines, respectively, and the measured curve crosses over between these two as the logarithmically spaced τ intervals exceed the rotation period. The fit parameters are $r/w = 0.13$, $\gamma = 24\text{Hz}$, $D/w^2 = 1.14\text{ s}^{-1}$. For $D = 6.5\text{ }\mu\text{m}^2/\text{s}$, these corresponds to a beam waist $w = 2.4\text{ }\mu\text{m}$. The fit is also corrected for photobleaching decay using Eq. (7.3).

solution to the Fokker-Planck equation can be written by expanding in sine functions:

$$p(x, y, t|x_0, y_0, 0) = \sum_{n,m=1}^{\infty} \frac{4}{L^2} \sin\left(\frac{n\pi x}{L}\right) \sin\left(\frac{n\pi x_0}{L}\right) \sin\left(\frac{m\pi y}{L}\right) \sin\left(\frac{m\pi y_0}{L}\right) \exp\left[-(n^2 + m^2)\frac{\pi^2 Dt}{L^2}\right]. \quad (7.4)$$

Now let $Q_{\mathbf{L}}(T)$ be the probability that a particle remains within \mathbf{L} given that it started within the square (with an otherwise flat distribution of starting positions).

Then we see immediately that

$$\begin{aligned} Q_{\mathbf{L}}(T) &= \int dx dy \frac{dx_0}{L} \frac{dy_0}{L} p(x, y, T|x_0, y_0, 0) \\ &= \left(\frac{8}{\pi^2}\right)^2 \left[\sum_{n \text{ odd}} \frac{1}{n^2} \exp\left(-n^2 \frac{T}{T_{\mathbf{L}}}\right) \right]^2 \end{aligned} \quad (7.5)$$

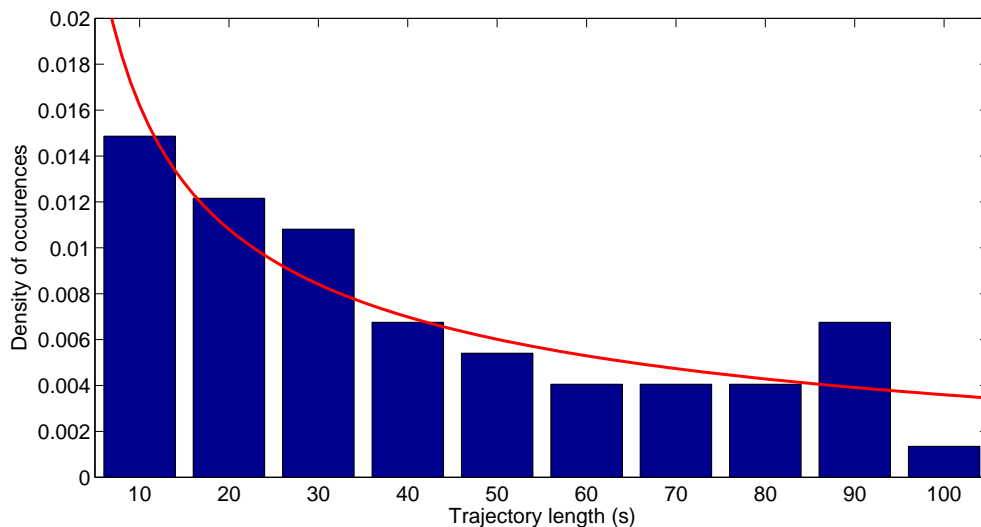


Figure 7.10: Histogram of trajectory lengths for trajectories of at least 10 s duration. The red line is a fit to $Q_{\mathbf{L}}(T)$ given by Eq. (7.5) with fit parameter $T_{\mathbf{L}} = 351$ s. Since our trajectories are all much shorter than this, we do not worry about statistical post-analysis effects in our estimation of the diffusion coefficients D .

where $T_{\mathbf{L}} = \frac{L^2}{\pi^2 D}$. For a given value of $T_{\mathbf{L}}$, this series will only require a number of terms that is large compared to $\sqrt{T_{\mathbf{L}}/T}$ terms to converge. In particular, for $L = 100$ μm and $D = 6.5$ $\mu\text{m}^2/\text{s}$, we have $T_{\mathbf{L}} \approx 156$ s. Of course $Q_{\mathbf{L}}(T)$ will have a different form for a different initial starting distribution of particles, for example, all of the particles starting at the center of the square. But in each case, $T_{\mathbf{L}}$ sets the timescale of the statistics.

In Fig. 7.10, we show a histogram of observed trajectory lengths and a fit to $Q_{\mathbf{L}}(T)$. The fit is reasonably good for $T_{\mathbf{L}} = 351$ s, at least a factor of 3.5 longer than our longest observed trajectories (and a factor of 35 longer than the shorter ones). Our trajectories are therefore not particularly long compared to the statistical exit time from a square and we disregard trajectory post-selection effects for this reason.

7.4 Comparison with the theory

With the addition of the fluorescence intensity servo discussed in Sect. 6.1.3, we gain the capability to lock a particle's fluorescence intensity during tracking. This servo

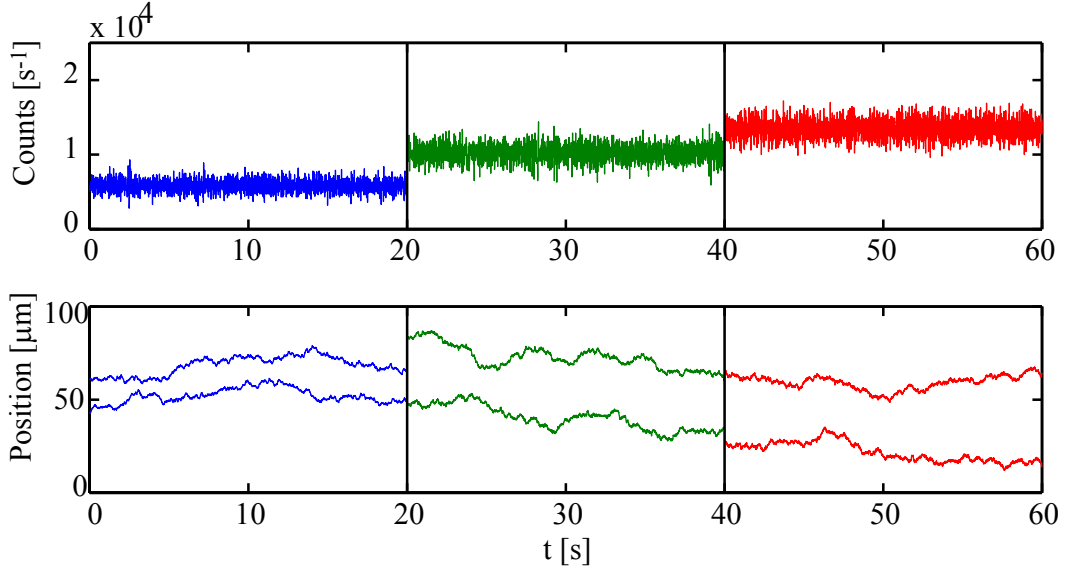


Figure 7.11: Tracking trajectories for a single bead excited at three different fluorescence intensities using the fluorescence lock servo. The same particle was tracked and the servo set point was manually adjusted between records. The fluorescence set points were 5.8 kHz, 10.2 kHz, and 13 kHz. Mean-square deviations and fluorescence autocorrelation functions for these trajectories are shown in Figs. 7.12 and 7.13.

immediately eliminates the photobleaching decays seen in previous data, but serves a much more important and fundamental purpose as well. Our entire control system is *linear*, meaning that an increase in fluorescence intensity from a tracked particle results in a proportional increase in the tracking control loop gain. This variation of the gain essentially rules out the possibility of tracking particles of different brightness within a heterogeneous ensemble. The fluorescence servo gives us this capability for heterogeneous tracking and also provides a convenient knob for adjusting the brightness (and therefore gain) of the servo. As an interesting application of this capability, and a nice demonstration of the variation in control loop gain with a particle’s brightness, we recorded tracking data from a single particle at three different brightness levels. The trajectories are shown in Fig. 7.11. By analyzing these three trajectories, we can give a full demonstration of the linear control system model of both the tracking and fluorescence statistics.

In Fig. 7.12, we begin by displaying $\hat{D}_{\Delta t}$ as defined in Eq. (7.2) for each trajectory. Note that I often use the terms “ $\hat{D}_{\Delta t}$ ” and “mean-square deviation” or “ $MSD(\Delta t)$ ”

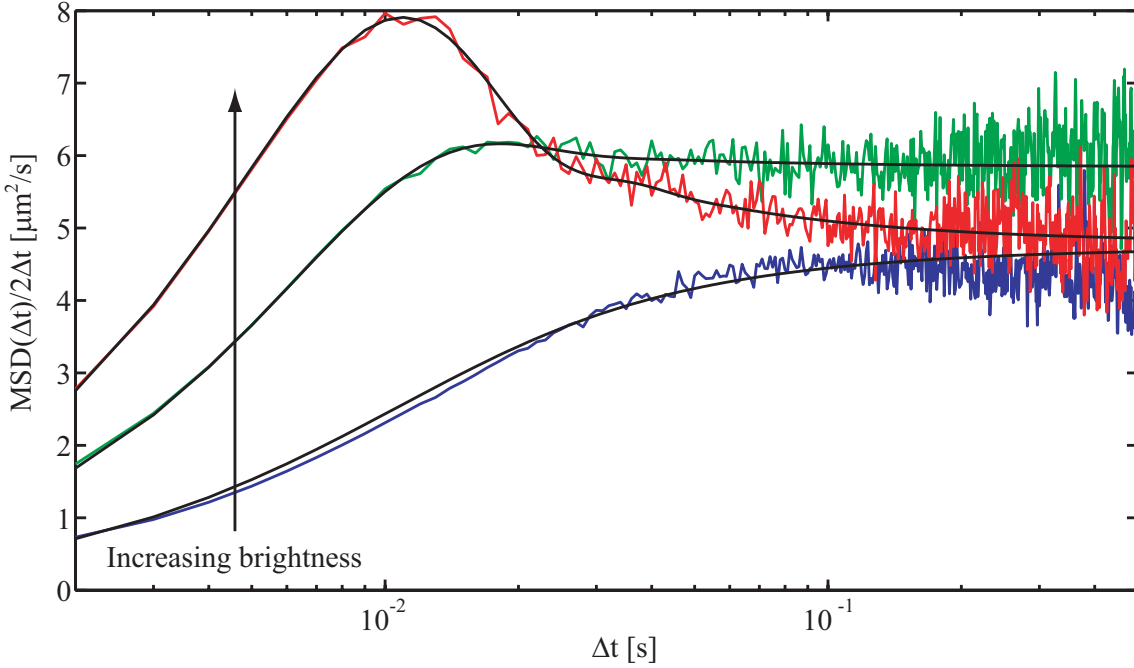


Figure 7.12: Mean-square deviations for the trajectories shown in Fig. 7.11 showing the coupled nature of the particle’s brightness and the control loop gain. The dark curves are fits to the second-order theory in Ch. 5 including measurement noise of about $10 \text{ nm}/\sqrt{\text{Hz}}$. At the highest intensity, 13 kHz, the mean-square deviation shows resonant peaking behavior. At higher count rates, the lock became unstable and the particle was lost.

synonymously, because they differ only in the scaling by Δt [see Eqs. (7.1)-(7.2)]. This scaling is mostly for visual convenience, so that a plot of this quantity asymptotically approaches the particle’s diffusion coefficient D rather than asymptotically approaching a straight line whose slope is $4D$ (or $2D$ for data along one Cartesian direction only).

From Fig. 7.12 we see that at higher gains, the mean-square deviation reaches its asymptotic value for smaller bin time Δt , and resonant peaking behavior clearly appears at the highest gain (largest brightness, 13 kHz). Similar features appear in the fluorescence autocorrelation functions $g(\tau)$ shown in Fig. 7.13. In these plots, the increasing gain manifests itself through the earlier rolloff in fluorescence fluctuations and the revival of oscillations at the gain-induced oscillation frequency. For both the mean-square deviation and fluorescence autocorrelation curves, we fit the data to the second-order-plus-noise model discussed in Ch. 5.1.4. For fits to $g(\tau)$, we fixed the

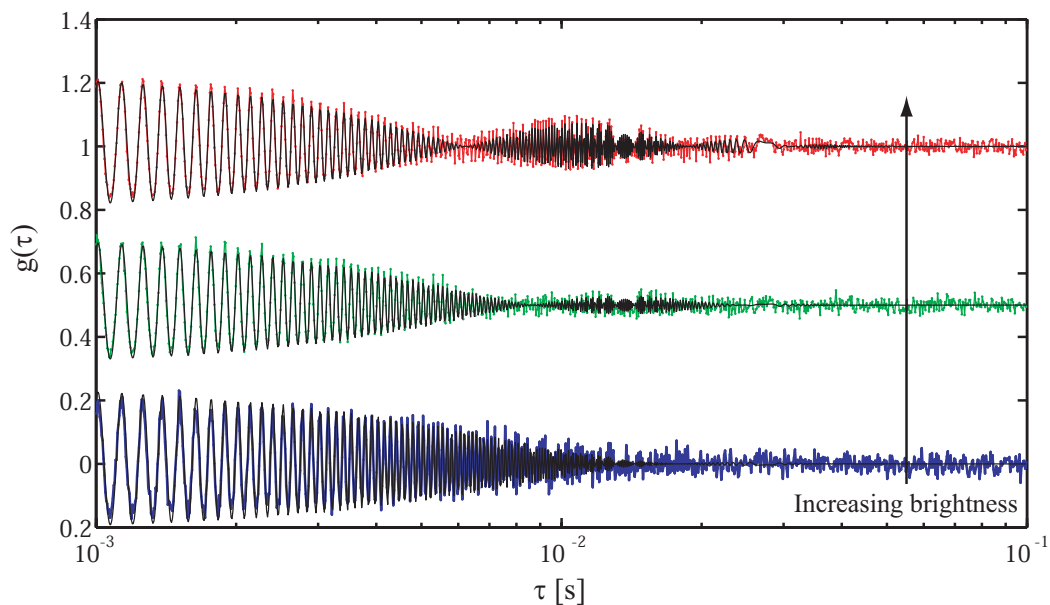


Figure 7.13: Autocorrelation functions $g(\tau)$ for a particle tracked at varying brightness, the same data as in Figs. 7.11 and 7.12, together with fits to the second-order plus noise theory of Ch. 5. The curves have been offset for clarity and ordered according to brightness with the brightest at the top.

diffusion coefficient to be $D = 5.1 \mu\text{m}^2/\text{s}$, the average value determined by the mean-square deviation for each run. We also used the beam waist $w = 1 \mu\text{m}$ as measured by scanning an immobilized fluorescent bead. The fits are shown together with the data in Figs. 7.12 and 7.13, and the fit parameters are summarized in Table 7.1. The accuracy of the fits together with the agreement of fit parameters determined from the disparate data channels, the position of the sample stage and the fluorescence photon arrival rates, shows the quantitative applicability of the linear control system model. At this stage, as evident in Fig. 7.11, the experiment is capable of tracking 60 nm fluorescent beads at count rates of about 5.8 kHz, well beyond the moderate targets defined in our original tracking proposal of Ch. 2.

		5.8 kHz		10.2 kHz		13.0 kHz	
		$MSD(\Delta t)$	$g(\tau)$	$MSD(\Delta t)$	$g(\tau)$	$MSD(\Delta t)$	$g(\tau)$
D	$\mu\text{m}^2/\text{s}$	4.7	5.1*	5.8	5.1*	4.8	5.1*
γ_c	Hz	170	120	203	217	361	384
γ_p	Hz	602	300	270	261	191	186
n	$\text{nm}/\sqrt{\text{Hz}}$	0.0	0.0	10.7	8.5	9.9	8.0
w	μm	–	1.0*	–	1.0*	–	1.0*
r	μm	–	0.6	–	0.6	–	0.6

Table 7.1: Table of fit parameters for the mean-square deviation curves of Fig. 7.12 and fluorescence autocorrelation functions of Fig. 7.13. Each figure contains three curves from tracking the same particle at three different brightness values. Each set of fit parameters is labeled above by the brightness in kHz. For the fits to $g(\tau)$, the beam waist and diffusion coefficient were constrained to $w = 1 \mu\text{m}$ and $D = 5.1 \mu\text{m}^2/\text{s}$ (the average value determined from the mean-square deviation of each separate curve), indicated by *. Aside from the diffusion coefficient constraint in $g(\tau)$, the two parameter sets are otherwise independent.

Chapter 8

Detailed Studies of a Binary Mixture

In this chapter, the most up-to-date experimental results in the thesis are presented. For these experiments, we monitored a binary mixture of fluorescent microspheres with different sizes and therefore different diffusion coefficients. A host of raw data from a long tracking run is presented, followed by two systematic investigations of that data set. In the first study, we compare our data to the statistical model developed in Ch. 5 to determine feedback control loop parameters and infer the localization, or tracking error, in our experiment. In the second study, we demonstrate the capability to differentiate between particles rapidly using a simple particle classification algorithm based on diffusion coefficient estimation. Many of the results presented here are in preparation as Refs. [27, 28].

8.1 Raw data

For this data run, recorded in June 2006, we used an ultra-dilute mixture of roughly equal concentration 60 nm and 210 nm diameter fluorescent microspheres. Because our microspheres are embedded with dye molecules throughout their volume, the larger particles appear much brighter than the smaller particles when illuminated by the same laser intensity. In order to track both types of particles, the fluorescence servo described in Sect. 6.1.3 is an absolute necessity.

Each single shot of the experiment consists of a 100 s period in which the fluo-

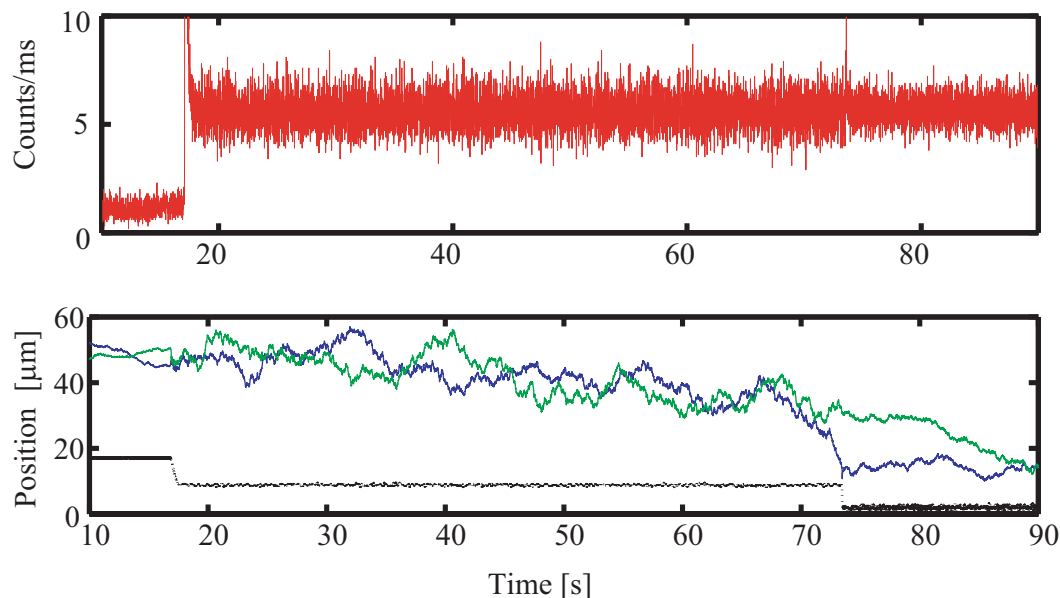


Figure 8.1: Data from a single shot of the binary mixture experiment. The upper plot shows the rate of photon detections. In the lower plot, the upper curves are the x and y positions of the sample stage during the same trajectory. The lower curve on the lower plot shows the excitation laser power (in arbitrary units) required to lock the number of detected photons to 5600 s^{-1} . Three regions are discernible, in which no particle is present (until 17 s), a 60 nm diameter particle is tracked (until 74 s) and a 210 nm diameter particle is tracked (until 90 s).

rescence photon arrival times, x and y positions of the piezoelectric stage, and the excitation laser power are recorded. The data is then written to the computer hard drive, and after a brief pause, the process is repeated. Details of the apparatus are given in Ch. 6.1. Analog integrators were used as controllers, and the microcontroller was programmed to monitor the piezoelectric stage position and send a digital reset pulse whenever the stage reaches its boundaries at 0 and $100 \mu\text{m}$. The reset pulse triggers a switch that grounds both integrators, bringing the sample stage back to a centered position (determined by a DC offset on the high voltage amp) and discarding any currently tracked particle in the process.

Data from a single shot of the experiment is shown in Fig. 8.1. In that particular run, the apparatus tracked a 60 nm particle for about 55 s before colliding with a 210 nm particle. Upon incidence of the larger (brighter) particle, the fluorescence servo

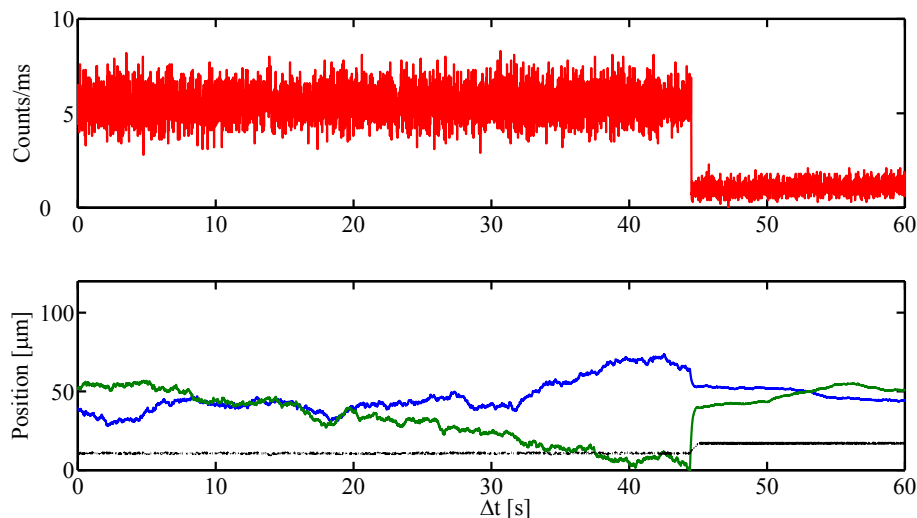


Figure 8.2: Another trajectory from the same data set as Fig. 8.1. One axis of the piezoelectric stage reached $0 \mu\text{m}$ at $t = 45 \text{ s}$, which triggered the controller reset procedure, ending the trajectory and discarding the tracked particle as the sample stage was reset to its center.

automatically cut the laser power, effectively rendering the smaller (dimmer) particle invisible. Because of the asymmetric visibility of the particles (the bright particles are visible when a dim one is being tracked at high laser power, but not *vice versa*), the apparatus preferentially tracks 210 nm particles. However, at our extremely dilute concentrations, these particle “collisions” are fairly rare. We observed only 3 such events in a data set containing 62 total trajectories recorded over a few hours. Another example tracking trajectory showing the controller reset procedure is displayed in Fig. 8.2.

To analyze the data, we inspected 44 shots of the experiment (4400 s of data) and found 62 individual tracking trajectories. For example, for the data shown in Fig. 8.1, we (conservatively) labeled one trajectory as extending from 20 to 70 s and another trajectory from 75 s to the end of the run. For this data set, no trajectories ended with the loss of a particle due to a tracking failure; each trajectory ended either at a particle collision, or at the boundary of the tracking region. We only analyzed trajectories of at least 10 s duration, and of course the maximum trajectory length was 100 s when a particle was tracked for the entire recording period. Having

partitioned the data into an ensemble of individual particle trajectories, we are able to analyze the data efficiently. Among other quantities, the diffusion coefficient estimate $\hat{D}_{\Delta t}$, the sample stage velocity autocorrelation function $\langle \Delta X_{\Delta t}(t) \Delta X_{\Delta t}(t + \tau) \rangle$, and the fluorescence autocorrelation function $g(\tau)$ were calculated from the data. The excitation laser power required to lock the particle's fluorescence to 5.8 kHz was also recorded, and provides a measure of a particle's brightness since a brighter particle requires less power to reach the same fluorescence intensity. These and other statistics are displayed in Figs. 8.1-8.12 and discussed in the figure captions.

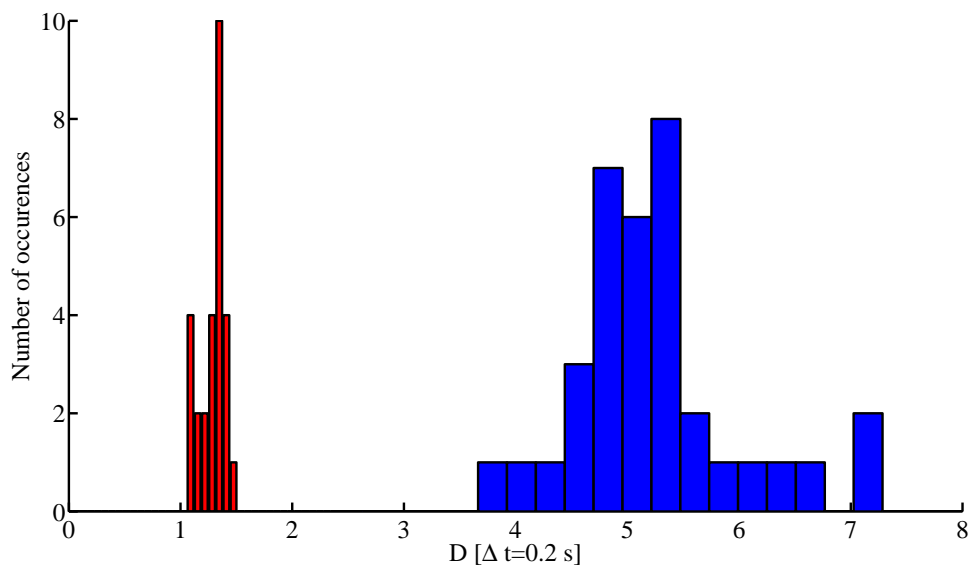


Figure 8.3: Histogram of observed diffusion coefficients $\hat{D}_{\Delta t}$ with $\Delta t = 0.2$ s. The distribution is clearly bimodal, with the 210 nm particles clustered around the mean value $1.3 \mu\text{m}^2/\text{s}$ and 60 nm particles clustered at $5.4 \mu\text{m}^2/\text{s}$. For this and subsequent plots, we color code each individual data point as red (210 nm diameter) or blue (60 nm diameter) according to this histogram.

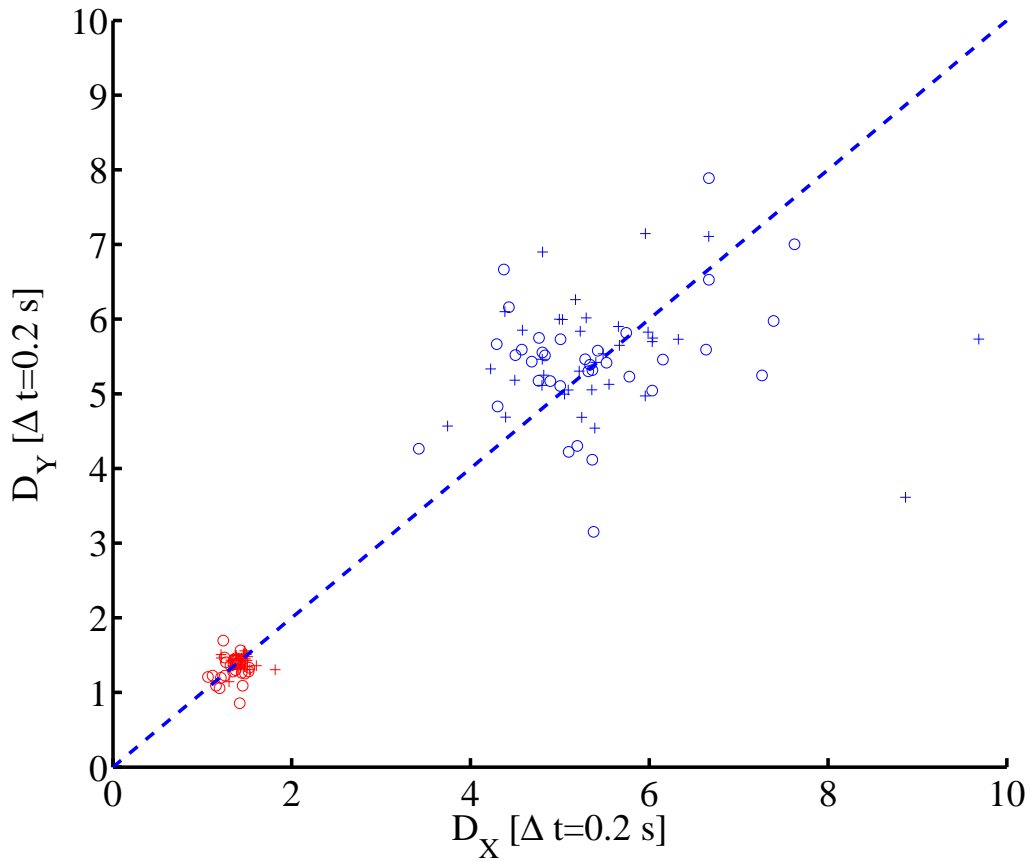


Figure 8.4: Scatter plot of diffusion coefficients $D_X = \hat{D}_{\Delta t}(X)$ and $D_Y = \hat{D}_{\Delta t}(Y)$ along the x and y . Points marked with circles (o) were derived from the mean-square deviation and those marked with (+) were derived from a fit of the second-order model (assuming no measurement noise, $n = 0$) to the velocity autocorrelation function $\langle \Delta X_{\Delta t}(t) \Delta X_{\Delta t}(t + \tau) \rangle$ discussed in Ch. 5. See Fig. 8.5 for more discussion of these two quantities.

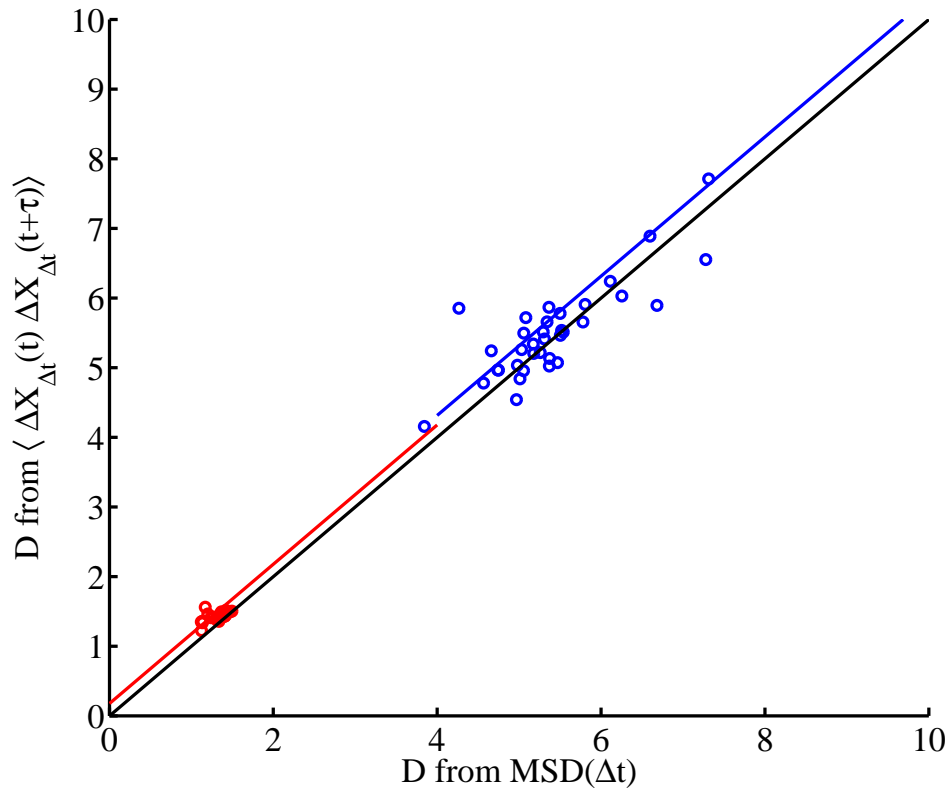


Figure 8.5: Comparison of the diffusion coefficient determined from the mean-square deviation and velocity autocorrelation of the sample stage, when measurement noise is *not* included in the analysis. When measurement noise is not considered, the diffusion coefficient inferred from the velocity autocorrelation is artificially inflated and lies systematically above the line $y = x$ on this plot. On the other hand, at time scales beyond the tracking bandwidth, the mean-square deviation asymptotically approaches the free diffusion value and is immune to measurement noise.

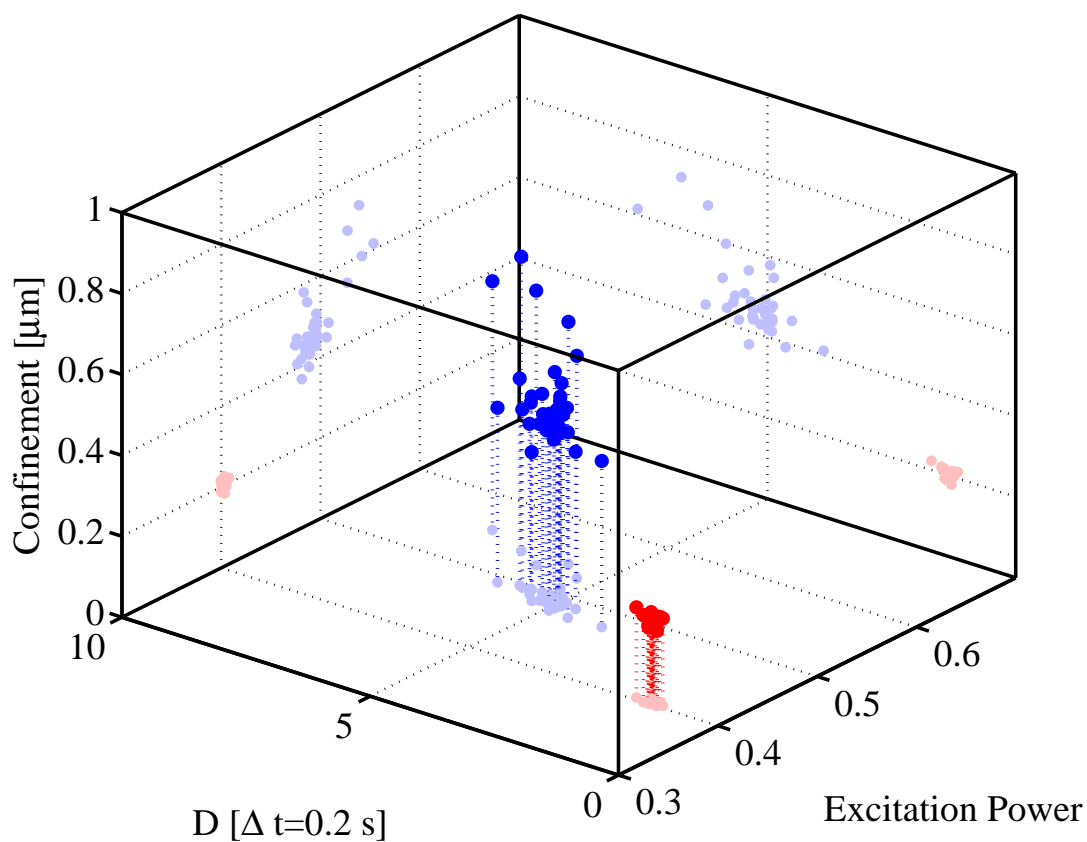


Figure 8.6: Three-dimensional scatter plot of diffusion coefficient $\hat{D}_{\Delta t}$, excitation laser power and confinement estimated from $g(\tau)$ via Eq. (5.75), assuming $w = 1 \mu\text{m}$ and $r = 0.6 \mu\text{m}$. The “brightness,” or perhaps more appropriately the “dimness,” of a particle is proportional to the excitation laser power (arbitrary units) required to lock the fluorescence to 5.8 kHz. The (smaller, faster, dimmer) and (larger, slower, brighter) particles cluster in the parameter space and are clearly differentiated by all three of these quantities.

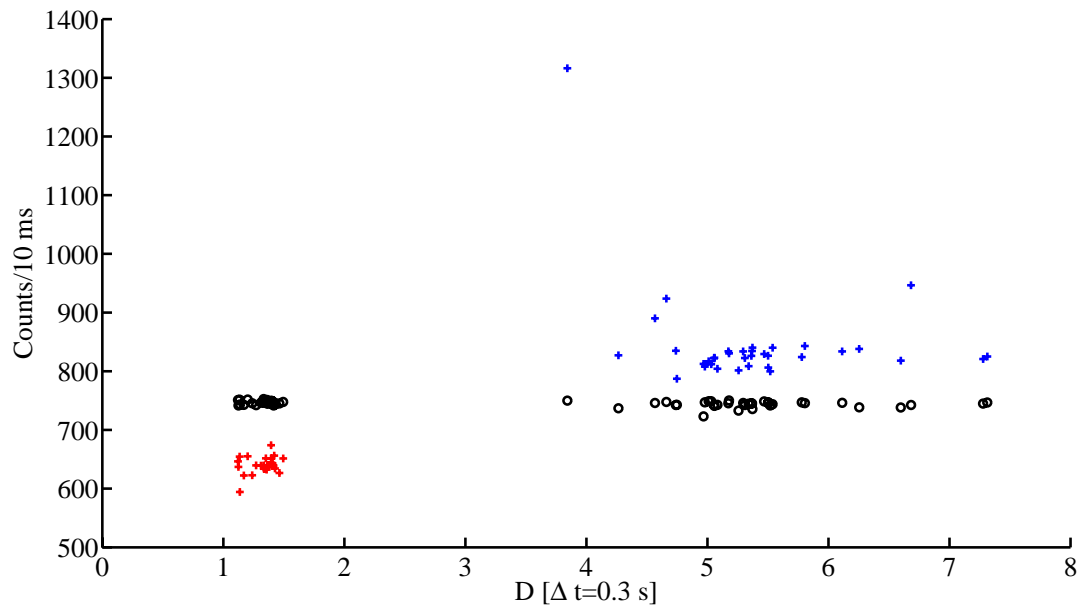


Figure 8.8: The standard deviation (RMS) value (+) of the fluorescence photon count rate recorded during tracking along with and the expected value from Poisson statistics at the same average rate (o) are plotted against the diffusion coefficient. The “sub-shot-noise” values are not a violation of classical statistics, but are a result of the fluorescence servo’s ability to control fluorescence fluctuations at slow timescales.

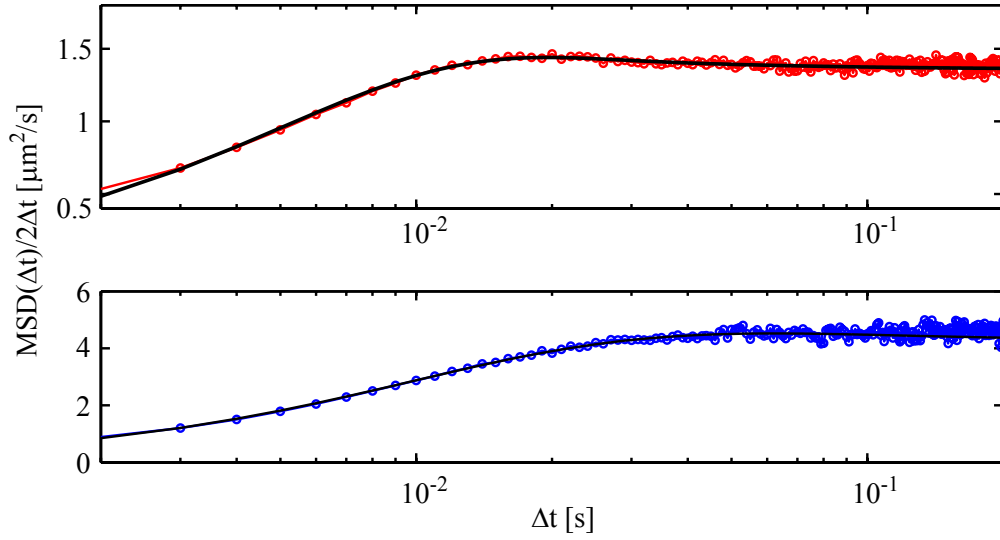


Figure 8.9: $\hat{D}_{\Delta t}$ as defined by Eq. (7.2) for two typical (60 and 210 nm diameter) tracking trajectories together with fits to the second-order-plus-noise model of Ch. 5. At long times, the curves asymptote to the particle diffusion coefficient, while the short time behavior depends on the tracking feedback performance. The solid curves are fits to the second-order-plus-noise model. The fit parameters for the 60 nm particle (blue) were $D = 4.6 \mu\text{m}^2/\text{s}$, $\gamma_c = 67 \text{ Hz}$, $\gamma_p = 222 \text{ Hz}$, $n = 35 \text{ nm}/\sqrt{\text{Hz}}$. The fit parameters for the 210 nm particle (red) were $D = 1.4 \mu\text{m}^2/\text{s}$, $\gamma_c = 135 \text{ Hz}$, $\gamma_p = 385 \text{ Hz}$, $n = 11 \text{ nm}/\sqrt{\text{Hz}}$.

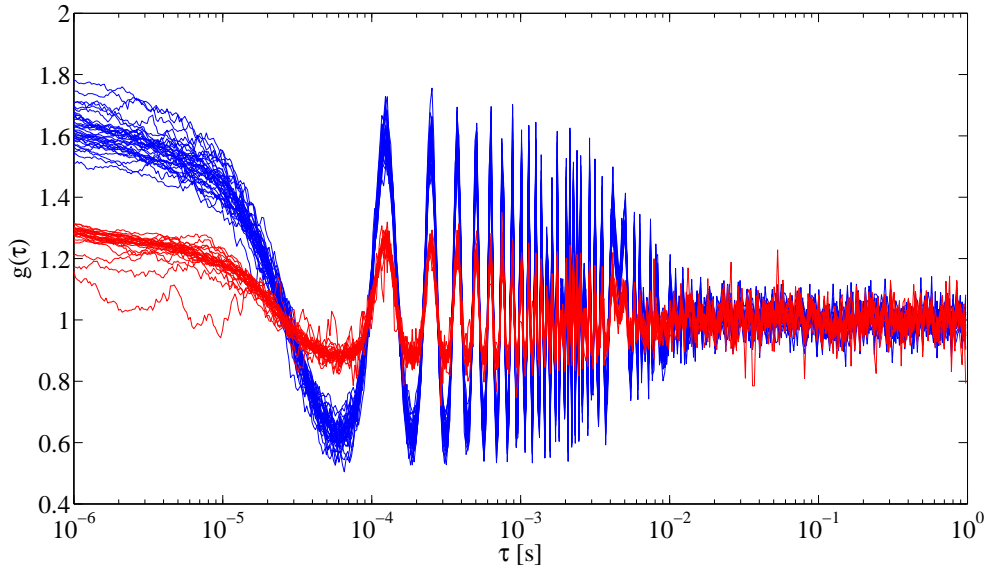


Figure 8.10: Fluorescence autocorrelation functions $g(\tau)$ for all 62 trajectories. These exhibit shot-to-shot uniformity as well as a clear partitioning by particle type.

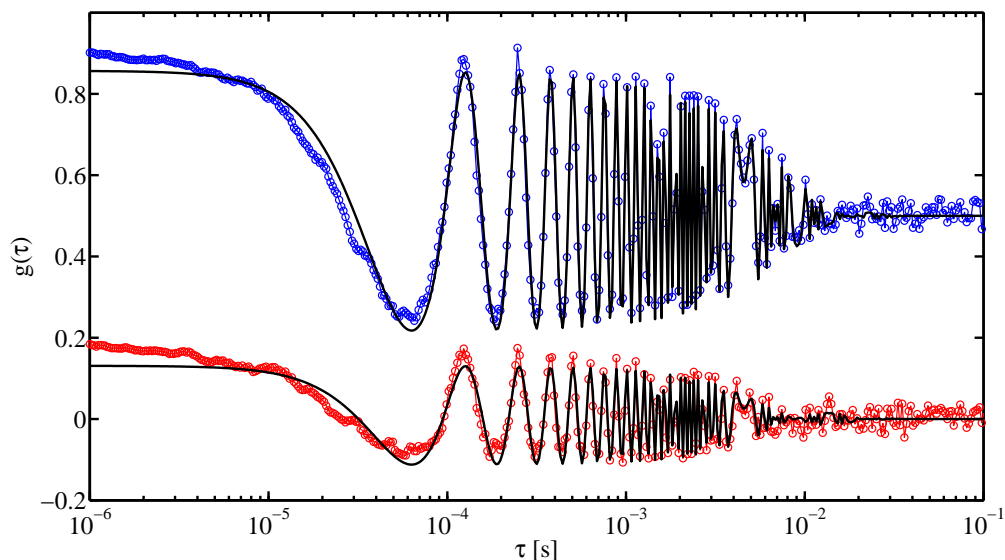


Figure 8.11: Fits of $g(\tau)$ to the second-order-plus-noise model of Ch. 5 for two of the curves displayed in Fig. 8.10. We used $w = 1 \mu\text{m}$ and D as determined from the mean-square deviation, as discussed in Table 7.1. For the 60 nm particle (blue), the parameters were $r = 0.6$, $D = 5.0 \mu\text{m}^2/\text{s}$, $\gamma_c = 127 \text{ Hz}$, $\gamma_p = 291 \text{ Hz}$, $n = 22 \text{ nm}/\sqrt{\text{Hz}}$. for the 210 nm particle (red), the parameters were $r = 0.5$, $D = 1.3 \mu\text{m}^2/\text{s}$, $\gamma_c = 250 \text{ Hz}$, $\gamma_p = 296 \text{ Hz}$, $n = 15 \text{ nm}/\sqrt{\text{Hz}}$.

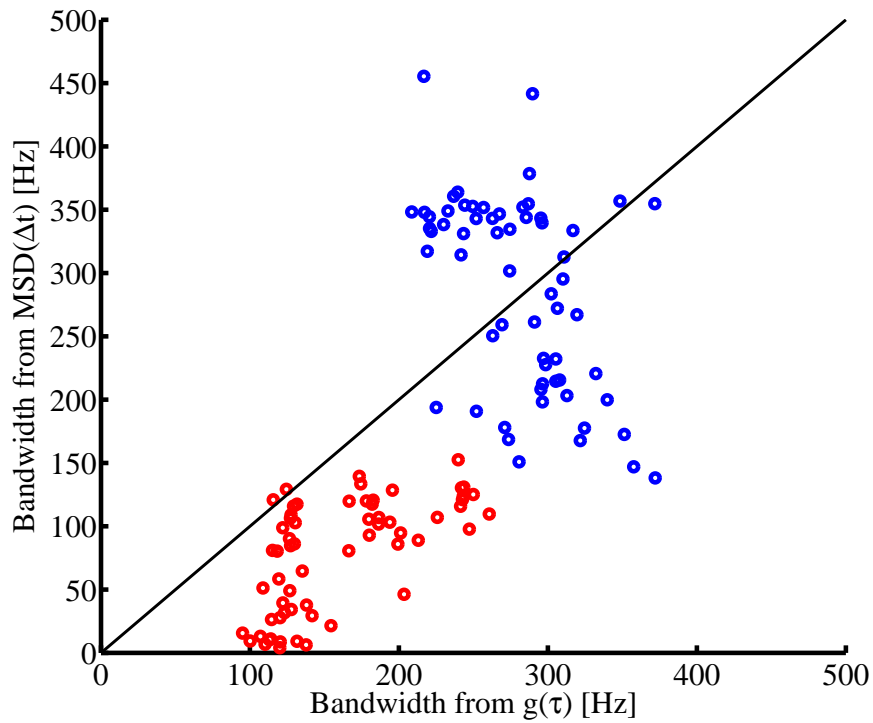


Figure 8.12: Comparison of feedback bandwidth parameters as determined from fits such as those in Figs. 8.11 and 8.9. The red points show the integrator bandwidth γ_c and the blue points show the low-pass Plant bandwidth γ_p . The color code is different from previous figures! $g(\tau)$ tends to underestimate the integrator bandwidth γ_c relative to $MSD(\Delta t)$, while the values of γ_p are commensurate across the separate analyses.

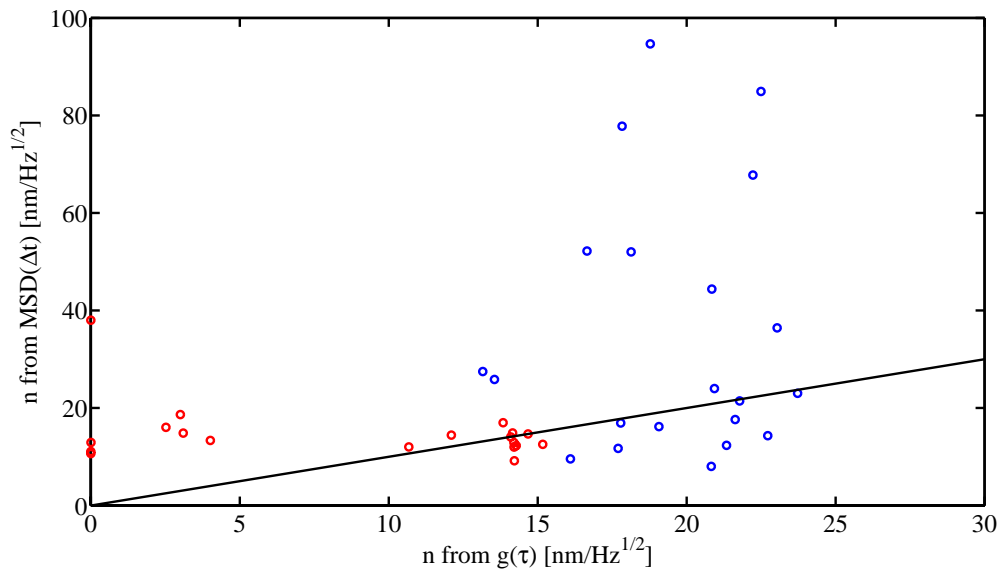


Figure 8.13: Comparison of measurement noise n determined from fits such as those in Figs. 8.11 and Fig. 8.9. Note the different scales on the axes, showing the large spread in n as determined from $MSD(\Delta t)$.

8.2 Near-optimal tracking

In Ch. 4, we discussed in detail the limitations on particle localization that arise from the fundamentally noisy fluorescence photon counting process. This optical shot-noise tracking limit imposes the constraint that a diffusing particle cannot be tracked arbitrarily well at a finite fluorescence count rate, since an overly aggressive feedback controller will feed photon counting noise back into the system [26]. In this section, we use our statistical tracking model and the large data set displayed in Figs. 8.3-8.12 to make quantitative inferences about particle localization during tracking in our experiment. We will see that in some cases we approach quite close to the shot-noise limit.

In particular, we will assume the second-order-plus-noise model of Ch. 5 and use the mean-square deviation $MSD(\Delta t)$ and the fluorescence autocorrelation function $g(\tau)$ to determine the system parameters D , γ_c , γ_p and n in two separate ways. From Sect. 5.1.4, we know that the steady-state tracking error for our second-order system with these parameters is

$$L = \sqrt{\mathbb{E}[E(t)^2]} = \sqrt{D \left(\frac{1}{\gamma_c} + \frac{1}{\gamma_p} \right) + \frac{n^2 \gamma_c}{2}}. \quad (8.1)$$

Having found these parameters by curve fitting to our data, we may then extract each particle's localization using Eq. (8.1). The resulting values of L are plotted versus the measured diffusion coefficient D in Fig. (8.14). In order to confirm the validity of this curve fitting technique for estimating L , we generated Monte Carlo simulations of the second-order control system model driven by particle diffusion and measurement noise, using typical values of the parameters n , γ_c , γ_p , and D . We then estimated L and D on the resulting "data" using the mean-square deviation, and these results are shown in gray in Fig. 8.14. The 60 nm beads are more poorly localized, due to their faster diffusion, and the inference of L from mean-square deviation data is also much more prone to noise for these particles, as seen from the large spread in inferred L values for the Monte Carlos simulations.

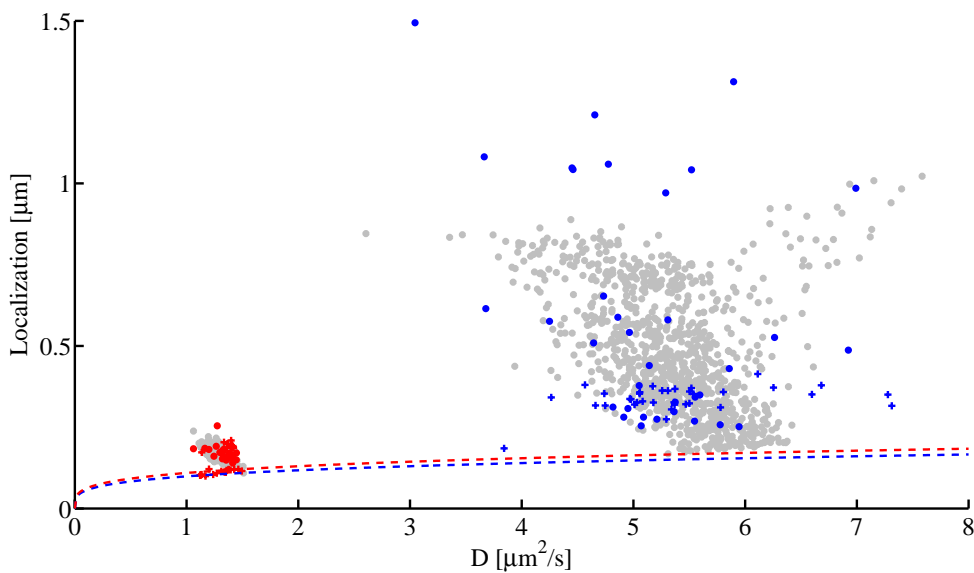


Figure 8.14: Inferred localization L versus D for 62 individual tracking trajectories (dark circles). The lighter circles are the results of simulations described in the text. The dashed line is the localization limit based on optical shot noise. Typical fit parameters for the 210 nm beads (red) are $D = 1.3 \mu\text{m}^2/\text{s}$, $n = 15 \text{ nm}/\sqrt{\text{Hz}}$, $\gamma_c = 111 \text{ Hz}$, $\gamma_p = 343 \text{ Hz}$. The localization values marked by (+) were determined from $g(\tau)$ with the value of D set from the tracking data and assuming $w = 1 \mu\text{m}$, but the localization determined from $g(\tau)$ is fairly robust to the choice of w .

Values of L inferred from fits to $g(\tau)$ with D determined from the mean-square deviation are also shown in Fig. 8.14, and these appear much more robust to the data analysis procedure. Note that for the 60 nm particles, the localization values determined from $g(\tau)$ are more tightly clustered than those determined from $MSD(\Delta t)$. As with all fluorescence autocorrelation methods, the length scale is set by the beam waist w , which we must calibrate separately, however the inferred values of the localization are fairly robust to variations in w and tend to depend more strongly on the beam shape through r/w and on the damping parameters γ_c and γ_p .

The dashed line in Fig. 8.14 is the shot-noise localization limit derived in Ch. 4 for our experimentally determined values of the beam waist $w = 1 \mu\text{m}$, rotation radius $r = 0.6 \mu\text{m}$ and maximum fluorescence count rate at the peak laser intensity, Γ_0 . Γ_0 was inferred from the beam parameters w and r , the localization L , and the observed

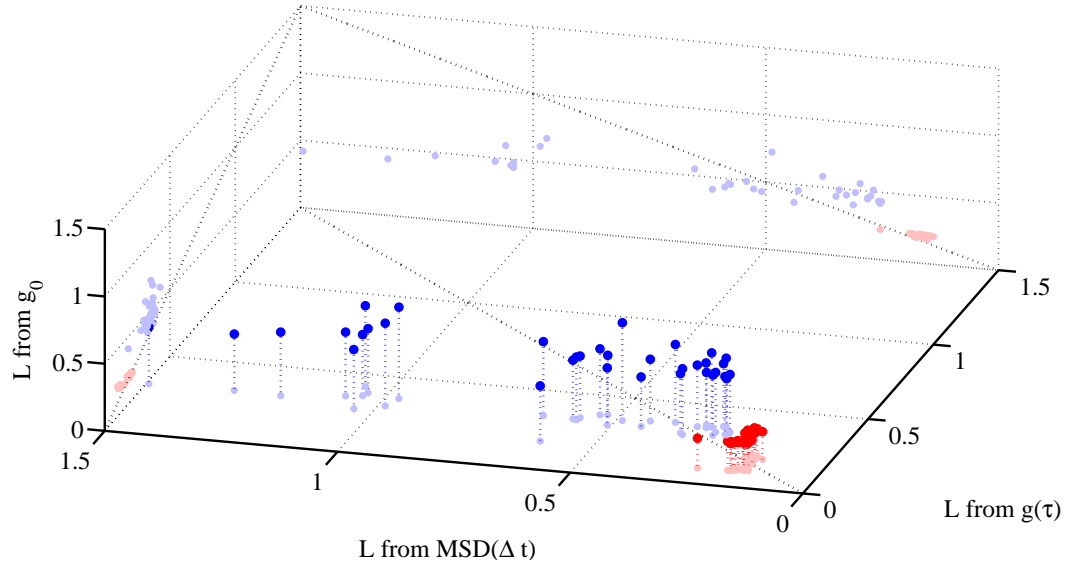


Figure 8.15: Comparison of the localization L determined from $MSD(\Delta t)$, $g(\tau)$, and g_0 .

(average) fluorescence intensity $\langle \Gamma \rangle$, which are related by

$$\langle \Gamma \rangle = \frac{\Gamma_0 w^2}{(w^2 + 4L^2)} \exp \left[\frac{2r^2}{(w^2 + 4L^2)} \right]. \quad (8.2)$$

For the 210 nm particles we find $\Gamma_0 = 9.8$ kHz and for the 60 nm particles we find $\Gamma_0 = 15.1$ kHz. The shot-noise localization limit in this case is given by combining Eqs. (4.12) and (4.18b) to find

$$L_{min} = \sqrt{\frac{w^2}{r} \sqrt{\frac{D}{4\Gamma_0}} \exp \left(\frac{r^2}{w^2} \right)}. \quad (8.3)$$

Finally, we can also estimate the localization L from autocorrelation functions near $g(\tau = 0) = g_0$, as in Eq. (5.75). This fit requires the values of w and r which we take to be 1.0 and 0.6 μm , respectively. A comparison of L determined in all three different ways is shown in Fig. 8.15.

Our results for the localization L as determined by all of these different methods are summarized in Tables 8.1 and 8.2. $MSD(\Delta t)$ is simply not very sensitive to the measurement noise n for the 60 nm particles as evident from the standard deviation

	210 nm particles			
	$MSD(\Delta t)$	$g(\tau)$	g_0	Opt.
L [nm]	169 ± 21.2	143 ± 40	204 ± 10	117
n [nm/ $\sqrt{\text{Hz}}$]	15.4 ± 5.4	6.3 ± 6.5	–	9.4

Table 8.1: Table comparing the localization and measurement noise determined from $MSD(\Delta t)$, $g(\tau)$, and g_0 for the 210 nm diameter particles. Shot-noise limited optimal values are denoted by “Opt.” The error values are the standard deviation in observed parameters.

of this parameter. This is because the measurement noise contributes at small time scales, while the mean-square deviation is sensitive all the way out to very long times where it asymptotically approaches the diffusion coefficient D . On the contrary, $g(\tau)$ tends to be extremely sensitive to short timescales; after all, we can measure it deep into the sub- μs range. However, $g(\tau)$ damps away at the feedback timescale and is not particularly sensitive to long-time statistics. As a result, when we determine D from the mean-square deviation at long times and insert this into $g(\tau)$ in order to find n at short times, we find tightly constrained and high quality results.

8.3 Classification by diffusion coefficient estimation

In this section, we consider an application of closed-loop particle tracking in which we classify particles as small (60 nm diameter) or large (210 nm diameter) according to an estimate of the diffusion coefficient. In particular, we want to know just how much data is required to make classifications with a specified error rate. The problem requires a good statistical description of the system, which we have spent a lot of time and effort developing and confirming in preceding sections. We will see that classifications can be made with very little data and with a very simple algorithm that could easily be implemented in real-time, offering the tantalizing possibility of triggering an event, such as a microfluidic pressure pulse for steering a particle or a photocatalytic laser flash for initiating a chemical reaction, using fast particle classification. In this binary scenario, we achieve 90% success rates on the basis of only

		60 nm particles			
		$MSD(\Delta t)$	$g(\tau)$	g_0	Opt.
L [nm]		611 ± 359	340 ± 41	481 ± 79	150
n [nm/ $\sqrt{\text{Hz}}$]		152 ± 190	18.0 ± 6.2	–	7.3

Table 8.2: Table comparing the localization and measurement noise determined from $MSD(\Delta t)$, $g(\tau)$, and g_0 for the 60 nm diameter particles. Note the unacceptably large spread in the measurement noise n determined from $MSD(\Delta t)$ for these particles. As discussed in the text, the values of L determined from $g(\tau)$ are considered the most reliable here because they rely on the sensitivity of $g(\tau)$ at short times and $MSD(\Delta t)$ at long times (through the diffusion coefficient D).

~ 600 detected photons collected over 120 ms, and our counting rates and diffusion coefficients are comparably to those of fluorescent proteins in a cellular environment.

8.3.1 Statistics of $\hat{D}_{\Delta t}$

We now return to the basic problem of diffusion coefficient estimation, which has already been discussed on a few separate occasions. We will begin by explicitly defining our estimators, because we will also want to know their distributions. During tracking, we measure the coordinates $X(t)$ and $Y(t)$ of a particle by recording the x and y positions of the sample stage. We can form an estimate of the diffusion coefficient along each direction by calculating the variance in the trajectory step size over N time intervals of length Δt , where the choice of N and Δt will determine the statistical accuracy of the estimate as well as the total estimation time $T = N\Delta t$. Let

$$\Delta X_{\Delta t}(k) = X[(k+1)\Delta t] - X[k\Delta t] \quad (8.4)$$

be the change in the particle's position over the k th time interval of length Δt , a slight modification of the earlier definition. $X(t)$, T , Δt , and $\Delta X_{\Delta t}$ are shown for an individual trajectory in Fig. 8.17. With N samples, we may estimate the mean μ

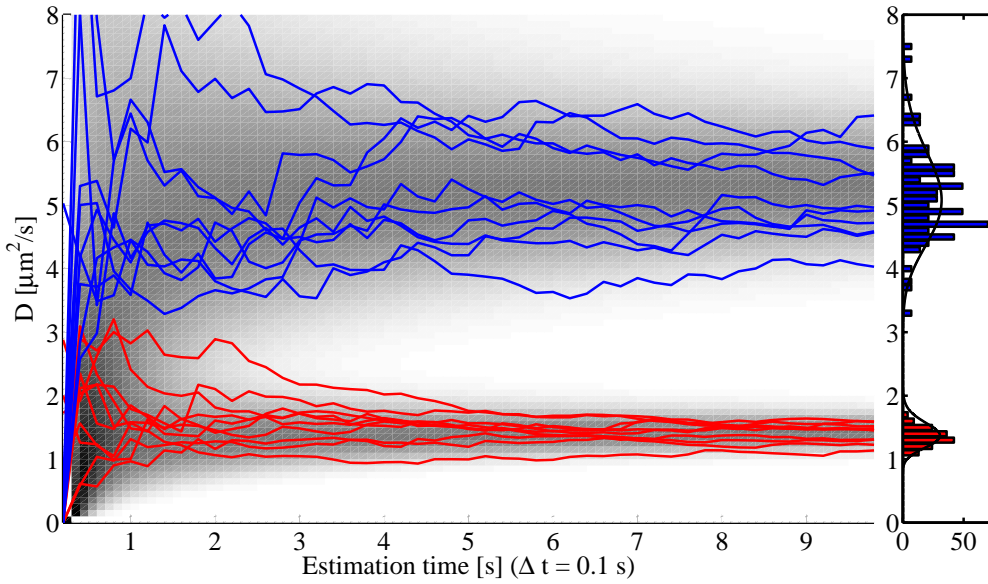


Figure 8.16: Convergence of $\hat{D}_{\Delta t}$ as the number of samples is increased by increasing Δt . Only the first 10 trajectories of fast (60 nm diameter) and slow (210 nm diameter) tracked beads are shown on the left for clarity. Underneath is a colored contour plot of the distribution $p_N(\hat{D}; D)$ given by Eq. (8.9). At the right, the final value of the estimate (at $T = 10$ s) is shown for the entire data set, together with the expected distribution based on χ^2 statistics. The solid curves on the right have only one free parameter, the diffusion coefficient D .

and variance σ^2 of $\Delta X_{\Delta t}$ by

$$\hat{\mu}_{\Delta t}(X) = \frac{1}{N} \sum_{k=1}^N \Delta X_{\Delta t}(k) \quad (8.5a)$$

$$\hat{\sigma}_{\Delta t}^2(X) = \frac{1}{N-1} \sum_{k=1}^N [\Delta X_{\Delta t}(k) - \hat{\mu}_{\Delta t}(X)]^2 \quad (8.5b)$$

and form an unbiased estimator of the diffusion coefficient D with

$$\hat{D}_{\Delta t}(X) = \frac{1}{2\Delta t} \hat{\sigma}_{\Delta t}^2(X). \quad (8.6)$$

The normalization by $N-1$ in $\hat{\sigma}_{\Delta t}^2(X)$ defined by Eq. (8.5) gives an *unbiased* estimate, canceling the contribution to the variance arising from error in the estimated mean [58]. We could have used other prefactors: normalization by N gives the sample vari-

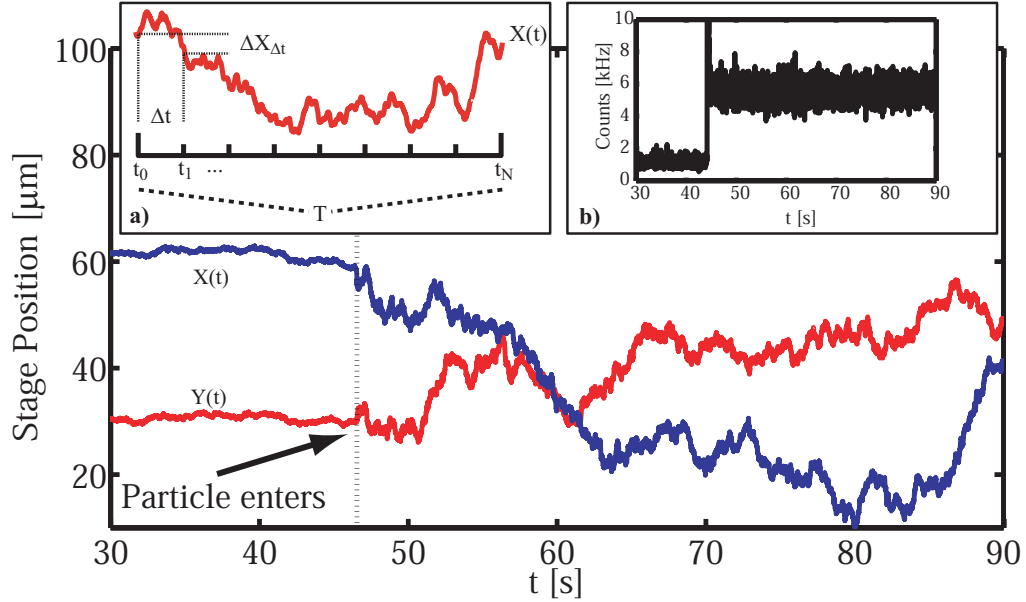


Figure 8.17: Typical trajectory of a single tracked particle. The main plot shows the coordinates $X(t)$ and $Y(t)$ of the sample stage. A particle enters the focus near $t = 47$ s and is tracked for the remainder of the data run. Inset (a) shows a $T = 2$ s portion of $X(t)$, illustrating T , Δt , $\Delta X_{\Delta t}$ and N as used in the text. Inset (b) shows the fluorescence photon count rate during the same trajectory.

ance (as distinct from the variance of the underlying distribution), and normalization by $N + 1$ gives the estimate of the sample variance with the minimum mean-square error. For large N these distinctions become negligible. Estimates of μ , σ^2 and D from two-dimensional data are simply formed by averaging the quantities $\hat{\mu}_{\Delta t}$, $\hat{\sigma}_{\Delta t}^2$, and $\hat{D}_{\Delta t}$ along each Cartesian direction. Whenever we do not include the argument X or Y in these quantities, it is implied that they are calculated in two dimensions. Other estimators of D exhibiting varying convergence rate, bias, and computational complexity may be defined [3, 21], but we have chosen $\hat{D}_{\Delta t}$ specifically for its ease of implementation and consequent potential for future real-time applications.

When the measured trajectories $X(t)$ and $Y(t)$ represent pure Brownian motion with drift velocity v and diffusion coefficient D , the estimators $\hat{\mu}_{\Delta t}$ and $\hat{\sigma}_{\Delta t}^2$ have

expectation values

$$\mathbb{E} [\hat{\mu}_{\Delta t}(X)] = v\Delta t \quad (8.7a)$$

$$\mathbb{E} [\hat{\sigma}_{\Delta t}^2(X)] = 2D\Delta t \quad (8.7b)$$

$$\mathbb{E} [\hat{D}_{\Delta t}(X)] = D \quad (8.7c)$$

with the same results for Y . The last line shows that $\hat{D}_{\Delta t}$ is an *unbiased* estimator of D . In contrast to many of the other quantities we have consider thus far, the estimate $\hat{D}_{\Delta t}$ is *not* a Gaussian random variable, rather its distribution is given by the χ^2 distribution with $N - 1$ degrees of freedom [58]. This is of course a standard fact concerning the distribution of the sample variance of a Gaussian process. The cumulative density (F_N) and probability density (f_N) of the χ^2 distribution, with N degrees of freedom, are given by

$$F_N(x) = \frac{\gamma(N/2, x/2)}{\Gamma(N/2)} \quad (8.8a)$$

$$f_N(x) = \frac{\partial}{\partial x} F_N(x) = \frac{2^{-N/2}}{\Gamma(N/2)} x^{N/2-1} e^{-x/2} \quad (8.8b)$$

where $\Gamma(N)$ and $\gamma(x, N)$ are the gamma function and incomplete gamma function, respectively [59].¹ Define $p_N(\hat{D}; D)$ to be the probability density for our estimate $\hat{D}_{\Delta t}$ to assume the value \hat{D} . Then we find

$$p_N(\hat{D}; D) = \frac{N-1}{D} f_{N-1} \left(\frac{N-1}{D} \hat{D} \right). \quad (8.9)$$

The corresponding cumulative density function $P_N(\hat{D}; D)$ is given by

$$P_N(\hat{D}; D) = \int_0^{\hat{D}} p_N(x; D) dx = F_{N-1} \left(\frac{N-1}{D} \hat{D} \right). \quad (8.10)$$

The distributions $p_N(\hat{D}; D)$ and $P_N(\hat{D}; D)$ depend only on the underlying diffusion

¹Be careful with the incomplete gamma function, because it is defined differently in Matlab, Mathematica, and Abramowitz and Stegun [59], whose definition and notation we use here.

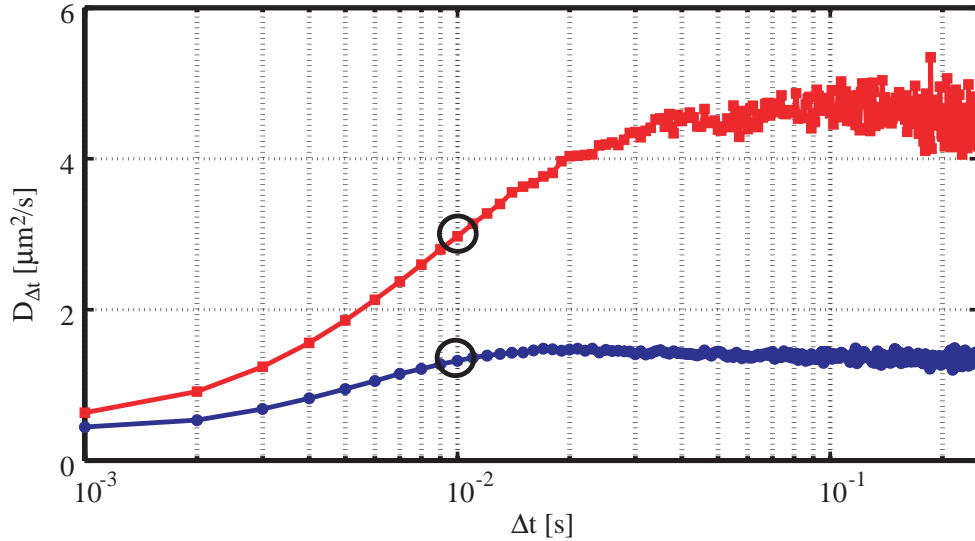


Figure 8.18: Diffusion coefficient estimate $\hat{D}_{\Delta t}$ as Δt is varied over the tracked trajectory of a 60 nm (red squares) and 210 nm (blue circles) diameter fluorescent microsphere. At small Δt , the estimate $\hat{D}_{\Delta t}$ is smaller than the asymptotic value due to the finite tracking bandwidth.

coefficient D and the number of samples N ; they do not depend explicitly on the time interval Δt at which the trajectory is sampled. However, for fixed overall estimation time T , a smaller Δt allows more samples in that interval. Assuming that the measurement interval T is broken up into an integer number of sample times Δt , we have $N = T/\Delta t$.

The value of $\hat{D}_{\Delta t}$ (with T equal to the total tracking time) is shown in Fig. 8.18 as a function of Δt , for a measured trajectory of each type of particle. As detailed in Ch. 5, $\hat{D}_{\Delta t}$ *underestimates* the particle's diffusion coefficient at small Δt due to the finite response bandwidth of the feedback loop. Qualitatively, this effect arises because our piezoelectric stage cannot move sufficiently fast to track the particle's motion at arbitrarily small timescales, and of course this effect is a generic feature of all realistic control systems. For pure (uncontrolled) Brownian motion, the step sizes $\Delta X_{\Delta t}$ obey Gaussian statistics and the estimate $\hat{D}_{\Delta t}$ obeys χ^2 statistics with mean value D [58]. Because our feedback control system is *linear*, $\hat{D}_{\Delta t}$ still obeys χ^2 statistics even for small Δt , albeit with a value of D that is below the asymptotic

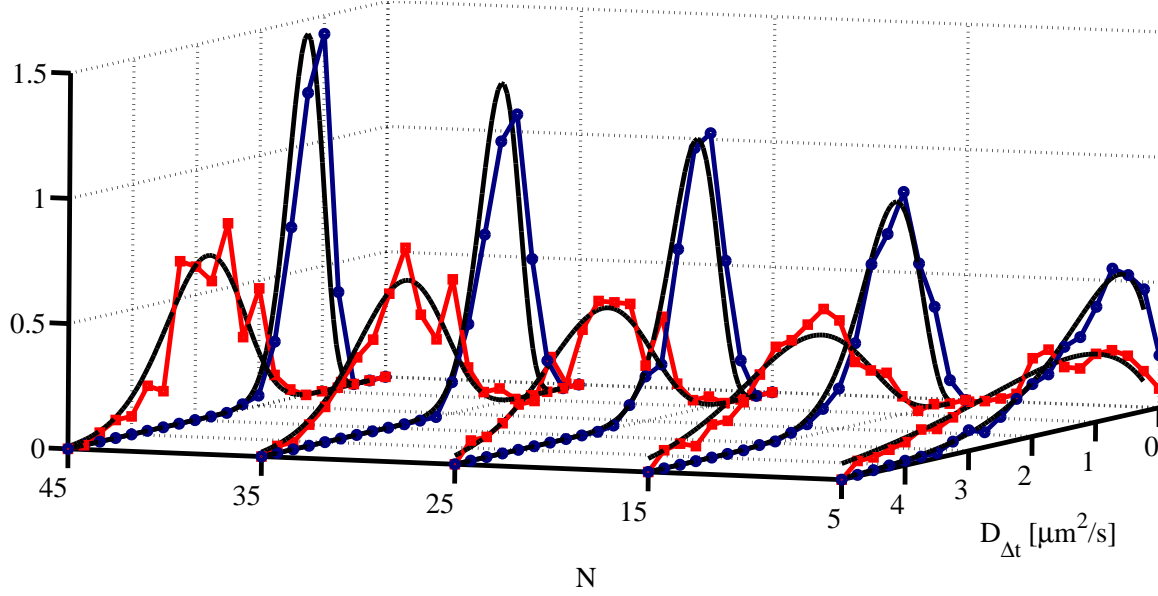


Figure 8.19: Histogram of the estimate $\hat{D}_{\Delta t}$ for $\Delta t = 10$ ms (indicated by dark circles in Fig. 8.18) versus the number of samples N used for the estimate. The solid black curves show the expected distribution $p_N(\hat{D}; D)$ with mean value D set equal to the mean value from each data set.

value. This fact is confirmed in Fig. 8.19, where we show the full distribution of $\hat{D}_{\Delta t}$ for $\Delta t = 10$ ms and varying numbers of samples N .

8.3.2 Hypothesis testing

Now consider a binary mixture of particles, such as the one used for our measurements, consisting of a fraction λ_1 of particles of type 1 (diffusion coefficient D_1) and a fraction $\lambda_2 = 1 - \lambda_1$ of particles of type 2 (diffusion coefficient $D_2 \geq D_1$). We now wish to find a threshold value of the diffusion coefficient D_{th} such that we may assign a particle to class 1 if $\hat{D}_{\Delta t} < D_{th}$ and class 2 for $\hat{D}_{\Delta t} \geq D_{th}$. Let P_{corr} denote the probability that a classification is correct under this thresholding algorithm. For any given threshold value D_{th} , the probability of a correct classification is

$$P_{corr} = \lambda_1 P_N(D_{th}; D_1) + \lambda_2 [1 - P_N(D_{th}; D_2)], \quad (8.11)$$

and straightforward calculation shows that, the value of P_{corr} is maximized by choosing the threshold value

$$D_{th} = D_{th}^* = \frac{D_1 D_2}{D_2 - D_1} \left(\log \frac{D_2}{D_1} + \frac{2}{N-1} \log \frac{\lambda_1}{1-\lambda_1} \right). \quad (8.12)$$

D_{th}^* is a weak function of λ_1 and N for even moderately large N , and if $\lambda_1 = \lambda_2$, *i.e.*, if the particles occur with equal likelihood (or we have no prior knowledge of their distribution), then D_{th}^* does not depend on N at all. D_{th}^* given by Eq. (8.12) may become negative or unbounded, but these limits simply indicate regimes in which the measurement is too noisy to warrant any correction to the prior distribution.

In a more general scenario, particle classification based on a measurement record may be formulated as a problem of *hypothesis testing* [58]. In the binary form of this problem, an m -component measurement is made with result $\boldsymbol{\theta}$, which may represent a single measurement or it a sequence of measurements. The experimenter knows that this measurement results was drawn from one of two distributions, $p_1(\boldsymbol{\theta})$ and $p_2(\boldsymbol{\theta})$ with corresponding probabilities λ_1 and $\lambda_2 = 1 - \lambda_1$, and wishes to decide which of these distributions was most likely to have produced the observed value. Let H_1 represent the hypothesis that the underlying distribution was $p_1(\boldsymbol{\theta})$ and similarly for H_2 . Then we define a test procedure by the following threshold criterion: we accept hypothesis H_1 if $\lambda_1 p_1(\boldsymbol{\theta}) > \lambda_2 p_2(\boldsymbol{\theta})$, and reject it otherwise. A standard theorem states that this test procedure minimizes the probability of an incorrect classification; furthermore, the Neyman-Pearson Lemma states that any other test procedure that *decreases* the probability of incorrectly accepting H_1 necessarily *increases* the probability of incorrectly accepting H_2 [58]. For our specific case of particle classification based on the scalar estimate $\hat{D}_{\Delta t}$, the test described above divides the positive real line into regions corresponding to particles of type 1 ($\hat{D}_{\Delta t} < D_{th}^*$) and type 2 ($\hat{D}_{\Delta t} \geq D_{th}^*$) where D_{th}^* is simply the point where

$$D_{th}^* \quad : \quad \lambda_1 p_N(D_{th}^*; D_1) = \lambda_2 p_N(D_{th}^*; D_2), \quad (8.13)$$

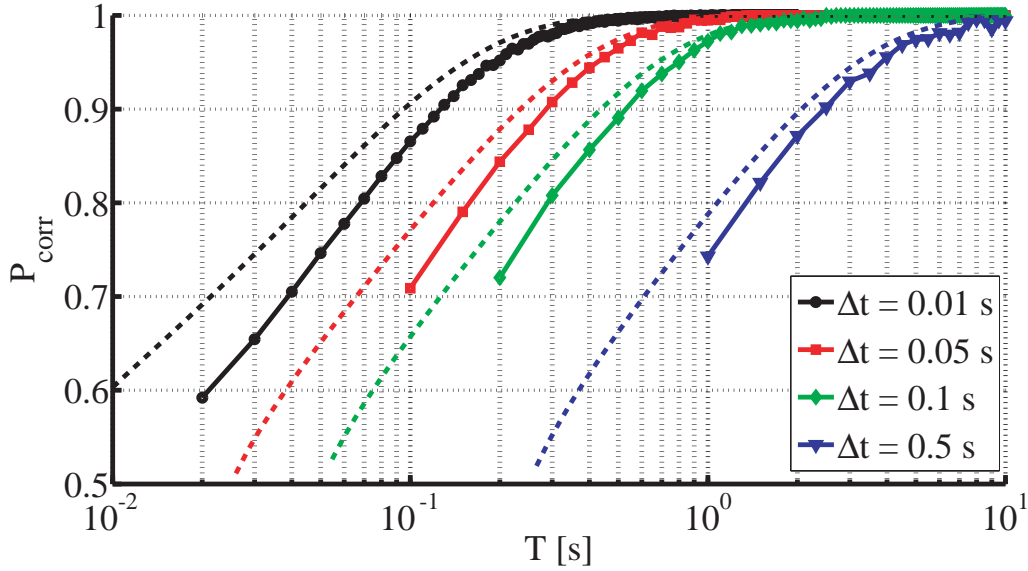


Figure 8.20: Measured probability of correct classification P_{corr} as the estimation time T and the sample time Δt are varied. The dashed curves show the expected success probability from Eq. (8.11).

exactly as defined in Eq. (8.12). This general formulation can be applied to the case of a two-dimensional estimate of diffusion coefficients D_x and D_y along two Cartesian directions, even for the case that these are not identically distributed, *i.e.*, the diffusion is not isotropic. In that case, the measurement vector $\boldsymbol{\theta} = [\hat{D}_{\Delta t}(X), \hat{D}_{\Delta t}(Y)]$ lies in a D_x - D_y plane, and the threshold criterion is a *line* dividing the plane into regions corresponding to each type of particle. For higher-dimensional measurement vectors, the hypothesis testing criterion is a surface partitioning the measurement space into regions corresponding to H_1 and H_2 .

8.3.3 Results

We implemented the above classification procedure on the first 48 individual tracking trajectories from our data set, with various values of T , Δt and N . We usually form our estimate using short segments of very long trajectories, so we may confirm whether a particular estimate based on a sample of length T correctly identified a particle by comparing it to a high-fidelity identification using data from the entire trajectory. In this way, we retain the ability to calculate the success probability, P_{corr} .

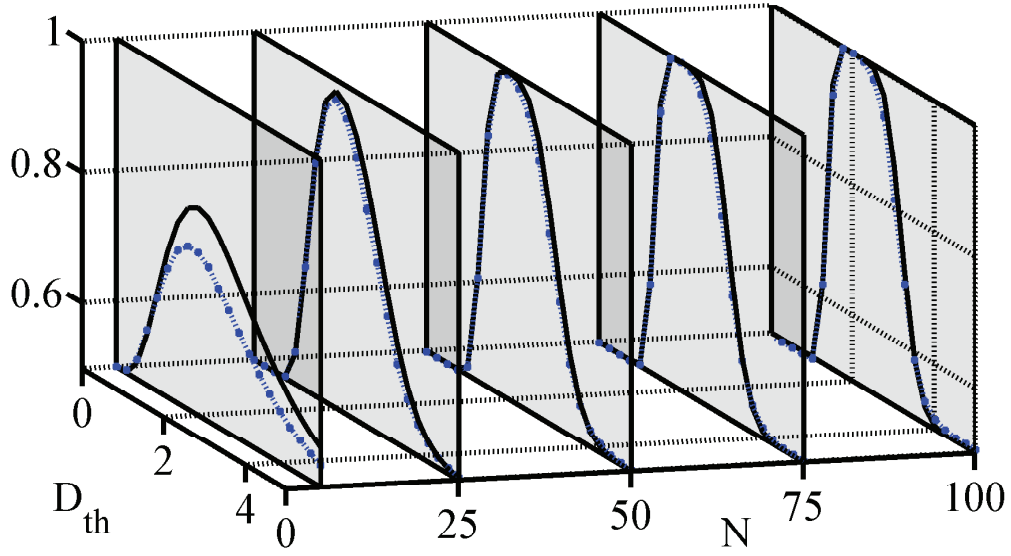


Figure 8.21: P_{corr} for $\Delta t = 10$ ms as the threshold D_{th} and number of samples N are varied. The observed values are shown as blue circles while the solid lines is the expected value based on Eq. (8.11). From the figure, we find that the derived value of D_{th}^* that maximizes P_{corr} also maximizes the observed classification success probability.

The results are shown in Fig. 8.20. At fixed estimation time T , P_{corr} strictly increases with decreasing Δt down to about 10 ms. At shorter times, our particles move (on average) only 250–500 nm, comparable to the localization values L determined in Sect. 8.2, and we are no longer able to make fast determinations of position with the accuracy required to form a good estimate $\hat{D}_{\Delta t}$.

At $T = 60$ ms we collect only (on average) 275 fluorescence photons but still identify particles with >75% success; over this interval the larger 210 nm particles move on average only 600 nm, while the smaller 60 nm particles move only 1150 nm. When the observation time is doubled to $T = 120$ ms, the success rate reaches 90%. At $T = 1$ s, the success rate is >99% and even the faster (60 nm) particles move less than $5 \mu\text{m}$. We emphasize that these success rates are essentially limited by the tracking error and feedback bandwidth, which are in turn nearly limited by photon counting shot noise as shown in Sect. 8.2.

Although we derived the optimal value of the threshold D_{th}^* for particle classification, we may still test the optimality of this threshold in our data. In Fig. 8.21, we

show the probability of a correct classification P_{corr} given by Eq. (8.11) with $\Delta t = 10$ ms, as N and D_{th} is varied. The figure shows that even for small N where the observed value of P_{corr} falls away from the expected value, the optimum classification threshold remains very near D_{th}^* .

Note that since individual particles are tracked for times much longer than are required for accurate characterization, our method could be used to detect real-time *changes* in the diffusive behavior of an individual particle caused, *e.g.*, by binding events or conformational switching in the case of a single biomolecule.

8.4 Summary and commentary

Throughout this chapter, we drew on the theoretical apparatus developed in Chs. 2-5 to demonstrate the full quantitative capability of closed-loop particle tracking for localizing and monitoring fluorescent Brownian particles. Our purpose has been not only to demonstrate the experimental capability for such feedback-assisted control, but also to give a unified description of the apparatus in the most natural language, that of linear stochastic control theory. We have now shown that such an analysis can describe and predict the response of the apparatus in terms of the transfer functions of its components and the inferred or derived measurement noise. We understand the fluctuations in a particle's fluorescence in terms of the competition between free diffusion and tracking control; we have demonstrated the nearly optimal localization of particles by analyzing the controller response and also examining the fluorescence fluctuations. Finally, we applied many of these methods to the task of performing real-time particle classification with high fidelity based on very few photons collected over small spatial scales that should carry over with direct applicability to experiments involving single quantum dots or fluorescent biomolecules.

The future of this project offers interesting and exciting prospects both for technical and scientific development. The results presented throughout this thesis fully characterize the tracking system, with the theoretical apparatus in no way restricted to the measured two-dimensional tracking results. Our surprising capability to track

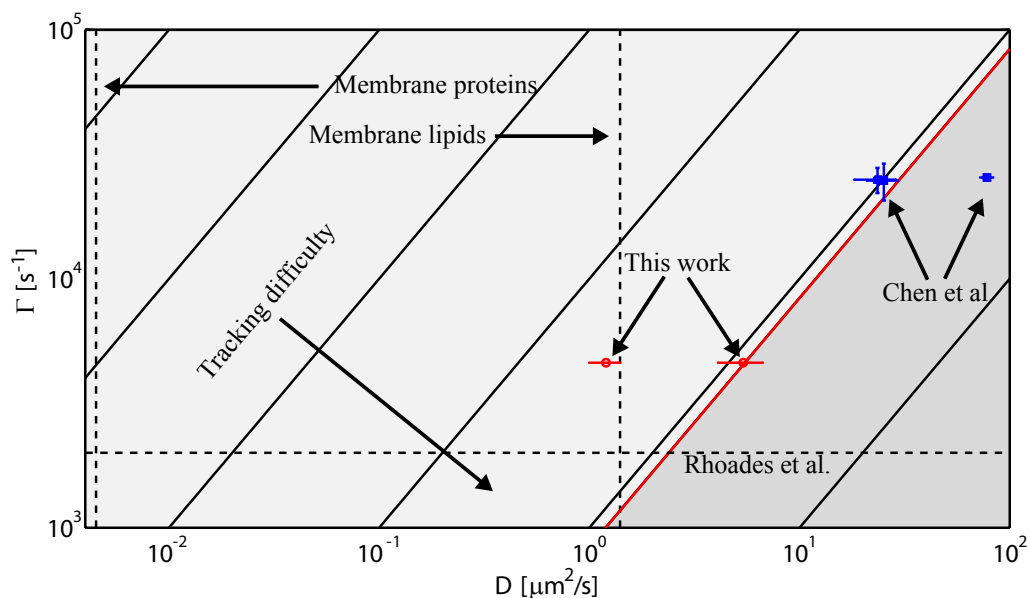


Figure 8.22: Plot of the D - Γ parameter space for values relevant to single-molecule biophysics; contours of constant “trackability” $D/(\Gamma w^2)$, with w fixed, are shown as solid black lines. D and Γ for EGFP (a fluorescent protein) in the cellular cytoplasm, nucleus, and free in solution (blue squares, from left to right respectively) were taken from Chen *et al.* [60]; the brightness of individual vesicle-immobilized, FRET-labeled adenylate kinase molecules, shown as a horizontal line labeled by “Rhoades *et al.*,” was taken from Ref. [61]; approximate diffusion coefficients for lipids and proteins integrated into a cell membrane are shown as dashed vertical lines, taken from Ref. [62]. The results from this chapter are shown as red circles, and the lighter shaded area represents the region of parameter space where single-molecule tracking presents no technical challenge beyond the results in this thesis.

the two-dimensional motion of fast moving particles at fluorescent count rates as low as 5 kHz with tracking errors approaching the photon counting shot-noise limit, gives me great confidence that these techniques can reach a very exciting target in the near future: we can extend the tracking into three dimensions, with the straightforward addition of a third axis of fluorescence modulation and tracking control, and track a single fluorescent protein molecule in free solution. The feasibility of this goal can be investigated using the general tracking considerations in Ch. 4. In that chapter, we saw that fundamental noise processes limit the “trackability” of a particle with diffusion coefficient D and fluorescent count rate Γ in a Gaussian laser with beam waist w . The difficulty of tracking a particle can be encapsulated in the dimensionless

parameter $D/(\Gamma w^2)$, meaning brighter or, equivalently, slower-moving particles are easier to track than dim, fast ones (at fixed w).

In Fig. 8.22, the diffusion coefficient D is plotted versus the fluorescent count rate Γ for our results, and some important regions of the parameters space relevant to single-molecule biophysics are indicated as well. We see from the figure that our results are already consistent with the technical requirements for tracking individual EGFP proteins in a cellular environment. Furthermore, an increase of our beam waist by a factor of 2 (to $w \approx 2 \mu\text{m}$) should bring EGFP in free solution (the blue point in the upper right of Fig. 8.22) into our accessible parameter regime, with a corresponding loss of spatial resolution. In order to reach these goals, we must move to three-dimensional tracking in order to remove the final “perturbative” aspect of our experiment, the nearby glass cover-slips. Such a move into three-dimensions is already in progress; it requires the addition of a third axis for spatially modulating the excitation laser along with a third piezo-electric stage and controller. The achievement of our protein-tracking benchmark will complete the technical development of the closed-loop particle tracking microscope and open an era of single-molecule fluorescence spectroscopy in which the noise sources discussed in Ch. 1 will be suppressed to the maximum extent allowed by fundamental processes such as photon counting statistics and Brownian motion.

Appendix A

Closed-Loop Correlation Spectroscopy with Internal State Transitions

In chapter 5, we developed a theory to describe the fluctuations in a tracked (or trapped) particle's fluorescence arising from deterministic laser motion and partially controlled transverse diffusion, and in Chs. 6-8 we saw that the theory agrees quite well with experiment. It is the aim of this appendix to extend that theory to include linearized chemical reaction kinetics, in a manner analogous to the original theory of (open-loop) FCS [6–9]. These reaction kinetics take the form of internal state transitions that affect the diffusion and fluorescence properties of the particle. Some results along these lines have been obtained by Monte Carlo simulation of a similar system in [13].

Unlike the model in Ch. 5, we will not be able to solve the general form of the problem presented here. We will concentrate on the case that the particle has $n = 2$ internal states and the feedback control is first order. We will find some approximate results for the case when dynamical timescales are well separated and an adiabatic elimination procedure is available, and we will find an exact solution for the special case that state transitions do not affect the particle's steady-state diffusion statistics. Finally, we will give a solution in the form of an eigenfunction expansion for the general two-state problem that hides the complexity of the results in infinite-dimensional matrices. There is certainly room for more theoretical development of these ideas,

but until they become relevant to the experiment, that effort may not be warranted.

Special thanks are due to Luc Bouten for many helpful discussions of this topic, including the key insight that the generators of different Ornstein-Uhlenbeck processes do not commute, and this fact is responsible for the substantial increase in complexity over the free-particle case.

A.1 Review of the scalar case and statement of the general problem

Consider a single fluorescent particle whose motion is actively tracked (or trapped) by first-order feedback control. In this appendix, we will not use the matrix notation of Ch. 5, opting instead for an eigenfunction expansion approach to solving our PDEs. Of course, the resulting expressions are identical, but we review this different notation for the simplest (first-order) case here. For feedback control with bandwidth γ , we may represent the (one-dimensional) position of a tracked particle with diffusion coefficient D by a stochastic differential equation:

$$dX_t = -\gamma X_t dt + \sqrt{2D} dW_t \quad (\text{A.1})$$

where X_t is the particle's position at time t and dW_t is a stochastic Wiener increment. Denoting the two-time probability by $P(X_{t+\tau} = x_2 | X_t = x_1) \equiv p_\tau(x_2 | x_1)$, we have

$$p_\tau(x_2 | x_1) = \frac{1}{\sqrt{2\pi\sigma^2(1 - e^{-2\gamma\tau})}} \exp\left[-\frac{(x_2 - x_1 e^{-\gamma\tau})^2}{2\sigma^2(1 - e^{-2\gamma\tau})}\right] \quad (\text{A.2})$$

where $\sigma^2 = D/\gamma$. The stationary solution to Eq. (A.2) is given by

$$p_0(x) = \lim_{\tau \rightarrow \infty} p_\tau(x | x_0) = \frac{1}{\sqrt{2\pi\sigma^2}} \exp\left[-\frac{x^2}{2\sigma^2}\right]. \quad (\text{A.3})$$

The two-time probability function $p_\tau(x_2|x_1)$ is the solution $c(x_2, \tau)$ to the master equation (equivalent to a Fokker-Planck equation in this case, but not below)

$$\left[\frac{\partial}{\partial t} - D \frac{\partial^2}{\partial x^2} - \gamma \frac{\partial}{\partial x} x \right] c(x, t) = 0 \quad (\text{A.4})$$

with the initial condition $c(x, 0) = \delta(x - x_1)$.

When a particle whose motion is governed by Eq. (A.1) is excited at a rate proportional to a time-dependent laser intensity profile given at time t by $\Phi_t(x)$. The stochastic fluorescence signal is given by $s_t = \Phi_t(X_t)$, and the autocorrelation of this signal $G(\tau)$ is given by

$$G(\tau) = \left\langle \iint dx_1 dx_2 p_\tau(x_2|x_1) p_0(x_1) \Phi_{t+\tau}(x_2) \Phi_t(x_1) \right\rangle_t \quad (\text{A.5})$$

where the angle brackets denote averaging over the initial time t . In three dimensions, the statistics of a particle's vector-valued position $\mathbf{r} = (x, y, z)$ along different Cartesian directions is uncorrelated, so that $p_\tau(\mathbf{r}_2|\mathbf{r}_1) = p_\tau^{(x)}(x_2|x_1) p_\tau^{(y)}(y_2|y_1) p_\tau^{(z)}(z_2|z_1)$. The full fluorescence correlation function is given in this case by

$$G(\tau) = \left\langle \iiint d^3\mathbf{r}_1 d^3\mathbf{r}_2 p_\tau(\mathbf{r}_2|\mathbf{r}_1) p_0(\mathbf{r}_1) \Phi_{t+\tau}(\mathbf{r}_2) \Phi_t(\mathbf{r}_1) \right\rangle_t. \quad (\text{A.6})$$

Let us now turn to a much more general case. Consider a particle with n internal states, with state j contributing a normalized fluorescence intensity θ_j . That is, if the particle is in state j at position X_t at time t , then the rate of fluorescence in an excitation profile $\Phi_t(x)$ is given by $s_t = \theta_j \Phi_t(X_t)$. The probability that the particle is in state j and at position x at time t will be denoted by $c_j(x, t)$, so that the (ensemble) average fluorescence signal at time t is given by

$$\mathbb{E}[s_t] = \sum_{j=1}^n \int \theta_j c_j(x, t) \Phi_t(x) dx = \int \boldsymbol{\theta}^T \mathbf{c}(x, t) \Phi_t(x) dx \quad (\text{A.7})$$

where $\mathbf{c}(x, t)$ is a column vector whose j th component is $c_j(x, t)$ and similarly for $\boldsymbol{\theta}$. Now suppose that a particle in state j has a diffusion coefficient D_j and feels a

trapping force (or equivalently, a tracking bandwidth) characterized by γ_j . Suppose also that the rate of transitions from state k into state j is a constant given by λ_{jk} . Then the master equation governing the probability vector $\mathbf{c}(x, t)$ is

$$\left[\frac{\partial}{\partial t} - \begin{pmatrix} \mathbb{F}_1 & \cdots & 0 \\ \vdots & \ddots & \vdots \\ 0 & \cdots & \mathbb{F}_n \end{pmatrix} - \mathbf{\Lambda} \right] \mathbf{c}(x, t) = 0 \quad (\text{A.8})$$

where

$$\mathbb{F}_j = D_j \frac{\partial^2}{\partial x^2} + \gamma_j \frac{\partial}{\partial x} \quad (\text{A.9})$$

is the (scalar) Ornstein-Uhlenbeck diffusion operator for state j and the matrix $\mathbf{\Lambda}$ satisfies

$$\Lambda_{jk} = \lambda_{jk} \quad , \quad j \neq k \quad (\text{A.10a})$$

$$\Lambda_{kk} = - \sum_{j \neq k} \lambda_{jk}. \quad (\text{A.10b})$$

Van Kampen [36] refers to Eq. (A.8) as governing a ‘‘composite Markov process,’’ and gives a formal solution to the problem in terms of an inverse Laplace transform. His solution is valid, however, only for the case where all of the diffusion operators commute with each other (as is the case for free diffusion, the example he uses). Unfortunately, the Ornstein-Uhlenbeck operators do not commute in general:

$$[\mathbb{F}_j, \mathbb{F}_k] = \mathbb{F}_j \mathbb{F}_k - \mathbb{F}_k \mathbb{F}_j = 2(D_j \gamma_k - D_k \gamma_j) \frac{\partial^2}{\partial x^2} \neq 0. \quad (\text{A.11})$$

In the n -dimensional case, assuming none of the parameters D_j and γ_j are zero, then all operators commute only if $D_1/\gamma_1 = D_2/\gamma_2 = \cdots = D_n/\gamma_n$; of course, this is exactly the situation where the Ornstein-Uhlenbeck length-scales $\sigma_j^2 = D_j/\gamma_j$ are all equal, so that internal state transitions do not affect the steady-state diffusion statistics. For the remainder of this section, we will be concerned with solutions of Eq. (A.8) and the resulting fluorescence autocorrelation functions for two-state

systems $n = 2$. Note also that the composite Markov process has been proposed as a governing equation for very general processes in biophysics (as an example of an even more general Smoluchowski equation) including DNA and protein folding kinetics [63], and it also arises in financial models of market fluctuations.

A.2 The commuting case $[\mathbb{F}_1, \mathbb{F}_2] = 0$

As mentioned above, the diffusion operators \mathbb{F}_k do not commute in general. However, the special case that they do commute is not too trivial to give interesting and relevant results. Let us now explicitly solve Eq. (A.8) for $n = 2$ assuming that $D_1\gamma_2 = D_2\gamma_1$ which ensures $[\mathbb{F}_1, \mathbb{F}_2] = 0$. We will develop solutions in terms of the eigenfunctions of the diffusion operators defined by

$$F_n^{(k)}(x) \equiv H_n \left(\frac{x}{\sqrt{2}\sigma_k} \right) \exp \left(-\frac{x^2}{2\sigma_k^2} \right) \quad (\text{A.12})$$

satisfying

$$\mathbb{F}_k F_n^{(k)}(x) = -n\gamma_k F_n^{(k)}(x) \quad (\text{A.13})$$

$$\int_{-\infty}^{\infty} F_n^{(k)}(x) F_m^{(k)}(x) dx = \left(n! 2^n \sqrt{2\pi\sigma_k^2} \right) \delta_{mn} \quad (\text{A.14})$$

where δ_{mn} is the Kronecker delta. $H_n(x)$ is the Hermite polynomial of order n [37]. Any square-integrable function $f(x)$, including any spatial probability distribution, may be expanded in the basis of these eigenfunctions

$$f(x) = \sum_{n=0}^{\infty} \alpha_n^{(k)} F_n^{(k)}(x) \quad (\text{A.15})$$

where the expansion coefficients are given by

$$\alpha_n^{(k)} = \frac{1}{\sqrt{2\pi\sigma_k^2}} \frac{2^{-n}}{n!} \int_{-\infty}^{\infty} dx H_n \left(\frac{x}{\sqrt{2}\sigma_k} \right) f(x). \quad (\text{A.16})$$

We can drop the superscript (k) indicating the expansion basis because in this special commuting case, the operators \mathbb{F}_k share an eigenbasis. We now have $\sigma_2^2 = \sigma_1^2 = \sigma^2$, and only one basis of eigenfunctions $\{F_n(x)\}$.

The solution to Eq. (A.8) can now be found by expanding an arbitrary initial state in the eigenfunctions $F_n(x)$ and calculating the time evolution of the n th component directly. Let

$$\mathbf{\Gamma} = \begin{pmatrix} \gamma_1 & 0 \\ 0 & \gamma_2 \end{pmatrix} \quad (\text{A.17})$$

and let the initial state be given by

$$\mathbf{c}(x, 0) = \sum_{n=0}^{\infty} \begin{pmatrix} \alpha_n \\ \beta_n \end{pmatrix} F_n(x). \quad (\text{A.18})$$

Then the state at time t is given by

$$\mathbf{c}(x, t) = \sum_{n=0}^{\infty} \exp [(\mathbf{\Lambda} - n\mathbf{\Gamma}) t] \begin{pmatrix} \alpha_n \\ \beta_n \end{pmatrix} F_n(x) \quad (\text{A.19})$$

where the conditional dependence on the initial conditions has been omitted in the notation. Let us now calculate the full fluorescence autocorrelation function (in one dimension only) for this particle. Let $c_{j_2 j_1}(x_2, t_2 | x_1, t_1)$ be the probability to find the particle at position x_2 in state j_2 at time t_2 , given that it was at position x_1 and in state j_1 at time t_1 . This probability can be calculated using the solution defined in (A.19). Now the full fluorescence autocorrelation function is given by

$$\mathbb{E}[s_{t+\tau} s_t] = \sum_{j_1, j_2} \iint dx_2 dx_1 \Phi_{t+\tau}(x_2) \Phi_t(x_1) \theta_{j_2} \theta_{j_1} c_{j_2, j_1}(x_2, t + \tau | x_1, t) c_{j_1}^{(0)}(x_1) \quad (\text{A.20})$$

where $c_{j_1}^{(0)}(x_1)$ is the j_1 component of the steady state solution. In a Gaussian excitation laser whose centroid follows the (dimensionless) path $x_t/w = \chi_t$, we have

$$\Phi_t(x) = \exp \left[-2 \left(\frac{x}{w} - \chi_t \right)^2 \right]. \quad (\text{A.21})$$

We may plug into Eq. (A.20) and perform the integrals to find

$$\begin{aligned} \mathbb{E}[s_{t+\tau}s_t] &= \frac{\zeta \exp[-2\zeta(\chi_{t+\tau}^2 + \chi_t^2)]}{(\lambda_{12} + \lambda_{21})} \\ &\times \sum_{n=0}^{\infty} \frac{2^{-n}}{n!} H_n(\sqrt{2\zeta}\chi_{t+\tau}) H_n(\sqrt{2\zeta}\chi_t) (1-\zeta)^n \boldsymbol{\theta}^T \exp[(\boldsymbol{\Lambda} - n\boldsymbol{\Gamma})\tau] \begin{pmatrix} \theta_1 \lambda_{12} \\ \theta_2 \lambda_{21} \end{pmatrix} \end{aligned} \quad (\text{A.22})$$

where

$$\zeta = \frac{w^2}{w^2 + 4\sigma^2} = \frac{\gamma\tau_D}{1 + \gamma\tau_D} \quad (\text{A.23})$$

with $\tau_D = w^2/4D$ the usual diffusion time.

Eq. (A.22) is as far as we can go for this case. Note that although we treated the simple commuting case, the kinetic and diffusive contributions to the autocorrelation are still coupled through the matrix exponential. If, in the even simpler case, we have identical diffusion properties in both states, $\gamma_1 = \gamma_2$, which implies also that $D_1 = D_2$ giving a truly trivial case, then the autocorrelation factorizes into a kinetic term

$$\begin{aligned} \mathcal{G}_{\boldsymbol{\Lambda}}(\tau) &= \frac{1}{\lambda_{12} + \lambda_{21}} \boldsymbol{\theta}^T e^{\boldsymbol{\Lambda}\tau} \begin{pmatrix} \theta_1 \lambda_{12} \\ \theta_2 \lambda_{21} \end{pmatrix} \\ &= \left(\frac{\lambda_{12}\theta_1 + \lambda_{21}\theta_2}{\lambda_{12} + \lambda_{21}} \right)^2 + \lambda_{12}\lambda_{21} \left(\frac{\theta_1 - \theta_2}{\lambda_{12} + \lambda_{21}} \right)^2 e^{-(\lambda_{12} + \lambda_{21})\tau} \end{aligned} \quad (\text{A.24})$$

and a diffusive term

$$\begin{aligned} \mathcal{G}_{\mathbb{F}}(\tau; \chi_t) &= \zeta \exp[-2\zeta(\chi_{t+\tau}^2 + \chi_t^2)] \\ &\times \sum_{n=0}^{\infty} \frac{2^{-n}}{n!} H_n(\sqrt{2\zeta}\chi_{t+\tau}) H_n(\sqrt{2\zeta}\chi_t) [(1-\zeta)e^{-\gamma\tau}]^n \\ &= \frac{\zeta}{\sqrt{1-g_\tau^2}} \exp\left[-\frac{2\zeta(\chi_t^2 + \chi_{t+\tau}^2 - 2g_\tau\chi_t\chi_{t+\tau})}{1-g_\tau^2}\right] \end{aligned} \quad (\text{A.25})$$

with

$$g_\tau = (1-\zeta)e^{-\gamma\tau}. \quad (\text{A.26})$$

The summation in Eq. (A.25) has been performed using the identity [64]

$$\exp [-(x^2 + y^2)] \sum_{n=0}^{\infty} \frac{2^{-n}}{n!} H_n(x) H_n(y) z^n = (1 - z^2)^{-1/2} \exp \left[-\frac{x^2 + y^2 - 2xyz}{1 - z^2} \right].$$

In this special case, the two-time autocorrelation is given by

$$\mathbb{E} [s_{t+\tau} s_t] = \mathcal{G}_{\Lambda}(\tau) \mathcal{G}_{\mathbb{F}}(\tau; \chi_t). \quad (\text{A.27})$$

The expression for $\mathcal{G}_{\mathbb{F}}(\tau; \chi_t)$ in Eq. (A.25) is the same one given by Eq. (5.56) for the first-order tracking controller case.

A.3 Adiabatic elimination of fast dynamics

Let us now derive some simple limiting forms of the solution to Eq. (A.8) with $n = 2$ for the case that the transition kinetics and the diffusion dynamics are well separated in time. Our manipulations in this section are not rigorous, rather they follow our intuition closely.

Consider first the case that kinetic transitions occur on a very fast timescale compared to the diffusion dynamics, indicated by $\Lambda \gg \mathbb{F}_k$. At short times, Λ dominates the action of the diffusion operators \mathbb{F}_k , so we have (approximately):

$$\mathbf{c}(x, t) \approx e^{\Lambda t} \mathbf{c}(x, 0). \quad (\text{A.28})$$

At longer times, we may assume the system has relaxed to its kinetic steady state. For this case, we may change to new variables using the unitary matrix

$$\mathbf{U} = \frac{1}{\sqrt{\lambda_{12}^2 + \lambda_{21}^2}} \begin{pmatrix} \lambda_{12} & \lambda_{21} \\ \lambda_{21} & -\lambda_{12} \end{pmatrix} \quad (\text{A.29})$$

satisfying $\mathbf{U} = \mathbf{U}^T = \mathbf{U}^{-1}$. In terms of these new variables

$$\mathbf{U}\mathbf{c}(x, t) \equiv \bar{\mathbf{c}}(x, t) = \begin{pmatrix} \bar{c}_1(x, t) \\ \bar{c}_2(x, t) \end{pmatrix}, \quad (\text{A.30})$$

we have new equations of motion

$$\begin{aligned} \frac{\partial}{\partial t} \bar{\mathbf{c}}(x, t) &= \left[\mathbf{U} \begin{pmatrix} \mathbb{F}_1 & 0 \\ 0 & \mathbb{F}_2 \end{pmatrix} \mathbf{U}^T + \mathbf{U}\boldsymbol{\Lambda}\mathbf{U}^T \right] \bar{\mathbf{c}}(x, t) \\ &= \begin{bmatrix} \frac{\lambda_{12}^2 \mathbb{F}_1 + \lambda_{21}^2 \mathbb{F}_2}{\lambda_{12}^2 + \lambda_{21}^2} & \lambda_{21} - \lambda_{12} + O(\mathbb{F}) \\ \frac{\lambda_{12} \lambda_{21}}{\lambda_{12}^2 + \lambda_{21}^2} (\mathbb{F}_1 - \mathbb{F}_2) & -(\lambda_{12} + \lambda_{21}) + O(\mathbb{F}) \end{bmatrix} \bar{\mathbf{c}}(x, t) \end{aligned} \quad (\text{A.31})$$

where $O(\mathbb{F})$ is a term evolving much more slowly than the others. The second equation represents the fast dynamics, so we may assume that $\bar{c}_2(x, t)$ is in its steady state satisfying

$$\bar{c}_2(x, t) = \left(\frac{1}{\lambda_{21} + \lambda_{12}} \right) \left(\frac{\lambda_{12} \lambda_{21}}{\lambda_{12}^2 + \lambda_{21}^2} \right) (\mathbb{F}_1 - \mathbb{F}_2) \bar{c}_1(x, t). \quad (\text{A.32})$$

Note that the steady-state value of $c_x(x, t)$ is of order $O(\mathbb{F}/\lambda)c_1(x, t)$, so it represents a small correction in the fast kinetics limit. Plugging this steady-state expression for $\bar{c}_2(x, t)$ into the evolution equation for $\bar{c}_1(x, t)$, we find the slower term evolves as

$$\frac{\partial}{\partial t} \bar{c}_1(x, t) = \bar{\mathbb{F}} \bar{c}_1(x, t) \quad (\text{A.33})$$

with

$$\bar{\mathbb{F}} = \bar{D} \frac{\partial^2}{\partial x^2} + \bar{\gamma} \frac{\partial}{\partial x} \quad , \quad \bar{D} = \frac{\lambda_{12} D_1 + \lambda_{21} D_2}{\lambda_{12} + \lambda_{21}} \quad , \quad \bar{\gamma} = \frac{\lambda_{12} \gamma_1 + \lambda_{21} \gamma_2}{\lambda_{12} + \lambda_{21}}. \quad (\text{A.34})$$

The approximate solution $\bar{c}_1(x, t)$ in the fast kinetics limit is given by the Ornstein-Uhlenbeck process of Eq. (A.2) with the average diffusion and damping parameters \bar{D} and $\bar{\gamma}$. Denote by $p_\tau^{(\mathbb{F})}(x_2|x_1)$ the Ornstein-Uhlenbeck two-time probability function of Eq. (A.2) with diffusion and damping parameters taken from the operator \mathbb{F} , and similarly for $p_0^{(\mathbb{F})}(x)$. Then the Green's function $c_{jj_0}(x, t_0 + \tau|x_0, t_0)$ for the probability

to find the particle at time $t_0 + \tau$ in state j at position x , given that it began at time t_0 in state j_0 at position x_0 , is given by (letting \hat{j} be a unit vector representing state j)

$$c_{jj_0}(x, t_0 + \tau | x_0, t_0) \approx \left(\hat{j}^T e^{\Lambda \tau} \hat{j}_0 \right) p_{\tau}^{(\mathbb{F})}(x | x_0) \quad , \quad (\Lambda \gg \mathbb{F}_k). \quad (\text{A.35})$$

The first factor on the right-hand side of Eq. (A.35) dominates at short times and serves to bring the system into kinetic equilibrium. At longer times, the spatial probability evolves according to the kinetic-averaged diffusion term in the second factor. In this fast kinetic case, the kinetic and diffusive terms separate in the fluorescence autocorrelation function defined by Eq. (A.20):

$$\mathbb{E}[s_{t+\tau} s_t] \approx \mathcal{G}_{\Lambda}(\tau) \mathcal{G}_{\mathbb{F}}(\tau; \chi_t) \quad , \quad (\Lambda \gg \mathbb{F}_k). \quad (\text{A.36})$$

The individual terms are defined in Eqs. (A.24)–(A.25), using the average diffusion coefficient \bar{D} and damping rate $\bar{\gamma}$.

We may use similar arguments to find the approximate solution at the other extreme in which the kinetic transitions are much slower than the characteristic diffusion times, $\mathbb{F}_k \gg \Lambda$. An analogous argument shows that a particle initially in state j_0 evolves according to the diffusion operator \mathbb{F}_{j_0} at short times. At long times, the system is always in a mixture of the steady-state solutions, independent of the initial state. We may summarize these with the approximate solution

$$c_{jj_0}(x, t_0 + \tau | x_0, t_0) \approx \hat{j}^T \begin{pmatrix} p_{\tau}^{(\mathbb{F}_1)}(x | x_0) & 0 \\ 0 & p_{\tau}^{(\mathbb{F}_2)}(x | x_0) \end{pmatrix} e^{\Lambda \tau} \hat{j}_0 \quad , \quad (\mathbb{F}_k \gg \Lambda). \quad (\text{A.37})$$

The fluorescence autocorrelation function in this case is given by

$$\begin{aligned} \mathbb{E}[s_{t+\tau} s_t] = & \\ & \frac{\begin{pmatrix} \theta_1 & \theta_2 \end{pmatrix}}{\lambda_{12} + \lambda_{21}} \begin{pmatrix} (e^{\Lambda \tau})_{11} \mathcal{G}_{\mathbb{F}_1 \mathbb{F}_1}(\tau; \chi_t) & (e^{\Lambda \tau})_{12} \mathcal{G}_{\mathbb{F}_1 \mathbb{F}_2}(\tau; \chi_t) \\ (e^{\Lambda \tau})_{21} \mathcal{G}_{\mathbb{F}_2 \mathbb{F}_1}(\tau; \chi_t) & (e^{\Lambda \tau})_{22} \mathcal{G}_{\mathbb{F}_2 \mathbb{F}_2}(\tau; \chi_t) \end{pmatrix} \begin{pmatrix} \theta_1 \lambda_{21} \\ \theta_2 \lambda_{12} \end{pmatrix} \quad , \quad (\mathbb{F}_k \gg \Lambda). \end{aligned} \quad (\text{A.38})$$

The cross terms are given by

$$\mathcal{G}_{\mathbb{F}_j\mathbb{F}_k}(\tau; \chi_t) \equiv \iint dx_2 dx_1 \Phi_{t+\tau}(x_2) \Phi_t(x_1) p_\tau^{(\mathbb{F}_j)}(x_2|x_1) p_0^{(\mathbb{F}_k)}(x_2) \quad (\text{A.39})$$

with $\Phi_t(x)$ given by Eq. (A.21). $(e^{\Lambda\tau})_{jk}$ is the jk entry of the matrix $e^{\Lambda\tau}$. Although they are just given by tractable Gaussian integrals, we do not need to calculate the full expression for the cross terms $\mathcal{G}_{\mathbb{F}_j\mathbb{F}_k}(\tau; \chi_t)$ because Eq. (A.37) was derived for the case that the kinetic transitions are much slower than the diffusion time. In that case, the 2×2 matrix in Eq. (A.37) is diagonal at short times, when $e^{\Lambda\tau} \approx \mathbf{I}$, so we need not calculate the off-diagonal cross terms. At long times, when $e^{\Lambda\tau}$ is no longer diagonal, the diffusion terms have relaxed to their steady states where the cross terms become uncorrelated:

$$\mathcal{G}_{\mathbb{F}_j\mathbb{F}_k}(\tau; \chi_t) \approx \sqrt{\zeta_j \zeta_k} \exp[-2\zeta_j \chi_{t+\tau}^2 - 2\zeta_k \chi_t^2] \quad , \quad (\mathbb{F}_k \gg \Lambda) \quad (\text{A.40})$$

with ζ_j given by Eq. (A.23) with parameters taken from operator \mathbb{F}_j .

A.4 Generalization of van Kampen's method to the noncommuting case

In this section, we will attempt a solution to the full, noncommuting case of Eq. (A.8) with $n = 2$. We will attack the problem using the trajectory averaging approach found in Ref. [36]. However, as mentioned earlier, van Kampen's treatment of this problem is equivalent to our commuting case $[\mathbb{F}_j, \mathbb{F}_k] = 0$ and we have already solved that problem. We therefore require a generalization of that approach to this noncommuting case.

In contrast to earlier sections, we will now expand our solution in eigenfunctions of the two diffusion operators \mathbb{F}_1 and \mathbb{F}_2 , which no longer share an eigenbasis. We will use superscripts to indicate the basis in which a quantity is written. For example, we may represent a function $f(x)$ in the basis of eigenfunctions of \mathbb{F}_k as an infinite-

dimensional column vector $\boldsymbol{\alpha}^{(k)}$ whose n th component is $\alpha_n^{(k)}$:

$$f(x) = \sum_{n=0}^{\infty} \alpha_n^{(k)} F_n^{(k)}(x) \leftrightarrow \boldsymbol{\alpha}^{(k)}. \quad (\text{A.41})$$

We may calculate the infinite dimensional matrix $\mathbf{V}^{(jk)}$ that transforms a vector from basis k to basis j :

$$\boldsymbol{\alpha}^{(j)} = \mathbf{V}^{(jk)} \boldsymbol{\alpha}^{(k)} \iff \alpha_m^{(j)} = \sum_{n=0}^{\infty} V_{mn}^{(jk)} \alpha_n^{(k)}. \quad (\text{A.42})$$

The explicit form of $\mathbf{V}^{(jk)}$ may be found using known properties of the Hermite functions [37]. The nm component of this matrix is 0 wherever $m > n$ and wherever $(m + n)$ is odd (note that the indexing begins at $n = 0, m = 0$). We will refer to such a matrix as ‘‘Even Lower-Triangular’’ or ELT. The only (potentially) non-zero entries are of the form $V_{n+2m,n}^{(jk)}$ with $m = 0, 1, \dots$. These entries are given by

$$V_{n+2m,n}^{(jk)} = \frac{2^{-2m}}{m!} \left(\frac{\sigma_k}{\sigma_j} \right)^{n+1} \left(\frac{\sigma_k^2}{\sigma_j^2} - 1 \right)^m. \quad (\text{A.43})$$

Of course, $\mathbf{V}^{(kj)}$ is the inverse of $\mathbf{V}^{(jk)}$.

We may now calculate the time evolution of a state under the action of the operator \mathbb{F}_k . Suppose the system starts in state k at time $t = 0$ in the spatial distribution $f(x, 0)$ represented by the vector $\boldsymbol{\alpha}^{(k)}(0)$. Then, given that *no internal state transitions occur*, the state at time t is given by

$$f(x, t) = \sum_{n=0}^{\infty} e^{-n\gamma_k t} \alpha_n^{(k)}(0) F_n^{(k)}(x). \quad (\text{A.44})$$

We may represent time evolution under operator \mathbb{F}_k , in the basis of this operator’s eigenfunctions, by a diagonal matrix $\mathbf{T}_{\mathbb{F}_k}^{(k)}(t)$ whose entries are given by

$$\left[\mathbf{T}_{\mathbb{F}_k}^{(k)}(t) \right]_{nn} = \exp(-n\gamma_k t). \quad (\text{A.45})$$

Using the basis change matrices, we may also write the time evolution matrix under operator \mathbb{F}_k in basis j

$$\mathbf{T}_{\mathbb{F}_k}^{(j)}(t) = \mathbf{V}^{(jk)} \mathbf{T}_{\mathbb{F}_k}^{(k)} \mathbf{V}^{(kj)}. \quad (\text{A.46})$$

Note that the operators \mathbf{T} are valid only conditionally; that is, they represent time evolution over macroscopic time intervals given that no internal state transitions occur during the evolution. In order to construct full, unconditional solutions to Eq. (A.8), we must average the time evolution over all possible sequences of state transitions. Suppose that a particle starts in state 1 at time $t = 0$, in a spatial state specified by $\boldsymbol{\alpha}^{(k)}(0)$, and that it undergoes exactly $2N$ transitions after time intervals $\Delta_1, \Delta'_1, \Delta_2, \Delta'_2, \dots, \Delta_N, \Delta'_N$, respectively. For bookkeeping, we define the final interval $\Delta_f = t - \Delta_1 - \Delta'_1 - \dots - \Delta_N - \Delta'_N$. We then know that the (conditional) spatial state of the system at time t is given by

$$\boldsymbol{\alpha}_{cond}^{(k)}(t) = \mathbf{T}_{\mathbb{F}_1}^{(k)}(\Delta_f) \mathbf{T}_{\mathbb{F}_2}^{(k)}(\Delta'_N) \mathbf{T}_{\mathbb{F}_1}^{(k)}(\Delta_N) \cdots \mathbf{T}_{\mathbb{F}_2}^{(k)}(\Delta'_1) \mathbf{T}_{\mathbb{F}_1}^{(k)}(\Delta_1) \boldsymbol{\alpha}^{(k)}(0) \quad (\text{A.47})$$

while an elementary probability argument shows that the probability density for the sequence of transitions to occur after time intervals $\Delta_1, \Delta'_1, \dots, \Delta_N, \Delta'_N, \Delta_f$ (within the macroscopic interval $[0, t]$) is given by

$$e^{-\lambda_{21}\Delta_f} \left(\lambda_{12} e^{-\lambda_{12}\Delta'_N} \right) \left(\lambda_{21} e^{-\lambda_{21}\Delta_N} \right) \cdots \left(\lambda_{12} e^{-\lambda_{12}\Delta'_1} \right) \left(\lambda_{21} e^{-\lambda_{21}\Delta_1} \right). \quad (\text{A.48})$$

Now suppose that the particle starts in internal state 1 in a spatial state given by $\boldsymbol{\alpha}^{(k)}(0|1)$. Then the *unconditional* probability that it is in state 1 and at position x

at time t is given by an average over these sequences

$$\begin{aligned}
\boldsymbol{\alpha}^{(k)}(1, t|1) &= \sum_{N=0}^{\infty} \int \cdots \int d\Delta_f d\Delta'_N d\Delta_N \cdots d\Delta'_1 d\Delta_1 \\
&\times \left\{ \delta(t - \Delta_f - \Delta'_N - \Delta_N - \cdots - \Delta'_1 - \Delta_1) \left[e^{-\lambda_{21}\Delta_f} \mathbf{T}_{\mathbb{F}_1}^{(k)}(\Delta_f) \right] \right. \\
&\times \left[\lambda_{12} e^{-\lambda_{12}\Delta'_N} \mathbf{T}_{\mathbb{F}_2}^{(k)}(\Delta'_N) \right] \left[\lambda_{21} e^{-\lambda_{21}\Delta'_N} \mathbf{T}_{\mathbb{F}_1}^{(k)}(\Delta_N) \right] \cdots \\
&\times \left. \left[\lambda_{12} e^{-\lambda_{12}\Delta'_1} \mathbf{T}_{\mathbb{F}_2}^{(k)}(\Delta'_1) \right] \left[\lambda_{21} e^{-\lambda_{21}\Delta'_1} \mathbf{T}_{\mathbb{F}_1}^{(k)}(\Delta_1) \right] \right\} \boldsymbol{\alpha}^{(k)}(0|1). \quad (\text{A.49})
\end{aligned}$$

We recognize the integrand as a matrix multiconvolution integral, which may be written as a simple matrix product in terms of Laplace transforms. Let $\tilde{\boldsymbol{\alpha}}(s, 1|1)$ denote the Laplace transform of the state vector $\boldsymbol{\alpha}(t, 1|1)$ with respect to t (for vector and matrix arguments, the transform is performed element-wise) and let

$$\mathbf{Q}_{\mathbb{F}_1}^{(k)}(s) = \lambda_{21} \int_0^{\infty} e^{-\Delta s} e^{-\lambda_{21}\Delta} \mathbf{T}_{\mathbb{F}_1}^{(k)}(\Delta) d\Delta \quad (\text{A.50a})$$

$$\mathbf{Q}_{\mathbb{F}_2}^{(k)}(s) = \lambda_{12} \int_0^{\infty} e^{-\Delta s} e^{-\lambda_{12}\Delta} \mathbf{T}_{\mathbb{F}_2}^{(k)}(\Delta) d\Delta. \quad (\text{A.50b})$$

Then we see immediately that

$$\begin{aligned}
\tilde{\boldsymbol{\alpha}}^{(k)}(s, 1|1) &= \frac{1}{\lambda_{21}} \mathbf{Q}_{\mathbb{F}_1}^{(k)}(s) \sum_{N=0}^{\infty} \left[\mathbf{Q}_{\mathbb{F}_2}^{(k)}(s) \mathbf{Q}_{\mathbb{F}_1}^{(k)}(s) \right]^N \boldsymbol{\alpha}^{(k)}(0|1) \\
&= \frac{1}{\lambda_{21}} \mathbf{Q}_{\mathbb{F}_1}^{(k)}(s) \left[\mathbf{I} - \mathbf{Q}_{\mathbb{F}_2}^{(k)}(s) \mathbf{Q}_{\mathbb{F}_1}^{(k)}(s) \right]^{-1} \boldsymbol{\alpha}^{(k)}(0|1). \quad (\text{A.51})
\end{aligned}$$

Note that $\mathbf{Q}_{\mathbb{F}_k}^{(k)}(s)$ is diagonal with

$$\left[\mathbf{Q}_{\mathbb{F}_1}^{(1)}(s) \right]_{nn} = \frac{1}{s + \lambda_{21} + n\gamma_1} \quad (\text{A.52})$$

and similarly for state 2. Furthermore, $\mathbf{Q}_{\mathbb{F}_j}^{(k)}(s) = \mathbf{V}^{(kj)} \mathbf{Q}_{\mathbb{F}_j}^{(j)}(s) \mathbf{V}^{(jk)}$. Finally, note that $\tilde{\boldsymbol{\alpha}}^{(k)}(s, 1|1)$ is the Laplace transform of the state vector representing the spatial probability of finding the particle at position x at time t and in state 1, given that it started in state 1 at time $t = 0$. Now let $\boldsymbol{\alpha}^{(j_2)}(s, j_2|j_1)$ denote the corresponding

probability to find the particle in state j_2 at time t given that it began in internal state j_1 and spatial state $\boldsymbol{\alpha}^{(j_1)}(0|j_1)$, and let $\tilde{\mathbf{R}}_{j_2 j_1}^{(j_2 j_1)}(s)$ be the operator relating these vectors:

$$\boldsymbol{\alpha}^{(j_2)}(s, j_2|j_1) = \tilde{\mathbf{R}}_{j_2 j_1}^{(j_2 j_1)}(s) \boldsymbol{\alpha}^{(j_1)}(0|j_1). \quad (\text{A.53})$$

Note that we have written the components of the initial and final states in their natural bases (*i.e.* the j_1 component of the initial state is written in basis j_1). There are four allowable pairs of values for j_1 and j_2 , and analogous arguments to those given above show that the probability densities for each case are given by

$$\tilde{\mathbf{R}}_{11}^{(11)}(s) = \frac{1}{\lambda_{21}} \mathbf{Q}_{\mathbb{F}_1}^{(1)}(s) \left[\mathbf{I} - \mathbf{Q}_{\mathbb{F}_2}^{(1)}(s) \mathbf{Q}_{\mathbb{F}_1}^{(1)}(s) \right]^{-1} \quad (\text{A.54a})$$

$$\tilde{\mathbf{R}}_{21}^{(21)}(s) = \frac{1}{\lambda_{12}} \mathbf{V}^{(21)} \mathbf{Q}_{\mathbb{F}_2}^{(1)}(s) \left[\mathbf{I} - \mathbf{Q}_{\mathbb{F}_1}^{(1)}(s) \mathbf{Q}_{\mathbb{F}_2}^{(1)}(s) \right]^{-1} \mathbf{Q}_{\mathbb{F}_1}^{(1)}(s) \quad (\text{A.54b})$$

$$\tilde{\mathbf{R}}_{12}^{(12)}(s) = \frac{1}{\lambda_{21}} \mathbf{V}^{(12)} \mathbf{Q}_{\mathbb{F}_1}^{(2)}(s) \left[\mathbf{I} - \mathbf{Q}_{\mathbb{F}_2}^{(2)}(s) \mathbf{Q}_{\mathbb{F}_1}^{(2)}(s) \right]^{-1} \mathbf{Q}_{\mathbb{F}_2}^{(2)}(s) \quad (\text{A.54c})$$

$$\tilde{\mathbf{R}}_{22}^{(22)}(s) = \frac{1}{\lambda_{12}} \mathbf{Q}_{\mathbb{F}_2}^{(2)}(s) \left[\mathbf{I} - \mathbf{Q}_{\mathbb{F}_1}^{(2)}(s) \mathbf{Q}_{\mathbb{F}_2}^{(2)}(s) \right]^{-1}. \quad (\text{A.54d})$$

Let us summarize these results using the following notation. Suppose that the system starts in the state

$$\mathbf{c}(x, 0) = \sum_{n=0}^{\infty} \begin{pmatrix} \alpha_n^{(1)}(0) F_n^{(1)}(x) \\ \beta_n^{(2)}(0) F_n^{(2)}(x) \end{pmatrix} \leftrightarrow \begin{pmatrix} \boldsymbol{\alpha}^{(1)}(0) \\ \boldsymbol{\beta}^{(2)}(0) \end{pmatrix} \quad (\text{A.55})$$

where the vector on the right is doubly infinite, and should only be thought of as a shorthand notation for writing both (infinite) vectors. Denoting the solution at time t by

$$\mathbf{c}(x, t) = \sum_{n=0}^{\infty} \begin{pmatrix} \alpha_n^{(1)}(t) F_n^{(1)}(x) \\ \beta_n^{(2)}(t) F_n^{(2)}(x) \end{pmatrix} \leftrightarrow \begin{pmatrix} \boldsymbol{\alpha}^{(1)}(t) \\ \boldsymbol{\beta}^{(2)}(t) \end{pmatrix}, \quad (\text{A.56})$$

we may summarize the full solution computed above by

$$\begin{pmatrix} \boldsymbol{\alpha}^{(1)}(t) \\ \boldsymbol{\beta}^{(2)}(t) \end{pmatrix} = \begin{pmatrix} \mathbf{R}_{11}^{(11)}(t) & \mathbf{R}_{12}^{(12)}(t) \\ \mathbf{R}_{21}^{(21)}(t) & \mathbf{R}_{22}^{(22)}(t) \end{pmatrix} \begin{pmatrix} \boldsymbol{\alpha}^{(1)}(0) \\ \boldsymbol{\beta}^{(2)}(0) \end{pmatrix}. \quad (\text{A.57})$$

In principle, at least, we have given an explicit solution to the full noncommuting problem to an arbitrary order in terms of its Laplace transform. Although Eqs. (A.54a-A.54b) represent infinite-dimensional matrix multiplication and inversion, we may still make a bit more analytical progress in many cases. It is straightforward to show that products and inverses of ELT matrices are themselves ELT matrices, so that $\tilde{\mathbf{R}}_{j_1 j_2}^{(j_1 j_2)}(s)$ is an ELT matrix. Furthermore, ELT matrix inverses have the special property that the upper-left $N \times N$ block of the inverse of an ELT matrix is exactly the inverse of the upper-left $N \times N$ block. A similar relation holds for ELT matrix sums and products. Therefore, we may calculate *finite-order* matrix elements of $\tilde{\mathbf{R}}_{j_1 j_2}^{(j_1 j_2)}(s)$ by manipulating truncations of $\mathbf{Q}_{\mathbb{F}_j}^{(k)}(s)$ at the same order. In other words, if the system begins in a state that can be approximated by a finite truncation of the eigenfunction expansion, then its time evolution will remain inside that truncated subsystem. As a result of this nice subsystem decoupling, in principle at least, we can explicitly calculate the matrix elements of $\tilde{\mathbf{R}}_{j_1 j_2}^{(j_1 j_2)}(s)$ to any order. In practice this is quite cumbersome, of course.

References

- [1] A. J. Berglund, A. C. Doherty, and H. Mabuchi. Photon statistics and dynamics of Fluorescence Resonance Energy Transfer. *Phys. Rev. Lett.*, 89:068101, 2002.
- [2] A. J. Berglund and H. Mabuchi. Feedback controller design for tracking a single fluorescent molecule. *Appl. Phys. B*, 78:653–659, 2004.
- [3] K. McHale, A. J. Berglund, and H. Mabuchi. Bayesian estimation for species identification in single-molecule fluorescence microscopy. *Biophys. J.*, 86:3409–3422, 2004.
- [4] A. J. Berglund. Nonexponential statistics of fluorescence photobleaching. *J. Chem. Phys.*, 121:2899–2903, 2004.
- [5] S. Weiss. Fluorescence spectroscopy of single biomolecules. *Science*, 283:1676–1683, 1999.
- [6] D. Magde, E. L. Elson, and W. W. Webb. Thermodynamic fluctuations in a reacting system - measurement by fluorescence correlation spectroscopy. *Phys. Rev. Lett.*, 29:705–708, 1972.
- [7] E. L. Elson and D. Magde. Fluorescence correlation spectroscopy. 1. Conceptual basis and theory. *Biopolymers*, 13:1–27, 1974.
- [8] D. Magde, E. L. Elson, and W. W. Webb. Fluorescence correlation spectroscopy. 2. Experimental realization. *Biopolymers*, 13:29–61, 1974.
- [9] O. Krichevsky and G. Bonnett. Fluorescence correlation spectroscopy: The technique and its applications. *Rep. Prog. Phys.*, 65:251–297, 2002.

- [10] H. C. Berg. How to track bacteria. *Rev. Sci. Instr.*, 42:868–871, 1971.
- [11] T. Ha, D. S. Chemla, Th. Enderle, and S. Weiss. Single molecule spectroscopy with automated positioning. *Appl. Phys. Lett.*, 70:782–784, 1997.
- [12] J. Enderlein. Tracking of fluorescent molecules diffusing within membranes. *Appl. Phys. B*, 71:773–777, 2000.
- [13] J. Enderlein. Positional and temporal accuracy of single molecule tracking. *Sing. Mol.*, 1:225–230, 2000.
- [14] S. B. Andersson. Tracking a single fluorescent molecule in a confocal microscope. *Appl. Phys. B*, 80:809–816, 2005.
- [15] R. S. Decca, C.-W. Lee, and S. R. Wassall. Single molecule tracking scheme using a near-field scanning optical microscope. *Rev. Sci. Instr.*, 73:2675–2679, 2002.
- [16] V. Levi, Q. Ruan, K. Kis-Petikova, and E. Gratton. Scanning FCS, a novel method for three-dimensional particle tracking. *Biochem. Soc. Trans.*, 31:997–1000, 2003.
- [17] K. Kis-Petikova and E. Gratton. Distance measurement by circular scanning of the excitation beam in a two-photon microscope. *Microsc. Res. Tech.*, 63:34–49, 2004.
- [18] V. Levi, V. Ruan, and E. Gratton. 3-D particle tracking in a two-photon microscope. Application to the study of molecular dynamics in cells. *Biophys. J.*, 88:2919–2928, 2005.
- [19] V. Levi, V. Ruan, Matthew Plutz, A. S. Belmont, and E. Gratton. Chromatin Dynamics in Interphase Cells Revealed by Tracking in a Two-Photon Excitation Microscope. *Biophys. J.*, 89:4275–4285, 2005.

- [20] H. Cang, C. M. Wong, C. S. Xu, A. H. Rizvi, and H. Yang. Confocal three dimensional tracking of a single nanoparticle with concurrent spectroscopic readout. *Appl. Phys. Lett.*, 88:223901, 2006.
- [21] D. Montiel, H. Cang, and H. Yang. Quantitative characterization of changes in dynamical behavior for single-particle tracking studies. To appear in *J. Phys. Chem. B*, 2006.
- [22] A. E. Cohen and W. E. Moerner. Method for trapping and manipulating nanoscale objects in solution. *Appl. Phys. Lett.*, 86:093109, 2005.
- [23] A. E. Cohen. Control of nanoparticles with arbitrary two-dimensional force fields. *Phys. Rev. Lett.*, 94:118102, 2005.
- [24] A. E. Cohen and W. E. Moerner. Suppressing Brownian motion of individual biomolecules in solution. *Proc. Natl. Acad. Sci. USA*, 103:4362–4365, 2006.
- [25] A. J. Berglund and H. Mabuchi. Tracking-FCS: Fluorescence Correlation Spectroscopy of individual particles. *Opt. Express*, 13:8069–8082, 2005.
- [26] A. J. Berglund and H. Mabuchi. Performance bounds on single-particle tracking by fluorescence modulation. *Appl. Phys. B*, 83:127–133, 2006.
- [27] A. J. Berglund, K. McHale, and H. Mabuchi. Feedback localization of freely diffusing fluorescent particles near the optical shot-noise limit. To appear in *Opt. Lett.*, 2006.
- [28] A. J. Berglund, K. McHale, and H. Mabuchi. Fast classification of freely-diffusing fluorescent nanoparticles. *In preparation*, 2006.
- [29] K. McHale, A. J. Berglund, and H. Mabuchi. Near-optimal dilute concentration estimation via single-molecule detection. *In preparation*, 2006.
- [30] O. L. R. Jacobs. *Introduction to Control Theory*. Oxford University Press, New York, 2nd edition, 1996.

- [31] C. W. Gardiner. *Handbook of Stochastic Methods for Physics, Chemistry and the Natural Sciences*. Springer-Verlag, New York, 2nd edition, 1985.
- [32] R. S. Lipster and A. N. Shiryaev. *Statistics of Random Processes I*. Springer, New York, 2001.
- [33] P. E. Kloeden, E. Platen, and H. Shurz. *Numerical Solution of SDE Through Computer Experiments*. Springer, New York, 1997.
- [34] K. Zhou, J. C. Doyle, and K. Glover. *Robust and Optimal Control*. Prentice Hall, 1996.
- [35] J. Doyle, B. Francis, and A. Tannenbaum. *Feedback Control Theory*. Macmillan Publishing Co., 1990.
- [36] N. G. Van Kampen. *Stochastic processes in physics and chemistry*. Elsevier Science Pub. Co., North-Holland, Amsterdam, 2001.
- [37] I. S. Gradshteyn and I. M. Ryzhik. *Table of Integrals, Series and Products*. Academic press, San Diego, 6th edition, 1980.
- [38] C. W. Gardiner and A. Eschmann. Master-equation theory of semiconductor lasers. *Phys. Rev. A*, 51:4982–4995, 1995.
- [39] A. Yildiz, J. N. Forkey, S. A. McKinney, T. Ha, Y. E. Goodman, and Paul R. Selvin. Myosin V walks hand-over-hand: Single fluorophore imaging with 1.5-nm localization. *Science*, 300:2061–2065, 2003.
- [40] H. Risken. *The Fokker-Planck Equation: Methods of Solution and Applications*. Springer, 2nd edition, 1989.
- [41] S. Saffarian and E. L. Elson. Statistical analysis of Fluorescence Correlation Spectroscopy: The standard deviation and bias. *Biophys. J.*, 84:2030–2042, 2003.

- [42] T. Meyer and H. Schindler. Simultaneous measurement of aggregation and diffusion of molecules in solutions and in membranes. *Biophys. J.*, 54:983–993, 1988.
- [43] M. A. Digman, C. M. Brown, P. Sengupta, P. W. Wiseman, A. R. Horwitz, and E. Gratton. Measuring fast dynamics in solutions and cells with a laser scanning microscope. *Biophys. J.*, 90:1317–1327, 2005.
- [44] L. L. Smith and P. M. Koch. Use of four mirrors to rotate linear polarization but preserve input-output collinearity. *J. Opt. Soc. Am. A*, 13:2102–2105, 1996.
- [45] E. J. Galvez and P. M. Koch. Use of four mirrors to rotate linear polarization but preserve input-output collinearity. ii. *J. Opt. Soc. Am. A*, 14:3410–3414, 1997.
- [46] E. Wolf. Electromagnetic diffraction in optical systems. I. An integral representation of the image field. *Proc. Roy. Soc. London*, 253:349–357, 1959.
- [47] M. Mansuripur. Distribution of light at and near the focus of high-numerical-aperture objectives. *J. Opt. Soc. Am. A*, 3:2086–2094, 1986.
- [48] M. Mansuripur. Certain computational aspects of vector diffraction problems. *J. Opt. Soc. Am. A*, 6:786–805, 1989.
- [49] M. Mansuripur. Effects of high-numerical-aperture focusing on the state of polarization in optical and magneto-optic data storage systems. *Appl. Opt.*, 30:3154–3162, 1991.
- [50] L. Novotny, R. D. Grover, and K. Karrai. Reflected image of a strongly focused spot. *Opt. Lett.*, 26:789–791, 2001.
- [51] M. Doi and S. F. Edwards. *The Theory of Polymer Dynamics*. Oxford University Press, Oxford, 1986.
- [52] A. Gennerich and D. Schild. Fluorescence correlation spectroscopy in small cytosolic compartments depends critically on the diffusion model used. *Biophys. J.*, 79:3294–3306, 2000.

- [53] L. P. Faucheux and A. J. Libchaber. Confined Brownian motion. *Phys. Rev. E*, 49:5158–5163, 1994.
- [54] B. Lin, J. Yu, and S. A. Rice. Direct measurements of constrained Brownian motion of an isolated sphere between two walls. *Phys. Rev. E*, 62:3909–3919, 2000.
- [55] K. Schätzel, M. Drewel, and S. Stimac. Photon correlation measurements at large lag times: Improving statistical accuracy. *J. Mod. Opt.*, 35:711–718, 1988.
- [56] T. A. Laurence, S. Fore, and T. Huser. Fast, flexible algorithm for calculating photon correlations. *Opt. Lett.*, 31:829–831, 2006.
- [57] G. Chirico, C. Fumagalli, and G. Baldini. Trapped Brownian motion in single- and two-photon excitation fluorescence correlation experiments. *J. Phys. Chem. B*, 106:2508–2519, 2002.
- [58] M. H. DeGroot. *Probability and Statistics*. Addison-Wesley, Reading, MA, 1986.
- [59] M. Abramowitz and I. Stegun, editors. *Handbook of Mathematical Functions, with Formulas, Graphs, and Mathematical Tables*. Dover Publications, New York, 9th edition, 1972.
- [60] Y. Chen, J. D. Müller, V. Ruan, and E. Gratton. Molecular brightness characterization of EGFP in vivo by fluorescence fluctuation spectroscopy. *Biophys. J.*, 82:133 – 1414, 2002.
- [61] E. Rhoades, E. Gussakovsky, and G. Haran. Watching proteins fold one molecule at a time. *Proc. Natl. Acad. Sci. USA*, 100:3197–3202, 2003.
- [62] D. E. Koppel, M. P. Sheetz, and M. Schindler. Matrix control of protein diffusion in biological membranes. *Proc. Natl. Acad. Sci. USA*, 78:3576–3580, 1981.
- [63] H. Qian. Equations for stochastic macromolecular mechanics of single proteins: Equilibrium fluctuations, transient kinetics and nonequilibrium steady-state. *J. Phys. Chem. B*, 106:2065–2073, 2002.

- [64] W. Magnus, F. Oberhettinger, and R. P. Soni. *Formulas and Theorems for the Special Functions of Mathematical Physics*. Springer-Verlag, New York, 1966.